



LATVIJAS
UNIVERSITATE
ANNO 1919

U N I V E R S I T Y O F L A T V I A

Faculty of Physics and Mathematics
Department of Physics

The Modelling of the Behaviour of Solid Inclusions in the EM Induced Recirculated Turbulent Flows of Liquid Metal

Mihails Ščepanskis

Advisor: Dr. phys. Andris Jakovičs

Submitted for the degree of Doctor of Physics
Subfield of Mechanics of Fluids and Gases

Rīga, 2013



**LATVIJAS
UNIVERSITĀTE**
ANNO 1919

EIROPAS SAVIENĪBA

IEGULDĪJUMS TAVĀ NĀKOTNĒ

This work has been supported by the European Social Fund within the project «Support for Doctoral Studies at University of Latvia».

Acknowledgements

Four years and half ago I came back to my native Latvia from Moscow, where I spent my student years. Since that time I am very happy to be among the friendly team of the Laboratory of Mathematical Modelling of Environmental and Technological Processes. I am very thankful to the colleagues for a warm atmosphere at the working place, nice volleyball evenings and holiday trips.

I would like to acknowledge my supervisor asoc. prof. Andris Jakovičs for his valuable advises, scientific support, understanding and help in the personal questions, as well as motivation at the moments of creative criseses.

I am also thankful to prof. Andrejs Cēbers and asoc. prof. Andris Muižnieks for valuable scientific consultations as well as Dr. Maksims Kirpo for the introduction in *Linux* and *OpenFOAM*.

The numerical calculations of this thesis were not be possible without the computational cluster of the Physical Department of the Faculty of Physics and Mathematics of the University of Latvia; therefore, I am very thankful to the administration and the employees of the department who response for the cluster operation.

I would like to thank the technical and the scientific employees of the Institute of Electrotechnology of University of Hanover where the experiment was carried out. I would like to express a special acknowledgement to prof. Egbert Baake and prof. Bernard Nacke for the management of the experiment as well as Vadims Geža and Peter Turewicz for a help and breakthrough ideas during the development of experimental technique.

The PhD studies were possible because of the financial support of European Social Fund within the project „Support for Doctoral Studies at University of Latvia”.

Finally, I would like to apologize to my wife Anna Vladimirova-Kryukova for all time I spend on my thesis but not with her and thank for the understanding and the support as well as help correcting my English publications and the present thesis.

Abstract

The thesis presents a numerical and an experimental investigation of the particle laden recirculated turbulent flow of liquid metal, which is driven by electromagnetic force. The class of such flows is typical for induction metallurgical furnaces.

The LES-based Euler-Lagrange model with the extended set of forces that influence the motion of inertial particles, is proposed in the work. Experimental investigation of the particle concentration at the quasi-stationary stage is fulfilled utilizing the the novel idea: ferromagnetic particles are proposed as a physical model of the non-conductive inclusions in liquid metal. This investigation is the first known experimental work for the distribution of solid inclusions in the bulk of electromagnetically driven liquid metal flows. The experiment proves the relevance of the proposed mathematical model under dilute conditions for modelling of the turbulent flows of liquid metal.

The behaviour of solid inclusions admixed from the surface of melt is examined, varying density and size of the particles. The investigation clarify the general scheme of particle motion in the flow, properties of the particle oscillating behaviour between the main eddies of the flow, particle agglomeration on the wall of the vessel and other key phenomena of the transport process in the concerned flows.

The particle growth extension of the transportation model estimated the deposition formation process on the wall of the vessel as a result of the changes in the thermal regime of the flow.

Content

Acknowledgements.....	3
Abstract	5
List of Figure	9
List of Tables.....	15
1. Introduction	17
1.1. Motivation.....	17
1.2. Objectives of the work	19
2. Background and literature overview.....	20
2.1. Turbulence	20
2.2. Turbulent recirculation flow inside induction furnaces.....	24
2.3. Particle transport in turbulent flows.....	30
2.4. Previous investigations of particle transport in recirculated flows	34
2.4.1. Modelling	34
2.4.2. Experimental investigation.....	35
2.5. Simulation of the deposition formation during the long-term operation of the furnaces.....	36
3. Mathematical model	38
3.1. General scheme and coupling.....	38
3.2. Lagrange particle tracking	40
3.2.1. Non-stationary flow around a sphere	40
3.2.2. Lagrange equation in turbulent flow.....	41
3.2.3. Statistical analysis of the forces	43
3.2.4. Trajectories of particles.....	45
3.3. Numerical realization of the algorithm	48
3.3.1. Solver for EM driven flow.....	50
3.3.2. Numerical mesh for HD simulation	51
3.3.3. Lagrangian tracking	59
3.3.4. Collision with the wall	62
4. Experimental verification of the model	64
4.1 Preface for the experimental investigation of the particle distribution in liquid metals	64
4.2 Experimental idea	69
4.3 Description of the experiment	71
4.4 Comparison of the experimental and numerical results.....	74
4.5 The outlook for the neutron imaging experiment	76

4.5.1.	Preliminary experiment.....	76
4.5.2.	Conclusions for the preliminary experiment.....	79
5.	Transportation of solid inclusions in the turbulent flow of ICF.....	80
5.1.	Inclusions admixture from the top surface of ICF.....	80
5.1.1	Initial admixing from the surface	80
5.1.2	Scheme of the motion of particles in the bulk of the melt	82
5.1.3	Quasi-stationary particle exchange between the zones of the main vortices.....	84
5.2.	Oscillating particle exchange between the zones of the main vortices.....	85
5.2.1	Flow velocity oscillation	86
5.2.2	Oscillation of the particle number	91
5.3.	Homogenization of the alloying particles in ICF.....	94
5.3.1	Regression model for an optimization problem	95
5.3.2	Qualitative explanation of the dependences.....	101
5.4.	The dynamics of conglomeration of the inclusions on the wall of ICF	104
6.	Estimation of the growth of inclusions in the bulk of the flow and their deposition during the long-term operation of the furnaces.....	110
6.1.	Size evolution of oxide inclusions in the bulk of the melt.....	111
6.1.1	Theoretical description	111
6.1.2	Estimation of the size evolution rate	113
6.2.	Agglomeration of the particles with the wall.....	116
1.	Surface diffusion.....	116
2.	Simulation of the neck growth during the sintering process.....	116
3.	Sintering of particles to the wall	118
7.	Summery	121
8.	Conclusions	122
9.	Outlook.....	123
	References.....	124
Appendix1.	Implementation of EM force to <i>pisoFoam</i> solver in OpenFOAM.....	134
Appendix2.	Modification of OpenFOAM libraries for particle tracking	136
Appendix3.	Particle-wall collision treatment	143

List of Figure

Figure 1.1: (a) - the scheme of the build-up formations in the channel of 1200 kW cast-iron-inductor CIF after a 14-month-long operation (<i>Drewek, 1996</i>). (b) and (c) – the photos of the clogged cross-sections of the neck and the channel of the CIF respectively (courtesy ABB Dortmund).....	18
Figure 2.1: Turbulence in nature: (a) a large-scale turbulence in the atmosphere of Earth; (b) the turbulent trace behind the pillar of the bridge across the river Daugava in Daugavpils.....	21
Figure 2.2: Sketch of axis-symmetric induction system on the example of an induction crucible furnace.	25
Figure 2.3: (a) Axial velocity profile at the middle of a lower eddy ($z = 13$ cm); (b) Axial velocity profile at the axis of the symmetry. From <i>Kirpo (2008-PhD)</i>	27
Figure 2.4: (a) Average velocity pattern measured using the Vives' probe; (b) the LES calculated average flow velocity. From <i>Kirpo (2008-PhD)</i>	28
Figure 2.5: (a) Maximal axial velocity dependence on the inductor current for different frequencies in the geometry of ICF-1; (b) Dependence of axial velocity at the central axis and the wall at the center of eddy on the inductor current for 364 Hz frequency. From <i>Kirpo et al. (2007)</i>	29
Figure 2.6: (a) tracer particles illuminated by a green laser (courtesy E. Bodenschatz); (b) A trajectory of a particle in a small-scale vortex filament in a turbulent flow. From <i>Toschi & Bodenschatz (2009)</i>	33
Figure 2.7: Time dependence of the overheat in the channel (a) and of the free cross section area of the channel (b) in the CIF with Todnem inductor, which is operated at 450/600 kW power, the reference temperature is 1500 °C. From <i>Bethers et al. (1995)</i>	37
Figure 3.1: General scheme of the algorithm.	38
Figure 3.2: (a) Different approximations for the lift coefficient C_L (here $Sr = 0.1$); (b) the McLaughlin-Legendre-Magnaudet approximation for the lift coefficient C_L for different Sr	42
Figure 3.3: The half width of the calculated statistical distribution of Re_p . (a) $S = \rho_f/\rho_p = 1.5$; (b) $S = 1.0$	44
Figure 3.4: The half width of the calculated statistical distribution of the drag, lift, acceleration and added mass force densities F/V_p , where V_p is a particle volume, for the particles with (a) $S = \rho_f/\rho_p = 1.5$, (b) $S = 1.5$	45
Figure 3.5: The trajectories of 100 μm particles, which start their motion at the 10th s after the beginning of the stirring near the top surface of ICF-1. The first row – the view from the top surface; the second row – the view from the side.	46
Figure 3.6: The trajectories of the particles with the drown force vectors: the first row – $-F_{em}$; the second row - F_{lift} . EM force is shown in the direction from the wall as it is defined in the equation (3.16), however, due to the negative sign in the equation, it pushes the particle to the wall.	47
Figure 3.7: The trajectories of particles taking into account different sets of forces: additional forces are sequentially added to the basic set (see the legend).	48

Figure 3.8: Trajectories of particles with the different diameter (see in the legend) that begin their motion at the same position near the top surface of the melt. The first row - view from the top surface; the second row – view from the side.....	49
Figure 3.9: Different meshes of ICF-1. The 1 st row – a homogeneous mesh without any refinement; the 2 nd row – a mesh with the refinement only in the radial direction; the 3 rd row – a mesh with the refinement in the radial and axial directions; the left column – a mesh in a horizontal cross-section of the crucible; the middle column – the enlargement of the mesh in the left column near the wall; the right column – the enlargement of the mesh in a central vertical cross-section of the crucible near the wall.	52
Figure 3.10: The distribution of turbulent kinetic energy in the ICF-1 (experimental results, from <i>Kirpo, 2009-PhD</i>). (a) axial component, (b) radial component, (c) tangential component, (d) total.	54
Figure 3.11: Numerical results of the distribution of the axial component (the 1 st row) and full (the 2 nd row) turbulent energy in ICF-1 (the left column – the central vertical plane; the right column – isosurface), which are calculated in ANSYS CFX software on the homogeneous mesh without refinement near the wall (Figure 3.9 – 1 st row).	55
Figure 3.12: The distribution of the component of turbulent energy, calculated with the LES turbulence model in ANSYS CFX using the mesh with only radial refinement (Figure 3.9 – 2 nd row). From <i>Umbraško (2011-PhD)</i>	56
Figure 3.13: Numerical results of the distribution of turbulent energy in the central vertical plane, which is calculated using the mesh with the radial refinement near the wall (Figure 3.9 – 2 nd row) in the open-source OpenFOAM software.	57
Figure 3.14: Numerical results of the distribution of the axial component of turbulent energy in the central vertical plane. The distribution is calculated using the mesh with the radial & axial refinement near the wall (Figure 3.9 – 3 rd row) in the open-source OpenFOAM software. (a) central vertical cross section of ICF-1, (b) central horizontal cross section of ICF-1.	58
Figure 3.15: Angular averaged numerical results of distribution of the axial component of turbulent energy in the central vertical plane. The distribution is calculated using the mesh with radial & axial refinement near the wall (Figure 3.9 – 3 rd row) in the open-source OpenFOAM software.	58
Figure 3.16: Axial distribution of particle volume concentration in ICF-2 at different moments of time: (a) 0.25 s; (b) 0.4 s; (c) 1 s; (d) 10 s. Initially the particles were situated on the top surface of the melt (Figure 5.6). The calculations were done with (the blue line) and without (the red line) artificial random angular velocity with the amplitude 4 cm/s.	59
Figure 3.17: Radial distribution of particle volume concentration in ICF-2 at different moments of time: (a) 0.05 s; (b) 0.2 s; (c) 0.5 s; (d) 15 s. Initially the particles were situated on the top surface of the melt (Figure 5.6). The calculations were done with (blue line) and without (red line) artificial random angular velocity with amplitude 4 cm/s....	60
Figure 3.18: Trajectories of particles, calculated in ICF-1 using different number of the Lagrange time steps n per one HD time step.....	61
Figure 3.19: Residual Γ depending on the iteration number n . The residual is defined by the expression (3.18).	61

Figure 4.1: The results (velocity – left column, temperature – right column) of transient 2D k-ε simulation of 41.2% KCl-LiCl system without any artificial cooling. The time is shown under each column. The temperature of environment is 23 C.....	67
Figure 4.2: The results (velocity – left column, temperature – right column) of transient 2D k-ε simulation of 41.2% KCl-LiCl system with intensive artificial cooling of the side wall. The time is shown under each column. The temperature of environment is 23 C.	68
Figure 4.3: Magnitude of the EM force density (radial component) in the case of non-conductive & non-magnetic and well-conductive & ferromagnetic particles (see equations (4.2) and (4.4) respectively).....	70
Figure 4.4: Microscope photo of the spherical iron particles that are used in the experiment. The sizes of some particles are marked.	71
Figure 4.5: The cover with the holes for the pipette on the ICF-2.	72
Figure 4.6: The photos of the experimental devices.....	73
Figure 4.7: The image of the drained crucible after the series of the experiment (view from the top of the crucible).	74
Figure 4.8: Experimental and numerical results of the concentration of solid $300\pm 50\ \mu\text{m}$ inclusions in the flow of ICF at $11\pm 2\ \text{s}$ from the beginning of stirring (quasi-stationary regime). The experimental samples were taken in the areas, which are marked with the red rectangles on the sketch of the crucible (left image).....	75
Figure 4.9: Two cross-sections of the solid sample of the Rose’s metal including the solid particles. The particles are indicated with green circles. The sample was used for the preliminary experiment of neutron imaging.....	77
Figure 4.10: The neutron images of different horizontal slices of the sample (the pictures are obtained as a superposition of images from two perpendicular beams). The white dots correspond to the inclusions, black regions mean voids, but grey area remains to the metal.	77
Figure 4.11: 3D reconstruction of the distribution of the solid inclusions in solid samples of Rose’s metal using neutron-imaging technique.	78
Figure 5.1: Snapshots of the admixing of 4 kg carbon into 4 t steel alloy in industrial ICF, applying different frequency and power. Courtesy Otto Junker GmbH.	81
Figure 5.2: The surface of the Wood’s metal with iron particles after 10 s of the steering in the ICF-2. The particles were situated on the surface before steering (like on the left picture).	82
Figure 5.3: The surface of the Wood’s metal with SiO_2 (the upper row) and ZrO_2 (the lower row) particles after 10 s of steering in the ICF-2. The particles were situated on the surface before steering (like on the left picture of Figure 5.1).....	83
Figure 5.4: The admixing of the $100\ \mu\text{m}$ carbon particles into the steel alloy in 2 kW ICF (125 Hz). Snapshots of the industrial process by Otto Junker GmbH (the first row). The simulated results: view from the top of the furnace (the second row); particles in the bulk of the flow, view from the side of furnace (the last row).....	84
Figure 5.5: Axial (a) and radial (b) distribution of the particle concentration in ICF-2. Different curves correspond to different moments of time that are shown in the legend (in seconds from the beginning of the stirring).	85

Figure 5.6: The scheme of the initial motion of the inclusions, which are situated on the open surface of the melt with the developed flow in ICF. The flow velocities are qualitatively shown in the vertical plane at the appropriate time moment (the time is defined from the zero velocity state).....	86
Figure 5.7: The evolution of the concentration of the particles with the diameter 50 μm in ICF-1. Concentrations are shown in the central vertical plane.....	87
Figure 5.8: Dynamics of the concentration of the particles in different areas of ICF-2 (simulated results). Areas are numbered on the sketch of the crucible (left image).....	88
Figure 5.9: The sketch of an axial-symmetric ICF-1 with a vertical scale, which is measured from the bottom of the crucible.....	88
Figure 5.10: The axial distribution of the axial part of turbulent kinetic energy in the ICF-1, integrated in a radial direction.....	89
Figure 5.11: The spectrum of the axial flow velocity at the half height of the inductor near the wall $r=150$ mm, $h=280$ mm (from the experimental data).....	90
Figure 5.12: The spectra of integral pulsations in the middle zone of the ICF-1 between the mean vortices (from the experimental data). Different curves correspond to the different interval of integration. The height of the lower and the upper borders of these intervals are shown in the brackets in the legend (mm from the bottom). The total height of the ICF-1 is 570 mm. The integral spectra are calculated according to the expression (5.1).....	91
Figure 5.13: Oscillation of the number of particles in the middle zone of the ICF-1 (in the interval [260-310] mm from the bottom). The upper row: different $S=\rho_l/\rho_p$, but common diameter - (a) $D = 50$ μm , (b) $D=100$ μm ; the lower row: different diameter D , but common liquid-to-particle density ratio - (c) $S=1.0$, (d) $S=1.1$. Numerical results.....	92
Figure 5.14: The oscillations of the number of 100- μm particles with liquid-to-particle density ratio $S = 1.0$ in the middle zone of ICF (numerical results). Different curves correspond to a different width of the middle zone. The height of the lower and the upper borders of these intervals is shown in the brackets in the legend (mm from the bottom).	93
Figure 5.15: The spectra of the integral pulsations of the flow velocity (experimental data) and the number of particles in the middle zone of the ICF in the interval [260-310] mm from the bottom (numerical data). The spectrum of the particle oscillations is created for 100- μm inclusions with the liquid-to-particle density ratio $S=1.0$	93
Figure 5.16: The scheme of the zones of the upper and the lower eddy. The location of zones is illustrated on the background of (a) an average flow and (b) turbulent kinetic energy (both are drawn on the half of the crucible).....	96
Figure 5.17: Difference between the number of the particles in the zone of the upper and the lower eddies normalized with respect to the number of particles in both zones. Liquid-to-particle density ratio: (a) $S = 1$; (b) $S = 1.1$; (c) $S = 1.5$	97
Figure 5.18: Total number of the particles in both zones of the eddies. Liquid-to-particle density ratio: (a) $S = 1$; (b) $S = 1.1$; (c) $S = 1.5$	98
Figure 5.19: $\Delta N/N$ for particles with the diameter 200 μm : the illustration of the homogenization quantitative parameters.	99

Figure 5.20: Quantitative parameter δ (see Figure 5.19) as a function of the liquid-to-particle density ratio S (a) and the diameter of particle D (b).	100
Figure 5.21: Quantitative parameter a (see Figure 5.19) as a function of the liquid-to-particle density ratio S (a) and the diameter of particle D (b).	100
Figure 5.22: (a) simplified trajectories of the particle on the lower border of the upper mean eddy near the wall for cases with different diameters (the arrow shows the increasing of the diameter); (b), (c) directions of different forces applied to the big particles at $S > 1$ ($\rho_p < \rho_f$) and $S = 1$ ($\rho_p = \rho_f$) respectively.	102
Figure 5.23: Possible ways for the particles after coming to the middle zone near the wall and the changes in the probability to choose one of the ways with respect to the particle diameter D and $S = \rho_p/\rho_f$. The arrows point to the zone, where the probability increases with the parameter increase over the arrow.	103
Figure 5.24: Percentage of the 200 μm particles conglomerated on the wall.	103
Figure 5.25: Axial distribution of surface concentration (cm^{-2}) of the conglomerated on the wall 300 μm particles in ICF-1. The columns correspond to a different softness of particle-wall collisions (the coefficients, which characterize the rate of semi-soft collision $\varepsilon = \mu$ are defined in Chapter 3.3.4). The rows correspond to different liquid-to-particle density ratio S . The results are angularly averaged.	105
Figure 5.26: Axial distribution of surface concentration (cm^{-2}) of the 300 μm particles conglomerated on the wall in ICF-1A. The columns correspond to a different softness of particle-wall collisions (the coefficients, which characterize the rate of semi-soft collision $\varepsilon = \mu$ are defined in the Chapter 3.3.4). The rows correspond to different liquid-to-particle density ratio S . The results are angularly averaged.	106
Figure 5.27: Percentage on the conglomerated 300 μm particles on the wall for different coefficients of semi-soft collision. $S = 1.1$. (a) ICF-1; (b) ICF-1A.	107
Figure 5.28: Dynamics of the axial distribution of concentration of the conglomerated 300 μm particles (the upper part of the crucible). (a) $S = 1.0$; (b) $S = 1.1$; (c) $S = 1.5$. The coefficients of semi-soft collision $\varepsilon = \mu = 0.9$. The results are angularly averaged.	108
Figure 5.29: Axial distribution of the concentration of the conglomerated 300 μm particles (the upper part of the crucible) at the 18 th second from the beginning of stirring. (a) ICF-1; (b) ICF-1A. The coefficients of semi-soft collision $\varepsilon = \mu = 0.9$. The results are angularly averaged.	109
Figure 6.1: The diffusion limited growth / dissolution of a particle, assuming instant supersaturation rate Δ and the critical radius R_{cr} . Non-dimensional radius r depending on non-dimensional time ($t \cdot \theta$) for different non-dimensional critical radius r_{cr}	112
Figure 6.2: Temperature distribution in the central vertical cross-section of 215kW CIF ($^{\circ}\text{K}$). From <i>Kirpo (2008-PhD)</i>	115
Figure 6.3: The initial stage of sintering of Al_2O_3 balls. The arrows point the tracks of broken initial necks. From <i>Rao & Culter (1972)</i>	117
Figure 6.4: Dynamics of the neck growth during the sintering of two spheres: 20 μm and 2 μm in diameter. (a) The cross section in different time moments from the beginning of sintering; (b) The minimal neck diameter as the function of time. The curve is fitted	

with the function $Dn = a \cdot t + t_0b$. The least square method gave $a = (1.4 \pm 0.5)e-1 \mu\text{m} \cdot \text{s}^{-b}$; $t_0 = 13 \pm 1 \text{ s}$; $b = (28.4 \pm 0.7)e-2$118

Figure 6.5: Compressive and tensile strength for Al_2O_3 at different temperatures. From *Shackelford & Alexander (2001)*.....119

List of Tables

Table 2.1: Parameters of ICF-1.	28
Table 2.2: Parameters of ICF-2.	28
Table 2.3: Characteristic velocity and period of the flow and velocity pulsations in geometry of ICF-1. From <i>Kirpo et al. (2005)</i>	30
Table 2.4: Comparison of physical properties of liquid Wood's metal and steel.	30
Table 2.5: Non-dimensional numbers for the flows in ICF-1 and ICF-2.	30
Table 4.1: Material properties of 41.2% KCl – LiCl eutectic.	65
Table 4.2: The estimation of the minimal penetration depth and the maximal full-effective current in the inductor for the melt of KCl-LiCl eutectic.	66
Table 4.3: The calculated induced power in the melt of KCl-LiCl eutectic.	66
Table 4.4: Comparison of the conditions in the experiment and the simulation.	72
Table 5.1: Density of the typical alloying elements.	94
Table 5.2: The values of the quantitative parameters of the homogenization $\delta(S,D)$ and $a(S,D)$ (see Figure 5.19).	99
Table 5.3: The time of the homogenization in ICF-1 for the particles with different D and S . The values are calculated taking into account equations (5.2–5.4).	101
Table 5.4: Deposition rate (percentage from the total number of particles per second) of 200 μm particles in ICF-1.	103
Table 6.1: Time necessary to change twice the volume of a Al_2O_3 particle in a steel melt. Comparison of the collision and the Ostwald ripening models. Presented results are calculated for 215 kW CIF, assuming the homogeny distributed inclusions with the common volume concentration 1%, the concentration of particles in the each size group is assumed equal. The degree of turbulent energy dissipation rate E is calculated equal to $1\text{e-}2 \text{ m}^2/\text{s}^3$	114
Table 6.2: Time necessary to change twice the volume of a Al_2O_3 particle in a steel melt, assuming the relative supersaturation 0.472, which corresponds approximately to the transitions from working to weekend regime of the CIF operation. The other parameters are the same as in the Table 6.1.	115
Table 6.3: The estimation of the increase of a particle after the travel through the channel of CIF. The channel overheat is assumed linearly distributed from the neck to the maximum of 34 K over the neck temperature at the lower point of the channel. The time of the particle travel is assumed equal to 1 min.	115
Table 6.4: Values of surface diffusion coefficient for Al_2O_3 at the temperatures $T_a = 1748 \text{ K}$ (Dsa) and $T_b = 1688 \text{ K}$ (Dsb). The values are calculated according to expression (6.13) using the values of D_0 and E_{diff} from the references mentioned in the last column. The temperatures T_a and T_b correspond to the ordinary and the weekend regimes of CIF operation (see the Chapter 2.5).	117
Table 6.5: Estimation of the forces acting on the attached to the wall Al_2O_3 particle in 215 kW CIF (N/m^3). Drag and lift forces depend on the particle size, therefore, they are given in respect to the particle radius in the reference case (10 μm) for better comparison with other forces.	120

Table 6.6: The minimal thickness of the sintering neck normalized to the particle size $R_{break}R$ and time to growth to critical thickness t_{sint} (according to the model (6.15)) in the channel of CIF.....120

1. Introduction

The present PhD thesis deals with a specific class of turbulent flows and describes behavior of solid inclusions in the flows of this class. The recirculated (closed) flows, where induced electromagnetic (EM) force is the cause of a turbulent motion of liquid, constitute the mentioned class of turbulent flows.

The metallurgical equipment for induction melting and stirring of metals usually are operated such way that the flow of a liquid metal inside the equipment belongs to the described class of turbulent flows. Such technological application reinforces a fundamental interest for the investigation of this flow class. Apparently, the efficiency of induction equipment and processes can be improved by modeling of the flow.

Generally, the turbulence itself was studied during the whole 20th century by numerous scientific groups, but, as it is a very complex phenomenon of the liquid motion, the turbulence in different geometries is still urgent area of interest, especially, the specific complex geometries like that, which will be analyzed in this work. Thus, such specific flows are also of the fundamental interest.

Chapter 2 of the present thesis covers the status quo in the research of turbulence and, particularly, the mentioned specific class of EM induced recirculated turbulent flows. However, the present work goes beyond a one-phase flow and proposes a numerical model for the investigation of a particle laden (solid-liquid two phase) flow of such class. This case has a very sufficient industrial application, which will be shown below.

1.1. Motivation

The turbulence properties of EM induced recirculated turbulent flows were studied only in the last two decades with a significant progress in the last years when the Large Eddy Simulation (LES) approach allowed to research the essential peculiarities of the flow, such as low frequency pulsations between mean eddies (see Chapter 2.2). Despite the fact that the velocity distribution and heat transfer are satisfactory examined in such flows, the transportation of impurities, that is solid inclusions, has not been researched until nowadays. Therefore, the present study, apparently, is of the interest as a fundamental research.

Moreover, despite the fact that EM heating and stirring is one of the most effective and widespread methods for melting and processing of conductive materials, there are some essential industrial problems concerning the inclusion transportation, and these processes are still poor investigated.

The alloying particles are mixed in a steel melt to improve properties like strength, hardness and a wear resistance. It is important to achieve a homogeneous admixtures distribution to ensure a high quality of the alloy. Furthermore, it is desirable to reduce the time of mixing to decrease the energy consumption and prevent the melt from excessive overheating. Most impurities and alloying elements have higher melting temperature than metal. Thereby the melt can contain inclusions as solid particles. Carbon admixing in steel from the open surface of the melt in an induction crucible furnace (ICF) can be mentioned as an example of such technology. As far as steel is not transparent, the optimization of this industrial process is the challenge for

the numerical modeling. The application of a numerical model, which is presented in the Chapter 3 and verified experimentally in the Chapter 4, for investigation of mentioned industrial process is presented in the Chapter 4.5.

Another industrial problem addressing the operation of induction furnaces and the quality of alloys is the deposition of impurities like oxides as well as the erosion of the wall of crucible. This problem mostly appears in a channel induction furnace (CIF). The deposition can significantly reduce the efficiency of the equipment up to breakdown (channel clogging). As it is shown on the Figure 1.1, the rate of the clogging dramatically increases when the impurities start to deposit in the porous substance, like a sponge. This regime of a fast clogging, which reduces the active cross section of the channel very fast, attracts the attention of the operators of furnaces. The author believes that this sponge-like clogging can be fulfilled by the depositing big particles, which previously grew in the bulk of the melt.

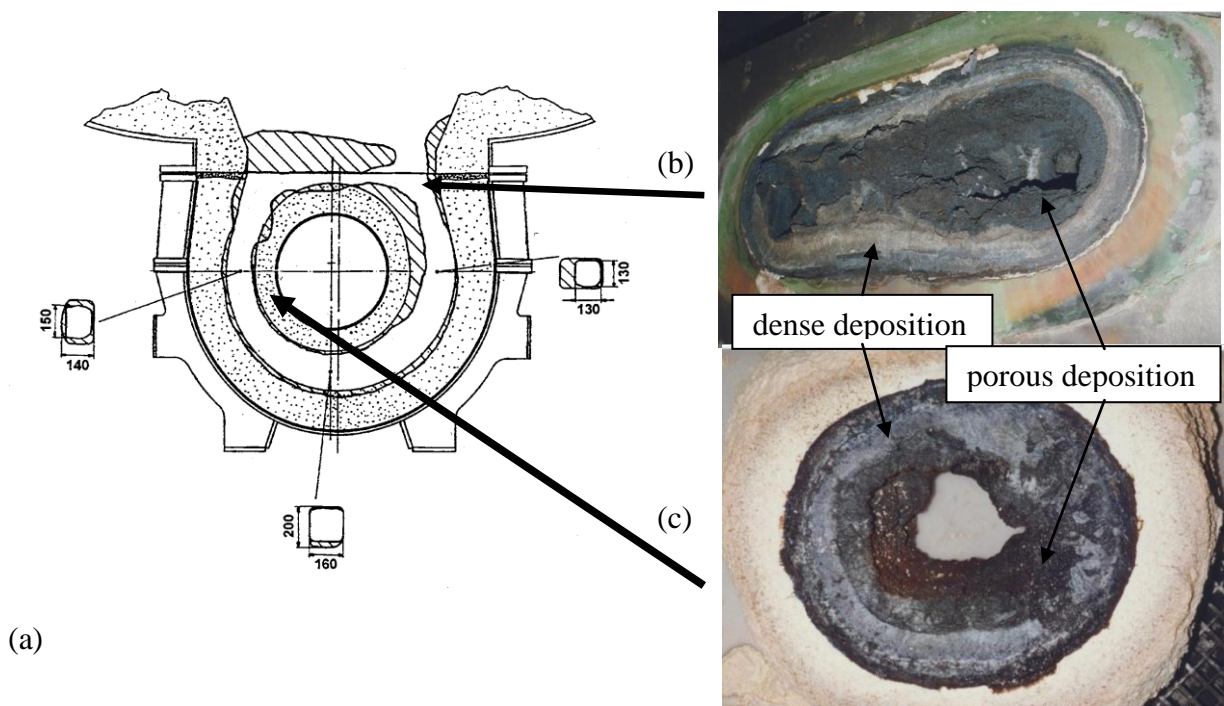


Figure 1.1: (a) - the scheme of the build-up formations in the channel of 1200 kW cast-iron-inductor CIF after a 14-month-long operation (*Drewek, 1996*). (b) and (c) – the photos of the clogged cross-sections of the neck and the channel of the CIF respectively (courtesy ABB Dortmund).

Taking into account this hypothesis, it is possible to state that the simulation of the particles with the invariable size is not completely relevant to the porous clogging problem and the size evolution of the inclusions should be taken into account. Thus, the full simulation of the described problem goes beyond the particle tracking model, which is the main focus of the present work. However, the deposition process and a particle growth in the bulk of the melt, which described the mentioned phenomenon, are definitely based on the particle transportation. The Chapter 6 contains the estimation of these processes in order to show the way for the extension of the tracking model for the goals of the described industrial problem, which, however, is not included in the main purpose of the present work.

Generally, the described industrial cases testify the importance of the relevant transportation model of the solid inclusions in the recirculated flows of induction furnaces. The

investigation, which will be done using such model, coupled with the deposition and particle size evolution models, can solve a wide range of the metallurgical problems, as well as they present a fundamental interest.

1.2. Objectives of the work

Research objects of this work are the transportation of solid inclusion in the specific class of the turbulent recirculated flow of liquid metal, and, secondly, the process of the deposition of particles and their growth in the bulk of the melt. The cylindrical vessel inside the solenoid of alternative current (such object is the simplified model of the induction crucible furnace) is the simple object; therefore, it is selected for this research as a representative of a recirculated flow class. Such relatively simple geometry also allows to carry out the experimental verification of the numerical models using an original self-developed technique (see Chapter 4).

This thesis will prove that *the LES based Euler-Lagrange approach in the limit of dilute conditions is able to simulate the dynamics of solid inclusions in the recirculated turbulent flow of liquid metal as well as it describes the related key phenomena.*

The goal of this work is *to build and experimentally verify the model, investigate dynamics of the solid inclusions in the flow of the described class.*

This goal will be achieved fulfilling several tasks:

1. To prepare the simulation tool for the investigation of the dynamic of inclusions in the described flows.
 - a) To create the relevant mathematical model of particle tracking in specific flows;
 - b) To propose the novel experimental technique for the investigation of particle distribution in liquid metals in the presence of EM field;
 - c) To verify the model experimentally.
2. To investigate the following key phenomena of the inclusion transport in the flow of the induction furnaces:
 - a) the initial stage of admixing of alloying inclusions from the open surface of the melt;
 - b) oscillating particle exchange between the zones of the mean vortices;
 - c) model the axial homogenization of the alloying inclusions in induction furnace;
 - d) dynamics of the agglomerations of the inclusions near the wall of the furnace.
3. To estimate the growth of the inclusions in the bulk of the flow and their deposition during a long-term operation of the furnaces.

2. Background and literature overview

The present PhD thesis deals with turbulent flows and the behavior of solid inclusions in the specific metallurgical applications, where induced EM force is the reason of the turbulent motion of liquid. Turbulence itself was studied during the whole 20th century by numerous scientific groups, but, as it is a very complex phenomenon of liquid motion, turbulence in different geometries is still an urgent area of interest, especially, the specific complex geometries like that, which will be analyzed in this work. Turbulence plays significant role in the operation of a metallurgical induction equipment, but is still researched fragmentary. At the first place the author will describe turbulence itself in this chapter while the previous studies of the turbulence in particular geometries of the metallurgical furnaces will be described after that.

2.1. Turbulence

Turbulence in fluid flows is a phenomenon that cannot be defined easily (see, e.g., *Tsenober, 2001*). However, these flows appear in nature and technologies very frequently and are easily recognized. Figure 2.1 (a) illustrates the formation of a large-scale atmospheric vortex, which indicates to the presence of atmospheric turbulence. Figure 2.1 (b) shows the turbulent trace behind the rock in the river. These two examples illustrate an easy recognition of turbulence in an everyday life. Nevertheless, the turbulence should be described below from the physical point of view.

Turbulent fluid motion is an irregular condition of the flow in which various quantities show a random variation with the time and the space coordinates, so that statistically distinct average values can be discerned (*Hinze, 1959*). The main reason of such motion is the fact that the classical momentum diffusion mechanism becomes second to the momentum convection. And when the flow gets unstable to perturbations, turbulence occurs. Such regime is characterized with the three-dimensional vortex generation mechanism and vortex fluctuations.¹

Turbulent flow is seemingly random, chaotic and unpredictable. However, it can be realized as a superposition of a spectrum of velocity fluctuations and eddies. The eddies can be loosely defined as coherent patterns of velocity, vorticity and pressure. Consequently, turbulent flows may be viewed as made of an entire hierarchy of eddies over a wide range of length scales and the hierarchy can be described by an energy spectrum that measures the energy in velocity fluctuations for each wave number.² The energy “cascades”, when it is transferred to the smaller scales units until it is finally dissipated on a molecular scale, was described in the poetic definition of turbulence by *Richardson (1922)*:

Big whorls have little whorls,
which feed on their velocity;
And little whorls have lesser whorls,
And so on to viscosity.

¹From the lecture on DNS/LES incompressible turbulent flows” by prof. R. Friedrich (Technical University of Munich) in PhD school “Modelling for Material Processing” in University of Latvia, Riga on September, 2010.

²From the article “Turbulence” in the free web-encyclopedia “Wikipedia” (<http://en.wikipedia.org/wiki/Turbulence>).

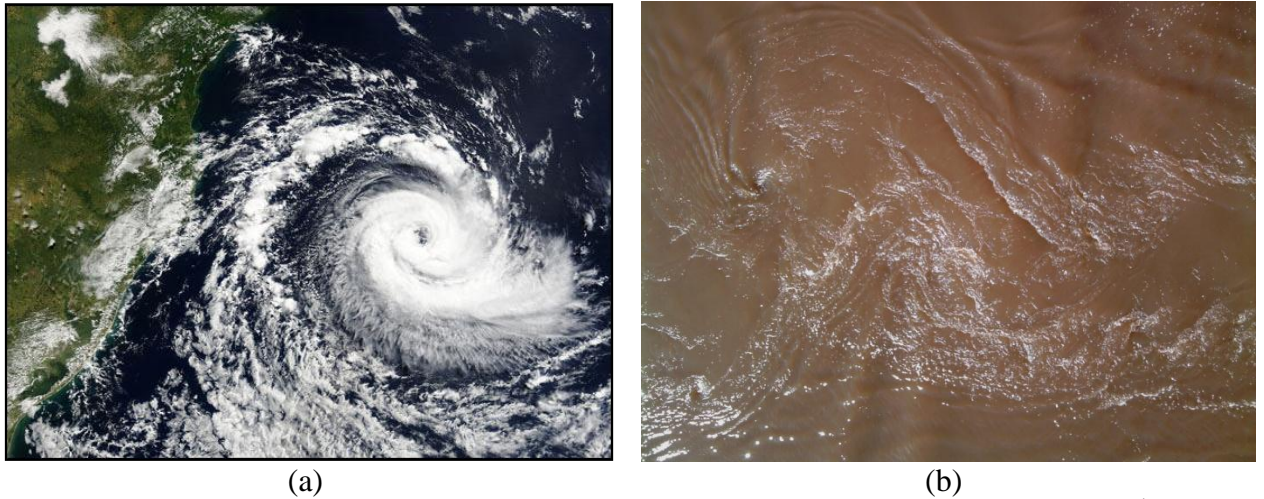


Figure 2.1: Turbulence in nature: (a) a large-scale turbulence in the atmosphere of Earth¹; (b) the turbulent trace behind the pillar of the bridge across the river Daugava in Daugavpils².

The beginning of the turbulent researches goes deep in the history. The figure of turbulent flow found in the sketch book of Leonardo daVinci (circa 1500), along with a remarkably modern description:

“... the smallest eddies are almost numberless, and large things are rotated only by large eddies and not by small ones, and small things are turned by small eddies and large.”

Such phenomena were termed “turbolenza” by da Vinci, and hence the origin of our modern word for this type of a fluid flow.³

But there was no substantial progress in its understanding until the late 19th century. *Bussinesq* (1877) brought forward the hypothesis that turbulent stresses are linearly proportional to mean strain rates, which becomes the cornerstone of the most turbulent models. Reynolds’ experiments and his seminar paper (*Reynolds*, 1894) led to the identification of the Reynolds number⁴ as the only physical parameter involved in the transition to turbulence. Reynolds concluded that turbulence was far too complicated ever to permit a detailed understanding, and he introduced the decomposition of flow variables into mean and fluctuating parts. Reynolds proposed the random description of turbulent flows. At approximately the same time *Poincaré* (1899) found that relatively simple nonlinear dynamical systems were capable of exhibiting chaotic random-in-appearance behaviour that was, in fact, completely deterministic. And only 70 years later *Lorenz* (1963) proposed possible links between the “deterministic chaos” and turbulence. Earlier *Laray* (1933; 1934) undertook the first truly mathematical analysis of the Navier-Stokes equations, which was the ground work for the developing analytical tools for the deterministic approach to the study of the Navier-Stokes equations and their turbulent solutions.

Nevertheless, following Reynolds’ introduction of the random view of turbulence and the proposed statistical approach, *Prandtl* (1925) obtained the first major result – he predicted the

¹From the web-page of the Center of Atmospheric Ocean Science, Courant Institute of Mathematical Science (http://caos.cims.nyu.edu/page/what_is)

²The photography was done by the author of the present thesis on 22nd of April, 2013 at the time of the spring flood.

³From the introductory lecture on Turbulence by J. M. McDonough (Department of Mechanical Engineering and Mathematics, University of Kentucky), 2004-2007.

⁴ Reynolds number $Re = \frac{uL}{\nu}$, where u is velocity of the flow, L is a characteristic linear dimension, ν is kinematic viscosity.

eddy viscosity (introduced by Boussinesq). His theory was based on an analogy between turbulent eddies and molecules or atoms of gas and purportedly utilized kinetic theory to determine the length and the time scales needed to construct eddy viscosity. *Taylor (1935)* made the next step forward and introduced formal statistical methods involving correlations, Fourier transforms and power spectra into the turbulent literature. He also showed that the flow through a mesh in wind tunnel could be viewed as homogeneous and isotropic. Later *Kolmogorov (1941)* published three papers that provided the often quoted results of turbulence theory, which is now referred to as the “K41 theory”. During the 1940s *Hopf (1948)* and *Landau & Lifshitz (1959)* independently proposed that as Reynolds number is increased a typical flow undergoes infinity of transitions during each of which an additional incommensurate frequency arises due to flow instabilities, leading to a very complicated, apparently random flow behaviour.

The experimental work during 1950s raised doubts on the issue of the validity of the random view of turbulence. *Emmons (1951)* showed that a completely random viewpoint was not really tenable. The measurement technique became sufficiently sophisticated to indicate existence of so-called “coherent structures” contradicting the random view of turbulence. As it was already mentioned (*Lorenz, 1963*) the progress on the mathematical understanding of the Navier-Stokes equation was achieved in 1960s. Studies were conducted in the context of a basic analysis (i.e., existence, uniqueness and regularity of solutions – *Ladyzhenskaya, 1963*) and in the field of dynamic systems (*Smale, 1965; Arnol'd, 1964*).

The “modern” view of turbulence was proposed in 1970s (*Ruelle & Takens, 1971*). It was shown that the Navier-Stokes equation, viewed as a dynamic system, is capable of production of chaotic solutions exhibiting sensitivity to the initial conditions and the equation associated with an abstract mathematical construct called “strong attractor”.

Turbulence experimentation became popular in 70s and 80s. The Kolmogorov ideas were tested in details. General correspondence between theory and experiment but a lack of complete agreement motivated numerous studies to explain discrepancies. Similar work is carried on even nowadays. Thereby, the attention began to focus on more practical flows such as wall-bounded shear flows (especially, boundary layer transition), flow over and behind cylinders and spheres, jets, plumes, etc.

The computation techniques were developed relatively recently. *Deardorff (1970)* proposed the LES method. This was rapidly followed by the first direct numerical simulation (DNS) by *Orszag & Patterson (1972)* and introduction of a wide range of Reynolds-averaged Navier-Stokes (RANS) approach (*Lauder & Spalding, 1972; Launder et al., 1975*).^{1,2}

It was immediately clear that the computational resources are not able to provide DNS in the 80s. However, the first DNS calculations for simple cases were carried out in the late 80s and 90s. As far as DNS results leave no doubt about their relevance, the progress in this field in last two decades will be described below.

Vincent & Meneguzzi (1991) performed DNS calculations of homogeneous isotropic turbulence found vortical tubes of a length comparable to the integral scales and diameter of a

¹LES, DNS and RANS will be discussed in Chapter 2.2.

² The overview of the historical development of turbulence is written mostly using the introductory lecture on Turbulence by J. M. McDonough (Department of Mechanical Engineering and Mathematics, University of Kentucky), 2004-2007.

few Kolmogorov length¹ scales. *Lee et al. (1987)* simulated homogeneous shear turbulence and demonstrated that streaky structures appear also in unbounded flows forming an array of high- and low-speed regions, which develop as a consequence of high shear rate rather than of wall blocking.

Many DNS provided the knowledge about wall bounded flows and near-wall effects. *Kim et al. (1987)* simulated fully developed channel flow and initiated a bulk of further investigations. This DNS results were used by *Choi et al. (1994)* to develop the techniques for an active turbulence control. Using Kim's data of the channel flow *Antonia & Kim (1994)* studied the low-Reynolds number effects on near wall turbulence. *Härtel & Kleiser (1998)* analysed and modelled a subgrid-scale motion in a wall layer. *Moiser & Moin (1987)* found Taylor-Görtler vortices² in a channel flow to be responsible for a half of the differences in the Reynolds and the wall shear stress between the convex and the concave sides. *Perot & Moin (1995)* isolated the viscous and kinematic mechanisms of the wall/turbulence interaction and developed improved near-wall models for dissipation, pressure-strain and turbulent transportation terms of the Reynolds stress equation³.

Eggels et al. (1994) discussed DNS data of a fully developed flow in a pipe with a circular cross-section. *Spalart (1988)* presented a direct simulation for self-similar and zero-pressure gradient boundary layers. Separate turbulent boundary layer along a flat plate was simulated by *Na & Moin (1998)*. *Neves et al. (1994)* investigated boundary layers with the convex transverse curvature developing on a long cylinder.

Clear that DNS of flow in the complex geometries needs significant computation resources. Therefore, there are only several such investigations. *Le et al. (1997)* investigated turbulent boundary layer separating at a backstep and re-attaching. A related problem, namely the turbulent flow in a sudden pipe expansion was studied by *Wagner (1996)*. *Choi et al. (1993)* simulated turbulent flow over surface-mounted riblets.⁴

Obviously, there are several resent DNS data of the complex geometries, however, they will be not discussed here. The main goal of the present work is to investigate mass transportation in turbulent flows of conductive liquid metal in induction furnaces. Therefore, the next chapter will be focused on the description of this type of flows and the induction equipment itself. Nevertheless, it should be mentioned, that there is no known DNS data of such flows, the

¹ Kolmogorov length is the smallest scale in turbulence, where viscosity dominates and the turbulent kinetic energy is dissipated into heat. $\eta = \left(\nu^3/\varepsilon\right)^{\frac{1}{4}}$, where ν is kinetic viscosity; ε is dissipation rate of turbulent kinetic energy.

² Taylor-Görtler vortices are the secondary flows that appear in a boundary layer flow along a concave wall. If the boundary layer is thin compared to the radius of curvature of the wall, the pressure remains constant across the boundary layer. On the other hand, if the boundary layer thickness is comparable to the radius of curvature, the centrifugal action creates a pressure variation across the boundary layer. This leads to the centrifugal instability (Görtler instability) of the boundary layer and consequent formation of Taylor-Görtler vortices. - From the article "Görtler vortices" in the free web-encyclopedia "Wikipedia" (http://en.wikipedia.org/wiki/G%C3%B6rtler_vortices).

$$\begin{aligned} \underbrace{\frac{\partial}{\partial t} \left(\overline{u_i u_j} \right)}_{\text{local time derivation of ReynoldsStress}} + \underbrace{\frac{\partial}{\partial x_k} \left(u_k \overline{u_i u_j} \right)}_{\text{convection}} = & - \underbrace{\frac{\partial}{\partial x_k} \left[\overline{u_i u_j u_k} + \frac{p}{\rho} \left(\delta_{kj} u_i + \delta_{ik} u_j \right) \right]}_{\text{turbulent diffusion}} + \underbrace{\frac{\partial}{\partial x_k} \left[\nu \frac{\partial}{\partial x_k} \left(\overline{u_i u_j} \right) \right]}_{\text{molecular diffusion}} - \\ & - \underbrace{\left(\overline{u_i u_k} \frac{\partial u_j}{\partial x_k} + \overline{u_j u_k} \frac{\partial u_i}{\partial x_k} \right)}_{\text{stress production}} + \underbrace{\frac{p}{\rho} \left(\frac{\partial u_i}{\partial x_j} + \frac{\partial u_j}{\partial x_i} \right)}_{\text{pressure strain}} - \underbrace{2\nu \frac{\partial \overline{u_i}}{\partial x_k} \frac{\partial \overline{u_j}}{\partial x_k}}_{\text{dissipation}} \end{aligned}$$

⁴ The overview of the DNS data of turbulence is written mostly using *Friedrich et al. (2001)* review article.

modern computational resources are not enough to provide direct calculations of the engineering systems like that. However, there are some more or less “warm” direct numerical investigations. *Lim et al. (1998)* demonstrated the DNS results of a near-wall coherent motion in electrically conducting fluids. *Wagner & Friedrich (2004)* conducted a direct simulation of the momentum and heat transportation in the idealized Czochralski crystal growth configurations.

2.2. Turbulent recirculation flow inside induction furnaces

As it was already discussed there are no known DNS data of the flow in induction furnaces, which are complex engineering systems. However, the LES calculations were made by *Kirpo (2008-PhD)* and *Umbraško (2011-PhD)* during the last years. These results corresponded to the experiment and significantly widened the understanding of the flow structure in such systems.

The turbulent flows of liquid metal in induction furnaces can be marked out as a certain flow class, which is characterized with several recirculation mean flow eddies in a closed volume and intensive turbulent pulsations between these eddies. Such flow can be presented in the simplest case by a close turbulent melt initiated by harmonic alternating current in a cylindrical crucible with an inductor around (induction crucible furnace – ICF).¹ However, the flows of this class are observed in many other metallurgical applications: channel induction furnaces (CIF – see e.g. *Baake et al., 2010*), cold crucible furnaces (see e.g. *Umbrashko et al., 2008*), metal melting and processing technology in a levitating droplet (see e.g. *Hyers, 2005*). The flow structure in the cross-section of CIF and in the vertical central plane of ICF, cold crucible furnace and levitating droplet is qualitatively the same – several mean eddies and strong turbulent pulsations between them. These flows have the similar structure in the active area because of the same physical principle of operation.

The sketch of an axis-symmetric induction system is shown on Figure 2.2. Alternating current in the inductor (\mathbf{j}_I is the current density) creates a magnetic field \mathbf{B} and induces an alternating current in the conductive liquid metal (\mathbf{j}_B is the density of the induced current). The directions of \mathbf{j}_B and \mathbf{j}_I are opposite. The result of the interaction of \mathbf{j}_B and \mathbf{B} is the Lorentz force, which can be expressed as $\mathbf{f}_{em}(t) = [\mathbf{j}_B \times \mathbf{B}]$. This force drives the liquid away from the wall. As far as \mathbf{f}_{em} has the maximum in the middle zone of the crucible (on the half-height of the inductor), the flow pattern consists of two eddies as it is shown on Figure 2.2 and in the case of the cylindrical 3D geometry it means two toroidal vortices. Generally, $\mathbf{f}_{em}(t)$ is harmonic but as far as the frequency of \mathbf{j}_I in the industrial electro-heat equipment and density of metal are sufficiently high, the time for the metal to respond to the changes of the current is not enough. Therefore, we can replace the harmonic force density with its average value (hereinafter we will type amplitude of the harmonic variables without any additional symbols):

$$\mathbf{f}_{em,ef} = \frac{1}{2} [\mathbf{j}_B \times \mathbf{B}^*], \quad (2.1)$$

where \mathbf{B}^* is complex conjugated magnetic field induction.

¹From *Kirpo (2009-PhD)*

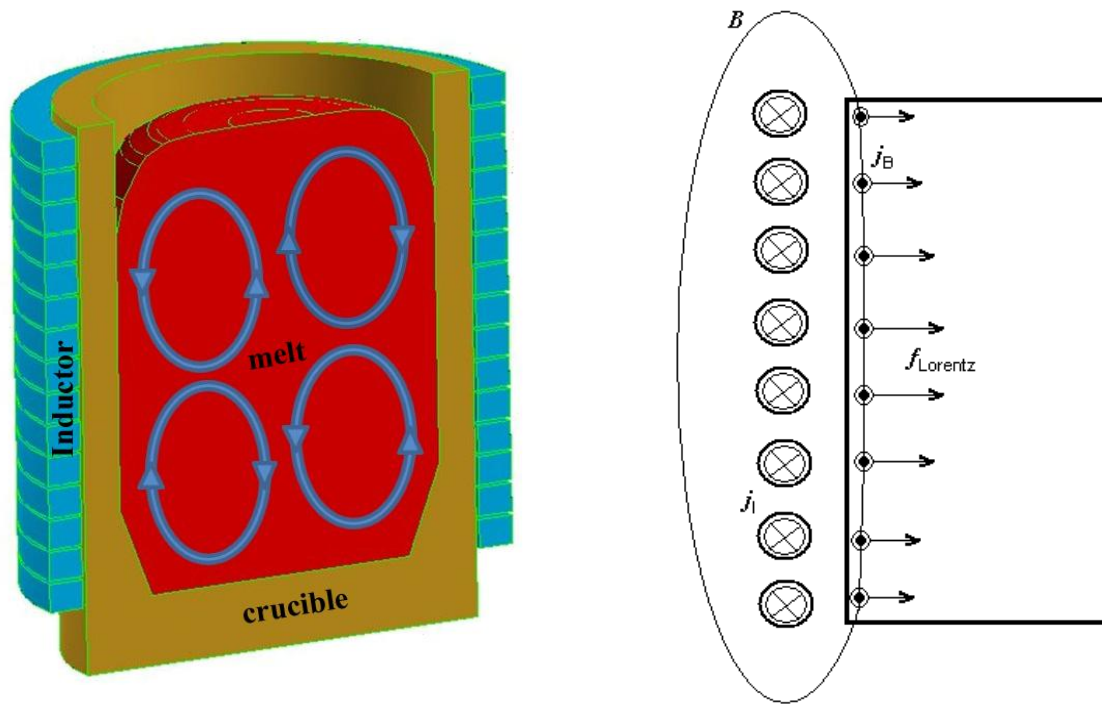


Figure 2.2: Sketch of axis-symmetric induction system on the example of an induction crucible furnace.¹

As far as ICF has axis-symmetric geometry of the melt and inductor EM field and, consequently, the driving Lorentz force can be calculated in a two-dimensional approximation. The distribution of average velocity is formed by the influence of EM force and can be also calculated in 2D (see e.g. *El-Kaddah et al., 1986*). However, the calculations of velocity state the high-Reynolds number flow, which leads to turbulence, which is a 3D phenomenon. Thereby, despite the axis-symmetric geometry the hydrodynamic process has a 3D character and requires a 3D modeling.

The flow of liquid metal created by a single-phase alternating magnetic field was studied experimentally in many published papers even in the 70s and the 80s. *Tarapore & Evans (1976)* estimated velocity of steering by a stroboscopic photography of the free surface. *Moore & Hunt (1983)* made measurements using a drag probe. *Trakas et al. (1984)* used a hot-film anemometer with the same aim. All mentioned authors investigated the distribution of a mean velocity. In addition, *Trakas et al. (1984)* found the characteristics of the turbulence (i.e. spectra) the similar to those of the classical shear flows. However, *Moore & Hunt (1983)* made some noteworthy observations concerning long-period fluctuations. Later *Umbrashko et al. (2006)* and *Kirpo et al. (2007)* researched these fluctuations with an advanced experimental technique – the Vives' probe². The observed phenomenon will be discussed later.

Despite of success in the experimental investigation, the development of numerical simulation was not so fast. However, obviously, only simulation is able to investigate the flow in industrial furnaces of a big scale. The success in the modeling was strongly connected to the development of computational resources, which extremely increased the power of calculation in the last decade. However, DNS scheme remains unusable for practical applications up to the present day. The mesh size grows as $Re^{2.25}$ (*Aldama, 1990*), which gives more than billion nodes

¹From *Umbrashko (2011-PhD)*.

²Vives' probe is also known as permanent magnet probe.

for a typical industrial scale flow with $Re > 10^4$. A computer memory needed to store only the main single precision variables exceeding 150 GBytes, which is maybe not completely unrealistic, considering modern computational clusters capabilities, but certainly is not a cost-effective solution.¹ In any case there is no known DNS data for such systems.

Reasonable comparison with the experimental results for time averaged quantities were obtained using two-equation turbulence models (k- ϵ) for the effective turbulent viscosity (quasi-steady flows) by *Tarapore & Evans (1976)*, *El-Kaddah & Szekely (1983)* and *Baake et al. (1995)*. *Kageyama & Evans (1998)* provided also k- ϵ time dependent numerical simulations. *A. Bojarevics et al. (1999)* proposed a pseudo-spectral k- ω model and received the results with a better tolerance. Finally, recent *Umbrashko (2011-PhD)* PhD thesis contains comparison of numerous modifications of RANS models for ICF. Figure 2.3 compares different RANS models with experimental and the LES results. This figure demonstrates that two-equation turbulence models simulate the average velocity very well. All of these models (k- ϵ , k- ω , RNG²) go relatively well with the experiment even in the 2D case, with RNG slightly in the lead. Figure 2.4 demonstrates the distribution of an average flow velocity in ICF. The LES calculation (Figure 2.4 b) finds the maximal velocity, which is about 25% less than the experimental value. This error is acceptable due to relatively large computational error and sophisticated calibration of the Vives' probe.

Despite a good agreement between the average velocities calculated with the RANS and the LES, the transient behavior of the flow leads to significant differences. The results produced by two-equation models show the highest values of turbulent kinetic energy in the eddy centers and the lowest between the eddies. Such distribution is characteristic for these models even in the case of a 3D transient simulation (*Umbrashko et al., 2006*). However, the experiment results by *Umbrashko et al. (2006)* and *Kirpo et al. (2007)* showed that the maximum of the turbulent energy is between the vortices of the averaged flow and close to the wall of the crucible. The average flow velocity in this area is close to zero (see Figure 2.4), therefore, the turbulent pulsations of velocity are large there. *Umbrashko et al. (2006)* and *Kirpo et al. (2007)* showed that the LES should be used for the flow modeling in such equipment to achieve more realistic results. *Umbrashko et al. (2006)* also discovered that the spectrum of axial pulsations between eddies near the wall has a clear low frequency maximum. The distribution of the turbulent energy in ICF and spectrum of these pulsations will be discussed in details in the Chapter 4.2 in context of the oscillations of a mass transportation in this region.

¹From *Umbrashko (2011-PhD)*.

²RNG (Renormalized-Group) is the modification of k- ϵ model, where the expression of turbulent viscosity $\mu_t = C_\mu \rho \frac{k^2}{\epsilon}$ is replaced with the following expression: $d \left(\frac{\rho^2 k}{\sqrt{\epsilon \mu}} \right) = 1.72 \frac{\hat{v}}{\sqrt{\hat{v}^3 - 1 + C_v}} d\hat{v}$, where k is turbulent kinetic energy, ϵ is turbulent kinetic energy dissipation rate, $\hat{v} = \mu_{eff}/\mu$, $C_\mu = 0.09$, $C_v \approx 100$. In the case of high Reynolds number these two equations give the same results. From *Yakhot & Orszag (1986)*.

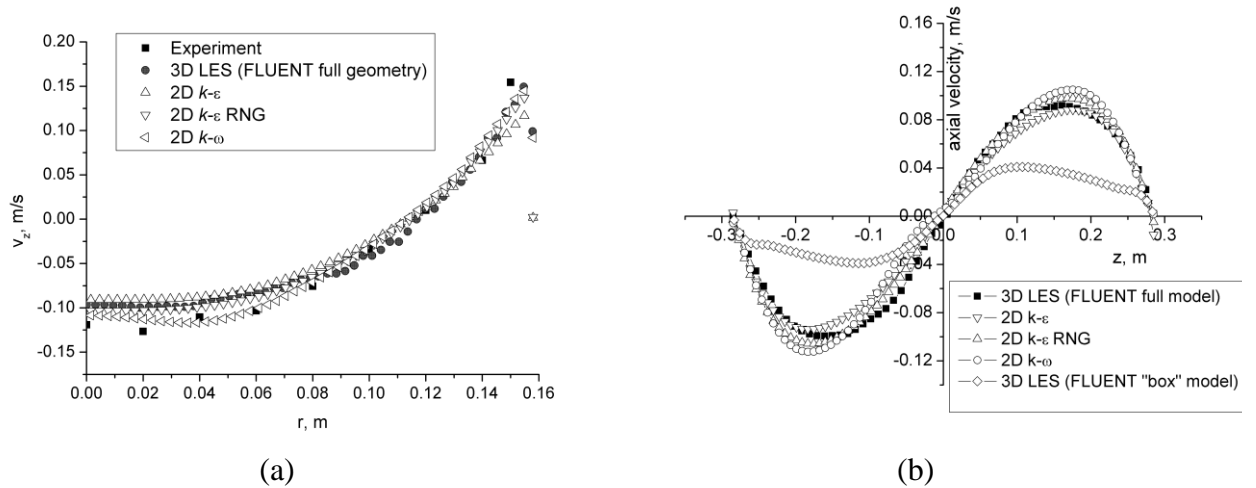


Figure 2.3: (a) Axial velocity profile at the middle of a lower eddy ($z = 13$ cm); (b) Axial velocity profile at the axis of the symmetry. From Kirpo (2008-PhD).

Apparently, the values of the velocities on Figure 2.3 and Figure 2.4 describe the flow in particular geometry of a specific size. However, the qualitative dependences will be the same for the different sizes of a cylindrical crucible. Only extremely high frequencies, that lead to the small penetration depth break the structure of two toroidal vortices of the same size (El-Kaddah, 1986).

As it was already mentioned, cylindrical geometry with an inductor around is the simplest case, which reproduces the turbulent flow of the recirculated metallurgical flows class. Therefore, ICF will be simulated for the goals of the present thesis. Moreover, ICF only of two sizes will be considered:

1) **ICF-1** repeats the furnace of laboratory scale, which is installed in Institute of Electrotechnology, University of Hannover (Germany). Both Umbraško's and Kirpo's experimental and simulated results, which are shown in this work, represent the flow in ICF-1. The sizes and EM setting of this furnace are shown on Table 2.1. This ICF is also simulated in the present thesis to compare results with the previous investigations.

2) **ICF-2** is a small crucible with parameters, which are shown on Table 2.2. This geometry was used for the experimental verification¹ of the numerical model for the particle tracking². The smaller crucible was used for this goal due to several reasons: 1) to reduce the number of particles, which are involved in the experiment; 2) to reduce the volume of the waste liquid metal³; 3) to use the simple pipette as the measurement device⁴.

¹The experimental verification is described in Chapter 3.

²The Lagrangian algorithm for the particle tracking is described in Chapter 2.3.

³Some liquid is inevitably polluted with the particles (see Chapter 3).

⁴See the description of the measurement technique in Chapter 3.

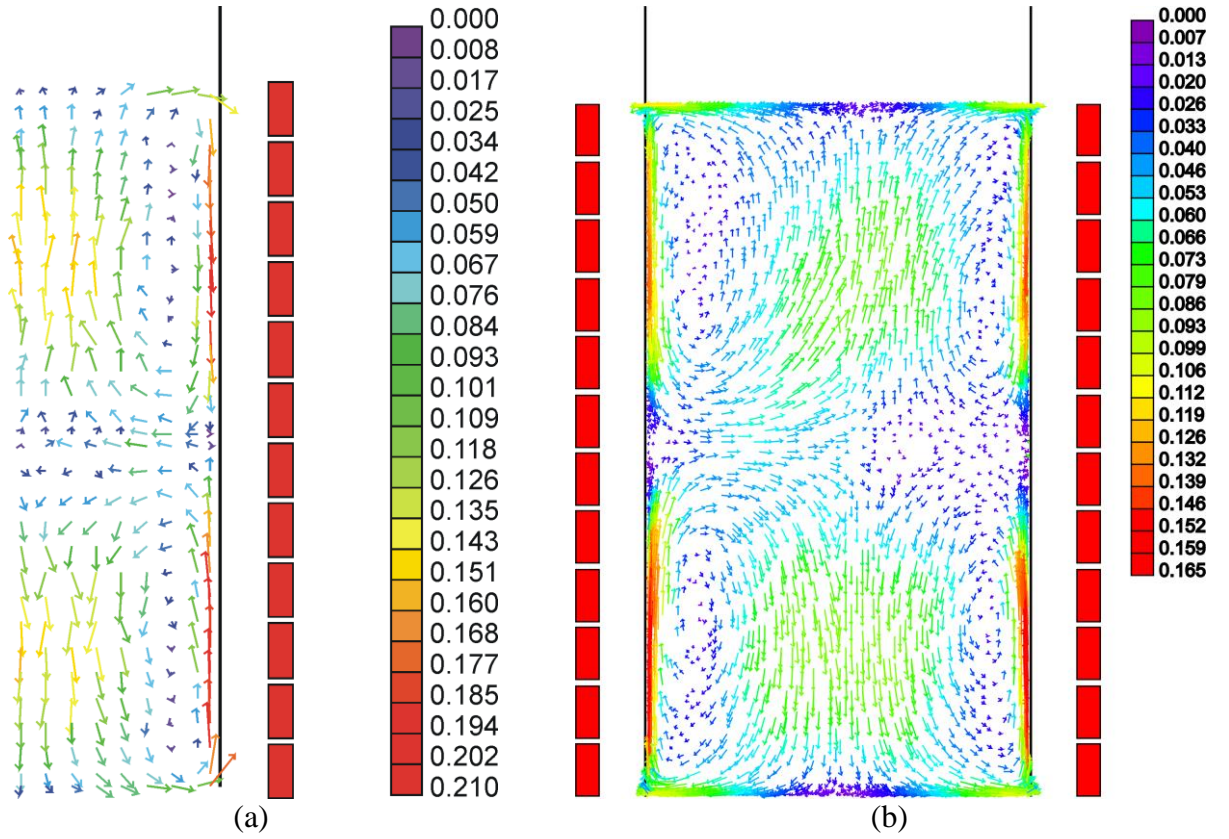


Figure 2.4: (a) Average velocity pattern measured using the Vives' probe; (b) the LES calculated average flow velocity. From *Kirpo (2008-PhD)*.

Table 2.1: Parameters of **ICF-1**.

Parameter	Value
Melt and inductor height	570 mm
Crucible radius	158 mm
Number of inductor turns	12
Inductor frequency	365 Hz
Inductor current	2000 A

Table 2.2: Parameters of **ICF-2**.

Parameter	Value
Melt and inductor height	100 mm
Crucible radius	45 mm
Number of inductor turns	6
Inductor frequency	4000 Hz
Inductor current	432 A

It should be mentioned that generally a meniscus shape of the free surface of the flow in ICF appears (see, e.g. *Spitāns et al., 2011*). Such deformation of the free surface is important in some applications, e.g. cold crucible melters and levitation (*Perrier et al., 2003*), but can be neglected in ICF-1 and ICF-2 (when the level of liquid metal is not less than the height of an inductor) due to its relative small height (*Kirpo, 2008-PhD*). Therefore, we will use the simple cylindrical geometry in the present work.

Kirpo et al. (2007) investigated the dependence of the flow velocity in the geometry of ICF-1 on current and found the approximately a linear regression even for different frequencies (Figure 2.5). *El-Kaddah et al. (1986)* and *Tarapore & Evans (1986)* obtained the similar results for different geometries.

Umbrashko et al. (2006) found the maximum amplitude of large-scale oscillations in the middle zone of ICF-1 near the wall in the same order of magnitude with the characteristic flow

velocity (15 cm/s) and the prevalent oscillations with the period of approximately 10 s. *Kirpo et al. (2005)* also recognized that this period of oscillations is the same order as the eddy circulation period (see Table 2.3).

In order to calculate the characteristic non-dimensional numbers, which describes the properties of the flow, the model liquid should be defined first. Obviously, the industrial metals (steel, aluminium, etc) cannot be used in experimental furnaces due to the high temperature of melting. Therefore *Umbraško (2011-PhD)* and *Kirpo (2008-PhD)* used Wood’s metal for the experimental investigation. Wood’s metal is 50% Bi – 25% Pb – 12.5% Sn – 12.5% Cd¹ eutectic, which becomes liquid approximately at 70 °C. Starting from approximately 150 °C the eutectic becomes toxic due to evaporation of cadmium (Cd). As it is shown on Table 2.4 Wood’s metal is a good conductor and has a low viscosity. These properties allow using this eutectic as the model liquid for metallurgical experiments. Nevertheless, there are other eutectics with the similar properties (e.g. In-Ga-Sn) but Wood’s metal is significantly cheaper.

Table 2.5 shows the non-dimension number, which characterized the flows and other transport phenomena in ICF-1 and ICF-2. The Reynolds number in both furnaces is enough to produce the turbulent flow. Prandtl number $Pr \ll 1$ means that heat conduction in Wood’s metal is stronger than convection, and heat diffusion dominates. It also means that the thermal boundary layer is much thicker than the viscous sub-layer. The ratio of thermal boundary layer compared to the viscous one is proposed as $\delta_{th}/\delta_{\eta} \sim Pr^{-1/2}$ as a result of the dimensional analysis (*Handbook, 2007*). Opposite significant Schmidt number for oxide impurities in Wood’s metal means the domination of convection transfer of impurities. Therefore dissolved oxides will mostly follow the turbulent flow and the influence of diffusion on the concentration distribution can be neglected. Finally, low magnetic Reynolds number ensures the absence of the influence of liquid motion on the magnetic field and allows using a one-way coupling for the modelling of EM problem and hydrodynamics.

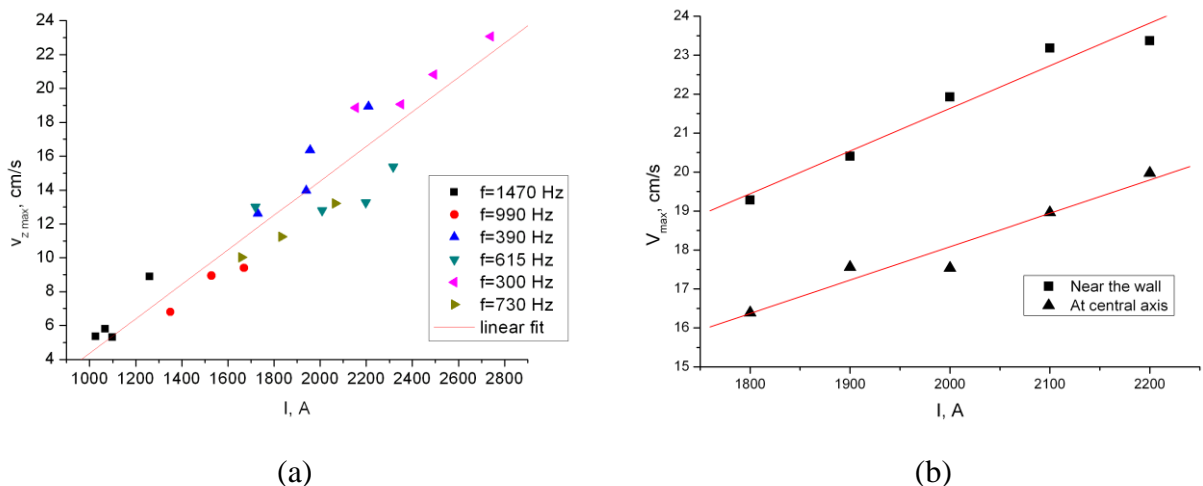


Figure 2.5: (a) Maximal axial velocity dependence on the inductor current for different frequencies in the geometry of ICF-1; (b) Dependence of axial velocity at the central axis and the wall at the center of eddy on the inductor current for 364 Hz frequency. From *Kirpo et al. (2007)*.

¹ This consistence of Wood’s metal is mentioned, e.g., in *Umbraško (2011-PhD)* and *Kuhn et al. (1962)*. However, the proportion of 50% Bi – 26.7% Pb – 13.3% Sn – 10% Cd is also mentioned in literature as Wood’s metal (see, e.g., the article “Wood’s metal” in the free web-encyclopedia “Wikipedia” - http://en.wikipedia.org/wiki/Wood%27s_metal).

Table 2.3: Characteristic velocity and period of the flow and velocity pulsations in geometry of ICF-1. From Kirpo *et al.* (2005).

Current, A	Frequency, Hz	Eddy period, s	Pulsation period, s	Maximum of average velocity, cm/s
1068	1444	12.6	13	5.50
1260	1470	10.5	15	6.62
1670	990	6.4	8	10.84

Table 2.4: Comparison of physical properties of liquid Wood's metal and steel.¹

	Wood's metal	Steel
Thermal conductivity λ , W/(m K)	18.8(85 °C)	33 (1600 °C)
Specific heat capacity c_p , J/(kg K)	168(85 °C)	775 (1500 °C)
Density ρ , kg/m ³	9.40e+3 (85 °C)	6.8 (1700 °C)
Dynamic viscosity η , (N s)/m ²	4.2e-3 (85 °C)	1.2e-3 (1600 °C)
Electrical conductivity σ , S/m	1.0e+6 (80 °C)	0.72e+6 (1535 °C)

Table 2.5: Non-dimensional numbers for the flows in ICF-1 and ICF-2.

	ICF-1	ICF-2
Characteristic velocity U , m/s	0.16	0.14
Reynolds number $Re = \frac{\rho UL}{\eta}$	6.7e+4	1.4e+4
Prandtl number $Pr = \frac{\eta c_p}{\lambda}$		3.8e-2
Schmidt number $Sc = \frac{\mu}{\rho D}$ ³		$\approx 0.5e+3$ ⁴
Magnetic Reynolds number $\mu_0 \sigma UL$	3.2e-2	7.9e-3

2.3. Particle transport in turbulent flows

The progress in the research of turbulence properties in the classical geometries (a pipe, a channel and other classical flows) has already been discussed above. However, the recirculated flow in metallurgical equipment significantly differs from that cases. It differs also from the

¹From *Umbráško (2011-PhD)*.

² L is the characteristic length, that is the radius of the crucible in this case.

³ D is diffusion coefficient of the impurities in the liquid metal.

⁴This value of Schmidt number is obtained for the oxides like Al_2O_3 in Wood's metal, estimated the diffusion coefficient $D \approx 1e-9$ m²/s². This value is obtained from the Einstein-Stokes equation (*Einstein, 1906*) assuming the molecules of oxide is a sphere. However, this value can a little overestimate diffusion coefficient, *Gmelin & Durrer (1964)* estimates it in wide range $1e-9 \dots 1e-11$ m²/s².

turbulent flow in a gap between two counter-rotating disks (the von Kármán flow – *Volk et al., 2008*). The distribution of mean vortices of this flow is similar but intensive axial pulsation in the region between them is the characteristic of recirculated metallurgical flows. Nevertheless, the progress of the knowledge of particle behavior in the classical turbulence is important for the understanding of a particular metallurgical case and will be discussed here.

First, following a statistical approach to description of turbulence, such theory treats the turbulence as a source of random forcing applied to particles. Earlier such treatment was developed by *Taylor (1921)* and was refined by many scientists culminating with the work of *Mei et al. (1991)*. The statistical theories treat particle dispersion like the diffusion of a passive contaminant. Often a turbulent diffusivity is calculated on the basis of the properties of turbulence and particles. These theories always predict that the particles will diffuse away from a point source and that the particles, which are initially uniformly distributed in a turbulent field, will remain uniformly distributed in the absence of body forces. The statistical theories of particle dispersion ignore the researched fact that the turbulence is dominated by quasi-deterministic coherent structures (see Chapter 2.1). The coherent vortical structures are the mechanisms that cause preferential concentration by producing directed (non-random) motion of the particles.¹

Generally, particles in turbulence are characterized by a large number of dynamically active and interacting degrees of freedom (see, e.g. *Frisch, 1995; Nelkin, 2000; Pope, 2000*). The description methods of the particle motion in turbulence can be divided in two groups: the Euler-Euler and the Euler-Lagrange approaches. The first “Euler” is common and means modeling of the flow in terms of variables defined at points fixed in space. The Euler-Euler approach does the same for the equations of a dispersed state. But the Euler-Lagrange methods deal with individual particles carried by the flow.²

The Euler-Euler methods are suitable for the simulation of a dissolved state or small particles, which move mostly like flow tracers. Only potential forces can be additionally taken into account within this approach. This approach, in fact, is used for the investigation of the redistribution of the impurities consisted of the smallest particles, even molecules. However, some smart extensions of such approach represent useful methods.

Pandya & Mashayek (2002) derived a set of dispersed phase equation in the LES context. *Carneiro et al. (2008, 2009)* proposed a moments model to describe polydisperse multi-phase flows based on the transportation of the moments of the particle-size-distribution function. Particle velocities size dependency is captured by transporting the moments with individual moment transport velocities (*Carneiro et al., 2010*). The phase interaction forces (formally obtained by integration over the diameter spectrum) can be expressed using the moments. Unknown moments, needed for the closure of the exchange terms, can be calculated assuming a functional form of the particle size distribution function.³

Another advanced Euler-Euler method is a statistical model of particle motion and dispersion developed by *Alipchenkov & Zaichik (2004)*. The model is based on a kinetic equation for the particle velocity probability density function. The anisotropy of the Lagrange autocorrelation functions and turbulence time scales are taken into account in this kinetic model.

¹From *Eaton & Fessler (1994)*.

²From *Toschi & Bodenschatz (2009)*.

³From *Dems et al. (2011)*.

However, the Euler-Lagrange methods have begun to advance our knowledge significantly with the increase of the computational capacity. The example applications include 1) analytical approaches for tackling the statistical properties of homogeneous and isotropic turbulence as a field theory (see *Kraichnan, 1966*); 2) the connection between turbulence intermittency and (*Velani & Vergassola, 2001; Falkovich et al., 2001*); 3) models for the evolution of the Lagrangian clusters (*Chertkov et al., 1999; Pumir et al., 2000, 2001*); 4) the Lagrangian evolution of material lines, vorticity and strain (*Guala et al., 2005; Lühti et al., 2005*); 5) the Lagrangian tools used to improve subgrid-scale modelling in the LES (*Pope, 2004; Bou-Zeid et al., 2005*); 6) stochastic models to regularize velocity gradients in turbulence (*Chevillard & Meneveau, 2006*); 7) studies of the singularities of the Euler equation (*Constantin, 2001*).¹ Moreover, the Lagrange description is preferable for the description of the dynamics of inertial particles in turbulence itself. Figure 2.6 b illustrates the trajectory of an inertia particle in turbulent vortice calculated with the Lagrangian approach.

Several years ago when the computational resources were not enough to model flows with the LES, the RANS was usually used. According to this approach velocity pulsations were averaged and no full transient results were available. Therefore, a random shift was applied to the trajectory of particles (a random walk model – see, e.g., *Kallio & Reeks, 1989*). The probability of a random shift is defined through the turbulence properties of the flow. Nowadays the LES based calculations are widespread and will be also employed in the simulations of the present work. The LES gives transient results of the flow dynamics, moreover, the largest part of the turbulent spectrum is resolved directly. It means that the motion of particles within the Lagrange approach can be simulated also directly. Only the smallest vortices is modeled, however, the response of the inertial particles on subgrid-scale vortices can be often neglected. Apparently, the DNS simulations take off all doubts about the relevance of the particle trajectories. Despite of the significant resources to be utilized, this approach was successfully employed in a number of studies of the simple geometries (see, e.g., *Biferale et al., 2005*). The DNS results light some interesting peculiarities of a particle motion, e.g., it came as a surprise that the Lagrangian traces can persist in a small-scale vortex for a time exceeding the local eddy turnover time (*Biferale et al., 2005; Toschi et al., 2005*). However, in the most part of the applications the LES based Lagrangian method is completely enough.

Experimental investigation of particle motion in turbulent flows is also a very important issue. As well as the approaches for the modelling, the experimental techniques can be also separated in the Euler and the Lagrange methods.

The Eulerian measurements are good for the flows, in which the mean velocities are larger than those of the turbulent fluctuations. The Laser Doppler anemometry and particle-image velocimetry (PIV) can be mentioned as the examples of such measurements. Doppler anemometry allows only point-wise measurements of velocity and, thus, has only limited utility. However, *Volk et al. (2008)* reported acceleration measurements of inertial particles using the extended laser Doppler velocimetry. The PIV method allows measurements of the velocity field, but its applicability to the high-Reynolds number flows is limited owing to camera resolution.

¹From *Toschi & Bodenschatz (2009)*.

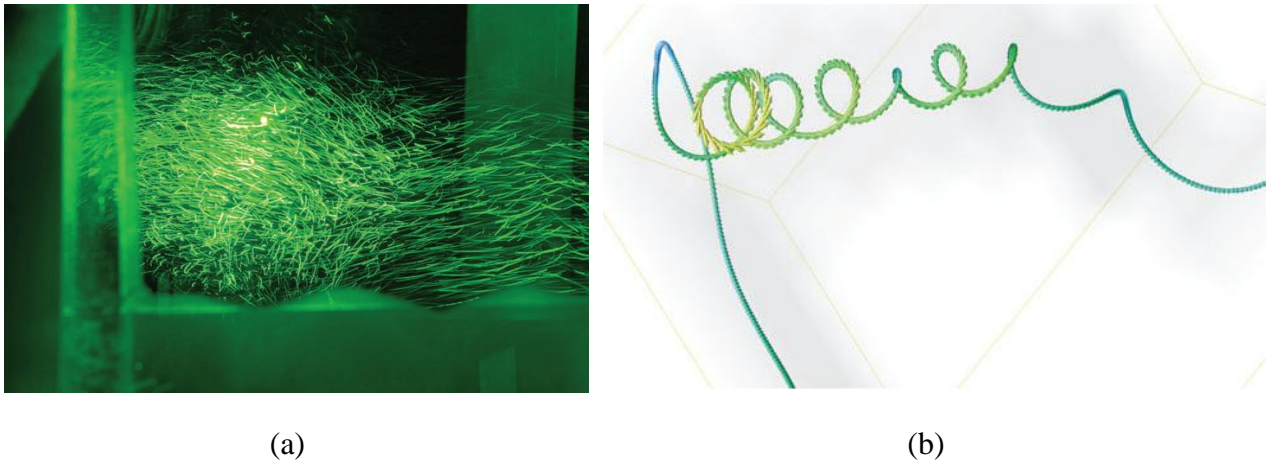


Figure 2.6: (a) tracer particles illuminated by a green laser (courtesy E. Bodenschatz); (b) A trajectory of a particle in a small-scale vortex filament in a turbulent flow. From *Toschi & Bodenschatz (2009)*.

Despite the fact, that the most of the experimental work concerning the high-Reynolds number flows has been obtained in the Eulerian framework (*Mordant et al., 2001*) at the moment the most successful technique for the investigation of the Lagrangian turbulence is the optical tracking of tracer particles. This technique is known as a particle-tracking velocimetry (PTV), when velocities are concerned, or the Lagrangian particle tracking, when a position and acceleration are also determined. Particles can be passive tracers that approximate the Lagrangian motion of fluid elements, have inertia, or have a size that is larger than the smallest scale of the flow. *Snyder & Lumley (1971)* provided the first systematic set of the PTV measurements for a wind-tunnel grid turbulence, whereas *Sato & Yamamoto (1987)* reported the similar measurements in a water-tunnel grid turbulence. Figure 2.6 (a) illustrates the particles illuminated by laser in 3D turbulence. *Virant & Dracos (1997)* were pioneers in 3D PTV using multiple cameras for the stereoscopic reconstruction of particle tracks. Further *Otto & Mann (2000)* developed this method. However, the Lagrangian measurements remain challenging for the high-Reynolds number turbulent flows.¹

A particle motion in fundamental flows was investigated on the basis of the described numerical and experimental technique. *Toschi & Bodenschatz (2009)* carefully described the Lagrangian properties of the particles in homogeneous turbulence. Moreover, *Arneodo et al. (2008)* compared three different experiments and five different numerical simulations and concluded the universality of the Lagrangian turbulence. The data, which covered the wide range of Reynolds numbers and came from different experimental and numerical setups, collapsed on one curve. This proves universality in the physics of the Lagrangian turbulence over the whole range of time lags.² *Wang & Squires (1996)* investigated particle deposition in a vertical turbulent channel flow. *Volk et al. (2008)* studied acceleration of heavy and light particles in the von Kármán flow.

And, finally, the author researched the interaction between turbulence and inertial particles in boundary layer. It is widely accepted that heavy particles have a tendency to migrate towards the wall (*McLaughlin, 1989; Brooke et al., 1992*) and in the wall layer they segregate preferentially in regions characterized by stream-wise velocity lower than the mean velocity

¹From *Toschi & Bodenschatz (2009)*.

²From *Toschi & Bodenschatz (2009)*.

(Niño & Garcia, 1996; Pan & Banerjee, 1996). Brooke et al. (1992) showed that particles are driven towards the wall by coherent eddies, which impart spin-wise wall parallel the motion to the particle trajectories before the particles deposit.¹

2.4. Previous investigations of particle transport in recirculated flows

2.4.1. Modelling

As it was already discussed the flow inside induction furnaces is sufficiently complex due to the presence of the EM forces, which drive a turbulent flow with two main toroidal recirculated vortices. Therefore, the case interesting for the thesis, significantly differs from the well-studied turbulence in a pipe, a channel and other classical flows. It also differs from the turbulent flow in a gap between two counter-rotating disks (the von Kármán flow) due to the intensive axial pulsations between the main eddies near the wall. Moreover, the EM field directly influences the non-conducting particles in the conducting liquid within the penetration depth and the transportation of them to the wall, which is another specific aspect of the considered system. The layer of a significant EM field is sufficiently thin (about 20% of the radius of the crucible in ICF-1 – $\delta/R = 0.2$). Due to the non-slip boundary conditions the flow velocity is zero at the wall and increases in a radial direction until it rapidly achieves the maximal value at the relative distance $\Delta/R = 0.04$ from the wall (for ICF-1). $\delta > \Delta^2$, therefore the maximum of velocity is inside the layer of EM penetration. Obviously, particles preferentially move in the streamline of maximal velocity. Therefore, the major part of the particles frequently goes to the layer of a significant EM field. The particle motion in turbulent flows without EM is well-researched (see previous chapter) but we cannot separate the large interior zone without EM field from the thin layer near the wall and should consider the motion of the particles in the whole volume. Moreover, the experimental results received by Taniguchi & Brimacombe (1994) and Takahashi & Taniguchi (2003) also show the significant influence of the EM field on the non-conductive particles in well-conductive liquid. In spite of probable inaccuracy of this experimental technique (the doubt about accuracy will be discussed later), the preferential concentration of the non-conductive particles near the wall at the height of the maximum of EM force corresponds to the industrial observations.³

Lennox & Kolin (1954) established the theoretical background of the influence of EM field on particles in conductive liquids. However, the goal of this investigation was far from the metallurgical applications. Later the movement of a spherical particle in a gradient force field was discussed in the book of Shilov et al. (1989).

One of the first Lagrangian particle tracking in conductive liquid in the vicinity of magnetic field was performed by McKee et al. (1999). He suggested greatly simplified model for calculation of a particle path in rotating magneto-hydrodynamic flow within a long cylinder. Taking into account the fundamental difference between the flow pattern in the McKee's simulation and the recirculated flow in induction furnaces, the numerical results of McKee et al. (1999) is out of interest, however, this model began the simulation of particles in MHD flows.

¹ From Marchioli et al. (2004).

² The values of δ/R and Δ/R are shown for ICF-1, however, this inequality is true for all ICFs with the high-Reynolds-number flow.

³ From Ščepanskis et al. (2011).

Umbrashko et al. (2006) followed the tracer particles in the flow of ICF using the LES based calculations in ANSYS Fluent software. Later *Kirpo et al. (2009)* used the same software to investigate the behaviour of inertia particles in ICF. Kirpo added EM force (see *Lennox & Kolin, 1954*) to the Lagrange equation but the model remained sufficiently rough: only drag, buoyancy and the EM forces were taken into account for the calculation of particle motion. Despite the fact that EM force is the most important force from engineering point of view (see experimental investigation of *Taniguchi & Brimacombe (1994)*), it will be statistically proved in Chapter 3.2.3¹, such set of forces is not enough for relevant simulation of particle motion in the flow of ICF-1. Moreover, as it will be shown later, the value of lift force in ICF-1 is significantly underestimated by *Kirpo et al. (2009)* using the Saffman approximation.

Umbrashko et al. (2006) and *Kirpo et al. (2009)* assumed dilute dispersion of the particles, that is the volume fraction is small so that particle-particle interaction is neglected and an individual particle's motion is determined only by its interaction with fluid phase. Moreover, *Kulick et al. (1994)* and *Kaftori et al. (1995)* experimentally demonstrated that turbulence modifications due to the presence of small particles at low enough concentration are negligible, and, consequently, one-way coupling can be used in the model. Such dilute approximation undoubtedly is also relevant for the case of the thesis (the particle-to-fluid mass rate does not exceed $1e-4$).

Kirpo et al. (2009) simulated the case, where the particles were initially distributed in a vertical plane. However, this simulated case does not correspond to any industrial case, e.g. in an industrial process alloying particles are injected on the top surface of the melt. Nevertheless, general peculiarity of the particle behavior was confirmed: big non-conductive particles were settling down on the wall in the zone between the main vortices. Over 90% of 1 mm-large-non-conductive particles were accumulated in the near-wall region under the influence of EM field. But the conductive particles move preferentially in the bulk of the flow. The influence of particle-to-liquid density ration on the distribution over the crucible height was also pointed out (*Kirpo, 2008-PhD*).

The model used by Kirpo was enhanced for the goals of the present thesis by means of the development of *OpenFOAM* software code: 1) the initial cloud of the particles was situated on the top surface of the melt, which corresponds to the industrial case of admixture injection, and 2) the Lagrange equation was supplemented with lift, acceleration and added mass forces. These two modifications significantly improve the model and allow obtaining new physical results, which helps to understand the industrially important processes in induction furnaces. Moreover, the statistical analysis of the forces and the non-dimensional parameters, which is reported in Chapter 3.2.3, proves the importance of the model expansion by adding additional forces.

2.4.2. Experimental investigation

Obviously, it is desirable to investigate particles distribution in such systems experimentally, at least, to verify the numerical model. But metals often have very high melting temperatures. Moreover, the electric well-conductive materials are not optically transparent, while transparent liquids have low conductivity. *Sadoway & Szekely (1980)* tried to use transparent LiCl-KCl eutectic² to reproduce the recirculation motion in an ICF, but they failed to do this. EM field not only produces the induced flow motion but also heats up the liquid within the penetration depth.

¹See also *Ščepanskis et al. (2011)*.

² 41.2% KCl - LiCl.

Thereby, the thermal convection dominates in low-conductive transparent liquids (see Chapter 4). In spite of the optimistic conclusions of *Sadoway & Szekely (1980)*, the simulation, which is done by the author of the present thesis, shows that it is not possible to avoid thermal motion by changing the EM conditions. Therefore, this liquid cannot be used to produce such flow patterns. The only more or less successful method, developed by *Taniguchi & Brimacombe (1994)*, provides an opportunity to investigate experimentally the rate of the particle deposition in the turbulent flow of liquid metal under EM force. However, because the results are obtained by cutting a solidified liquid, it is impossible to receive any information about the dynamics of the process inside the melt using such experimental technique. Moreover, the presence of a solidification front has an influence on the particles during the solidification and it is not clear, if this effect is negligible.

Finally, *Ščepanskis et al. (2012)* proposed the original experimental technique, where ferromagnetic particles were used. This experiment allowed verifying the numerical model and was the first known successful experimental investigation of the dynamics of inclusions in the bulk of liquid metal. The technique and the results are described in details in the Chapter 4. However, in spite of the satisfactory agreement between this experiment and numerical prediction, which was done by the mathematical model, the tolerance of this experiment was not very high and could not be improved. Moreover, the experiment was possible only at the quasi-stationary stage of the distribution of the inclusions in the flow and was almost impossible at the stages characterized by fast changes in the distribution.

The imaging of the system is not possible also by X-rays due to the high absorbance of the metal (especially the low-temperature alloys, which contain heavy metals like lead).

For all these reasons the idea to carry out the neutron imaging (see *Richards et al., 2004*) has appeared recently. Lead and other heavy metals are not obstacle for this technique; therefore, it can be very useful experimental methodology. Such technique can lead to the experimental investigation of the dynamical behaviour of solid inclusions in the complex turbulent flow inside induction melting and stirring equipment. The experimental idea and the results of the preliminary experiment are presented in the Chapter 4.5.

2.5. Simulation of the deposition formation during the long-term operation of the furnaces

As it was discussed in the Chapter 2.2 the transport of solid inclusions is the key phenomena in all types of induction furnaces and can be described by the common model of recirculated turbulent EM induced flows. However, specific aspects additionally appear in each type of a furnace. E.g., the meniscus and free surface dynamics are significant for the cold crucible induction furnace and the levitating droplet (*Spitans et al. 2013*). The long term operation of CIF also lights the specific processes of mass transportation, which is urgent from the industrial and engineering points of view. These processes and the proper extension of the particle transport model will be discussed within this chapter.

As it was discussed in the Chapter 1.1, the deposition formation is observed during the long term operation of CIF (see also Figure 1.1). Such process has significant negative effect on the efficiency and the sustainability of the equipment.¹

¹ See motivation in Chapter 1.1.

It was industrially observed that the typical situation, when the intensive deposition of oxide impurities appears, is the change of the operation power of equipment. The power of CIF can be decreased during a weekend or some interruption in a production process in order to minimize the energy consumption and, consequently, expenses. Nevertheless, the molten liquid metal is usually kept above the melting temperature in order to avoid the remelting of the metal, which consumes a lot of time and energy. Thus, such practice saves energy, however, it was observed that the build-up formation accelerated at the same time. *Bethers et al. (1994)* found the temperature dependence on the deposition rate due to the same dependence of the saturation concentration of impurities. Further, *Bethers et al. (1995)*, opposite to the practice of CIF operation, propose to increase the power of the furnace during the weekend in order to dissolve the build-up formation. Figure 2.7 (a) demonstrates the time dependence of the described CIF operation style. *Bethers et al. (1995)* also calculated the rate of the channel clogging in this case (Figure 2.7 b). These results are based on the model, which takes into account the diffusion limited impurity deposition on the walls of the channel. Later, *Kaupuzs et al. (2003)* analyzed theoretically the diffusion of impurities through the laminar near the wall layer in liquid metal. Finally, *Frishfelds et al. (2009)* investigated the clogging process of channel in CIF.

However, all of the above-described investigations simulated only the molecular diffusion of impurities from the bulk of the melt to the wall of the furnace. Such model can describe only the dense build-up formations (see Figure 1.1). Nevertheless, as it was already discussed in the Chapter 1.1, the sponge-like deposition of impurities is more dangerous for the efficiency and sustainability of metallurgical melting and stirring equipment, because the time of sponge-like clogging is much shorter than by dense deposition. Therefore, the model based on the particle growth in the bulk of the melt is proposed in the present work. This model as well as the estimations of the process are described in Chapter 6.

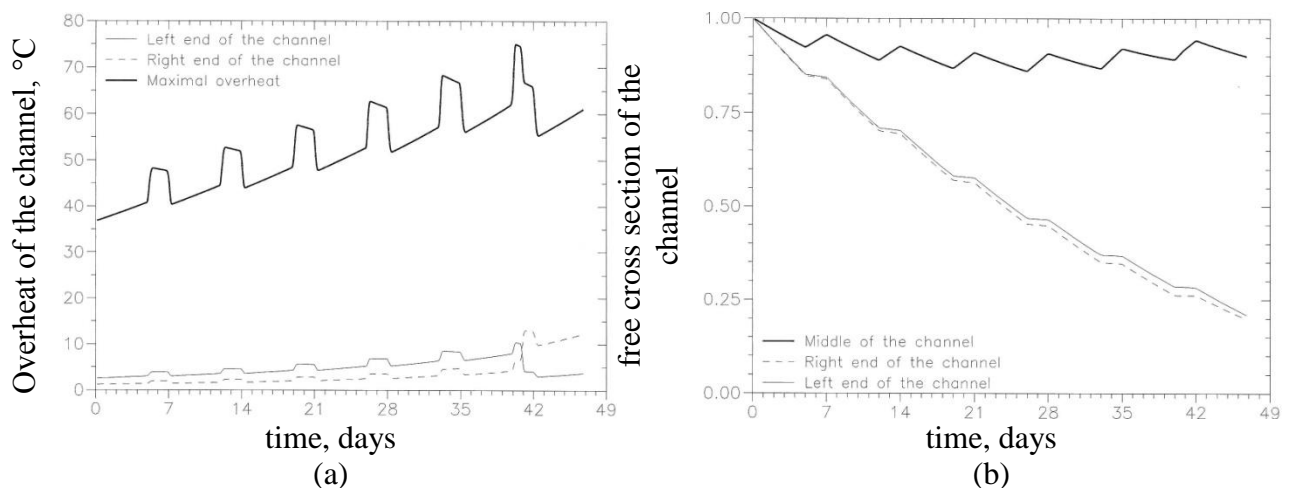


Figure 2.7: Time dependence of the overheat in the channel (a) and of the free cross section area of the channel (b) in the CIF with Todnem inductor¹, which is operated at 450/600 kW power, the reference temperature is 1500 °C. From *Bethers et al. (1995)*.

¹Todnem (1967).

3. Mathematical model

3.1. General scheme and coupling

The model for solid particle tracking in the EM induced liquid metal flow is described in the present chapter. The described problem is multiphysical, therefore the model consists of several coupled blocks for the different areas of physics. The general scheme of the algorithm is shown on Figure 3.1.

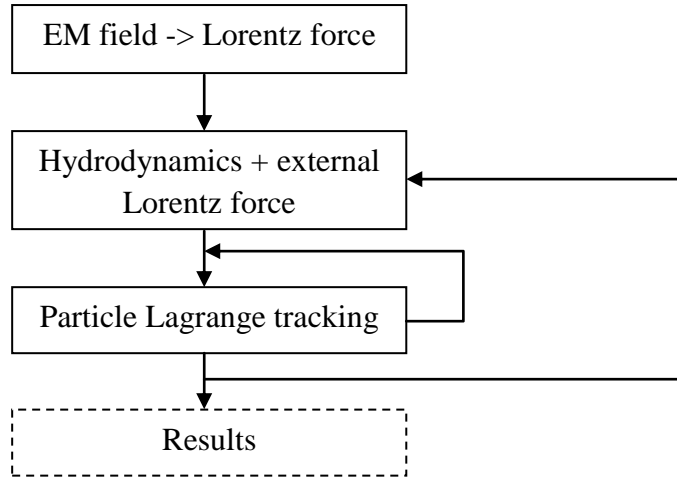


Figure 3.1: General scheme of the algorithm.

The blocks for EM field calculation and hydrodynamics (HD), which are used in the present model, were well discussed and utilized by *Kirpo (2008-PhD)* and *Umbraško (2011-PhD)*. Therefore, the present theses will focus on the Lagrange tracking algorithm, but EM and HD blocks will be described only briefly. Nevertheless, the coupling between them will be elucidated.

Generally, MHD consists of two-way coupled EM and hydrodynamic (HD) problems. That means that Navier-Stokes equation for HD has additional term – the Lorentz force (see equation (2.1)), and the Ohm's law in the Maxwell's system of equations is expressed as follows:

$$\mathbf{j} = \sigma(\mathbf{E} + \mathbf{v} \times \mathbf{B}), \quad (3.1)$$

where \mathbf{j} is current density, σ is electrical conductivity, \mathbf{E} and \mathbf{B} are vectors of electric field and magnetic flux respectively, \mathbf{v} is velocity of liquid metal flow. As it was already discussed in Chapter 2.2, the Lorentz force is the source of the flow motion and essential term in the Navier-Stokes equation. This force, which is counted from magnetic flux within the block for EM calculation, is used as a source in the HD block of the algorithm. Thus, one-way coupling between these two blocks is fulfilled.

However, as it is shown in equation (3.1), general MHD problems are coupled in another way too. Apparently, two terms in equation (3.1) should be compared in order to estimate the significance of the second-way coupling. Following equation for magnetic flux can be easily obtained from Maxwell's equations, including (3.1) (*Branover & Tsinover, 1970*):

$$\frac{\partial \mathbf{B}}{\partial t} = \text{rot}(\mathbf{v} \times \mathbf{B}) + \frac{1}{Re_m} \nabla^2 \mathbf{B}, \quad (3.2)$$

where magnetic Reynolds number $Re_m = \mu_0 \sigma v L$, μ_0 is the magnetic permeability of free space, L is the characteristic size of the system. Obviously, if $Re_m \ll 1$, then the first term in equation (3.2), which is responsible for the generation of magnetic flux due to the the flow motion, is negligible. Table 2.5 shows that $Re_m \ll 1$ for ICF-1 and ICF-2, therefore, only one-way coupling can be applied between EM and HD block of the algorithm in this case. Moreover, this conclusion can be generalized for all metallurgical equipment, because low magnetic Reynolds number is typical for such devices.

As it was discussed in the Chapter 2.2, EM block is solved only once in a quasi-stationary approximation. But HD and particle tracking are transient and are numerically solved with the HD time step Δt_{HD} , which forms a big loop of the algorithm (see Figure 3.1). A small loop within the Lagrange tracking algorithm will be discussed later.

The turbulent flow is calculated using the LES method with the isotropic Smagorinsky sub-grid viscosity model:

$$\nu_{SGS} = C_k \cdot \sqrt{k} \cdot \delta, \quad k = 2 \frac{C_k}{C_e} \cdot \delta^2 \cdot |D_{ij}|^2, \quad \delta = \sqrt[3]{V_C},$$

where D_{ij} is the deformation tensor, V_C is the volume of the computational cell, $C_k = 0.07$ and $C_e = 1.05$. No additional boundary treatment is applied as well as the slip boundary condition (BC) on the top surface and the non-slip BC on the walls are applied. The flow is driven by the Lorentz force (see equation (2.1)) and thermal buoyancy force in the Boussinesq approximation. The thermal BC is convective on the top surface and adiabatic on the walls of the crucible.

At each HD time step the results of the flow simulation give the field of flow velocities, which is used for the further calculation of the particle trajectories. The Lagrange equation describes the motion of the inertial particles. In the LES framework we know only the filtered velocity and assume the isotropy of the sub-grid part. The statistical approach to the analysis of the force distribution will be discussed below. In spite of the calculation of the individual trajectories of particles, the analysis will be done for a cloud of the particles so the unfiltered isotropic part of velocity should not significantly influence the results of inertial particles.

Now it is suitable to discuss the coupling between HD and the Lagrange tracking blocks. *Kirpo (2008-PhD)* examined the following criteria to prove relevance of dilute approximation (*Loth, 2000*):

$$\frac{Nd^2}{LH\sqrt{\gamma^2+1}} \ll 1, \quad (3.3)$$

where N is the total number of the particles in the fluid volume, $\gamma = v_{term}/v_{RMS}$ is the ration of the particle terminal velocity to the RMS velocity of turbulent pulsations. *Kirpo (2008-PhD)* found the expression (3.3) correct for $N \approx 3e+4$ particles with the diameter $d = 1$ mm in ICF-1. The maximal size of the particles that are used for the goals of the present work is 300 μm , while the total number is approximately the same. Therefore, the expression (3.3) is true for ICF-1 and ICF-2 also within the present investigation.

Moreover, the volume fraction of the particles is up to $\varepsilon_{p,ICF-1} \cong 9.5e-6$ for ICF-1 and $\varepsilon_{p,ICF-2} \cong 6.7e-4$ for ICF-2, which is much less than 1. The numerical and experimental results show that particle spacing exceeding $5d$ has only secondary effects with the respect to fluid dynamics and it is possible to neglect the particle-particle interaction (*Yuan & Prosperetti, 1994*). Therefore, the next criterion for dilute approximation is $\varepsilon_p < 1e-3$, which is also satisfied for ICF-1 and ICF-2.

The mentioned criteria proved that particle tracking in ICFs within the described problems can be fulfilled under dilute condition, which means a one-way coupling as well as the following assumptions:

- a neglect of particle-particle interaction;
- a neglect of the particle influence on the structure and velocity of the flow.

3.2. Lagrange particle tracking

The solution of the stationary Navier-Stokes equation for rigid sphere in viscous liquid, which is moved with velocity \mathbf{u}_f , classically leads to the Stokes force (*Batchelor, 1967*):

$$\mathbf{F}_{Stokes} = 3\pi d\mu \cdot \mathbf{u}_f, \quad (3.4)$$

where μ is dynamic viscosity. This force is the total contribution of the flow drag on the sphere that is parallel to the flow motion. This case is same as the case when the liquid moves and the particle is immovable. Therefore, the expression (3.4) is also known as the Stokes's law for the resistance to a moving sphere.

However, the Stokes force is valid only for a simple stationary case with a homogeneous velocity field and low Reynolds number, which is not relevant for the present application. Therefore, the solution of non-stationary equation will be analyzed.

3.2.1. Non-stationary flow around a sphere

The following non-stationary Navier-Stokes equation describes the motion of the viscous liquid around the movable solid sphere:

$$\frac{\partial \mathbf{u}_f}{\partial t} = -\frac{1}{\rho} \nabla p + \nu \Delta \mathbf{u}_f, \quad (3.5)$$

where \mathbf{u}_f is the velocity of the flow (the origin of the flow motion is only the motion of the particle), p is pressure, ρ is density, $\nu = \mu/\rho$ is kinematic viscosity.

Using *rot* operator we can get rid of e pressure in the equation (3.5) (*Landau & Lifshitz, 1959*) and write this equation for a flow function ψ in a spherical coordinate system (*Brennen, 2005; Basset, 1888*):

$$\left(L - \frac{1}{\nu} \frac{\partial}{\partial t}\right) L\psi = 0, \quad L = \frac{\partial^2}{\partial r^2} + \frac{\sin \theta}{r^2} \frac{\partial}{\partial \theta} \left(\frac{1}{\sin \theta} \frac{\partial}{\partial \theta}\right). \quad (3.6)$$

The boundary conditions are

$$\frac{1}{a^2 \sin \theta} \frac{\partial \psi}{\partial \theta} = u_p(t) \cos \theta, \quad \frac{1}{a \sin \theta} \frac{\partial \psi}{\partial r} = u_p(t) \sin \theta, \quad (3.7)$$

where $u_p(t)$ is velocity of the particle, a is the radius of the particle. The solution of equation (3.6) is found in the following form (*Brennen, 2005*):

$$\psi(r, \theta, t) = \sin^2 \theta \cdot f(r, t) + \cos \theta \cdot \sin^2 \theta \cdot g(r, t),$$

where

$$\left(L_1 - \frac{1}{\nu} \frac{\partial}{\partial t}\right) L_1 f = 0, \quad L_1 = \frac{\partial^2}{\partial r^2} - \frac{2}{r^2}, \quad (3.8)$$

$$\left(L_2 - \frac{1}{\nu} \frac{\partial}{\partial t}\right) L_2 g = 0, \quad L_2 = \frac{\partial^2}{\partial r^2} - \frac{6}{r^2}. \quad (3.9)$$

The form of the expression for the force \mathbf{F} on the spherical particle, obtained by evaluating the stress on the surface and integrating, is as follows (*Brennen, 2005*):

$$\frac{\mathbf{F}}{\rho V_p} = \frac{d\mathbf{u}_p}{dt} + \left\{ \frac{1}{r} \frac{\partial^2 f}{\partial r \partial t} + \frac{\nu}{r} \left(\frac{2}{r^2} \frac{\partial f}{\partial r} + \frac{2}{r} \frac{\partial^2 f}{\partial r^2} - \frac{\partial^3 f}{\partial r^3} \right) \right\}_{r=a},$$

where V_p is the volume of the particle. It transpires that this is independent of g . Hence only the solution to equation (3.8) for $f(r, t)$ needs be sought to find the force on a spherical particle.

Equation (3.8) is solved using the Laplace transformation (*Lavrent'ev & Shabat, 1973*) for non-slip boundary conditions (*(Brennen, 2005; Basset, 1888)*), and the force \mathbf{F} is as follows (*Brennen, 2005*):

$$\frac{\mathbf{F}}{\rho V_p} = -\frac{1}{2} \frac{d\mathbf{u}_p}{dt} + \frac{3}{2} \frac{d\mathbf{u}_f}{dt} + \frac{9\nu}{2a^2} \cdot (\mathbf{u}_f - \mathbf{u}_p) + \frac{9}{2a} \sqrt{\frac{\nu}{\pi}} \cdot \int_0^t \frac{d(\mathbf{u}_f - \mathbf{u}_p)}{d\tau} \frac{d\tau}{\sqrt{t-\tau}} \quad (3.10)$$

Expression (3.10) finds the force, which influences the motion of solid sphere in non-stationary homogeneous flow with low Reynolds number, however, it is not enough for description of the complex flow in ICF. Therefore, the Basset's result (3.10) will be generalized in the next subchapter.

3.2.2. Lagrange equation in turbulent flow

We can compare the result (3.10) to the result obtained for a potential liquid and generalize it by replacing the simple derivation $d\mathbf{u}_f/dt$ with the material derivation $D\mathbf{u}_f/Dt$ (*Brennen, 2005; Crowe, 1998*).

The contribution to the force made by the summand that contains the integral (Also known as Basset force), is not so significant because of the oscillating flow acceleration (*Kirpo et al., 2006*), thus, will be neglected.

It is necessary to note that the flow in our case is not the Stokes flow. Therefore, the drag coefficient C_D (*Schiller & Naumann, 1933*) should correct the third summand in (3.10), and the first summand should be multiplied by the acceleration coefficient C_A (*Odar & Hamilton, 1964*):

$$C_D = \frac{9\nu}{2a^2} \frac{\rho_f}{\rho_p} (1 + 0.15 \cdot Re_p^{0.687}), \quad C_A = 2.1 - \frac{0.132}{0.12 + Ac^2}, \quad (3.11)$$

where $Re_p = d \cdot U/\nu$ is the particle Reynolds number, $Ac = U^2 d^{-1} \cdot (dU/dt)^{-1}$ is the acceleration parameter, $U = \mathbf{u}_f - \mathbf{u}_p$ is relative particle velocity. It is clear from (3.11) that if $Re_p > 1$, then C_D should be expressed in Schiller-Naumann form, and it reduces to the Stokes drag otherwise.

As far as the flow is not homogeneous and external gravitation and EM fields exist, some additional forces should be taken into account in the Lagrange equation.

Lift force appears due to the flow circulation around a particle, like wing lifting force, which appears due to the pressure difference on the different side of the object. The simplest example of such force is that in the shear flow. The force expression depends on the parameter $\epsilon = \sqrt{Sr/Re_p}$, where non-dimensional shear stress $Sr = |\partial\mathbf{u}_f/\partial\mathbf{s}| \cdot d/U$, \mathbf{s} is a unit vector perpendicular to \mathbf{U} . For the case $\epsilon > 0.5$ it is possible to use *Saffman (1965)* approximation, which was generalized for 3D shear field by *Li & Ahmadi (1992)*. However, even rough estimation shows that $\epsilon < 1$ in the present case. Unfortunately, there is no model for lift force, which acts on a solid particle, in the case $\epsilon < 0.5$. There is the *Legendre & Magnaudet (1998)* model for bubbles:

$$\frac{1}{m} \mathbf{F}_{lift} = \frac{\rho_f}{\rho_p} C_L \cdot [\mathbf{U} \times \text{rot}\mathbf{U}], \quad (3.12)$$

where C_L is the lift coefficient that depends on Re_p and Sr . *Legendre & Magnaudet (1997)* generalized the analysis performed by *Saffman (1965)* and *McLaughlin (1991)* for the flows with the low particle Reynolds number, and C_L can be approximated as follows (the Saffman approximation) (*Legendre & Magnaudet, 1997, 1998; McLaughlin, 1991*):

$$C_L^{lowRe}(Re_p, Sr) = \frac{6}{\pi} \frac{1}{\sqrt{Re_p Sr}} J'(\epsilon), \quad J'(\epsilon) = \frac{2.255}{(1+0.2 \cdot \epsilon^{-2})^{3/2}}. \quad (3.13)$$

Legendre & Magnaudet (1998) propose following approximation for high particle Reynolds numbers:

$$C_L^{highRe}(Re_p) = \frac{1}{2} \frac{1+16 \cdot Re_p^{-1}}{1+29 \cdot Re_p^{-1}}. \quad (3.14)$$

For the particle Reynolds number between the approximations (McLaughlin-Legendre-Magnaudet) expression is as follows (Legendre & Magnaudet, 1998):

$$C_L(Re_p, Sr) = \left[(C_L^{lowRe}(Re_p, Sr))^2 + (C_L^{highRe}(Re_p))^2 \right]^{1/2} \quad (3.15)$$

As far as C_L depends on two parameters (Re_p and Sr), it is useful to plot down these dependences (Figure 3.2). The range of Re_p and Sr for the particular case will be obtained below as well as we will choose the suitable approximation.

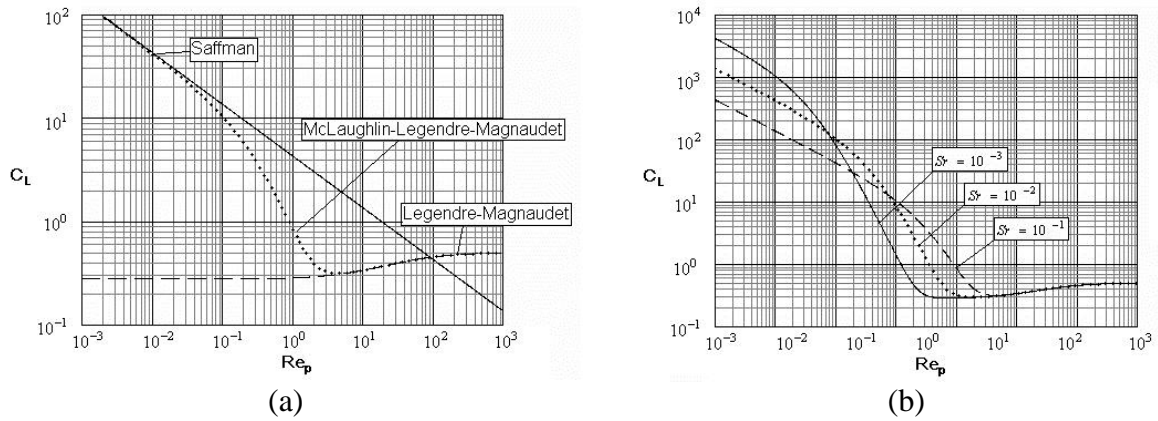


Figure 3.2: (a) Different approximations for the lift coefficient C_L (here $Sr = 0.1$); (b) the McLaughlin-Legendre-Magnaudet approximation for the lift coefficient C_L for different Sr .

However, the lift coefficient (3.13) – (3.15) is expressed for bubbles but the aim of the present investigation is the research of a solid particle motion. This model takes into account the momentum transfer between the flow around the bubble and the inner recirculation flow inside the bubble, which is caused by the flow stress at the interface. Therefore, the lift force for the bubbles is smaller than for solid spheres. Legendre & Magnaudet (1997) also showed that for $\epsilon \gg 1$ and small Re_p ratio between the lift coefficient for solid sphere and for a bubble is equal to $9/4$. The same coefficient will be extrapolated to the case of the present investigation. Thus, C_L for solid spheres will be assumed as that for bubbles (3.15) multiplied by $9/4$.

Another additional force is buoyancy, which appears due to difference between ρ_p and ρ_f .

As it was mentioned above, the particle laden flow is situated in a strong external EM field. Leenov & Kolin (1954) showed that the particles are influenced by EM field directly if their electrical conductivity σ_p differs from conductivity of the liquid metal σ . Current and magnetic induction values in the particle and in the surrounding liquid becomes different and additional force influences on the particle. This force can be derived solving the Laplace equation for current density (Leenov & Kolin, 1954):

$$\frac{1}{m} \mathbf{F}_{em} = -\frac{3}{2} \frac{\sigma - \sigma_p}{2\sigma + \sigma_p} \frac{1}{\rho_p} \mathbf{f}_{em},$$

where the specific Lorentz force \mathbf{f}_{em} is defined by expression (3.1). A great transition resistance appears on the surface between the particles and the metal, hence, we can consider the force influencing on the non-conducting particles ($\sigma_p \ll \sigma$), which can be expressed as follows

$$\frac{1}{m} \mathbf{F}_{em} = -\frac{3}{4} \frac{1}{\rho_p} \mathbf{f}_{em}.$$

Thus, taking into account all above-mentioned forces, the following Lagrange equation for the non-conductive spherical particle motion is used:

$$\underbrace{\left(1 + \frac{C_A \rho_f}{2 \rho_p}\right) \frac{du_p}{dt}}_{\frac{du_p}{dt} + \text{added mass force}} = \underbrace{C_D \mathbf{U}}_{\text{drag force}} + \underbrace{\left(1 - \frac{\rho_f}{\rho_p}\right) \mathbf{g}}_{\text{buoyancy force}} - \underbrace{\frac{3}{4} \frac{1}{\rho_p} \mathbf{f}_{em}}_{\text{EM force}} + \underbrace{\frac{\rho_f}{\rho_p} C_L \cdot [\mathbf{U} \times \text{rot} \mathbf{U}]}_{\text{lift force}} + \underbrace{\left(1 + \frac{C_A \rho_f}{2 \rho_p}\right) \frac{D\mathbf{u}_f}{Dt}}_{\text{acceleration} + \text{added mass}}. \quad (3.16)$$

3.2.3. Statistical analysis of the forces¹

This Chapter is devoted to the analysis of the significance of the forces in the Lagrange equation (3.16). This analysis will be done for ICF-1 determining the distribution of the forces that have influence on the particles with the different sizes and densities in the whole volume. 75 particles are injected into a horizontal plane near the top surface of the crucible. During the period of 10 s the initial cloud of the particles is distributed more or less homogeneous inside the zones of the main vortices (see Figure 2.4) but the number of the particles is different between the zones of the upper and the lower main eddies (Ščepanskis *et al.*, 2010). So we skip this transitional period and start to collect data. The values of the non-dimensional parameters and the magnitude of the forces are saved for each particle every 50 ms for the period of 20 s that corresponds approximately to 6 periods of a particle circulation in the main vortex. Therefore, the statistical database consists of $75 \times 20 / 0.05 = 30000$ information units. Thereby, it is assumed that the data from the whole volume and for all states of quasi-stationary turbulence are collected.

First, the statistical analysis of the non-dimensional parameters (Re_p , Sr and Ac – see Chapter 3.2.2) will be done to choose the approximation of the forces. Then we will evaluate the distribution of the force densities.

The particles with the liquid-to-particle density ratio $S = \rho_f / \rho_p$ equal to 1 and 1.5 and the diameter d from 10 μm to 200 μm (that is from 6 ppm to 0.1% of the radius of the main vortex) are analyzed.

The acceleration parameter Ac for all examined cases is between $1e+2$ and $1e+5$. Thereby, the acceleration coefficient (3.11) can be simply approximated as $C_A \cong 2.1$.

The half width of the calculated statistical distribution of the particle Reynolds number Re_p is shown on the Figure 3.3. The distribution of Re_p is more or less invariable for the particles with the density equal to the liquid density (Figure 3.3 b), except for the particles with a small diameter - 10 μm . For the particles with $S=1.5$ Re_p increases with the particle increase in the size. This increase is connected with the significant role of buoyancy force that produces an axial velocity and will be explained below. For $S=1.5$ and $d > 100 \mu\text{m}$ $Re_p > 1$, therefore, we should use the *Schiller-Naumann (1933)* approximation for the drag coefficient (3.11), in other cases it is possible to apply the Stokes form for C_D .

The calculations show that the non-dimensional shear stress Sr varies between $1e-3$ and $1e-1$. Taking into account also the Figure 3.3 and the behavior of the lift coefficient (Figure 3.2), we can conclude that C_L should be defined within the McLaughlin-Legendre-Magnaudet approximation (3.13) - (3.15) with the correction for solid spheres (additional coefficient $9/4$ – see Chapter 3.2.2).

¹ The analysis in this chapter is also published in Ščepanskis *et al.* (2011).

Apparently, EM force is localized near the wall due to the limited penetration depth of the EM field. Therefore there is no reason to investigate this force statistically.

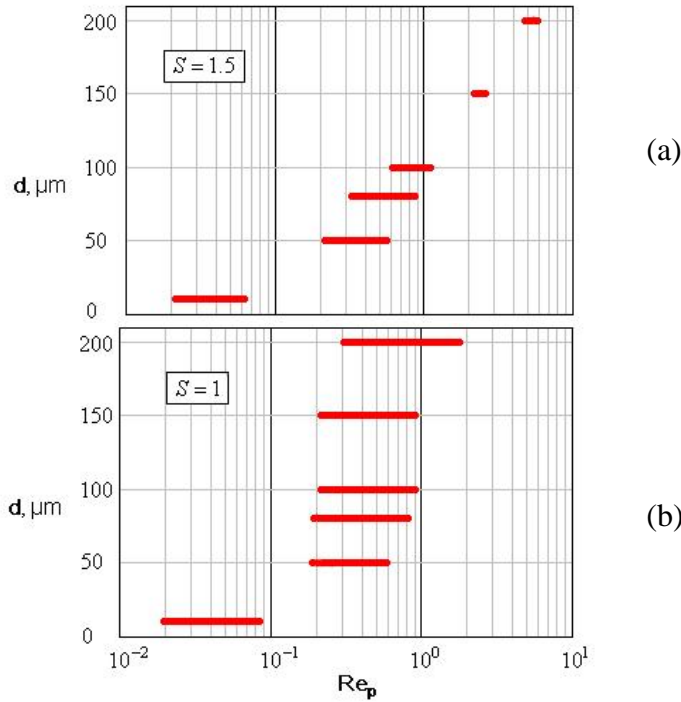


Figure 3.3: The half width of the calculated statistical distribution of Re_p . (a) $S = \rho_f/\rho_p = 1.5$; (b) $S = 1.0$.

The half width of the statistical distribution of drag, lift, acceleration and added mass force densities for the particles with the diameters from 10 μm to 200 μm and $S=1.0;1.5$ is shown on the Figure 3.4. The mentioned densities approximately correspond e.g. to the densities of steel – niobium and steel – grey tin alloys respectively.

We can notice that added mass and acceleration force densities are relatively independent of the particle size in the both cases ($S=1.0$ and $S=1.5$). On the other hand, the lift force density decreases with the increase of the particle size. The behavior of drag force density is different for the various S . It decreases with the decrease of a particle diameter like lift force density for the case $S=1.0$. But in the case $S=1.5$ drag force density decreases only until it achieves the value of buoyancy force density, and then it still remains distributed approximately around the buoyancy force point. Buoyancy leads to the axial motion and moves the particles to the surface. In the most cases drag force opposes buoyancy and mixes a particle deeper in the melt (e.g. in the zone of the upper eddy near the wall). As far as the drag coefficient C_D decreases with an increase of the particle size (3.11), buoyancy force and axial motion become relatively stronger for the larger particles. So the particle axial velocity increases and consequently the difference between the flow and particle velocities U also increases. Thereby, we can observe such a coupling of drag and buoyancy force for big light particles.

Figure 3.4 shows that for the particles with $d \geq 80$ μm and $S=1.0$ we should take into account all forces, but for $d < 80$ μm - only drag and lift forces. For the particles with $S=1.5$ and $d \leq 100$ μm drag, lift and buoyancy forces should be taken into account, but for the particles with $d \geq 150$ μm only drag and buoyancy forces dominate. So we find the separating size: $d = 80$ μm for $S=1.0$ and $d = 100$ μm for $S=1.5$. These values separate the sizes when different sets of forces are applicable. Apparently, the separating size for $S > 1.0$ rises with an increase of S .

Generally, the significance of acceleration and added mass forces decreases with the increase of S . The lift force also becomes unimportant for big particles. These regularities should be true also for such systems with the different parameters.

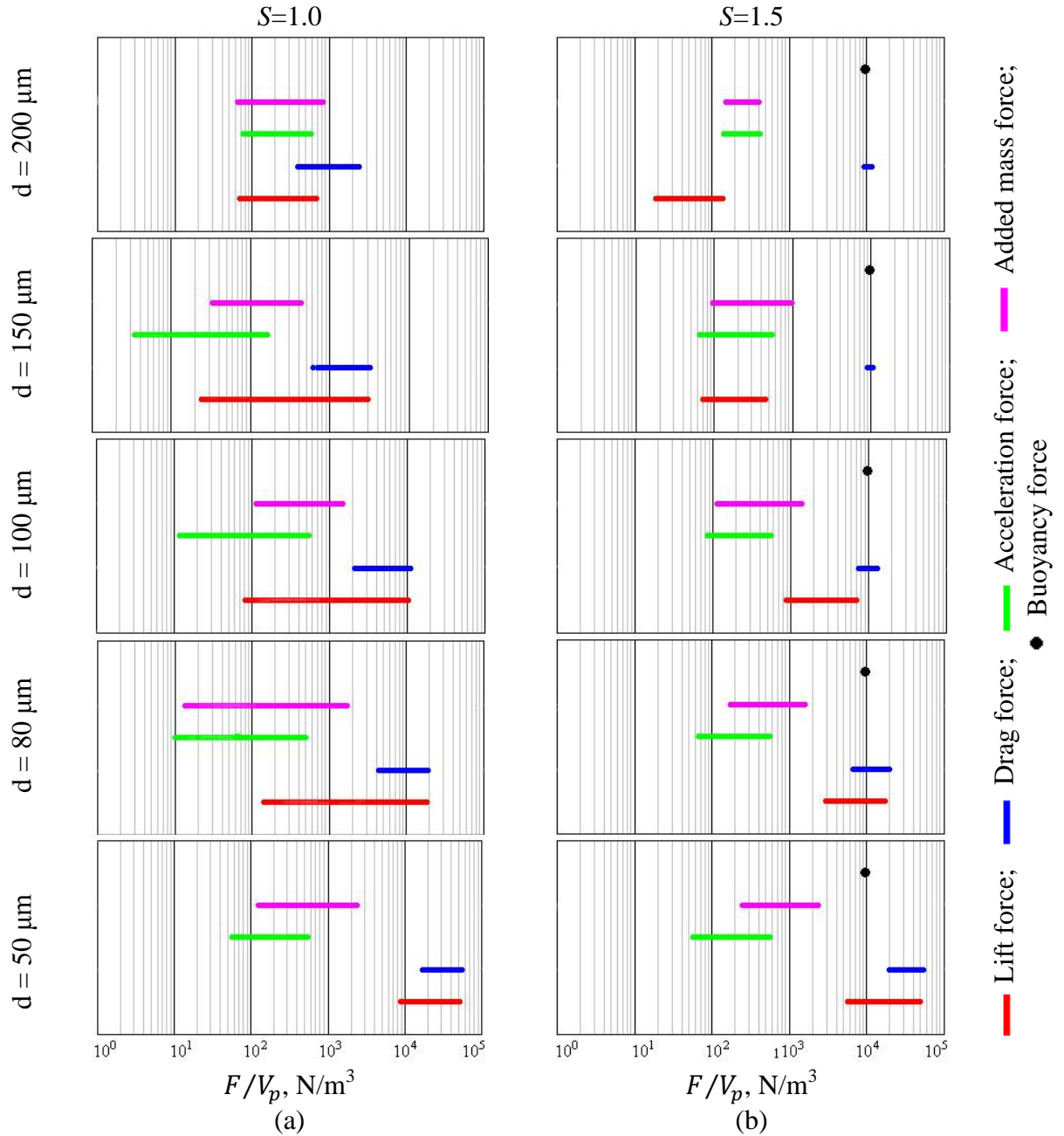


Figure 3.4: The half width of the calculated statistical distribution of the drag, lift, acceleration and added mass force densities F/V_p , where V_p is a particle volume, for the particles with (a) $S = \rho_f/\rho_p = 1.5$, (b) $S = 1.5$.

3.2.4. Trajectories of particles

The trajectories of $100 \mu\text{m}$ particles on Figure 3.5 illustrate the behavior of the particles in the flow of ICF-1. The particles start their motion at the 10^{th} second from the beginning of stirring near the top surface of ICF-1. Figure 3.5 (a) illustrates the particle that does not leave the upper vortex; the particle on Figure 3.5 (b) goes to the lower part of the crucible after one loop in

the upper vortex; and, finally, the trajectory on Figure 3.5 (c) illustrates the particle, which rapidly comes to the lower part of the crucible. Generally, Figure 3.5 demonstrates 3 possible types of the behavior of the particles. However, it will be discussed later that the larger part of the light particles ($S > 1$) follow the strategy on Figure 3.5 (a).

Figure 3.6 shows EM force (the first row) and lift force (the second row) following the trajectories of 3 different particles. Following the definition of EM force in equation (3.16), the vector of the force is shown on Figure 3.6 (the first row) in the direction from the wall, however, as far as the appropriate term in equation (3.16) has negative sign, EM force actually moves the particle in the direction to the wall. It is easy to recognize that EM force becomes significant when the particle is close to the wall (within the penetration depth of EM field, which can be expressed as $\delta_{em} = \sqrt{2/\mu_0\sigma\omega}$, where ω is a circular frequency). But in the bulk of the melt EM force is negligible. The layer of EM penetration is sufficiently thin (about 20% of the radius of ICF-1 – $\delta_{em}/R = 0.2$). Due to the non-slip boundary conditions the flow velocity is zero at the wall and it increases in a radial direction until it rapidly achieves the maximal value at the relative distance $\Delta/R = 0.04$ from the wall (see Figure 2.4). $\delta_{em} > \Delta$, therefore, the maximum of velocity is inside the layer of EM penetration. Obviously, particles preferentially move in the streamline of maximal velocity. Therefore, the major part of the particles comes frequently to the layer of significant EM field.

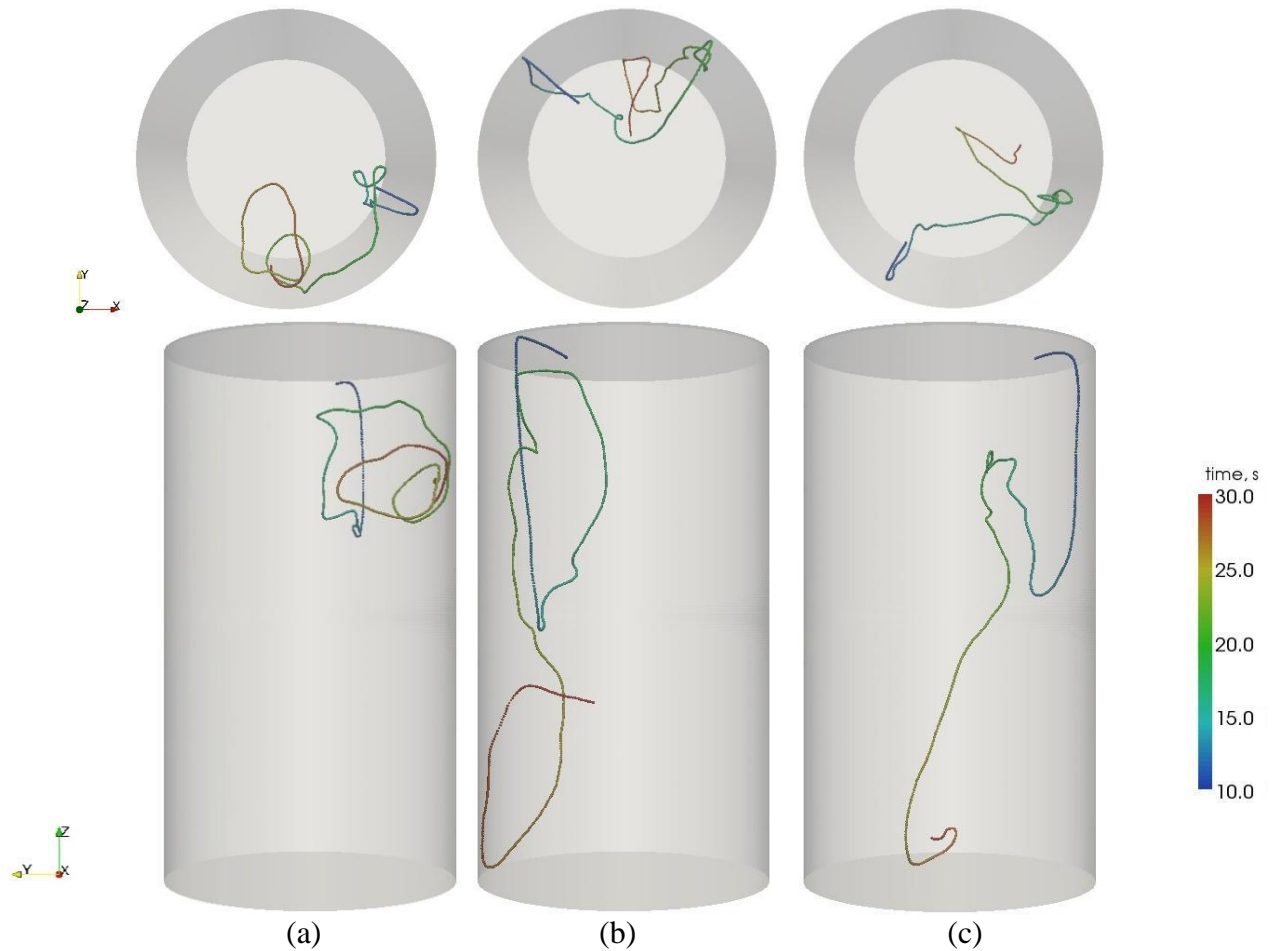


Figure 3.5: The trajectories of 100 μm particles, which start their motion at the 10th s after the beginning of the stirring near the top surface of ICF-1. The first row – the view from the top surface; the second row – the view from the side.

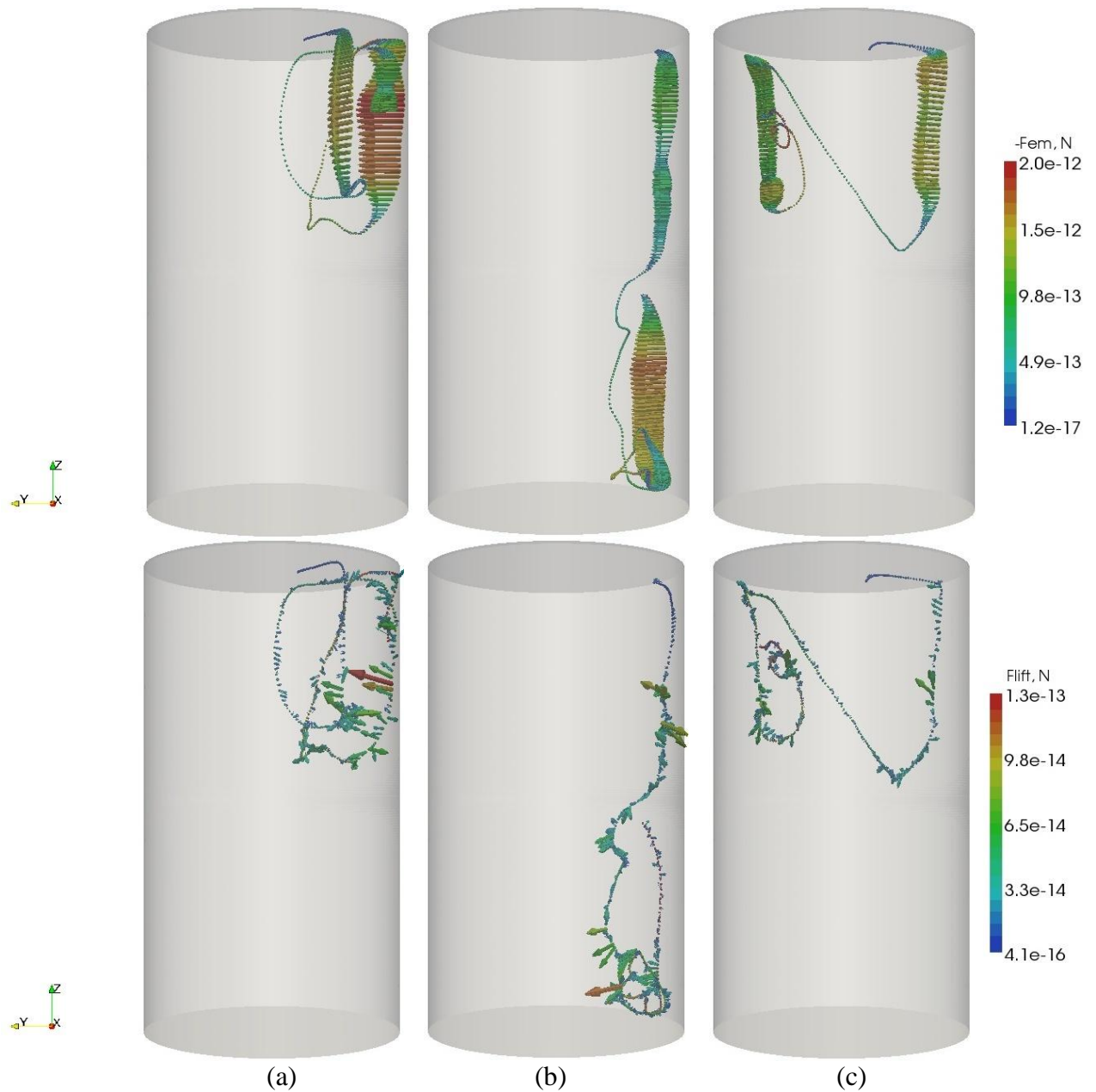


Figure 3.6: The trajectories of the particles with the down force vectors: the first row – $-F_{em}$; the second row - F_{lift} . EM force is shown in the direction from the wall as it is defined in the equation (3.16), however, due to the negative sign in the equation, it pushes the particle to the wall.

The second row on Figure 3.6 illustrates lift force, which moves the particle. This force becomes significant mostly in the zones of eddies near a wall. Figure 2.4 demonstrates the maximum of the flow velocity close to the wall and, consequently, also significant velocity gradient there. As far as lift force is proportional to $\mathbf{U} \times \text{rot}\mathbf{U}$ (see expression (3.12)), it is significant in the mentioned zone. However, Figure 3.6 also shows the vectors of lift force in the bulk of the flow due to instantaneous non-homogeneities that appear in the transient flow.

It was discussed in the Chapter 3.1 that the separate trajectory of the particle is not meaningful due to the LES approach, which assumes averaging of the high frequency pulsations of the flow. However, Figure 3.7 demonstrates the trajectories of the particles, which are down

taking into account different sets of the forces in the Lagrange equation (3.16), this figure only illustrate the significance of all forces. Figure 3.7 b shows that addition of acceleration force allows the particle to come to the lower part of the crucible. Even only the addition of EM force significantly changes the trajectory of the particle on Figure 3.7 (c). Despite the fact that the trajectories themselves are not meaningful, Figure 3.7 generally demonstrates that additional forces can significantly change the behavior of the particles; therefore, all mentioned forces in equation (3.16) should be taken into account.

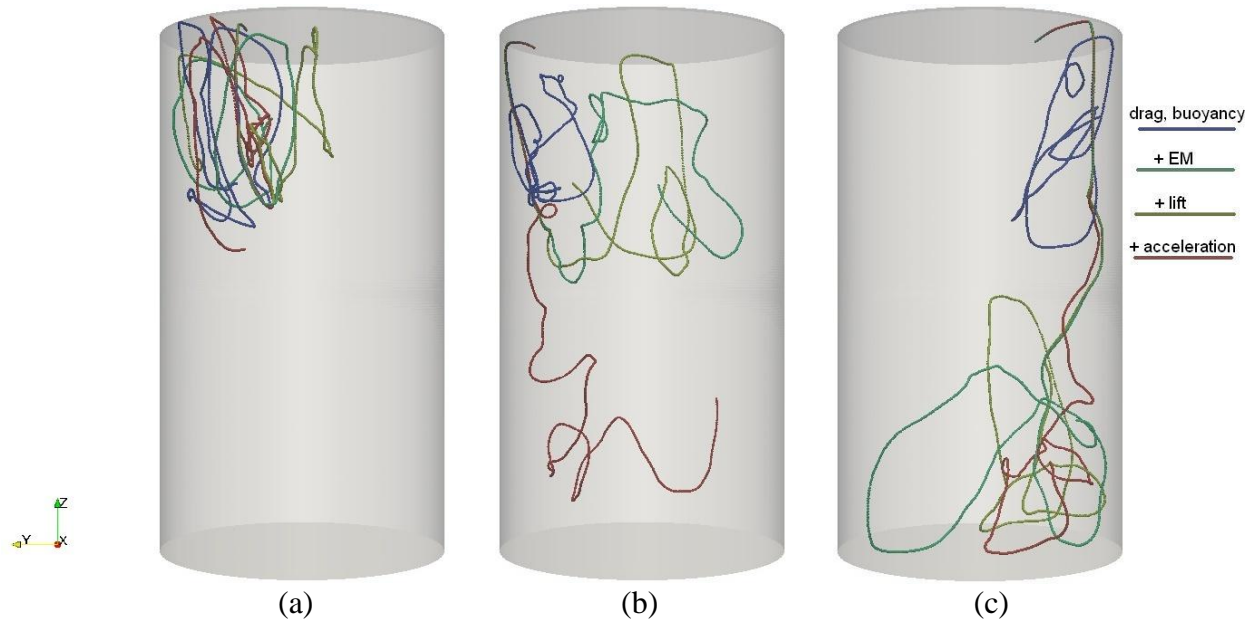


Figure 3.7: The trajectories of particles taking into account different sets of forces: additional forces are sequentially added to the basic set (see the legend).

Figure 3.8 shows the trajectories of the particles with the different diameters. The particles in each image begin their motion at the same point close to the top surface of the melt. This figure demonstrates that the size of the particles significantly influence their behavior, e.g. 50 μm particle on Figure 3.8 (b) comes to the lower part of the crucible, but 100 μm and 200 μm particles remains in the upper part. The opposite behavior is observed on Figure 3.8 (c).

3.3. Numerical realization of the algorithm

The numerical LES method for turbulence modelling was discovered by Joseph Smagorinsky in 1964. Since that time every scientific group and institution has begun to develop their own computation code for the simulation of turbulence in different complex geometries and conditions. Even in the 80s and the 90s every researcher began his/her investigation with the programming and the coding of numerical algorithm. Later with the increase of computational capacities, the universal commercial software becomes wide-spread in the 2000s, which gives the possibility to carry out turbulence simulations for industrial cases. Then many engineers start to carry out investigations and optimisations of complex flows, often even without or with minimal understanding of the numerical schemes, which are utilized in the commercial software. The computational fluid dynamics (CFD) software, such as FLUENT, ANSYS CFX, COMSOL and others, significantly changed the scientific community, industry and even high education

system. Scientists and industry began to believe the results of modelling trusting software brands. However, students lost the motivation and necessity to study numerical methods so deep to write their own codes. Hence, a significant breakthrough was done in the 2000s in the area of the simulation and the optimisation of the industrially oriented turbulent flows. But at the same time the engineers lost knowledge about numerics and often also fundamental physics that significantly limits possibility to extend the models for the investigations of new phenomena and challenges, like e.g. turbulent multiphase flows.

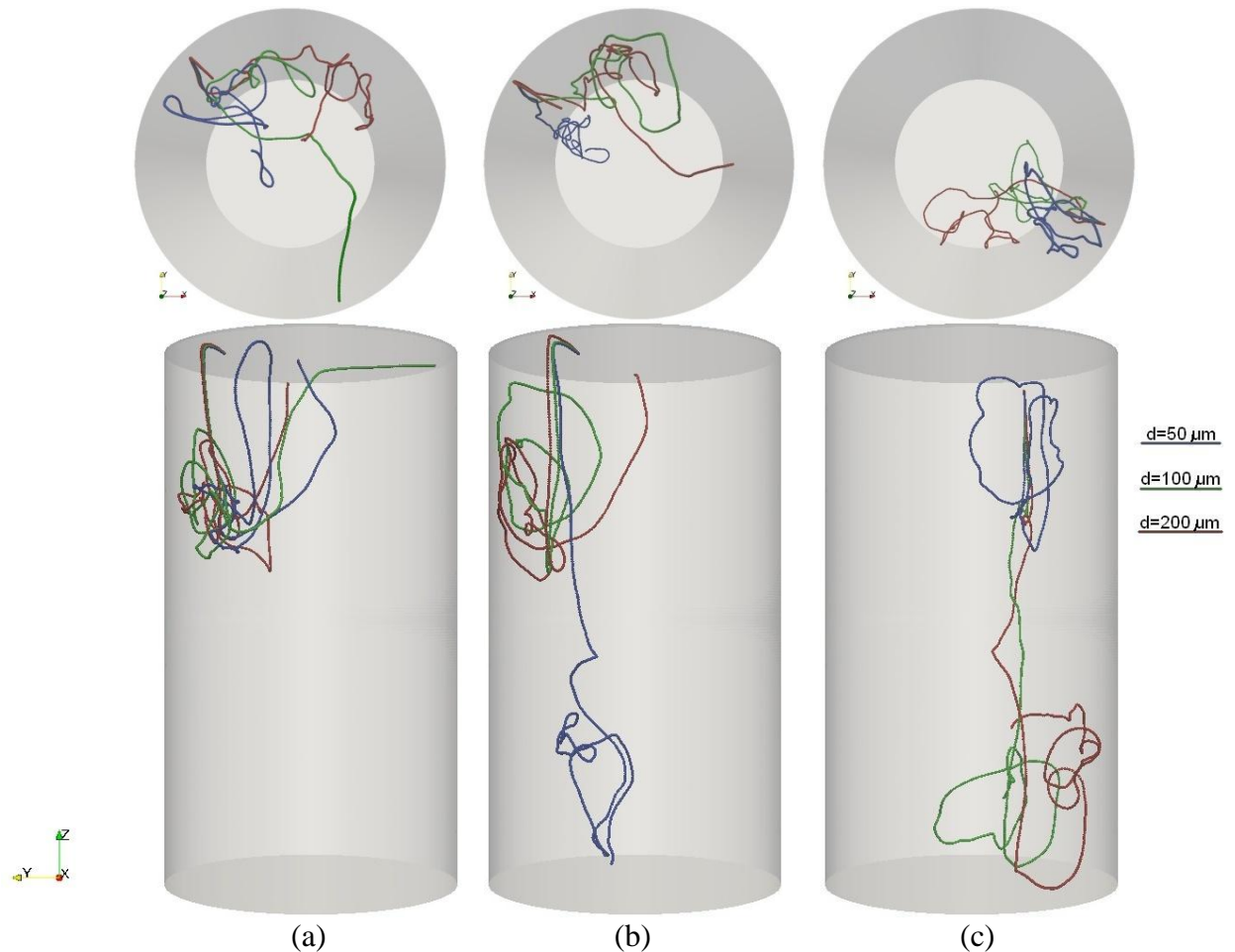


Figure 3.8: Trajectories of particles with the different diameter (see in the legend) that begin their motion at the same position near the top surface of the melt. The first row - view from the top surface; the second row – view from the side.

Finally, the open source approach began to diffuse into the scientific calculations in the 2010s. The CFD code OpenFOAM (Open Source Field Operation and Manipulation), which started as the commercial code, lost the competition on the engineering software market and decided to follow the fast developing open source philosophy in the IT industry (e.g. Linux operational system). OpenFOAM decided to open their code in 2004. It means that everybody can use it and get access to the code, as well as modify it and make improvements. This software is designed as the system of the C++ libraries for the solution of partial differential equations, especially, the CFD problems. The architecture of the libraries allows operating with differential operators and their numerical approximations easily. Thus, it is possible to make own solvers and modifications in powerful CFD tools, which are already compiled in OpenFOAM. The code

is released as free and open source software under the GNU General Public License¹. It is maintained by The OpenFOAM Foundation, which is sponsored by the ESI Group, the owner of the trademark to the name OpenFOAM. However, the open-source-CFD community splited and OpenFOAM-extend is maintained by Wikki Ltd. This fork has a large repository of community-generated contributions, much of which can be installed into the official version of OpenFOAM with minimal effort. It is developed in parallel to the official version of OpenFOAM, that incorporates its latest versions, although these are released one or two years later.²

However, open-source software has also disadvantages. The most significant is the lack of the user-friendly interface for pre-processing and the definition of parameters. This disadvantage makes inconveniencies for engineers to use it. Another point is numerous parameters and degrees of freedom, which should be defined for the particular problem. On the opposite, commercial software usually uses predefined parameters or hidden procedures to define them automatically. Thus, using commercial software, engineers are safer against possible numerical mistakes they can make. However, such solution is good in the standard or typical cases but strongly limits the researcher's opportunities solving more complicate problem.

Despite all mentioned disadvantages, the open-source CFD software (especially, OpenFOAM) became a strong trend in the 2010s. Many world leading universities, e.g. Technical University of Munich, Royal Institute of technology (Stockholm), Imperial College London, Polytechnic University of Milan and many others, use and develop OpenFOAM libraries. Even industrial companies, e.g. Volkswagen, Renault, Areva and others, do the simulation and optimisation in OpenFOAM. As far as the software libraries are open, wide community of OpenFOAM users instantaneously develop the software for their own needs and publish new solvers and libraries.

Concerning the present work, the analysis in the Chapter 3.2 showed the necessity to use the wide set of inertial forces in the Lagrange equation. The known tools for the Lagrange tracking in a commercial software (ANSYS CFX, FLUENT) are mostly oriented to tracer particles. And taking into account advantages of the open-source OpenFOAM it is more convenient to expand the standard algorithm in this software rather in ANSYS products. For this reason OpenFOAM was chosen for the Euler-Lagrange simulation of solid inclusions in the EM driven flow of ICF, that is for the goals of the present work.

3.3.1. Solver for EM driven flow

As it was discussed in the Chapter 3.1 and shown on Figure 3.1, the first step of the algorithm is the calculation of EM field. OpenFOAM has no solver suitable for such problem. Therefore, the proper calculation was done using commercial software ANSYS³.

ICF has simple axisymmetric geometry (Figure 2.2), therefore, neglecting the non-symmetrical supply of the inductor to the generator, we can calculate the EM field in 2D for the half of central vertical section and extrude it to cylinder after that. Following *Kirpo (2008-PhD)* and *Umbraško (2011-PhD)* ANSYS calculates the field of the effective value of a harmonic vector potential in a quasi-stationary approximation (see discussion in the Chapter 2.2) and

¹ The GNU General Public License (GNU GPL or GPL) is the most widely used software license, which guarantees end users (individuals, organizations, companies) the freedoms to use, study, share (copy), and modify the software. Software that ensures that these rights are retained is called free software (from the article "GNU General Public License" in the free web-encyclopedia "Wikipedia", http://en.wikipedia.org/wiki/GNU_General_Public_License).

² From the article "OpenFOAM" in the free web-encyclopedia "Wikipedia" (<http://en.wikipedia.org/wiki/OpenFOAM>).

³ However, last time open source software GetDP also become suitable for the calculation of EM problem.

reconstructs the field of a magnetic flux and the Lorentz force from the vector potential. The calculated Lorentz force and the Joule heat ($Q = j^2/\sigma$, where j is the induced current density and σ is the conductivity of the liquid metal) are exported from ANSYS and imported to OpenFOAM as the external sources.

As it is shown on Figure 3.1 HD calculation with the external Lorentz force is the next step of the algorithm. As it has already been discussed in the Chapter 3, HD is calculated within the LES approach. OpenFOAM contains the standard *pisoFoam* solver, which solves turbulence equations using the PISO (Pressure-Implicit with Splitting of Operators) algorithm (Issa, 1985; Jasak, 1996; Oliveira & Issa, 2001). Rather than solve all of the coupled equations in a coupled or an iterative sequential fashion, PISO splits the operators into an implicit predictor and multiple explicit corrector steps. This scheme is not thought of as iterative, and very few corrector steps are necessary to obtain desired accuracy.¹ The Navier-Stokes equation and the equation for a temperature field in standard *pisoFoam* code are supplemented with volume force, which contains EM force density and buoyancy force. The code and comments are given in Appendix 1.

Non-slip boundary conditions (zero velocity) are applied on the walls of the crucible and slip boundary conditions (zero normal component of velocity) on the free top surface. Adiabatic thermal conditions ($\nabla T = 0$) are used on the refractory walls and convective thermal conditions are applied on the surface of the melt:

The described above modifications of *pisoFoam* solver finds the new *EmThermalPisoFoam* solver. This solver was examined carefully, comparing the results of OpenFOAM simulation with ANSYS CFX results, which were verified by the experiment (Kirpo, 2009-PhD; Umbraško, 2011-PhD). The examination lighted some problems concerning near wall treatment of EM induced flow, which leads to special requirements for the numerical mesh. This aspect is described in the next chapter.

3.3.2. Numerical mesh for HD simulation

As it was discussed in the Chapter 2.2, the recirculated flow in metallurgical induction equipment has several peculiarities, which essentially differs this class of flows from the rest turbulence. The most important peculiarities are the intensive flow close to the wall of crucible and tearing off the flow in the middle zone of the crucible due to the Lorentz force influence (see Figure 2.4). These two facts lead to the necessity to refine the numerical mesh near the wall. The mesh should resolve the boundary layer to simulate the mentioned peculiarities of the flow correctly. Otherwise errors in the boundary layer will lead to incorrect simulation of the whole flow.

However, such refinement leads to heavy meshes, which can exceed 10 million elements even in the case of the laboratory scale ICF-1, which is the simplest induction equipment. Thus, very powerful computational resources are needed for such calculation, which is not often available. Therefore, the optimization of the mesh is very useful task before the start of the simulation.

¹ From the article “BuoyantBoussinesqPisoFoam” in unofficial OpenFOAM wiki web-page <http://openfoamwiki.net/index.php/BuoyantBoussinesqPisoFoam>.

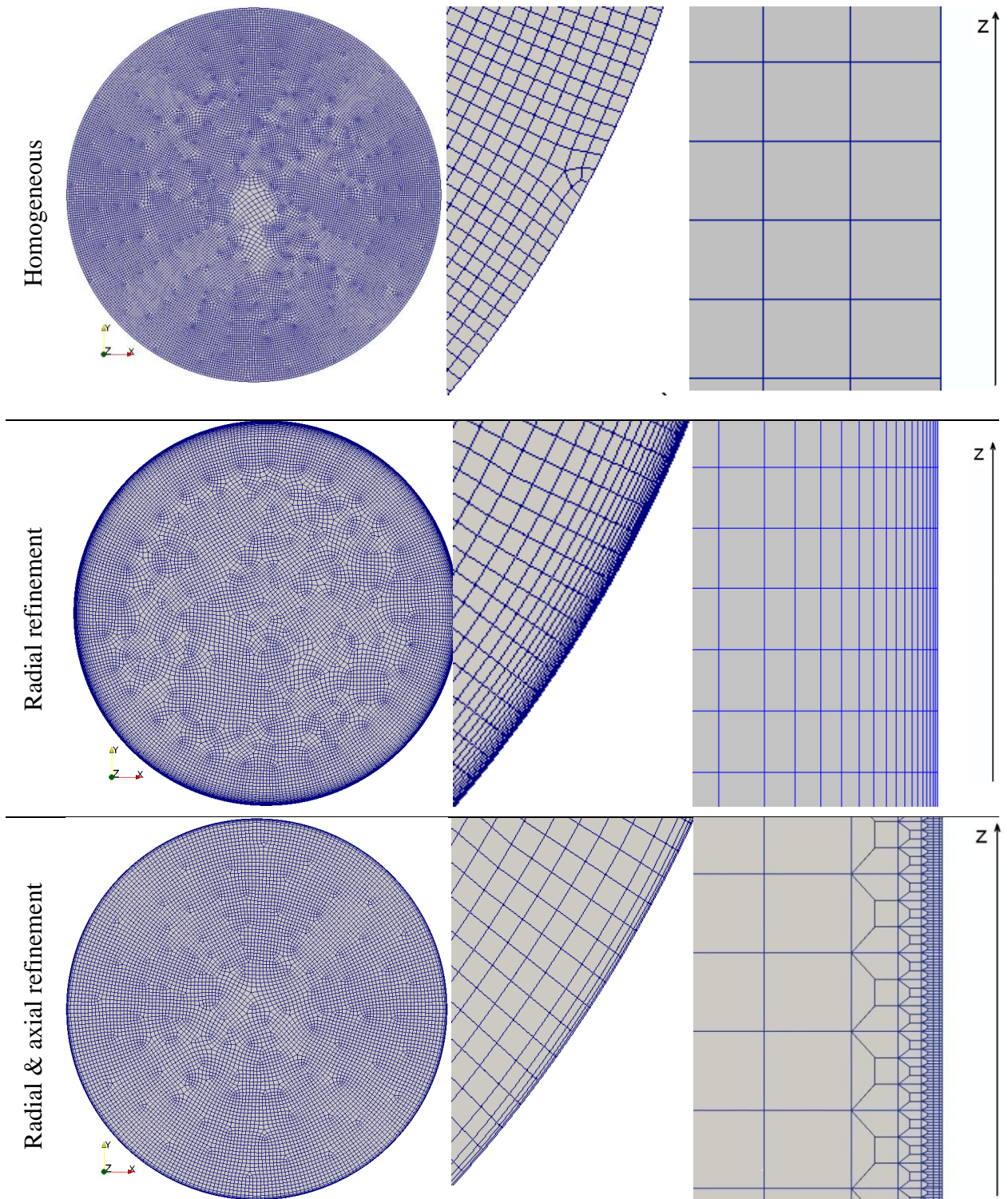


Figure 3.9: Different meshes of ICF-1. The 1st row – a homogeneous mesh without any refinement; the 2nd row – a mesh with the refinement only in the radial direction; the 3rd row – a mesh with the refinement in the radial and axial directions; the left column – a mesh in a horizontal cross-section of the crucible; the middle column – the enlargement of the mesh in the left column near the wall; the right column – the enlargement of the mesh in a central vertical cross-section of the crucible near the wall.

Figure 3.9 shows 3 different meshes:

- the homogeneous mesh with the average linear cell size 2 mm (the 1st row);

- the mesh with the linear cell size in the interior zone 3 mm and the radial near wall refinement up to a cell size 0.1 mm in the radial direction (the 2nd row);
- the mesh with the linear cell size in the interior zone 3 mm and the radial& axial near-wall refinement up to a cell size 0.1 mm x 0.1 mm in the vertical cross section (the 3rd row).

The second mesh with the refinement in the radial direction has 2.8 million elements. The refinement in the radial & axial directions (Figure 3.9 – 3rd row) already needs 8.3 million elements. The last mesh avoids disproportion in the refined cells near the wall in the radial and axial directions; however, the cell size in angular direction is still one order more than in other directions. The estimation shows that the fully-refined mesh (refined in radial, axial and angular directions) will have up to 20 million elements, which is very heavy task even for computational clusters. It is possible to calculate such mesh using only super computers and big clusters. However, the accelerated development of IT industry can bring us to this goal in the nearest future, but not now after all.

The results of the simulation shows that even a homogeneous mesh (Figure 3.9 – the 1st row) ensures relevant results of an average flow in ICF, because the main vortexes, which mostly create the average flow, are resolved with this mesh. However, the distribution of turbulent energy, which is obtained using this mesh, does not correspond to the experimental results by *Kirpo et al. (2007, 2009-PhD)* (Figure 3.10). The experimental results show the strong maximums at the middle of the crucible near the wall. But the simulation on the homogeneous mesh without refinement (Figure 3.9 – 1st row) finds the maxima of kinetic energy against the maxima of the average velocity (Figure 2.4) – at the middle of mean vortexes near the wall (Figure 3.11). Comparing Figure 2.4 and Figure 3.11 we can conclude, that the maxima of the average velocity and kinetic energy coincide. That means that the average velocity has the main impact in the turbulent energy. Oppositely, experimental results (Figure 3.10) show the maximum in the zone of low magnitude of the average velocity (Figure 2.4). *Kirpo (2009-PhD)* and *Umbraško (2011-PhD)* showed that the maximum of turbulent energy at the middle of the crucible – between the mean vortexes - is formed by intensive axial pulsations of velocity, which have fundamental role in the case of heat and mass exchange in ICF. Chapter 5.2 will contain the discussion of the influence of these pulsations on the particle exchange and homogenization. But now we can conclude, that a homogeneous mesh without refinement near the wall (Figure 3.9 – the 1st row) cannot be used for simulation of the EM induced turbulent recirculated flow in ICF.

Figure 3.12 shows the simulated distribution of the components of turbulent energy, which was obtained in ANSYS CFX software using the mesh with radial refinement near the wall (Figure 3.9 – 2nd row); the calculation was performed by *Umbraško (2011-PhD)*. This distribution qualitatively corresponds to the experimental results on Figure 3.10; however, the magnitude of turbulent energy is still a little bit underestimated.

But the calculation with the same mesh as in the previous case (refinement in the radial direction) using open source OpenFOAM software LES solver (see the Chapter 3.3.1) shows totally different result - Figure 3.13. The maxima of turbulent energy appears in the zone of mean eddies, which is like in the case of the homogeneous mesh (Figure 3.11) and contradicts the experimental results (Figure 3.10).

Thus, the simulation of the same problem using the same LES turbulence model gives different results, when the calculation is performed utilizing the commercial ANSYS CFX software (Figure 3.12) and the open source OpenFOAM software (Figure 3.13). Taking into

account the disproportional mesh elements close to the wall (the cells are much longer in the axial and angular direction than in the radial direction, see Figure 3.9 – 2nd row), it becomes clear that numerically the momentum transfer in the radial direction will be preferential within one cell. That leads to the observed numerical effect – sufficiently underestimation of the axial direction, which is the direction of a long edge of the cell. According to this explanation, the result of OpenFOAM software, which is shown on Figure 3.13, becomes clear. The maxima of the turbulent energy on Figure 3.13 are situated in the zones, where the mean flow starts to change direction and turn to the axis of the crucible (Figure 2.4). The pulsations that appear in the perpendicular direction of the general flow become significant there; however, further the flow turns and the pulsations are found in the axial direction, which is underestimated due to a disproportional mesh. Therefore, the absence of the maximum directly at the middle of the crucible near the wall is observed on Figure 3.13.

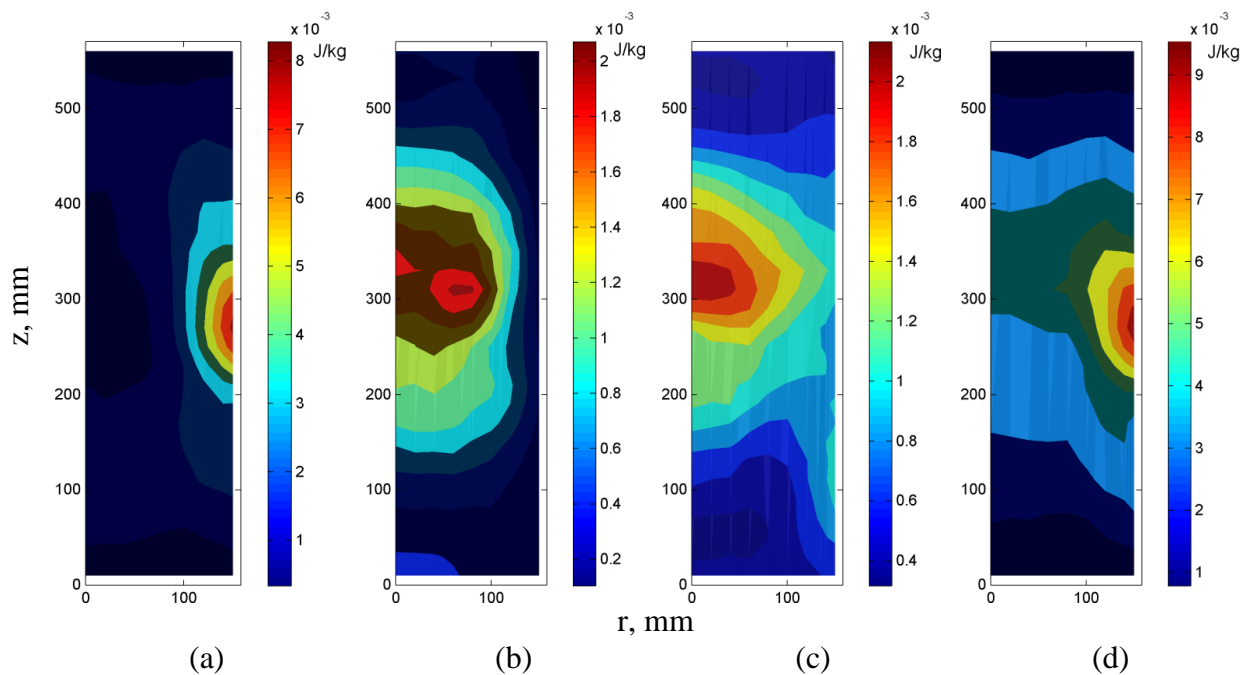


Figure 3.10: The distribution of turbulent kinetic energy in the ICF-1 (experimental results, from *Kirpo, 2009-PhD*). (a) axial component, (b) radial component, (c) tangential component, (d) total.

However, the simulation, which is carried out in ANSYS CFX (Figure 3.12) finds the right distribution of turbulent energy. That means that the commercial software contains either the additional numerical routine to treat a disproportional mesh, or the boundary function as boundary conditions on the wall. Unfortunately, the code of the commercial software is closed for users, moreover, the documentation of the software has no information relating on this question. Therefore, it seems to be impossible to know the peculiarities of the numerical treatment, which is applied in this case. However, it is obviously that both mentioned numerical procedures, which can be applied for the treatment of mentioned effect, lead to greater numerical assumptions than it is supposed within the LES approach. That means that despite the coincidence of the described results (Figure 3.12) within the experiment (Figure 3.10), the simulation of a near-wall zone in ANSYS CFX can contain the numerical effects and the results can be not generally relevant in the spirit of the LES approach.

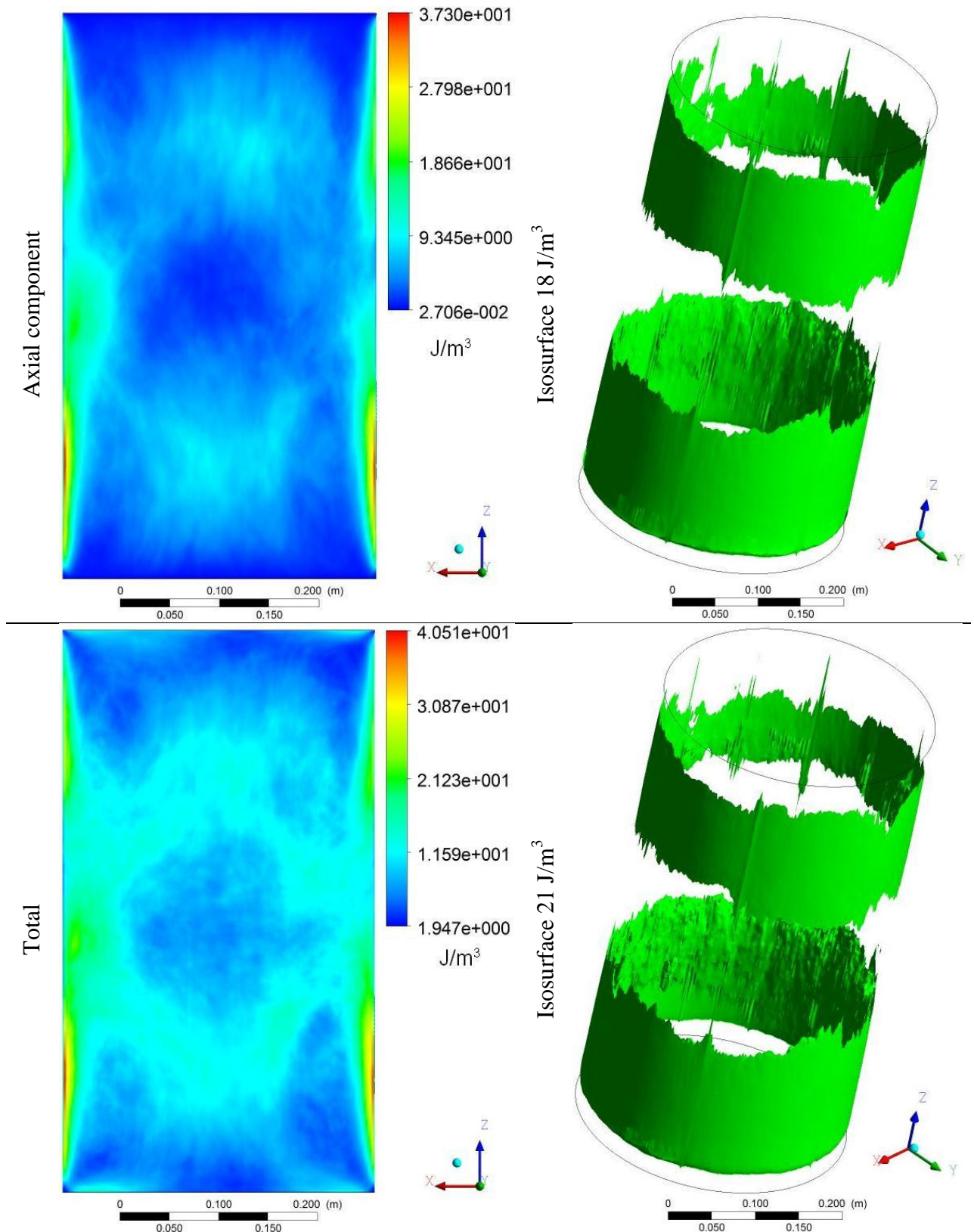


Figure 3.11: Numerical results of the distribution of the axial component (the 1st row) and full (the 2nd row) turbulent energy in ICF-1 (the left column – the central vertical plane; the right column – isosurface), which are calculated in ANSYS CFX software on the homogeneous mesh without refinement near the wall (Figure 3.9 – 1st row).

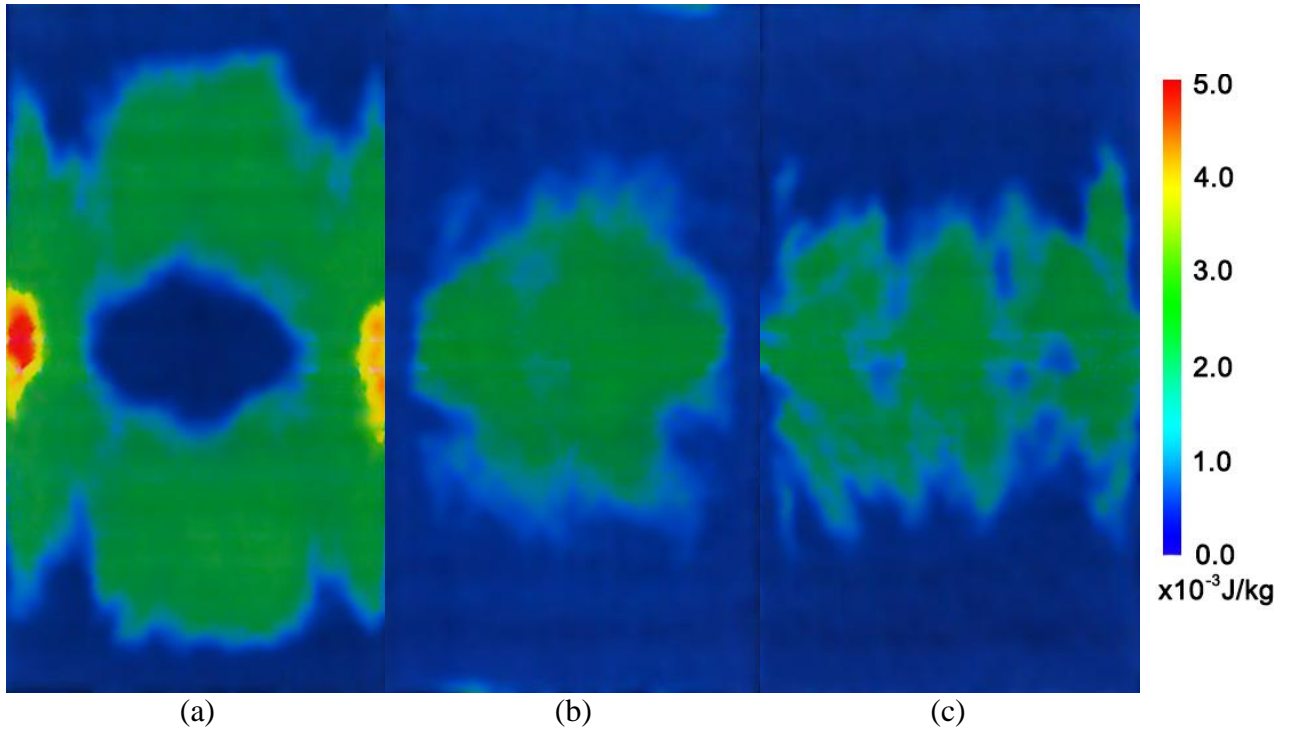


Figure 3.12: The distribution of the component of turbulent energy, calculated with the LES turbulence model in ANSYS CFX using the mesh with only radial refinement (Figure 3.9 – 2nd row). From *Umbraško (2011-PhD)*.

Then we examined the mesh with the refinement in the radial and axial directions (Figure 3.9 – the 3rd row). Such mesh treats the observed numerical effect, which appears in the case of disproportional mesh elements, and leads to the relevant distribution of turbulent energy in the vertical cross section of the crucible (Figure 3.14 a). However, as far as the mesh cells still remain disproportional in the angular direction, the momentum exchange in this direction is numerically underestimated, that leads to a non-homogeneous angular distribution (Figure 3.14 b). Nevertheless, angular averaging of the results (Figure 3.15) shows a good agreement with the experiment (Figure 3.10), which is after all also angular averaged.

Figure 3.10 (c) shows that the angular pulsations are of much less amplitude than the axial oscillations, especially, near the wall. At the same time, *Kirpo et al. (2009, 2009-PhD)* showed that the particle angular distribution in ICF rapidly becomes homogeneous and this process is not sufficient; it means that the axial and radial distributions are of the interest now. Therefore, all results within the present work are proposed to be analyzed in the angle averaged form. This proposal is based on the assumption that an error, which can arise in the axial and radial distribution of particles neglecting the angular momentum exchange, is not sufficient. However, the relevance of this assumption can be examined.

The small angular pulsations of particles can be simulated, by inclusion of artificially the random angular velocity in the particle transport routine, which will be described in the next subchapter. The amplitude of this random value can be derived from the experimental data on Figure 3.10 (c):

$$u_{\varphi,max} = \sqrt{2k_{\varphi}},$$

where k_{φ} is the tangential component of turbulent kinetic energy, which can be estimated from the experimental data as $k_{\varphi} \approx 8e-4$ J/kg near the wall. Thus $u_{\varphi,max} \approx 4$ cm/s.

Figure 3.16 and Figure 3.17 demonstrate the axial and radial distribution of particle volume concentration at different time moments. One curve on the mentioned figures is drawn taking into account artificial random angular flow velocity with the amplitude that corresponds to the experimental results (Figure 3.10) while another curve does not concern it. As it was expected, the difference between the curves on all figures is insignificant. Therefore, we can conclude that the angular flow pulsations can be neglected and the mesh with the radial and axial refinement near the wall (Figure 3.9 – the 3rd row) can be used for the goals of the present work.

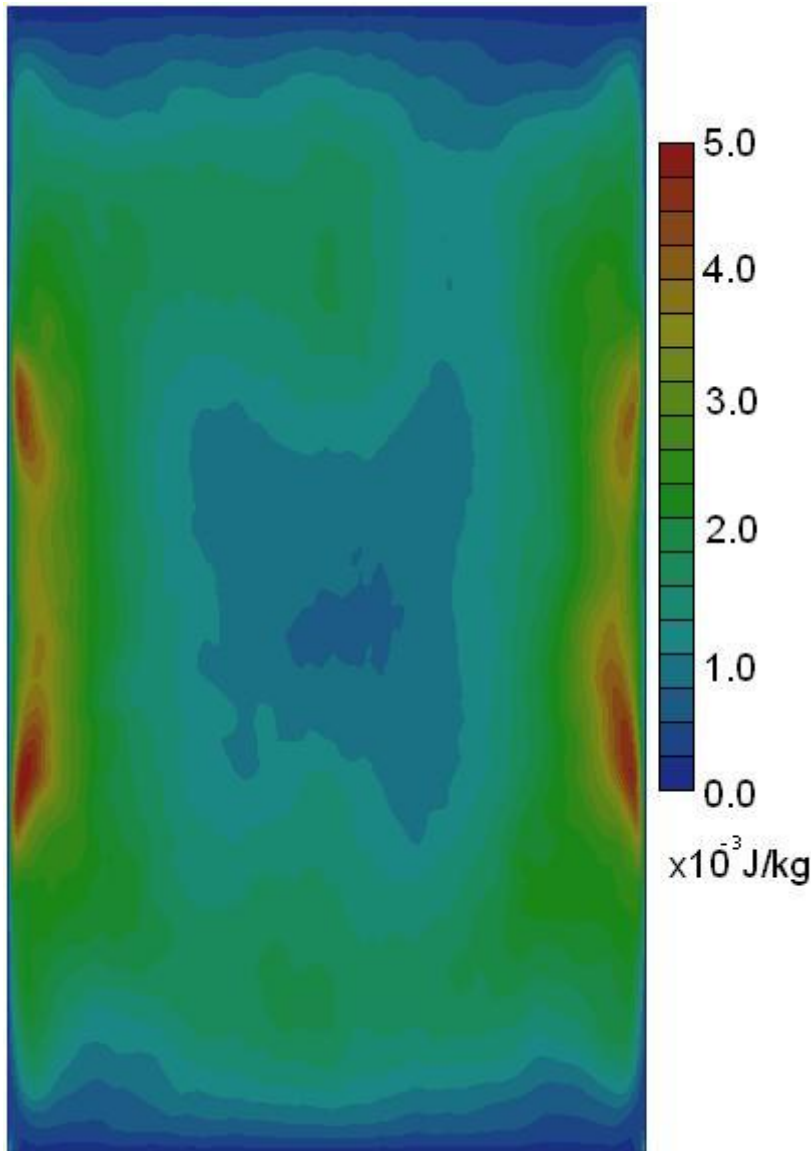


Figure 3.13: Numerical results of the distribution of turbulent energy in the central vertical plane, which is calculated using the mesh with the radial refinement near the wall (Figure 3.9 – 2nd row) in the open-source OpenFOAM software.

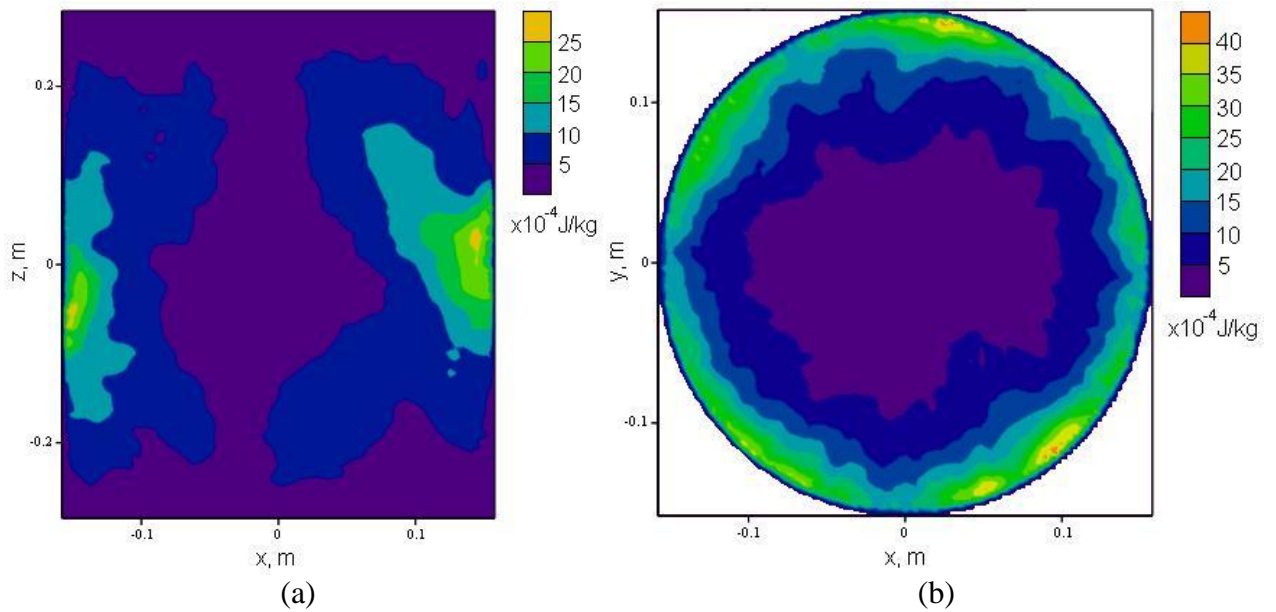


Figure 3.14: Numerical results of the distribution of the axial component of turbulent energy in the central vertical plane. The distribution is calculated using the mesh with the radial & axial refinement near the wall (Figure 3.9 – 3rd row) in the open-source OpenFOAM software. (a) central vertical cross section of ICF-1, (b) central horizontal cross section of ICF-1.

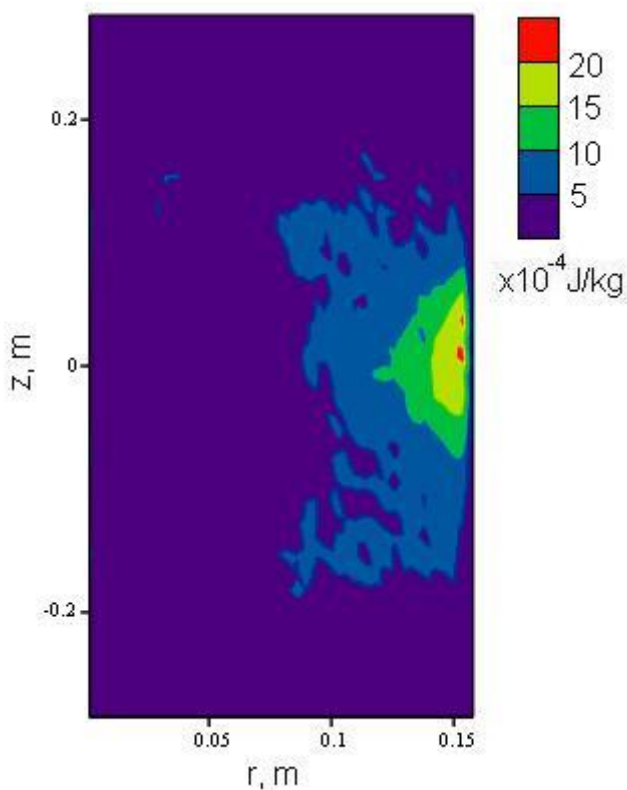


Figure 3.15: Angular averaged numerical results of distribution of the axial component of turbulent energy in the central vertical plane. The distribution is calculated using the mesh with radial & axial refinement near the wall (Figure 3.9 – 3rd row) in the open-source OpenFOAM software.

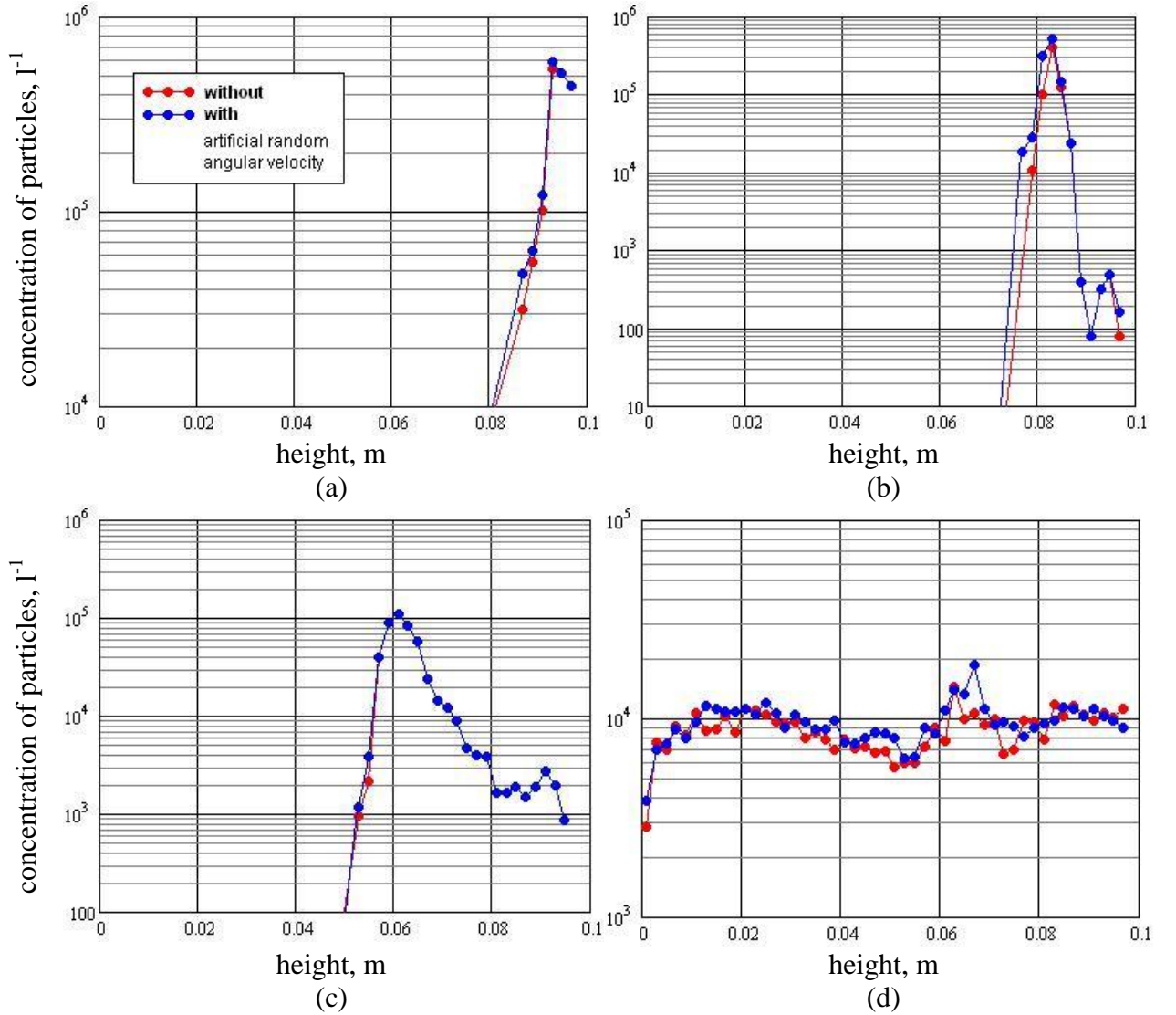


Figure 3.16: Axial distribution of particle volume concentration in ICF-2 at different moments of time: (a) 0.25 s; (b) 0.4 s; (c) 1 s; (d) 10 s. Initially the particles were situated on the top surface of the melt (Figure 5.6). The calculations were done with (the blue line) and without (the red line) artificial random angular velocity with the amplitude 4 cm/s.

3.3.3. Lagrangian tracking

When the numerical realization of single phase problem is discussed (Chapter 3.3.1 and Chapter 3.3.2), we can follow the scheme on Figure 3.1 further and describe the design of particle tracking code. This part of the algorithm is also realized within OpenFOAM libraries¹.

Firstly, the Lagrange equation (3.16) should be discussed. As far as C_A , C_D and C_L are the functions of U and dU/dt (see expressions (3.11, 3.13-3.15)), the Lagrange equation (3.16) becomes non-linear. Such equation is solved iteratively within the present algorithm. For this reason the equation is linearized: all mentioned coefficients are calculated using the particle velocity and acceleration from the previous iteration. The vector production in the term of lift force can be expressed as follows:

$$[\mathbf{U} \times \text{rot } \mathbf{U}] = [\mathbf{u}_f \times \text{rot } \mathbf{u}_f] - [\mathbf{u}_p \times \text{rot } \mathbf{u}_f]. \quad (3.17)$$

$[\mathbf{u}_f \times \text{rot } \mathbf{u}_f]$ and $\text{rot } \mathbf{u}_f$ fields are calculated from the flow velocity \mathbf{u}_f field and interpolated at the particle position.

¹ The particle tracking algorithm is fulfilled on the basis of *solidParticle* and *lagrangian* libraries in OpenFOAM-1.6.

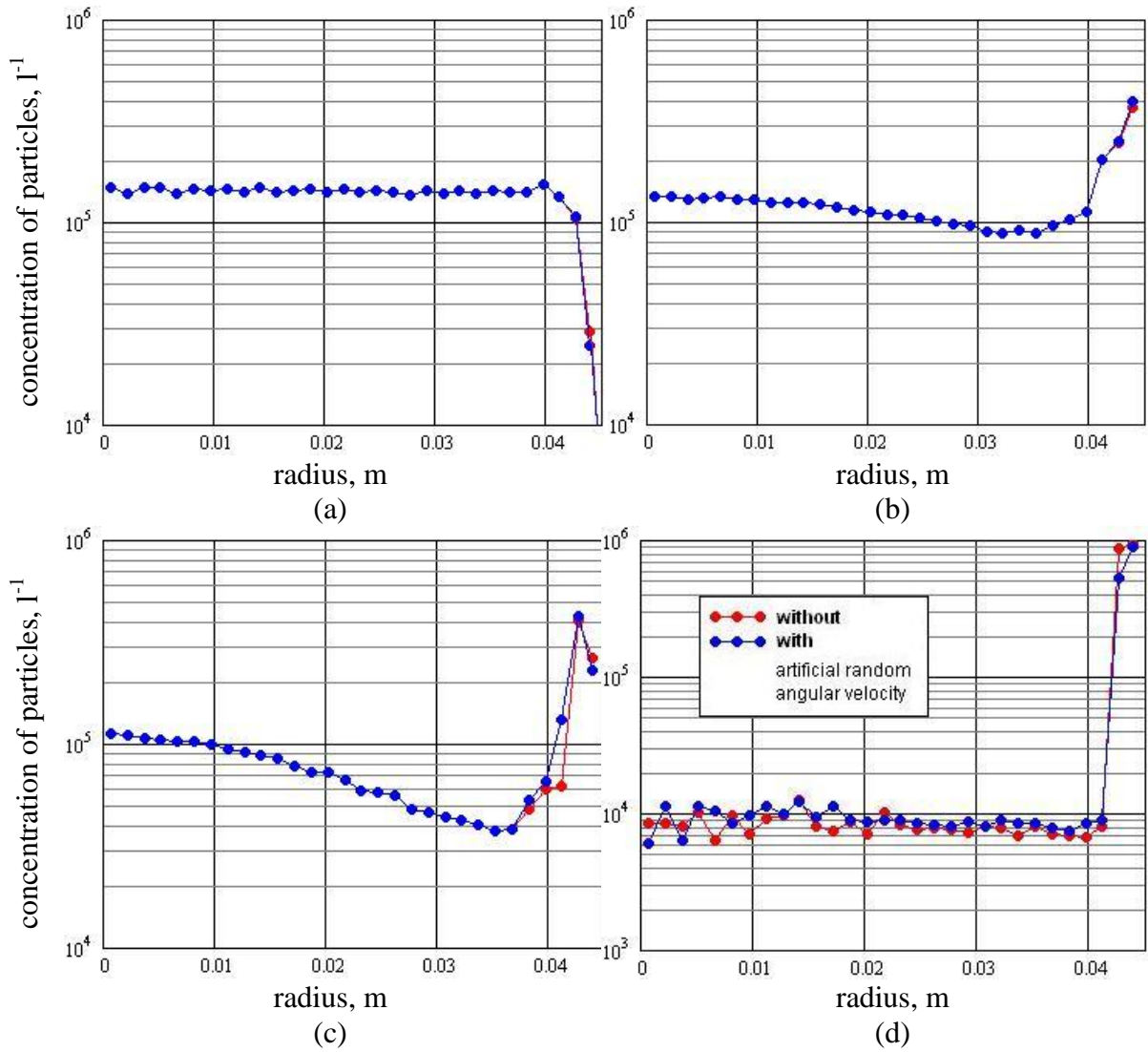


Figure 3.17: Radial distribution of particle volume concentration in ICF-2 at different moments of time: (a) 0.05 s; (b) 0.2 s; (c) 0.5 s; (d) 15 s. Initially the particles were situated on the top surface of the melt (Figure 5.6). The calculations were done with (blue line) and without (red line) artificial random angular velocity with amplitude 4 cm/s.

Thus, the equation (3.16) is linearized and can be solved for vector \mathbf{u}_p as the simple differential equation or as the system of differential equations for the components of the vector.

Secondly, it is necessary to discuss iterative algorithm and its convergence. The HD time step Δt_{HD} (corresponds to the large loop on Figure 3.1) is divided into several (further - n) Lagrange time steps $\Delta t_L = \Delta t_{HD}/n$ (the small loop on Figure 3.1). The flow is invariable from one HD time step to another one during all Lagrange time steps, therefore, the Lagrange time steps are used like iterations for calculation of the particle trajectory. The linearized Lagrange equation (3.16) is solved at each Lagrange time step, the particle is moved to the new position according to calculated velocity and finally all fields are interpolating at the new position for the next iteration. If the particle crosses the cell boundary at the last iteration, it is split and one additional iteration is calculated.

The convergence of the iterations and the optimal number of the Lagrange time steps n are investigated on the example of ICF-1. Figure 3.18 shows the trajectories of particle, which are calculated using different n . This trajectory represents the motion of inertial particle during

several HD time steps (balls on the image) in the zone of significant kinetic energy of the flow. Figure 3.19 shows the decrease of residual with increase of n . The residual is defined as follows:

$$\Gamma(n) = \frac{|r(2n) - r(n)|}{l(n)}, \quad (3.18)$$

where r is the radius-vector of the end of the trajectory, l stands for the length of the trajectory. Figure 3.18 and Figure 3.19 prove the convergence of the iterations (the residual decreases). Moreover, apparently, that 5 Lagrange time steps ($n = 5$) are enough to ensure a relevant result in the case of ICF-1.

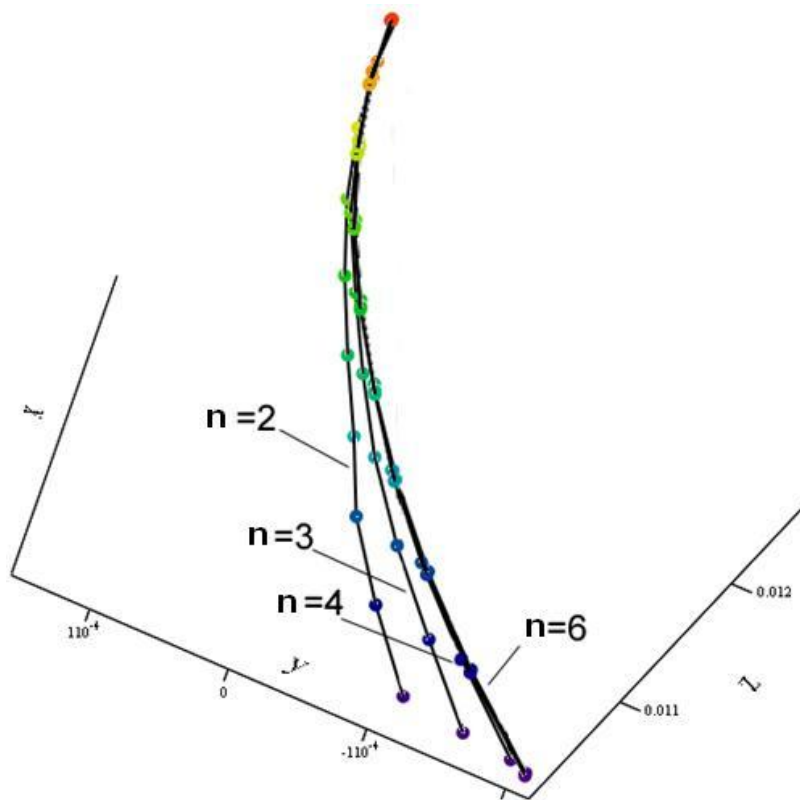


Figure 3.18: Trajectories of particles, calculated in ICF-1 using different number of the Lagrange time steps n per one HD time step.

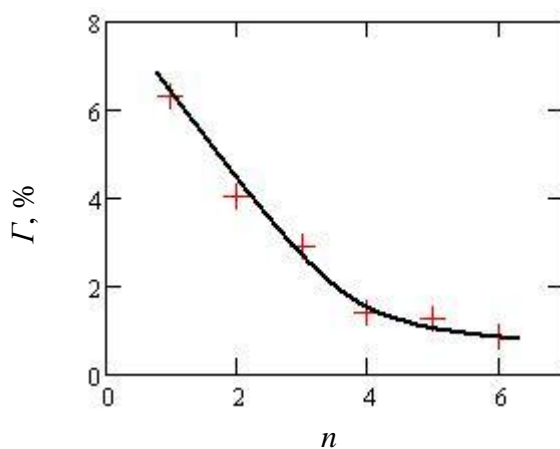


Figure 3.19: Residual Γ depending on the iteration number n . The residual is defined by the expression (3.18).

The OpenFOAM realization of described algorithm is discussed in the Appendix2. The standard OpenFOAM-1.6 code contains only the basic algorithm of the Lagrange particle

tracking, which consists of drag and buoyancy forces (see equation (3.16)). However, as it was shown in the Chapter 3.2, it is not enough for the relevant simulation of inertial particles. The proper libraries were sufficiently modified and supplemented by the author to solve the Lagrange equation in such form as it is described in the equation (3.16). Therefore, the mentioned code represents a sufficient contribution to the OpenFOAM libraries for the simulation of inertial particles in turbulent flows.

The described numerical code is checked in simple cases in order to avoid programming errors. Individual particles were put in different flows of simple configuration: homogeneous, rotating, shear, linear accelerated flows. The behavior of particles in such flows is predictable and can be easily calculated. The propriety of all components of the Lagrange equation (3.16) were checked this way: drag and buoyancy forces in homogeneous flow and rotating flow; lift force in shear flow; acceleration force in accelerated flow and, finally, added mass force during the gravitational acceleration of particle in a still liquid. All tests show the expected behavior of the particles. Thus, the numerical code is checked for errors. However, the full experimental verification of the model will be carried out in Chapter 4.

3.3.4. Collision with the wall

Another important numerical aspect of the particle tracking is the simulation of collisions with the wall of the crucible. The assumptions of the present model, including dilute condition, were described in the end of the Chapter 3.1. According to these assumptions and following the common Lagrange approach for an article tracking the particles are considered as the points that correspond to the centers of particles with the diameter as a property. The HD model contains nonslip boundary conditions on the walls ($\mathbf{u}_f = 0$). In this case if the particle-point will achieve the wall, it will remain there due to zero velocity. Such occurrence does not correspond to collision of a physical object, therefore, an additional near-wall treatment should be implemented in the code.

The mentioned treatment is implemented in the *trackToFace* function (see the Subchapter 3.3.3), which moves the particle according to the calculated velocity. The *trackToFace* function is defined in the *lagrangian* library and contains the control of the distance between a particle center and the faces of the cell, where the particle is situated. Such control prevent the situation when this distance is less than radius of the particle and the collision mechanism (the treatment of particle velocity) starts. However, the standard *trackToFace* routine takes into account only the faces of a current cell, where the center of a particle is in. It means that in the case a particle is bigger than the cell this algorithm fails. As it was described in the Chapter 3.3.2, the HD calculation of EM induced turbulent flow of ICF needs significant refinement of the mesh near the wall, which can lead to the mesh cells less than the particle size.

Different numerical algorithms for treatment of this effect were tried: 1) extend the particle-point to the set of particles on the boundary of the sphere, which gives the possibility to follow all cells these points are in; 2) add to the face list all faces of the walls and others. However, all such algorithms significantly extend the time of calculation or memory request or still lead to fails. Therefore, it was suitable to propose a very simple algorithm. When a particle is moved to a new position (the *trackToFace* function), the distance between the particle center and the wall is checked. If this distance is less than the radius of a particle, the position is corrected to situate the particle next to the wall (in the distance of the radius in normal direction). Such primitive correction does not take any significant time or memory, however, leads to

satisfactory results. Moreover, from the physical point of view, such mechanism can be interpreted as the model of collision with a significantly rough wall or also elastic collision when particle and the wall becomes deformed during the collision.

The *solidParticle* library also contains the treatment of the particle velocity when it collides with the wall. The proper code is described in the Appendix3. According to this algorithm the velocity of the particle after collision with the wall is described as follows:

$$\begin{aligned}u''_{p,\perp} &= -\varepsilon \cdot u'_{p,\perp}, \\u''_{p,\parallel} &= \mu \cdot u'_{p,\parallel},\end{aligned}$$

where double prime means the velocity after collision, but single prime means the velocity before the collision with the wall. Coefficients of the semi-soft collision ε and μ are defined in *constant/particleProperties* file. $\varepsilon = \mu = 0.8$ unless otherwise defined within this work.

4. Experimental verification of the model

4.1 Preface for the experimental investigation of the particle distribution in liquid metals

The only one more or less successful experimental method for the investigation of inclusion concentration in the near-wall region of EM governed liquid metal was developed by prof. Taniguchi's group (see e.g. *Taniguchi & Brimacombe, 1994*). This method provides an opportunity to investigate experimentally the rate of a particle deposition in the flow of the liquid metal under EM force. However, because the results are obtained by the cutting solidified liquid, it is impossible to receive any information about the dynamics of the process inside the melt using such experimental technique. Moreover, the presence of the solidification front has influence on the particles during the solidification and it is not clear, if this effect is negligible.

As it was discussed in the Chapter 2.4, lack of the experimental investigations of the behavior of solid inclusions of the conductive liquid flows till now was the significant problem in order to verify the numerical models. It was discussed that the electric well-conductive materials (e.g. metals) are not optically transparent but transparent liquids have low conductivity. *Sadoway & Szekely (1980)* tried to use transparent LiCl-KCl eutectic to reproduce the recirculation motion in an ICF, however, they failed to do this. EM field does not only produce the induced flow motion, but also heats up the liquid within the penetration depth. Thereby, the thermal convection dominates in low-conductive transparent liquids. Despite of the optimistic conclusions of *Sadoway & Szekely (1980)*, which were also corroborated by prof. D. R. Sadoway now, 30 years later¹, the simulation below shows that it is not possible to avoid the thermal motion by changing the EM conditions. Therefore, this liquid cannot be used to produce such flow patterns.

To be sure of the impossibility to use the molten salt eutectic as a physical model of liquid metal, it was decided to do the theoretical estimation and simulation for the powerful generator, which is available at Leibnitz University of Hanover, Institute of Electrotechnology. This generator can supply up to 300 kW and frequency up to 350 kHz that is one of the most powerful supply available at the scientific institutions, partners of University of Latvia. Thus, the possibility to induce the flow with several eddies in molten salt using such generator was examined.

Then, it is necessary to estimate the optimal size of the crucible for the EM parameters of the maximal power. If we assume the melt as an infinite cylinder then the amplitude of the induced current per height unit is

$$j_{0,lin} = \frac{B_0}{\mu_0},$$

where μ_0 is the magnetic constant; the amplitude of magnetic flux density $B_0 = \sqrt{2}\mu_0 I_{full}/l$, I_{full} is a full-effective current in inductor, l is the height of the inductor. In this case we can estimate induced power per area unit as

¹From the private communication of the author with prof. D. R. Sadoway (Massachusetts Institute of Technology), 2011.

$$q_{area} = \frac{j_{\delta,lin}^2}{2\sigma\delta},$$

where σ is the conductivity of the salt; the penetration depth $\delta = (\pi\mu_0 f \sigma)^{-1/2}$, f is frequency. So the full induced power in the melt is

$$q = q_{area} l \cdot 2\pi R = \frac{2\pi R \cdot I_{full}^2}{l} \sqrt{\frac{\pi\mu_0 f}{\sigma}},$$

and if we have maximal power, we can estimate the maximal current

$$I_{full} = \left(\frac{lq}{2\pi R}\right)^{1/2} \left(\frac{\sigma}{\pi\mu_0 f}\right)^{1/4}.$$

The material properties of transparent 41.2% KCl – LiCl eutectic are shown on Table 4.1. On the basis of the analytical estimation for infinite cylinder the minimal penetration depth (at 350 kHz) and the maximal full-effective current in the inductor (at 300 kW) are calculated for the mentioned generator and the crucible, which is 3 times larger than the penetration depth¹. These estimations are shown on Table 4.2.

Table 4.1: Material properties of 41.2% KCl – LiCl eutectic.

Temperature T , °C	400	500	600
Electrical conductivity σ^2 , S/m	124	187	239
Density ρ^3 , kg/m ³	1674	1621	1569
Kinematic viscosity ν^4 , m ² /s	2.17e-6	1.38e-6	9.81e-7
Thermal expansion coefficient β^5 , K ⁻¹	-3.151e-4, $T_{ref} = 400$ °C		

However, the infinite cylinder approach is used for the EM estimation mentioned above, therefore, the calculated current is not exact. The results, which are simulated using ANSYS software, are shown on Table 4.3. Now we can calculate the flow, which is induced in the eutectic within the induction furnace of optimal parameters. Figure 4.1 and Figure 4.2 show the results of the transient 2D k- ϵ simulation of 41.2% KCl-LiCl system. Radiation thermal boundary conditions with unity emissivity for all surfaces (except the symmetry axis – left) are applied on Figure 4.1. This case corresponds to the case without any artificial cooling. Figure 4.2 shows the case that corresponds to the case of the intensive artificial cooling of the side-wall

¹ Such penetration depth to the crucible radius ratio is optimal for EM stirring of liquid metal. *Moffatt (1991)* found that the maximal kinetic energy of a stirred fluid is observed at $Re_\omega = \omega L^2 / \eta \approx 20$, where Re_ω is the second magnetic Reynolds number based on the field frequency which can be also expressed through the skin depth of EM field δ : $Re_\omega = 2(L/\delta)^2$; L is the characteristic size of the system, which can be equal to the radius of the crucible R in the present case; $\eta = (\mu_0 \sigma)^{-1}$ is magnetic diffusivity of the fluid; σ is electrical conductivity. Thus, for the maximal stirring effect the penetration depth to radius ratio should be $R/\delta \approx \sqrt{10} \approx 3$.

² Electrical conductivity of the eutectic is calculated using quadratic approximation $\sigma = a + bT + cT^2$ (*Van Artsdalen & Yaffe, 1955*) and the values of coefficients, which are defined in the same paper.

³ Density of the eutectic is calculated using linear approximation $\rho = a - bT$ (*Van Artsdalen & Yaffe, 1955*) and the values of coefficients, which are defined in the same paper (see thermal expansion coefficient value and the reference temperature).

⁴ Dynamic viscosity decreases with the temperature exponentially (*Williams, 2006*). The values of kinematic viscosity are calculated from dynamic viscosity taking into account the approximation for density in Ref. 2.

⁵ *Van Artsdalen & Yaffe, 1955*.

(right), the heat transfer coefficient is $\kappa = 200 \text{ W} \cdot \text{m}^{-2} \cdot \text{K}$. The mentioned figures clearly show that the heating effect and, consequently, thermal convection dominate even in the case of the intensive cooling (Figure 4.2). Thus *Sadoway & Szekely (1980)* were wrong as the molten salt eutectic cannot be used as the model liquid for the EM induced flows even if we use the powerful generator.

Table 4.2: The estimation of the minimal penetration depth and the maximal full-effective current in the inductor for the melt of KCl-LiCl eutectic.

Temperature, °C	Min. penetration depth δ , cm	Height of inductor l , cm	Max. effective current in inductor I_{full} , A
400	7.64	3	843
		4	973
		5	1090
500	6.22	3	1040
		4	1200
		5	1340
600	5.50	3	1170
		4	1350
		5	1510

Table 4.3: The calculated induced power in the melt of KCl-LiCl eutectic.

T , °C	Radius of crucible R , cm	Height of crucible and inductor l , cm	Linear density of effective current j , A/m	Frequency f , kHz	Induced power Q , kW
400	20		3500		294
500	18	40	3875	350	286
600	15		4500		286

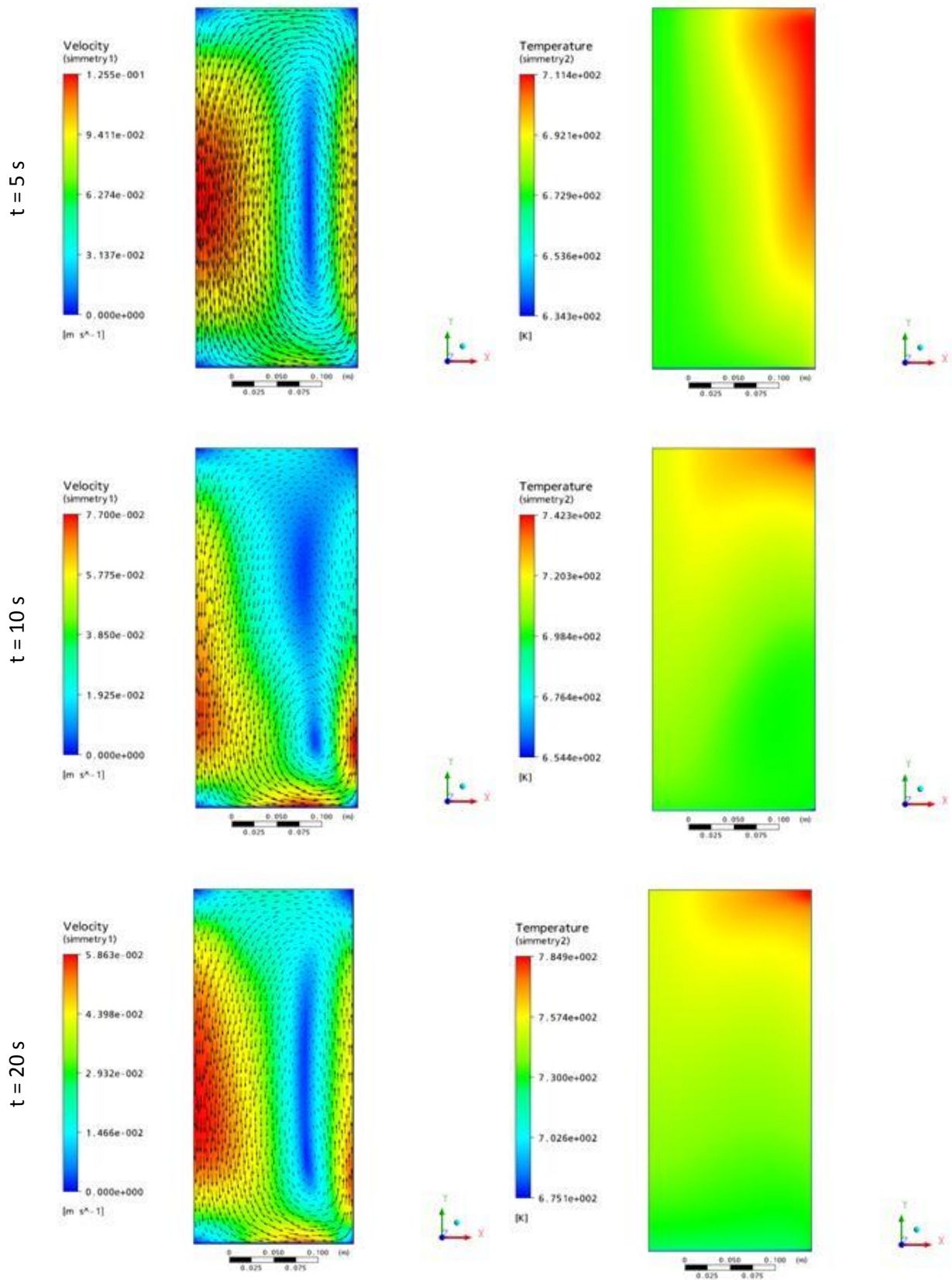


Figure 4.1: The results (velocity – left column, temperature – right column) of transient 2D $k-\epsilon$ simulation of 41.2% KCl-LiCl system without any artificial cooling. The time is shown under each column. The temperature of environment is 23 C.

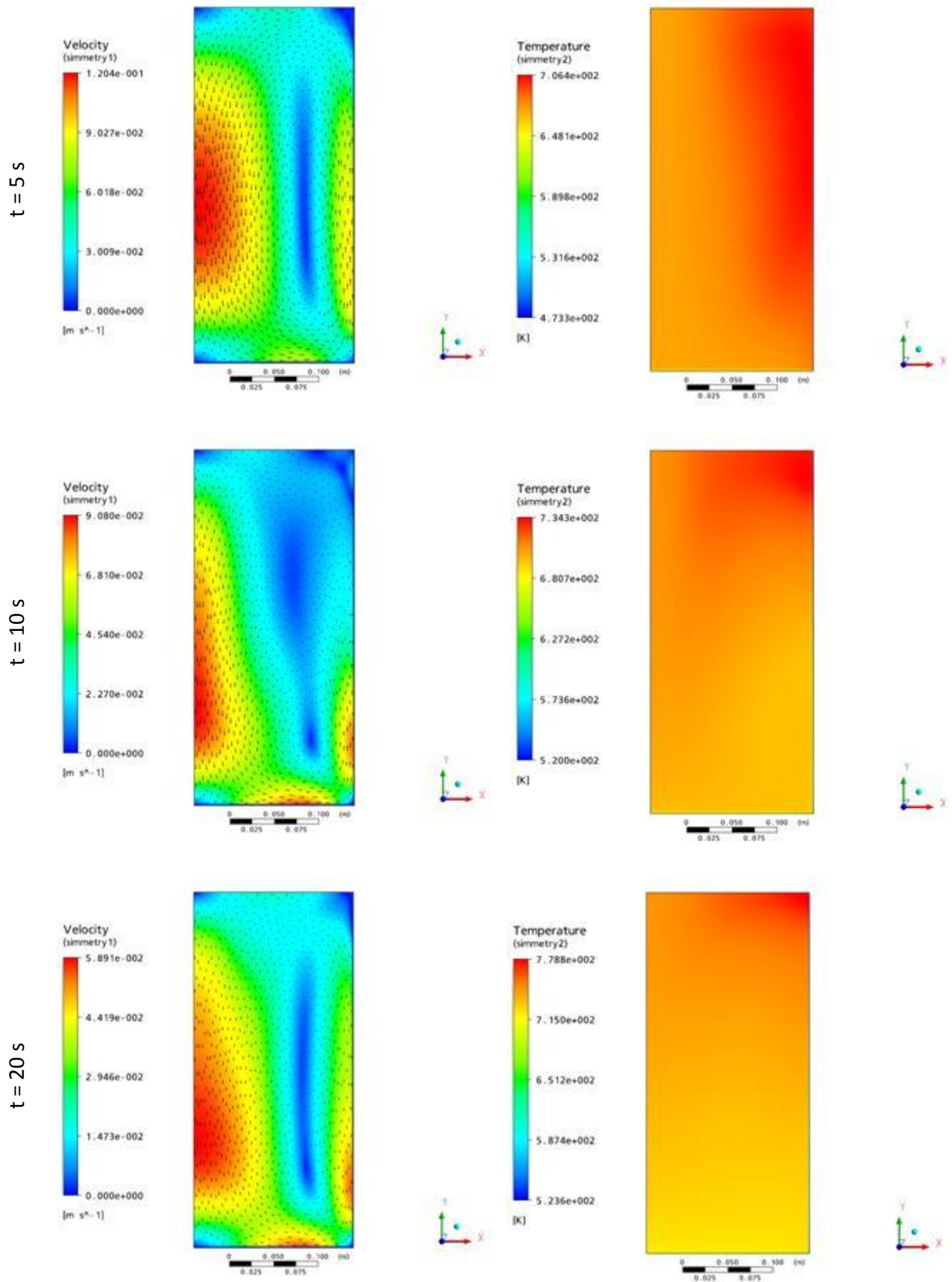


Figure 4.2: The results (velocity – left column, temperature – right column) of transient 2D k-ε simulation of 41.2% KCl-LiCl system with intensive artificial cooling of the side wall. The time is shown under each column. The temperature of environment is 23 C.

4.2 Experimental idea

The previous chapter described the essential lack of the experimental technique that is suitable for the experimental investigation of solid inclusions in the turbulent EM induced flow of liquid metal. The present chapter proposes the original experimental technique, which uses ferromagnetic particles. This experiment allows to verify the numerical model described in the Chapter 3.

The present technique proposes to use iron particles as a physical model for the tracking of non-conductive (oxide) inclusions in ICF, as far as typical inclusions are non-conductive or poor conductive. The described experimental technique is very useful because ferromagnetic particles can be easily separated from the liquid metal with the permanent magnet; thus, the metal remains pure after the experiment and can be used again.

Generally, the time dependent EM force should be written as follows¹ (the average expression of the force is placed in the equation (3.16)):

$$\mathbf{f}_{EM}(t) = -\frac{3}{2} \frac{\sigma_f - \sigma_p}{2\sigma_f + \sigma_p} (\mathbf{j}(t) \times \mathbf{B}(t)) + \frac{\mu - \mu_0}{2\mu\mu_0} \nabla B(t)^2, \quad (4.1)$$

where $\mathbf{j}(t)$ and $\mathbf{B}(t)$ are harmonic time dependent current density and magnetic flux respectively; σ_f and σ_p are the conductivity of the liquid and the particle respectively, μ and μ_0 are the magnetic permeability of a particle and vacuum respectively. Taking into account the Ampere's law ($\nabla \times \mathbf{B} = \mu_0 \mathbf{j}$), following expression can be written:

$$\mathbf{j} \times \mathbf{B} = \frac{1}{\mu_0} \left((\mathbf{B} \cdot \nabla) \mathbf{B} - \frac{1}{2} \nabla B^2 \right).$$

The poor conductive ($\sigma_p \ll \sigma_f$) inclusions are usually used in the metallurgical applications, and they are non-magnetic ($\mu = \mu_0$). Thereby, the equation (4.1) is reduced to the following expression:

$$\mathbf{f}_{EM,oxide} = -\frac{3}{4} (\mathbf{j} \times \mathbf{B}) = -\frac{3}{4\mu_0} \left((\mathbf{B} \cdot \nabla) \mathbf{B} - \frac{1}{2} \nabla B^2 \right). \quad (4.2)$$

And in the cylindrical coordinates

$$(\mathbf{B} \cdot \nabla) \mathbf{B} = \left(B_r \frac{\partial}{\partial r} + \frac{1}{r} B_\varphi \frac{\partial}{\partial \varphi} + B_z \frac{\partial}{\partial z} \right) \mathbf{B}.$$

In the area of the maximal magnetic flux – at the middle of the inductor – B_r and B_φ are negligible. Therefore,

$$(\mathbf{B} \cdot \nabla) \mathbf{B} \approx B_z \frac{\partial B_z}{\partial z} \mathbf{e}_z,$$

which is also negligible because $\partial B_z / \partial z \approx 0$. Thus, the term $(\mathbf{B} \cdot \nabla) \mathbf{B}$ is much less than the second term in (4.2) at the middle of the inductor:

$$\mathbf{f}_{EM,oxide} \approx \frac{3}{8\mu_0} \cdot \nabla B^2. \quad (4.3)$$

On the contrary, iron is a good conductor ($\sigma_p > \sigma_f$) and a ferromagnetic material ($\mu \gg \mu_0$), but due to partial wetting (see the next subchapter) and the transitional resistance, we can assume the equal conductivity of the particle and the liquid. Therefore, for this type of particles equation (4.1) can be reduced to

$$\mathbf{f}_{EM,iron} = \frac{1}{2\mu_0} \cdot \nabla B^2. \quad (4.4)$$

Following the discussion in Chapter 2.2, the average force in the quasi-stationary approximation can be written as follows (*Krumin, 1969*):

¹*Leenov & Kolin (1954)* defined the first term of this equation (for different electrical conductivity). The second term is defined in *Krumin (1969)*.

$$f_{EM,average} = \frac{1}{2} f_{EM,0},$$

where subindex “0” indicates the amplitude of the vector. As far as the quasi-stationary approximation for EM field is relevant for the present case, the average force $f_{EM,average}$ will be used instead of f_{EM} further, and the subindex “average” will be omitted. Thus,

$$f_{EM,oxide} \approx \frac{3}{16\mu_0} \cdot \nabla B_0^2, \quad f_{EM,iron} \approx \frac{1}{4\mu_0} \cdot \nabla B_0^2. \quad (4.5)$$

Apparently, the equations (4.5) show that $f_{EM,oxide} \approx f_{EM,iron}$ at the middle of inductor. The results of the EM simulation on Figure 4.3 also confirm the coincidence of the forces in the middle zone of the crucible, however, $f_{EM,iron} \approx 3/2 \cdot f_{EM,oxide}$ in the zone of the flow vortices. Despite the noncritical differences between the forces $f_{EM,iron}$ and $f_{EM,oxide}$ in the upper and the lower eddies, it is possible to conclude that iron particles can be used as a rough physical model of the typical metallurgical inclusions in the induction furnaces. And this experimental idea will be used in the further experiment.

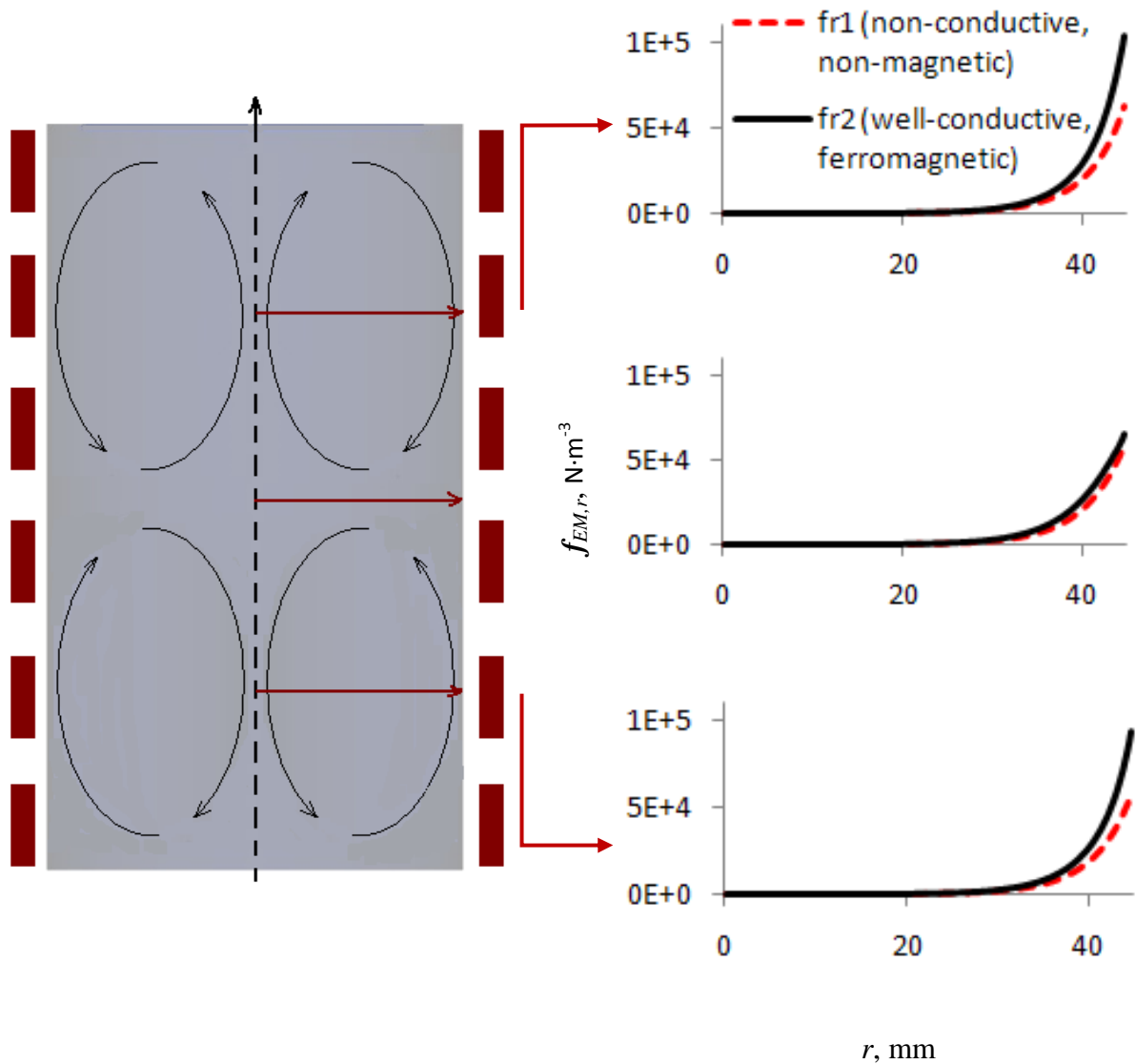


Figure 4.3: Magnitude of the EM force density (radial component) in the case of non-conductive & non-magnetic and well-conductive & ferromagnetic particles (see equations (4.2) and (4.4) respectively).

4.3 Description of the experiment

A small glass-wall crucible is used for the experimental investigation. The size and EM parameters of this crucible corresponded to ICF-2. The low-temperature-Wood alloy (50% Bi – 26.7% Pb – 13.3% Sn – 10% Cd eutectic), which becomes liquid at 70°C, was used as a model liquid metal. Such equipment induces 1.3 kW power in the melt that leads to heating with the rate $1.8\text{ }^{\circ}\text{C}\cdot\text{s}^{-1}$. Thus, the maximal duration of the experiment is limited, until the melt achieves 150 °C, which is the critical temperature for evaporation of the toxic cadmium from the alloy.

10.5 g of spherical iron particles with the diameter 250-350 μm (see Figure 4.4) are placed on the open surface of the liquid metal, which generally corresponds to the industrial case of the admixing of alloying particles in ICF. The power of the furnace is switched on when the particles are already on the surface, it is done to attempt to reduce the operation time of the furnace and, thereby, to prevent the Wood's metal from dangerous overheating. Obviously, this case differs from the industrial conditions where the inclusions are usually placed on the surface of an already stirring metal. However, the measurements of the particle concentration are carried out at the 11th s when the transition regime is already passed (see discussion of the stages of particle behaviour in the Chapter 5.1.3). The local 4 ml probes of the particle laden Wood's metal are taken with a preheated pipette. The temperature of the pipette should exceed the melting temperature of Wood's metal to avoid solidification. The coordinates, where the local probe is taken, are controlled by using a simple cover with holes (Figure 4.5) and the marks on the pipette to identify the deepness of the probe. Table 4.4 contains the comparison of the conditions in the experiment and the simulation. A particle-laden liquid sample was put from the pipette to the warm copper plate in order to keep the sample liquid. The iron particles are collected from this sample using a strong permanent magnet and are counted after that.

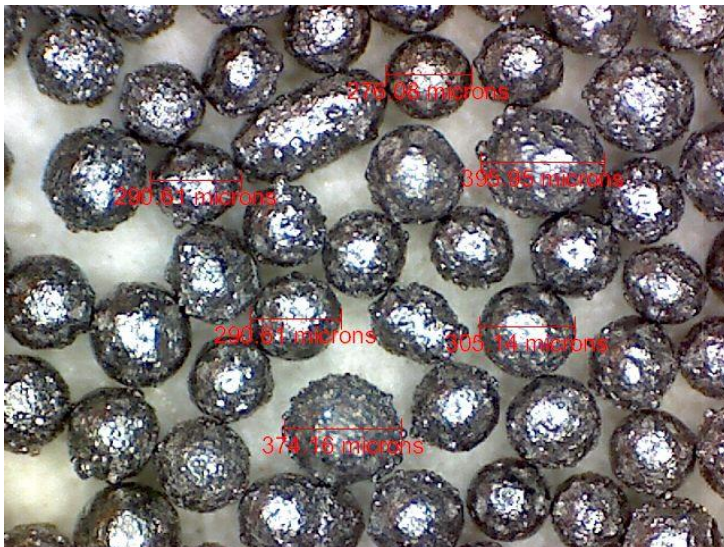


Figure 4.4: Microscope photo of the spherical iron particles that are used in the experiment. The sizes of some particles are marked.

Generally, the carried out experiment is classified as a “kitchen-style” experimental work. Figure 4.6 demonstrates the experimental devices, which were installed at the Institute of Electrotechnology, Leibnitz University of Hanover. However, despite the low tolerance of the experimental results, such experiment allowed to obtain for the first time the empirical data concerning the distribution of solid inclusions in the EM induced turbulent flow of liquid metal, which can be mentioned as a significant breakthrough in the attempt to investigate the particle laden flows of induction furnaces.

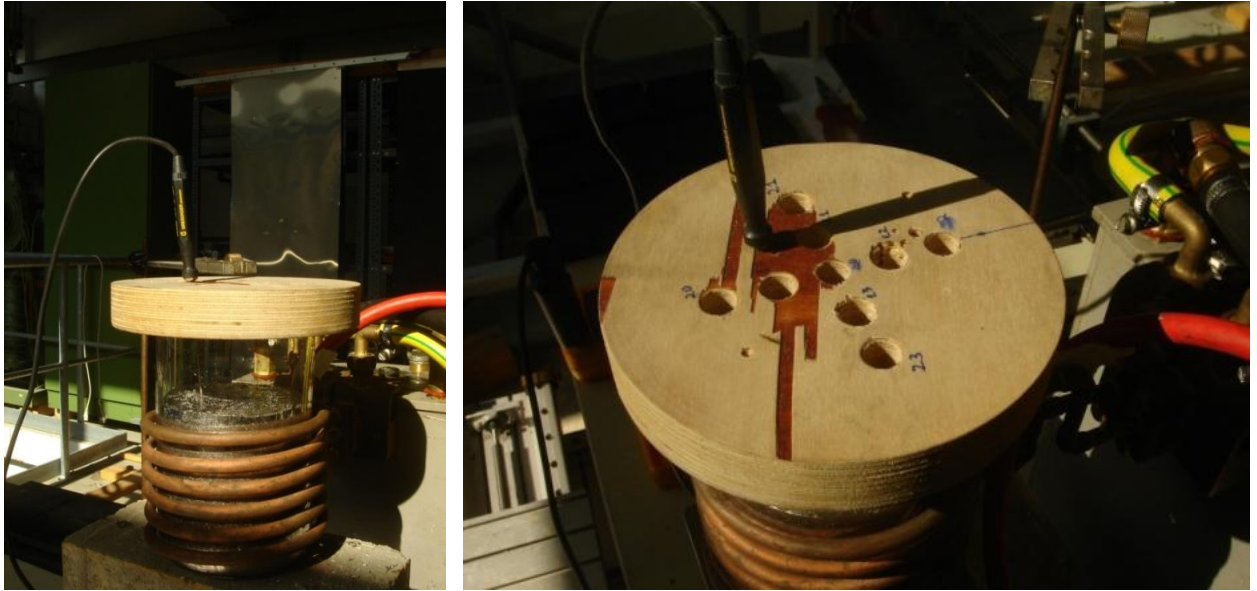


Figure 4.5: The cover with the holes for the pipette on the ICF-2.

Table 4.4: Comparison of the conditions in the experiment and the simulation.

	experiment	simulation
number (mass) of the particles	10.5±0.1 g ($\approx 9 \times 10^4$ particles)	83 635 particles
size of the particles	250 – 350 μm	300 μm
material (density) of the particles	iron (Fe) – well conductive, ferromagnetic	7 874 $\text{kg} \cdot \text{m}^{-3}$, non-conductive, non-magnetic
volume of sample (experiment) and the zone of numerical analysis	4±1 ml	Toroidal zone with approximately 36 mesh cells in the cross section
correspondence of the experimental and simulated results	number of particles in the sample	(the number of particles in the proper region) × (the vol. of the sample) / (the volume of the numerical zone)

Before discussing the results of the experiment, some difficulties of such experimental technique should be mentioned:

1. It was found that the Wood's metal wets the iron particles very poor. The power of 1.3 kW is not enough to mix the inclusions in ICF-2. The flow, induced by 2.4 kW field, can move the particles on the surface to the wall, but is also not enough to get them into the melt. Only the power of 3.7 kW is high enough, but at the same time the melt is heated too fast to carry out the experiment operating the furnace at such power. Supposedly, the main obstacle for the mixing in of the particles is poor wettability. Therefore, the particle should be artificially mechanically wetted to get them under the surface of the melt, then the power of 1.3 kW (432 A) is well enough to mix the particles in the melt. This current was used for the further experiments in ICF-2.

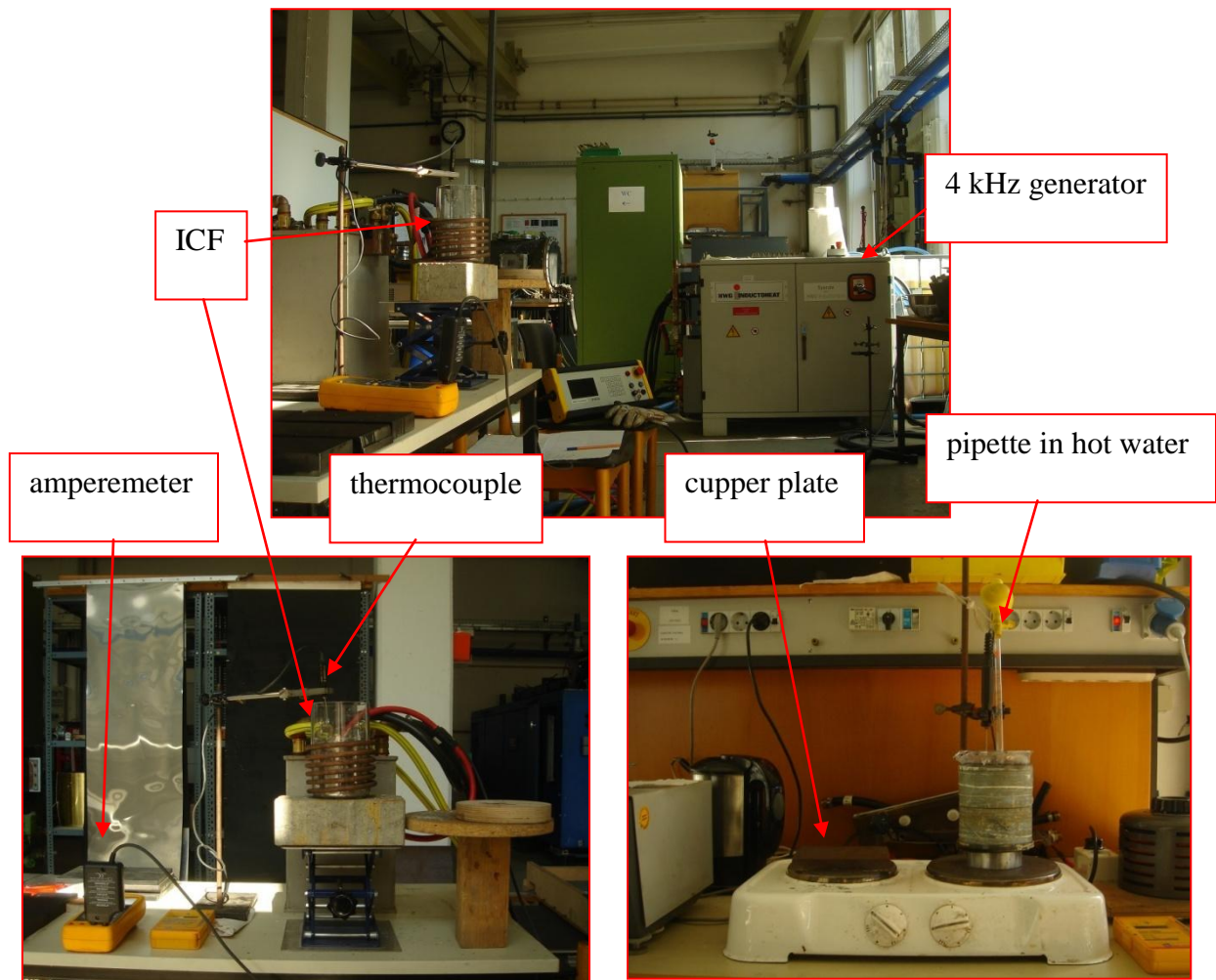


Figure 4.6: The photos of the experimental devices.

2. It was detected that the particles have trend to form agglomerations attached to the wall of the crucible near the top surface of the melt. Figure 4.7 represents the drained crucible after the series of the experiment. The agglomerations of the iron particles, covered with the Wood's metal, can be observed on the wall near the top surface of the melt. The agglomerations are formed during the initial motion of a wetted particle cloud from the surface, when the flow drags the particles along the wall. Moreover, the density of iron particles is less that the density of the Wood's metal, therefore, the concentration of particles in upper part of the melt is expected. The phenomenon of the agglomeration formation near the wall will be discussed and numerically investigated in the Chapter 5.3.2. The wall of the crucible near the surface was mechanically cleaned from the attached agglomerated particles after each experiment to neglect this phenomenon.

3. A surface tension of the particle laden droplet is significant, therefore, it is not so easy to collect all particles with the magnet. Density of the particles are lower than metal density, however, it was observed that not all particles rise up to the surface of the droplet due to the surface tension at the bottom. The droplet should be mechanically stirred several times to collect all particles with a magnet. Thereby, this stage of the experiment is time-consuming. The surface tension can be probably reduced by making the process of particle collection in water. Generally, it was observed, when the particle laden droplet is slowly solidified in warm water, all particles

are found on the surface and are easy-countable. However, such technique will significantly increase the total time of the experiment.

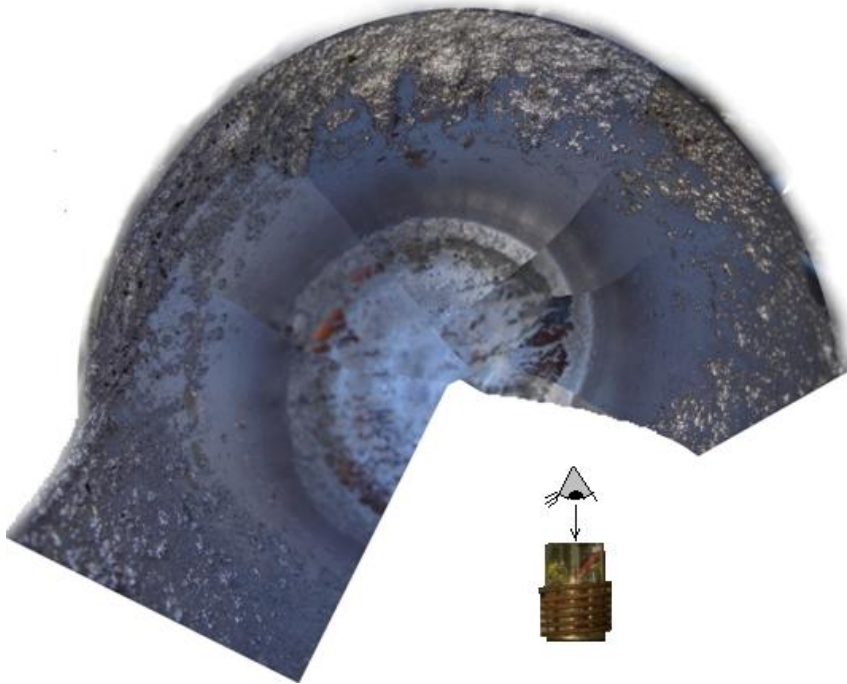


Figure 4.7: The image of the drained crucible after the series of the experiment (view from the top of the crucible).

4. Unfortunately, the precision of the experiment was very low. Despite the obtained quantitative results (see the next subchapter), the errors are sufficiently high. The experiment requires the automation of the probe-taking process. As far as the particle laden metal was sucked down by the hand operated pipette, there was impossible to take the equal volume of metal and define the time of probe without a significant error. The sucking process takes also approximately 2 s. However, all mentioned errors were taken into account while calculating the total error of the experimental results.

4.4 Comparison of the experimental and numerical results

The concentrations of the inclusions at the quasi-stationary stage of the particle admixing (see the Chapter 5.1.3) are shown on Figure 4.8. The experiment was carried out at the Institute of Electrotechnology, Leibniz University of Hanover, and contains two series of data: one was measured on March, 2012; the second series repeated the experiment on November, 2013. Summarizing the data of these two series in the experimental curve of Figure 4.8, we can conclude, that the experimental results correlate with the numerical LES-based Euler-Lagrange results. Thus, this experimental investigation proves the relevance of the used numerical model (see Chapter 3).

Nevertheless, the small differences of the experimental and numerical results at the 3rd – 6th points can be observed on Figure 4.8. These differences as well as the general distribution will be discussed in details now. The cloud of the particles following the main eddies frequently comes to the near wall region with the strong EM field. As far as the force directly influences the particle and moves it to the wall, the concentration of the inclusions near the wall (right points on the curves) is higher than in the bulk of the melt. This trend is more appreciable in the middle

zone of the crucible. EM force is stronger there and the average flow is slower, that means that other inertial forces (see equation (4.16)) are less compatible than EM force. Now let us analyze the difference between the experimental and the numerical results. It was observed during the experiment, that the iron spheres magnetize and make small clusters. Hence, the effective size of the inclusions increases within the penetration depth of EM field. The relative balance between the forces changes, and EM force has greater influence with the increase of the size of inclusions (Ščepanskis *et al.*, 2010). However, the present numerical model does not take into account the effect of magnetization and the clustering of the inclusions. Therefore, the small difference between the numerical and the experimental results appears at the 3rd point. However, this difference is only the effect of a second order. The same difference remains at the whole curve of the middle zone (the 4th – 6th points). Following the general scheme of the particle motion (Figure 5.6), the inclusions come to this zone through the area of the 3rd point. Therefore, apparently, the difference, which appears due to the clustering of ferromagnetic particles at the 3rd point, leads to the same difference in the middle zone (the 4th – 6th points). But the oscillating exchange between the upper and the lower zones (see the Chapter 5.2) minimizes this effect at the lower curve (the 7th – 9th points).

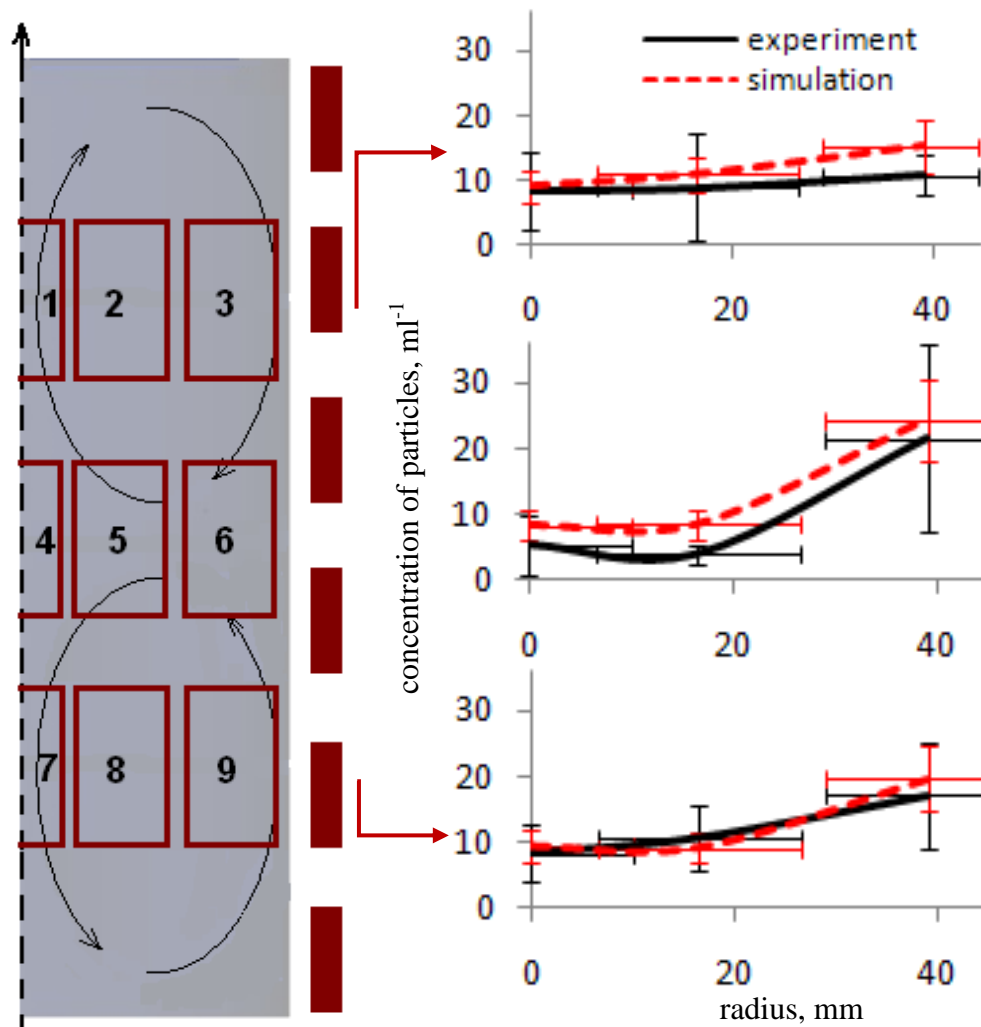


Figure 4.8: Experimental and numerical results of the concentration of solid $300\pm 50\ \mu\text{m}$ inclusions in the flow of ICF at 11 ± 2 s from the beginning of stirring (quasi-stationary regime). The experimental samples were taken in the areas, which are marked with the red rectangles on the sketch of the crucible (left image).

4.5 The outlook for the neutron imaging experiment

As it was already discussed in the Chapter 2.4.2 that the experiment, described in the previous subchapter, was carried out at the quasi-stationary stage of the distribution of the inclusions in the flow and is almost impossible at the stages characterized by fast changes in the distribution. Taking images by X-rays will be more suitable for the analysis of the dynamics of the inclusions in non-transparent liquids. However, due to the high absorbance of heavy elements that are situated in the low temperature alloys (e.g. lead), it is necessary to apply an extremely high power of a beam in order to look through even thin layer of metal.

Nevertheless, neutron beams have totally different principle of absorption in materials. Therefore, they can be used for the mentioned purpose. For this reason we came to an idea of neutron imaging. Many materials are transparent for neutron beams (see. e.g., neutron imaging in lead *Kumar et al., 2012*); therefore, it can be very useful experimental methodology. Such technique can lead to the experimental investigation of the dynamical behaviour of solid inclusions in the complex turbulent flow inside induction melting and stirring equipment.

ICF-2 can be used for such experiment. However, the Wood's metal is not suitable for neutron imaging as far as it contains cadmium, which absorbs neutrons. Another low temperature eutectic Rose's alloy (50% Bi, 25-28% Pb, 22-25% Sn) can be used as the model liquid. The metal becomes liquid between 94 °C and 98 °C. It should be additionally mentioned that the copper inductor will not significantly shade the imaging of the melt interior due to copper transparency for neutrons. Particle imaging is exercised in two perpendicular directions, in order to reconstruct 3D motion of inclusions and their concentration fields.

The neutron imaging facility is available in Paul Scherrer Institute (Villigen, Switzerland).¹ However, the expenses of time of the neutron beam is very high, therefore, it is necessary to carry out the preliminary check of a principal possibility of the experiment.

4.5.1. Preliminary experiment

For this reason the simplified preliminary experiment was carried out by Dr. Knud Thomsen and Dr. Eberhard Lehmann at Paul Scherrer Institute on May, 2013. The goal was to verify the general possibility to fulfill the proposed experimental investigation using neutron imaging. This preliminary check dealt with the solid samples of the Rose's metal of the diameter equal to that of ICF-2 (10 cm in diameter) with the spherical 0.5 mm inclusions inside it. Such solid samples were put under a neutron beam.

Cylindrical solid samples were created by Vadims Geža at Leibniz University of Hanover (Germany) on April, 2013. The example of the sample cut in two perpendicular directions is shown on the

Figure 4.9. The oxide particles in the cross-section of the sample are indicated with green circles.

The Figure 4.10 shows the neutron images of different horizontal slices of the sample (the pictures are obtained as a superposition of images from two perpendicular beams). The white dots correspond to the inclusions, black regions mean voids, but grey area remains to the metal.

It should be mentioned that the observed voids are the result of the complex technology of creation of the samples. The sample was grown sequentially by solidifying metal layers with admixed inclusions. Such technology was necessary to catch the particles of the lower density

¹ *Lehmann et al. (2011)*

than the metal density inside the sample. Such way some voids appeared between the layers, especially in the central vertical plane – the place of sintering of two half-cylinders. However, obviously, the observed voids are the result of artificial creation of samples; therefore, they are not expected during the main experiment.

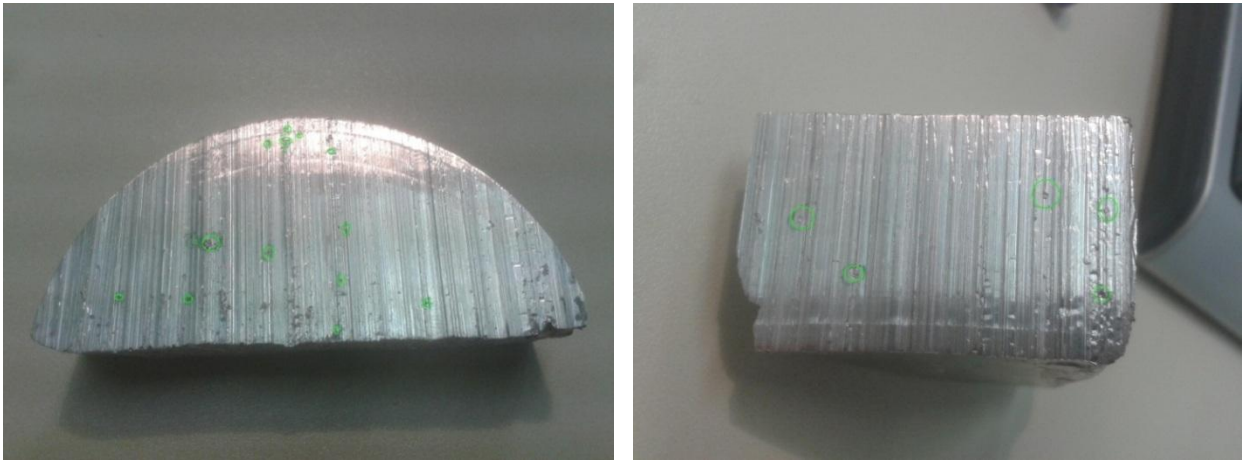


Figure 4.9: Two cross-sections of the solid sample of the Rose's metal including the solid particles. The particles are indicated with green circles. The sample was used for the preliminary experiment of neutron imaging.¹

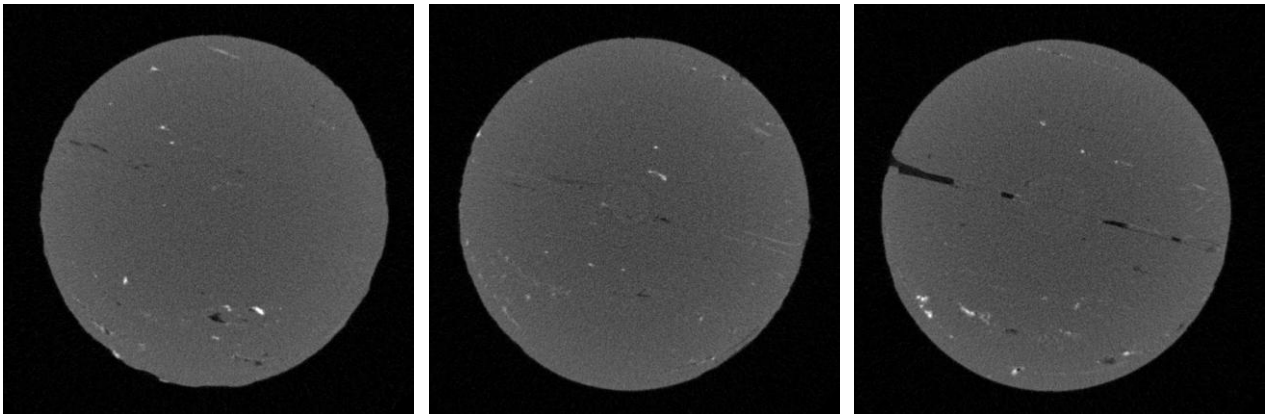


Figure 4.10: The neutron images of different horizontal slices of the sample (the pictures are obtained as a superposition of images from two perpendicular beams). The white dots correspond to the inclusions, black regions mean voids, but grey area remains to the metal.²

Some white points, which stand for the inclusions, are reflected as the lines. As it will be discussed later, that it happens in the case when a few particles are situated close to each other.

3D-image of the distribution of non-metallic inclusions (marked with a red color on Figure 4.11) and voids (blue color) was created by postprocessing of the experimental results. The

¹ The sample is created by Vadims Geža at Leibniz University of Hanover (Germany).

² The experiment and postprocessing of the results were done by Dr. Knud Thomsen and Dr. Eberhard Lehmann at Paul Scherrer Institute (Switzerland).

Figure 4.11 illustrates the distribution of particles in the different experimental samples that were created with a different area distribution of the inclusions with excessive concentration in some regions:

Sample 1 – homogeneous distribution of ZrO_2 inclusions;

Sample 2 – symmetrical distribution of SiO_2 inclusions concerning the central vertical symmetry plane, the areas, which are opposite to this symmetry plane, have significantly higher concentration of inclusions;

Sample 3 – excessive concentration of inclusions in the middle of sample.

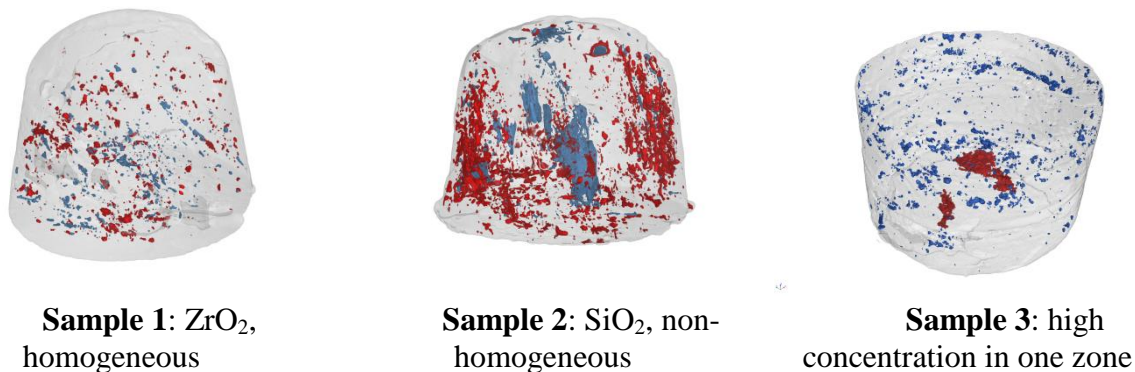


Figure 4.11: 3D reconstruction of the distribution of the solid inclusions in solid samples of Rose's metal using neutron-imaging technique.¹

All pictures certify the possibility to analyze the distribution of inclusions quantitatively; however, it is also clear that the conglomerations of two or more particles are reflected as one zone of a larger volume. Therefore, the quantification of the distribution of the inclusions should be done by the analysis of the volume of the proper regions instead of the particle number. Such technique, apparently, can lead to the additional error; however, it should be reasonable and can be estimated by the rate of total volume of cluster to the balls it is formed from. The calculation of the volume can be easily conducted as far as the experimental data are available in the form of the slices of sample images with a tiny step.

Let us analyze the neutron images of the different samples.

Sample 1. The experiment certifies approximate homogeneous distribution of ZrO_2 inclusions.

Sample 2. The blue plane in the central vertical cross-section of the sample corresponds to the void at the place of sintering of two half-cylinders. The common mass of particles in this sample was created equal to that in the Sample 1; and, consequently, as far as density of SiO_2 is approximately 1.5 times less than density of ZrO_2 , volume concentration of the inclusions in the Sample 2 is higher than that is the Sample 1. The higher concentration in the Sample 2 can be easily recognized on the proper image. Moreover, the significantly higher concentration of particles was observed in two symmetric regions opposite to the sintering place of the half-cylinders (the blue plane). This result is relevant to the real consistence of the sample.

Sample 3. This sample contains the excessive concentration of inclusions in one region – in the center of the sample. Neutron imaging detected it as a common area of inclusions.

¹ The experiment as well as the processing of the images were done by Dr. Knud Thomsen and Dr. Eberhard Lehmann at Paul Scherrer Institute (Switzerland).

Therefore, the concentration of particles in such consolidate areas should be quantified by measuring the volume of the proper zone.

4.5.2. Conclusions for the preliminary experiment

First, the inclusions can be recognized on the neutron images of the metal samples. Second, the experiment found the excessive concentrations of inclusions in the different samples in the right positions; however, there was not possible to compare the concentration rate with the experiment due to difficulties in the concentration quantification during the creation of the samples. Nevertheless, there should be no problem with the quantification of the experimental results by calculation of their volume.

Therefore, finally, we can conclude that the preliminary experiment certify 1) the possibility to use the Rose's metal for neutron imaging, 2) general possibility to obtain the quantitative results of the particle concentration, 3) the sizes of the samples (that means also the planed experiment) is suitable for the PSI neutron facility.

However, the only question remains: is the resolution of the images in the case of moving inclusions enough? It is not possible to check this point in the solid samples due to the lack of motion of inclusions. However, the estimation confirms the possibility of the experiment.

Thus, this chapter showed the possibility to carry out the experiment for tracking of particles in liquid metal. However, this experiment is expansive and, therefore, the author expresses the hope that enough funding will be found in the nearest future.

5. Transportation of solid inclusions in the turbulent flow of ICF

The numerical model of the transportation of the solid inclusions (the Chapter 3) was verified experimentally in ICF-2 in the previous chapter. Therefore, it is possible to investigate the behavior of the particles in ICF using the mentioned numerical model. The present chapter contains the general description of the dynamics of particle concentration in the turbulent flow of ICF, as well as the detailed analysis of the key phenomena: oscillating particle exchange between the zones of the main vortices and the conglomeration of the particles on the wall. These issues are significant also from the engineering point of view as it allows improving and optimizing the design and the operation regime of ICF for the higher efficiency of the equipment. Finally, the present chapter contains the proposed methodology, which yields the optimization of mixing time depending on the size and the type of inclusions.

5.1. Inclusions admixture from the top surface of ICF

5.1.1 Initial admixing from the surface

ICF ensures not only the efficient melting, but also intensive steering of liquid metal. Therefore, the alloying inclusions are often admixed to the liquid metal in the same furnace just after melting. However, the frequency of the current in the inductor can be changed for the better steering. Solid inclusions are simply put onto the open surface of the melt and turbulent flow takes them into the liquid metal.

The wide-spread example of this technology is admixing of carbon in steel. The carbon particles are sprinkled onto the open surface of the liquid steel in ICF and mixed in with the turbulent flow. The carbon inclusions usually remains in the solid state and act as a hardening agent, preventing dislocations in the iron atom crystal lattice from sliding past one another. Varying the amount of alloying elements in the steel the qualities such as the hardness, ductility, and tensile strength of the resulting steel are controlled.¹

The snapshots of the open surface of the melt with carbon particles on it are shown on Figure 5.1. This figure illustrates the real industrial process, which is carried out in the 4 t ICF designed by Otto Junker GmbH. The left column of the snapshots corresponds to the frequency of 250 Hz (the power of the furnace is 2.5 MW). The higher frequency leads to the smaller penetration of EM field and, consequently, Joule heating. Obviously, the local heating density increases with the decrease of the penetration depth, which is the positive effect for the melting. However, as it is shown on Figure 5.1 (the left column) the intensity of the steering is not enough to take the carbon from the surface. On the other hand, the two times lower frequency (125 Hz) leads to the effective mixing of the alloying inclusions (the right column on Figure 5.1). However, the low frequency is not effective for melting. Therefore, the melting and the processing of steel are sometimes optimized by using ICF with two frequencies (one – for melting, another – for steering), like the furnace from Otto Junkers GmbH, which is operated on Figure 5.1.

¹ From the article “Steel” in the free web-encyclopedia “Wikipedia” (<http://en.wikipedia.org/wiki/Steel>).

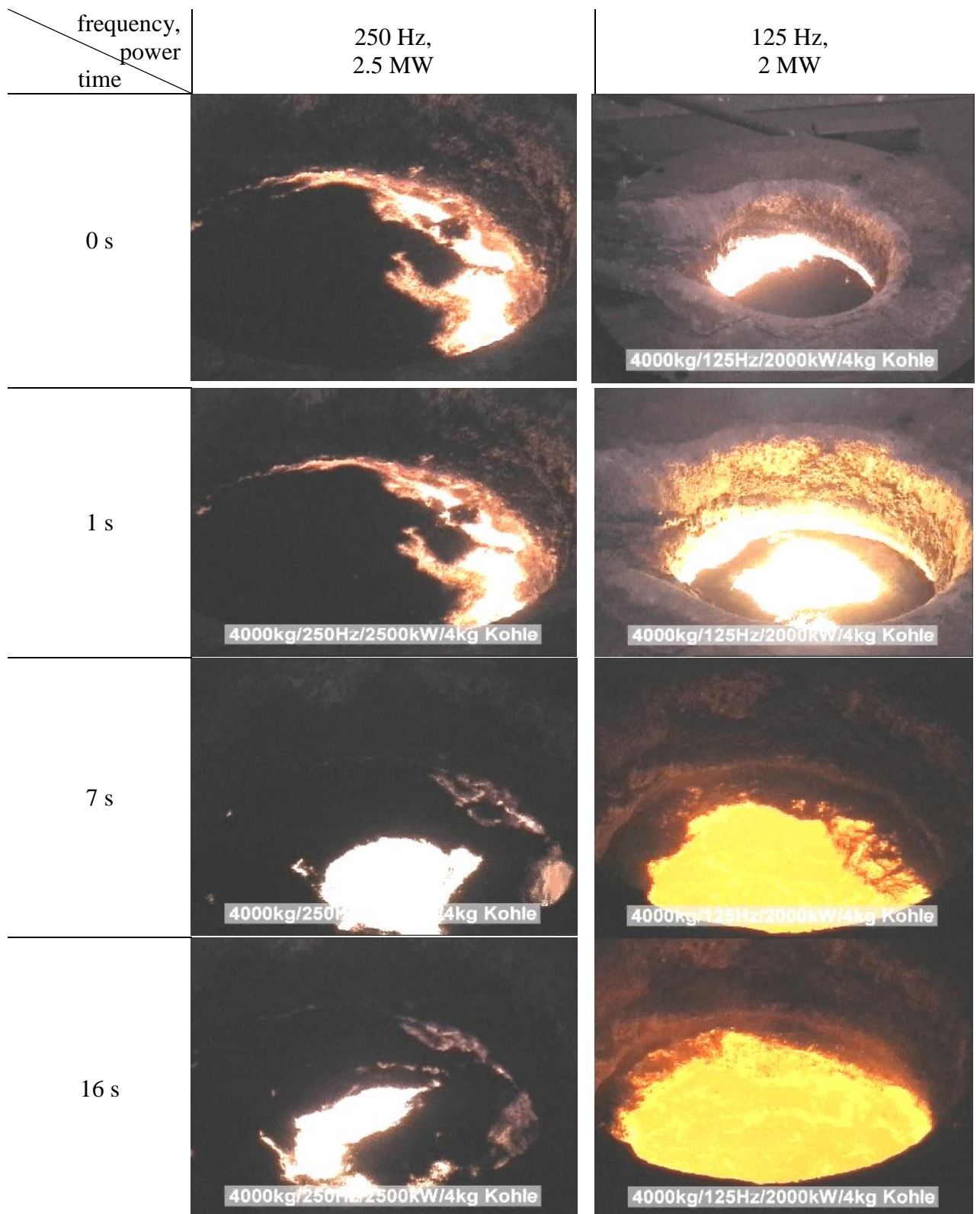


Figure 5.1: Snapshots of the admixing of 4 kg carbon into 4 t steel alloy in industrial ICF, applying different frequency and power. Courtesy Otto Junker GmbH.

The qualitative dependence of the efficiency of admixing from the surface on the power of ICF was also investigated experimentally (Figure 5.2). The 300 μm iron particles were put on the open surface of the Wood's metal in the ICF-2 (see Table 2.2). It was observed that the particles

are only partly wetted with the liquid metal and that significant surface tension appears on the surface of the liquid. Therefore, the low power (1.3 kW) of ICF does not produce enough steering on the surface of the melt to ensure the motion of the inclusions; thereby, the inclusions remain unmovable on the surface (Figure 5.2– left). With the increase of the power of ICF (2.4 kW) particles were moved to the corner between the open surface and the wall, but still remain there (Figure 5.2– middle). Finally, the 3.7 kW power were enough to take the particles into the bulk of the melt (Figure 5.2– right). However, such significant power leads to the excessive overheating of the metal and a high energy consumption.

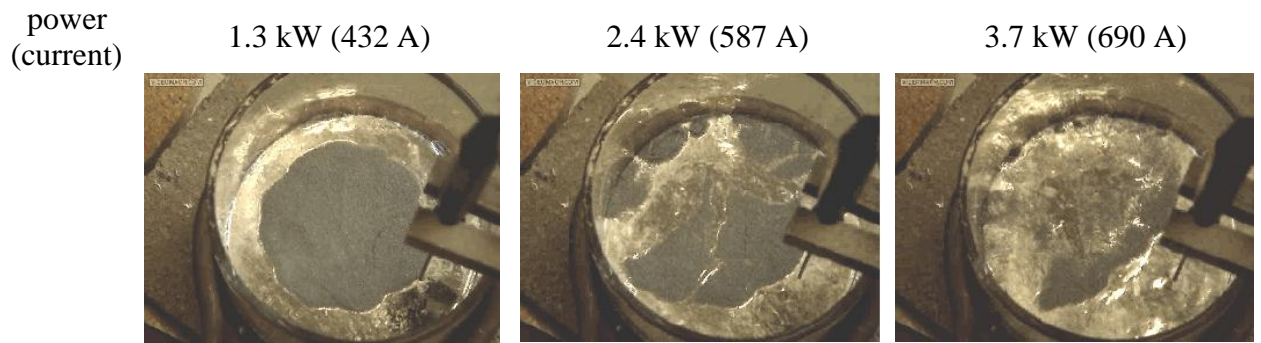


Figure 5.2: The surface of the Wood's metal with iron particles after 10 s of the steering in the ICF-2. The particles were situated on the surface before steering (like on the left picture).

The mentioned difficulty to admix the particles to the melt increases with the decrease of a particle density. Figure 5.3 shows the surface of the Wood's metal with the 500 μm SiO_2 (the upper row) and ZrO_2 (the lower row) particles. In this case density of the admixtures (SiO_2 – 2.5 g/cm^3 ; ZrO_2 – 3.8 g/cm^3) is significantly less than the density of the liquid metal – 9.4 g/cm^3 . We can see that only 4.6 kW power is enough to mix in the ZrO_2 inclusions (Figure 5.3 – right, down) and even such power is too low to mix in the SiO_2 particles. But the larger power cannot be applied to the non-cooled crucible due to an extremely fast heating.

We can conclude from the considered examples (Figure 5.1- Figure 5.3) that the wetting of the inclusions as well as the surface tension of the melt plays a great role for the admixing of the inclusions from the surface, i.e. it sufficiently decreases the efficiency of this process. However, this problem can be easily investigated experimentally (see Figure 5.2 and Figure 5.3) as well as practically solved in industrial cases. Therefore, this particular problem is not interesting from the modeling point of view, however, should be taken into account.

5.1.2 Scheme of the motion of particles in the bulk of the melt

More interesting issue for simulation is the behavior of the inclusions under the surface. Obviously, the motion of the particles becomes invisible when they disappear from the surface, therefore, the initial stage of the admixing of the particle cloud and the dynamics of the process are the challenge for the mathematical modeling.

The results of the simulation can be initially qualitatively compared with the industrial observations of the inclusions' behavior on the open surface of the melt. Figure 5.4 illustrates the carbon admixing process in steel in 2 kW ICF designed by Otto Junker GmbH. The simulated and the observed behavior of the particles on the surface are in a good qualitative agreement (Figure 5.4 – the first and the second rows).

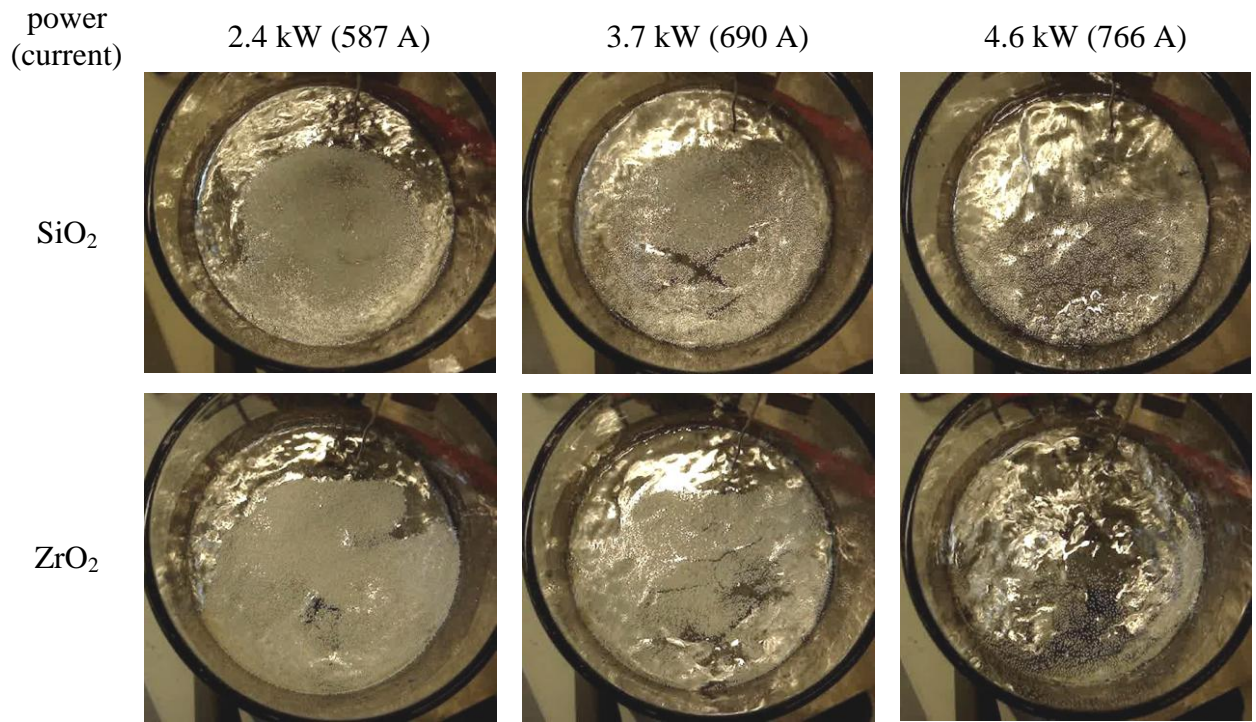


Figure 5.3: The surface of the Wood's metal with SiO₂ (the upper row) and ZrO₂ (the lower row) particles after 10 s of steering in the ICF-2. The particles were situated on the surface before steering (like on the left picture of Figure 5.1).

Motion of the particles in the bulk of the crucible, which is invisible, can be analyzed now. The illustration of this motion is shown on Figure 5.4 – last row. Figure 5.5 demonstrated the dynamic of the radial and the axial distribution of the concentration of particles in ICF-2. Taking into account the flow pattern (Figure 2.4) it becomes evidently that initially the flow drives the cloud of the inclusions to the corner between the surface and the wall, because it is not possible to take immediately it inside due to the surface tension and the partial wetting effects. After that the intensive flow takes the cloud inside in the corner and moves along the wall to the middle zone of the crucible. This motion corresponds to Figure 5.5 a (the upper image), which shows the increase of particle concentration in the upper part of the crucible. The direction of the flow changes in the middle zone (see Figure 2.4). The distribution of the Lorentz force produces the eddies, which turn the flow to the axis of symmetry in the middle zone of the crucible – the zone of the maximal Lorentz force magnitude. Thereby, following the flow, the particles are decelerated and are moved to the center of the crucible in the middle zone of the crucible. The decelerated cloud is blurred, but Figure 5.5 a (middle image) shows that the main part of the particle cloud moves in the upper flow eddy – the maximum of the concentration shifts to the top surface of the melt. After that the blurred cloud separated into the first one, which moves in the upper part of the crucible, and the second part of the particles goes to the lower part of ICF. As it has already been discussed in the Chapter 2.2 and *Umbrashko et al. (2006)*, the most intensive axial turbulent pulsations are observed exactly in this middle region. The intensive pulsations carry out the exchange of the particles between the two mean eddies (the upper and the lower part of the crucible) and, thereby, homogenize the distribution in the lapse of time. Figure 5.5 (b) (the lower image) shows that the concentration of the particles in small ICF-2 becomes

homogeneous in axial direction in 5 s. The oscillating exchange will be analyzed in details in the Chapter 5.2.

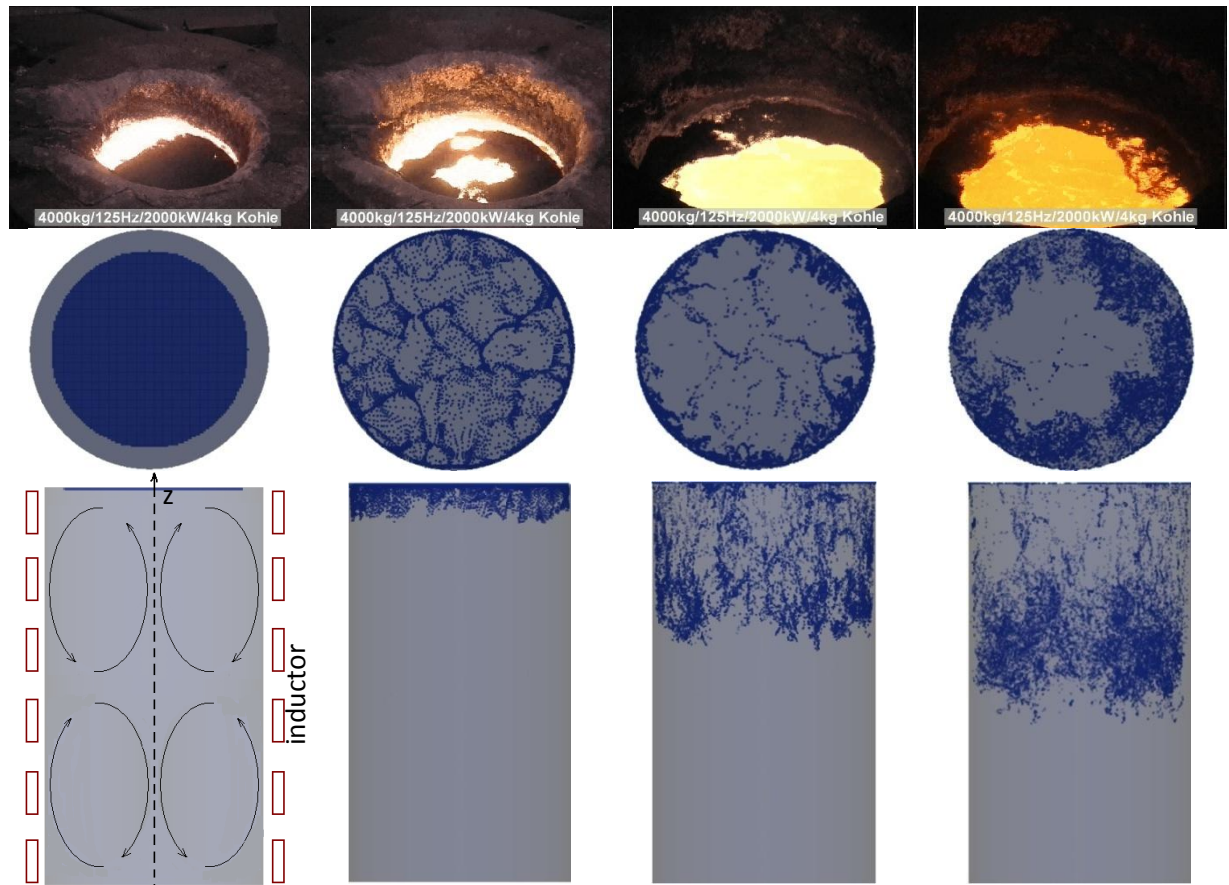


Figure 5.4: The admixing of the 100 μm carbon particles into the steel alloy in 2 kW ICF (125 Hz). Snapshots of the industrial process by Otto Junker GmbH (the first row). The simulated results: view from the top of the furnace (the second row); particles in the bulk of the flow, view from the side of furnace (the last row).

Generally, Figure 5.6 summarizes the discussion in this chapter and presents the scheme of the initial motion of the inclusions, which are situated on the open surface of the melt with the developed flow in ICF. And Figure 5.4 and Figure 5.5 illustrate this initial stage of the particle mixing in terms of concentrations.

Figure 5.5 (a) also shows that the significant concentration of light particles observed on the top surface of the melt, which corresponds to industrial observations of slag. Figure 5.5 (b) demonstrates the homogeneous radial distribution of inclusions after a short initial stage, however, the larger concentration near the wall of the crucible is observed due to the influence of EM force on the non-conductive inclusions.

5.1.3 Quasi-stationary particle exchange between the zones of the main vortices

Figure 5.8 demonstrates the dynamics of the concentration of the particles in the ICF at a different height (simulated results). At the first stage (0 – 4 s) significant peaks appear in the upper and the middle zone of the crucible (the 2nd and the 5th zones respectively). This corresponds to the initial motion of the cloud in the mean upper eddy (see the previous subchapter). After that the particles come to the lower eddy too, the initial cloud is blurred and

the concentration increases in the middle of eddies (4 – 10 s). This stage approximately corresponds to 2 loops of the particles in the upper eddy (the time of the turn in approximately 3.3 s). Figure 5.8 shows that the quasi-stationary stage in the particular ICF starts at the 10th s. The exchange of the inclusions between zones achieves the dynamic equilibrium at this stage.

The concentrations of the inclusions in ICF-2 at the quasi-stationary stage were shown on Figure 4.8. The experimental results at this stage were also shown and discussed in the Chapter 4.4.

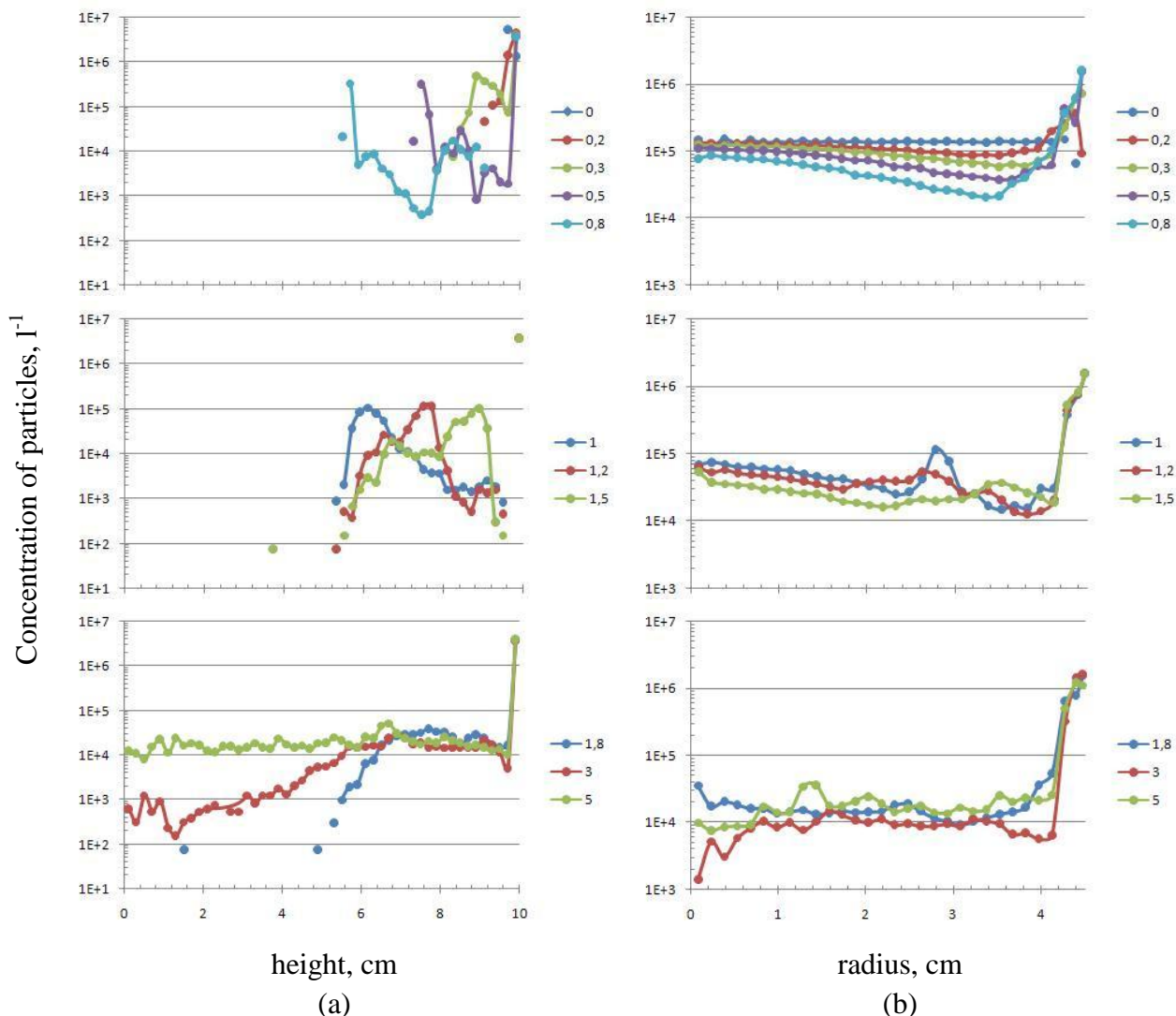


Figure 5.5: Axial (a) and radial (b) distribution of the particle concentration in ICF-2. Different curves correspond to different moments of time that are shown in the legend (in seconds from the beginning of the stirring).

5.2. Oscillating particle exchange between the zones of the main vortices¹

It has already been underlined in the previous chapter that the homogenization of particle concentration between the upper and the lower parts of ICF is fulfilled by strong oscillations of

¹ This chapter is already published in *Ščepanskis at al. (2012)*.

the flow in the middle zone of the crucible. *Umbrashko et al. (2006)* numerically predicted and *Kirpo (2008-PhD)* experimentally investigated the low-frequency velocity oscillations in the zone between the mean vortices. Both authors also discussed the importance of these pulsations for the heat and mass exchange in the melt.

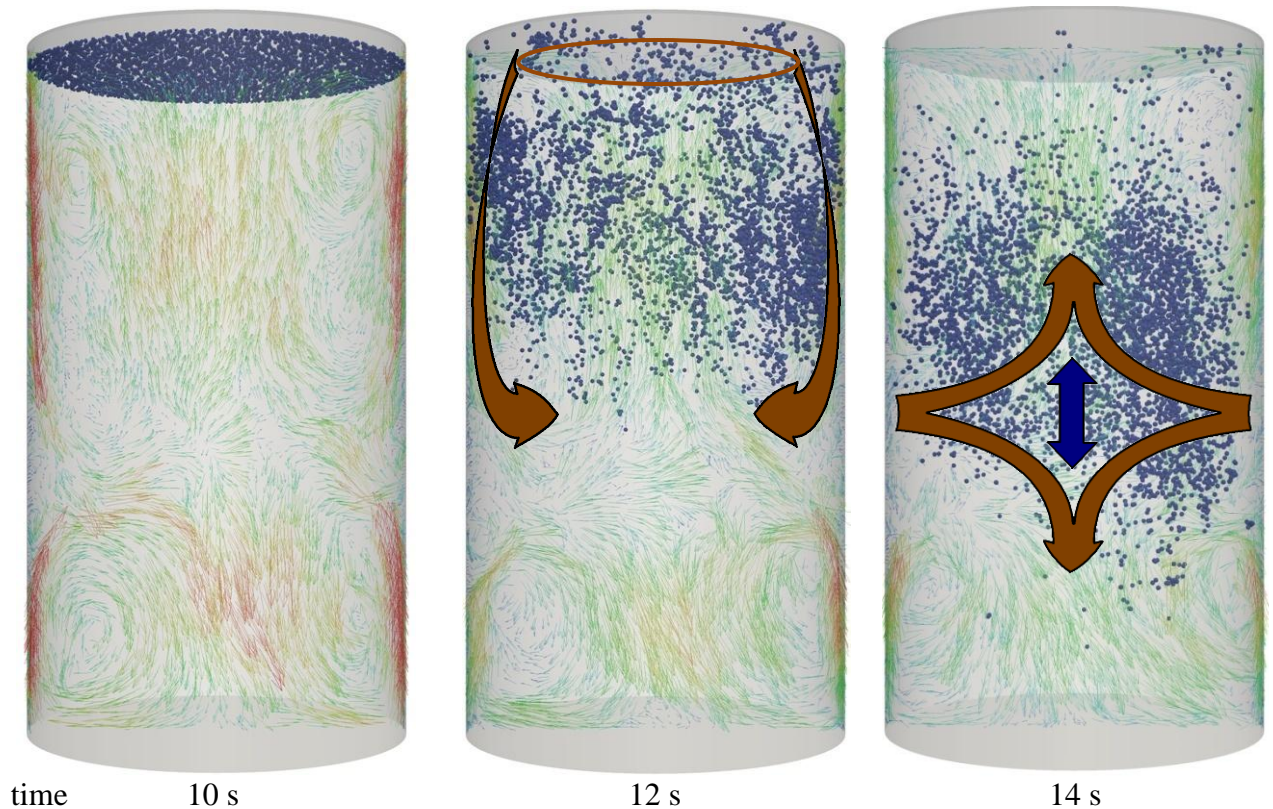


Figure 5.6: The scheme of the initial motion of the inclusions, which are situated on the open surface of the melt with the developed flow in ICF. The flow velocities are qualitatively shown in the vertical plane at the appropriate time moment (the time is defined from the zero velocity state).

The present chapter focuses the analysis on the behaviour of particles in the zone of maximal kinetic energy - the middle zone between the main vortexes (Figure 3.10), where intensive pulsations of the flow provide the exchange of the inclusions between the eddies, which is the mechanism of particle homogenization in ICF. Opposite to the heat exchange, the behavior of inertial particles can differ from the flow pulsations, therefore, the spectral analysis of particle oscillations is essential for the mentioned industrial application. However, the flow velocity oscillation should be discussed at first place.

5.2.1 Flow velocity oscillation

Figure 3.10 shows the distribution of turbulent kinetic energy in ICF-1 as the illustration of the intensity of the flow pulsations. The maximal contribution to the turbulent kinetic energy comes from the axial velocity pulsation (Figure 3.10 a) that is responsible for the exchange between the vortexes. The zone of the maximal kinetic energy in ICF-1 is between the mean vortexes around 280 mm from the bottom of the crucible (see the sketch of ICF-1 on Figure 5.9).

M. Kirpo's experimental database of the velocity measurements in ICF-1 is used in the present investigation. Some results based on these experimental data are already published by *Kirpo et al. (2007)*, however, the new analysis was done in order to compare the flow oscillations with the appropriate data for the particle exchange. As far as we are mostly interested in the mass exchange between the vortices, that is in axial direction, we will analyze the axial part of turbulent kinetic energy in i area point $K_i = \langle u_{z,i}^2/2 \rangle$ below. The same reasons confirm the interest for integral values that characterize the flow behavior in horizontal planes ($z=const$). Therefore, the experimentally obtained turbulent kinetic energy was averaged in the radial direction ($K(z) = \sum_i (K_i \cdot 2\pi r_i \cdot \Delta r_i) / \pi R^2$, where Δr_i is the distance between the area points and is compared with the results of the appropriate simulation that were also averaged in the angular and the radial directions (Figure 5.10). The experimental and the numerical results are in a satisfactory correlation, and the difference between the experimental and the numerical maxima is within the errors.

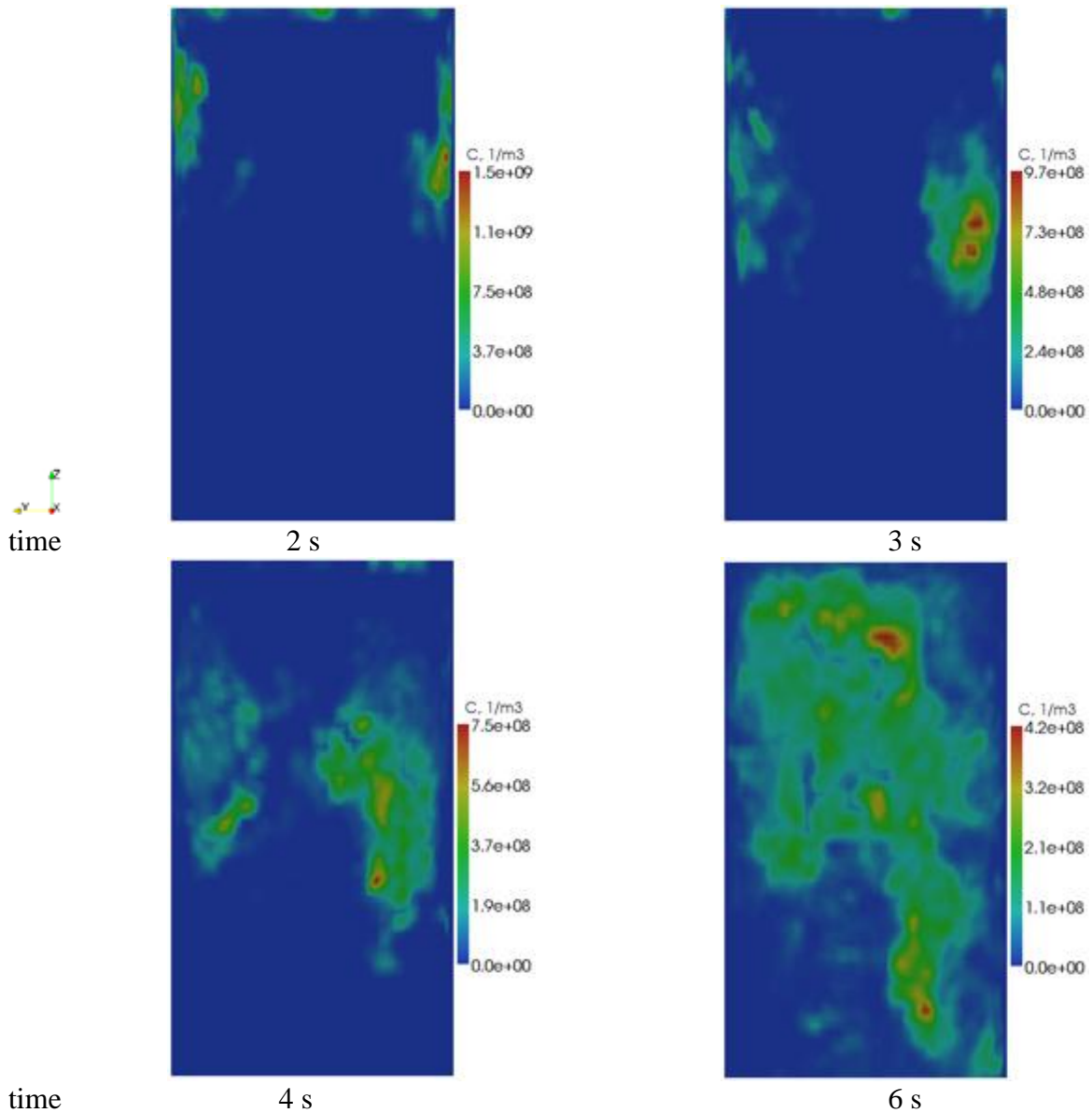


Figure 5.7: The evolution of the concentration of the particles with the diameter $50 \mu\text{m}$ in ICF-1. Concentrations are shown in the central vertical plane.

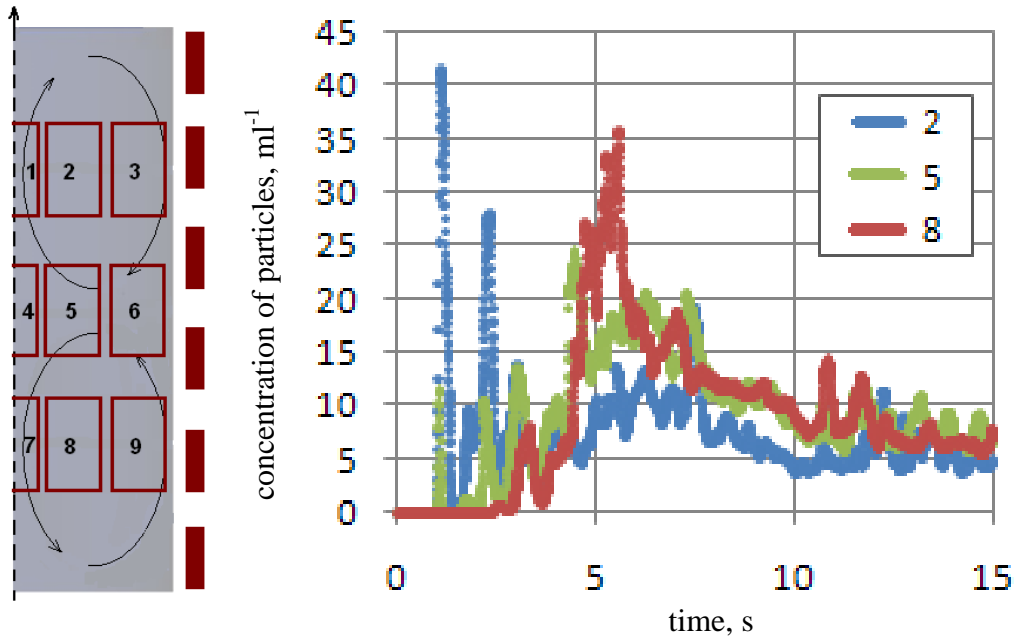


Figure 5.8: Dynamics of the concentration of the particles in different areas of ICF-2 (simulated results). Areas are numbered on the sketch of the crucible (left image).

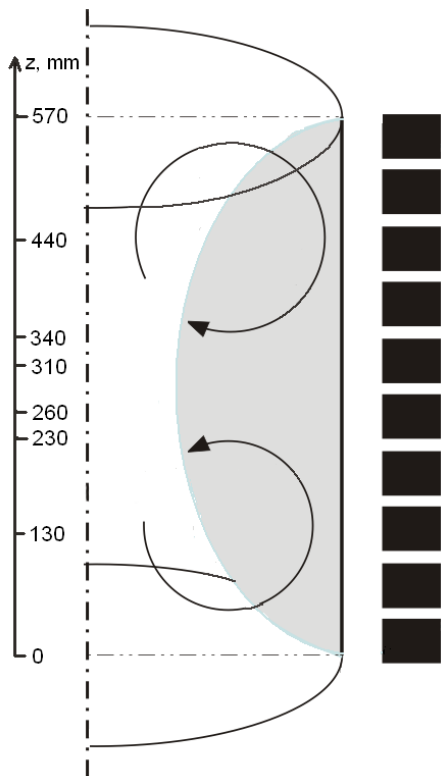


Figure 5.9: The sketch of an axial-symmetric ICF-1 with a vertical scale, which is measured from the bottom of the crucible.

The discrete Fourier transformation is done for the oscillations of the flow velocity's axial component in order to obtain the spectrum. Figure 5.11 testifies the clear maximum on the spectrum at the half-height of the inductor near the wall. This maximum registers the dominating oscillations with the frequency $1e-1$ Hz and the amplitude 7 ± 2 cm/s, which is approximately the

half of the maximal mean velocity. This spectrum significantly differs from the typical turbulent spectrum (Kolmogorov spectrum) that characterizes the flow in the bulk of the ICF (*Kirpo et al., 2007*). The difference - the presence of the low-frequency maximum - can be explained with hydrodynamic instabilities at the high-Reynolds number flow that disturbs the EM induced flow pattern and results in the oscillations of the zone where the flow changes its direction and tears off from the wall (see Figure 2.4). Low-velocity magnitude is typical for this zone and, oppositely, the maximal velocities are above and below it (Figure 2.4). Thereby, following the Euler approach of the flow description the significant oscillations are observed in the point between the mean vortexes close to the wall.

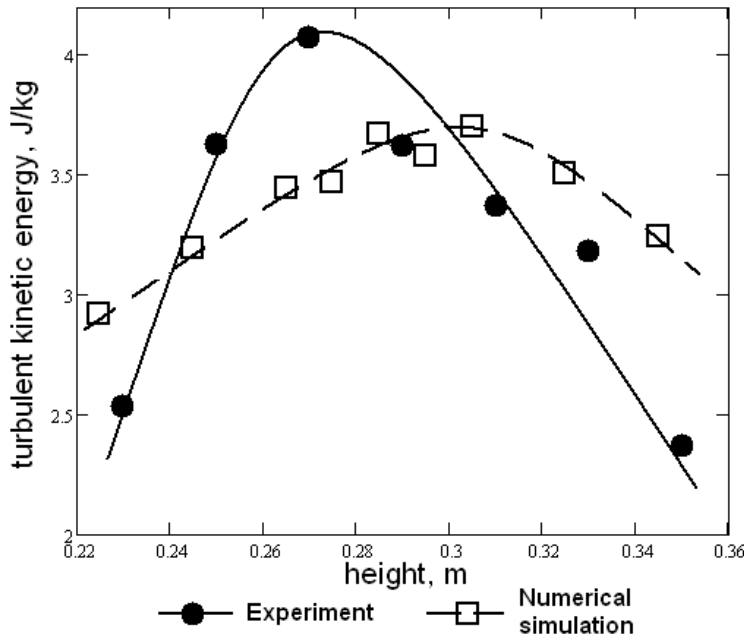


Figure 5.10: The axial distribution of the axial part of turbulent kinetic energy in the ICF-1, integrated in a radial direction.

Apparently, the significant kinetic energy together with the clear low frequency oscillations in the middle zone describe the momentum, heat and mass transfer between the upper and the lower mean vortexes, and the transport process in this zone has the oscillating nature. However, the whole zone between the eddies is involved in the heat and mass exchange process; therefore, the oscillations in the whole zone should be analyzed in order to describe this exchange.

The velocity spectra in the points that are situated close to the position at the half height of the inductor near the wall, but do not coincide with that position, have no more such clear maximum as on Figure 5.11, however, at the same time the kinetic energy remains significant. The further from the position of the described specific spectrum is (Figure 5.11) the less the low frequency oscillations are expressed. Therefore, the common spectrum of the pulsations of the flow in the whole zone between the mean eddies differs from Figure 5.11.

Figure 5.12 shows the integral spectra of the pulsations in the wide middle zone of the ICF-1 between the mean vortexes. These spectra $A_{int}(f)$ are calculated from the experimental data in the following way:

$$A_{int}(f) = \frac{\sum_i(A_i(f) \cdot K_i)}{\sum_i K_i}, \quad (5.1)$$

where $A_i(f)$ and K_i are the spectral velocity (amplitude) of the oscillations depending on the frequency (that is the spectrum) and the kinetic energy of pulsations respectively in i point; index i represents the points of the experimental data within the analyzed zone.

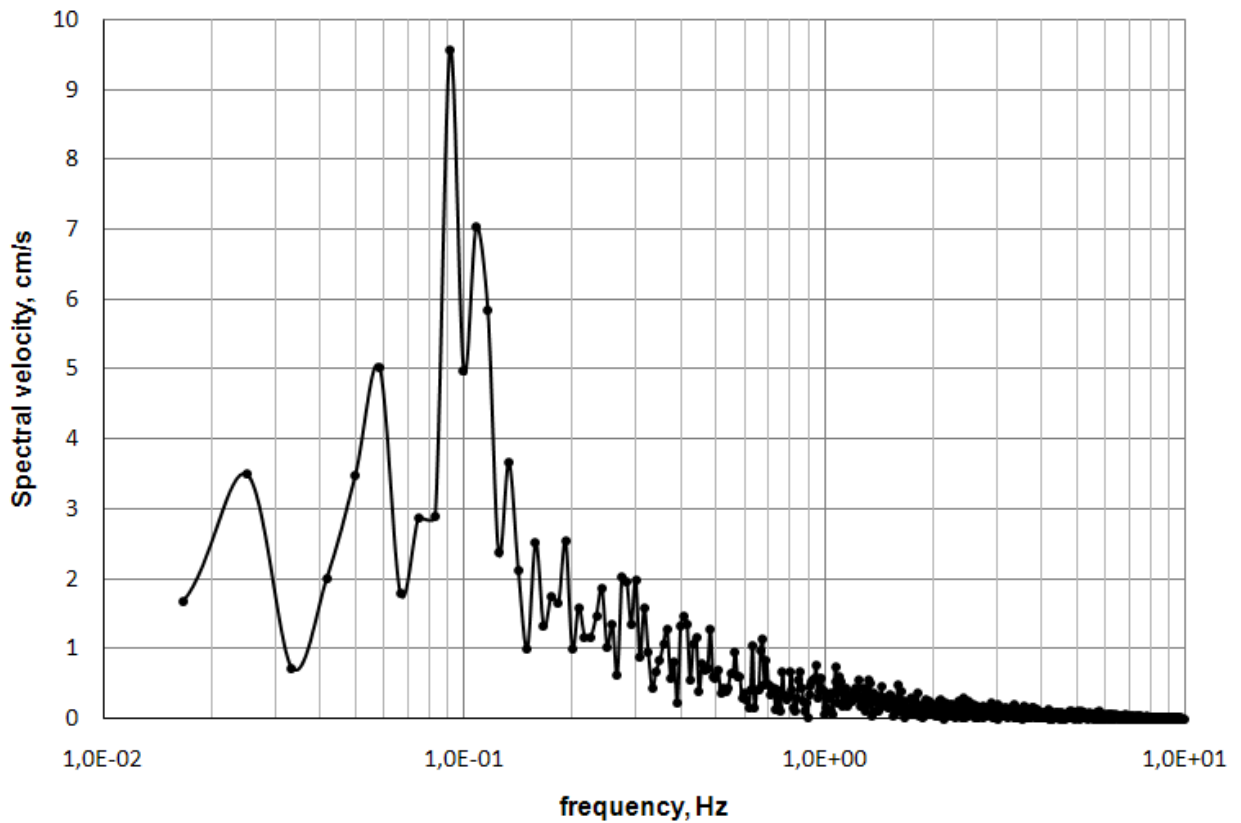


Figure 5.11: The spectrum of the axial flow velocity at the half height of the inductor near the wall $r=150$ mm, $h=280$ mm (from the experimental data).

Opposite to the spectrum of the single point (Figure 5.11) the integral spectrum (Figure 5.12) has a multi-pick shape. At least three of the low-frequency picks are formed by more than three points¹ and, consequently, are plausible: $5e-2$ Hz, $1e-1$ Hz, $1.5e-1$ Hz. The maximum at $1e-1$ Hz represents the integral oscillations with the largest amplitude and correspond to the pick on the spectrum of the single point (Figure 5.11). The amplitude of integral oscillations is lower than on the spectrum of the single point, however, generally that means that $1e-1$ Hz maximum corresponds to the strongest oscillations of the main EM induced vortexes. Thus, the mechanism of the oscillations, which was discussed for the single point at the half-height of the inductor near the wall, remains relevant for the common oscillations of liquid metal in the middle zone of crucible. However, as it is shown on Figure 5.12, several other picks appear on the spectra of the integral oscillations. Obviously, these oscillations are also significant for the transportation of the inclusions between the EM induced main vortexes. Their influence will be analyzed below.

¹ The spectra on Figure 5.11, Figure 5.12, Figure 5.15 are calculated from discrete experimental data using discrete Fourier transformation. Therefore the curves just smoothly connect the discrete spectra.

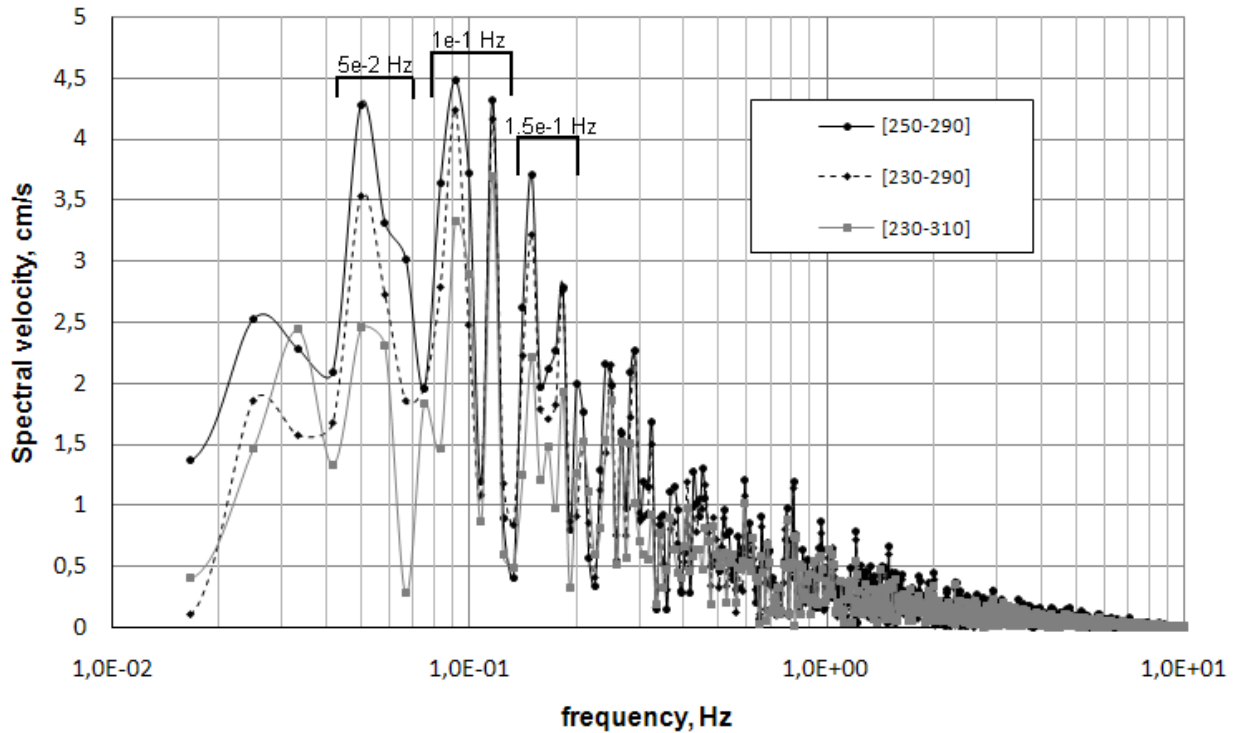


Figure 5.12: The spectra of integral pulsations in the middle zone of the ICF-1 between the mean vortices (from the experimental data). Different curves correspond to the different interval of integration. The height of the lower and the upper borders of these intervals are shown in the brackets in the legend (mm from the bottom). The total height of the ICF-1 is 570 mm. The integral spectra are calculated according to the expression (5.1)).

5.2.2 Oscillation of the particle number

As it has already been mentioned, the behavior of the particles in the middle zone determines the mass exchange in the whole crucible. Figure 5.13 illustrates the oscillating nature of the exchange process. It can be observed that the density of particles (liquid-to-particle density ratio $S = \rho_f / \rho_p$) influences minimally this process, however, this conclusion is not correct for the enough large particles (200 μm for the ICF-1 – see Figure 5.13 (d)) that start to deposit to the wall due to relatively large EM force (the trend line on Figure 5.13 (d) shows the decrease of the total number of 200 μm particles). Figure 5.13 (a-d) also show that the oscillations of the 50 μm and the 100 μm particles are approximately the same.

The oscillations of the number of particles in the middle zone of a different width are illustrated on Figure 5.14. The shape of these curves for narrow zones ([260 - 310] mm and [260 - 340] mm) are almost the same, the difference is only in the average value. However, when the zone comes so wide that it also involves a part of the main eddies, the amplitude of oscillations, apparently, decreases. Consequently, the narrowest interval ([260-310] mm) should be used for the description of the particle oscillations caused by the flow pulsations. A narrower interval will lead to the small number of particles, which will not be enough for spectral analysis. Moreover, as far as the curves on Figure 5.13 are rather similar, only one particle type – 100 μm , $S=1.0$ - will be analyzed further.

Figure 5.15 compares the spectrum of the integral flow pulsations and the oscillations of the particle number in the middle zone of the ICF (in the interval [260-310] mm from the bottom). The amplitudes in these spectra are normalized with the respect to their maximal values

in order to compare qualitatively the oscillations of different variables. Particle spectrum also contains several picks at approximately the same frequencies as on the flow spectrum, however, the amplitudes differ. The particle oscillations have not more dominating pick at approximately 1e-1 Hz, which is the pick of the fundamental oscillation of the main flow eddies. At the same time, the maximum of particle spectrum at the very low frequency is more significant than on the flow spectrum. And finally the high frequency tale of the particle spectrum is of the smaller amplitudes in comparison with the flow pulsations. Obviously, the high frequency flow oscillations cannot influence the inertial particles.

Generally, the spectra on Figure 5.15 show that the mass exchange and the migration of solid inclusions between the main flow vortexes in ICF are governed mostly by the pulsations of flow velocity and have the maxima at the same frequencies. However, the main oscillation of particle number appears on the lower frequency than the main pulsations of the flow.

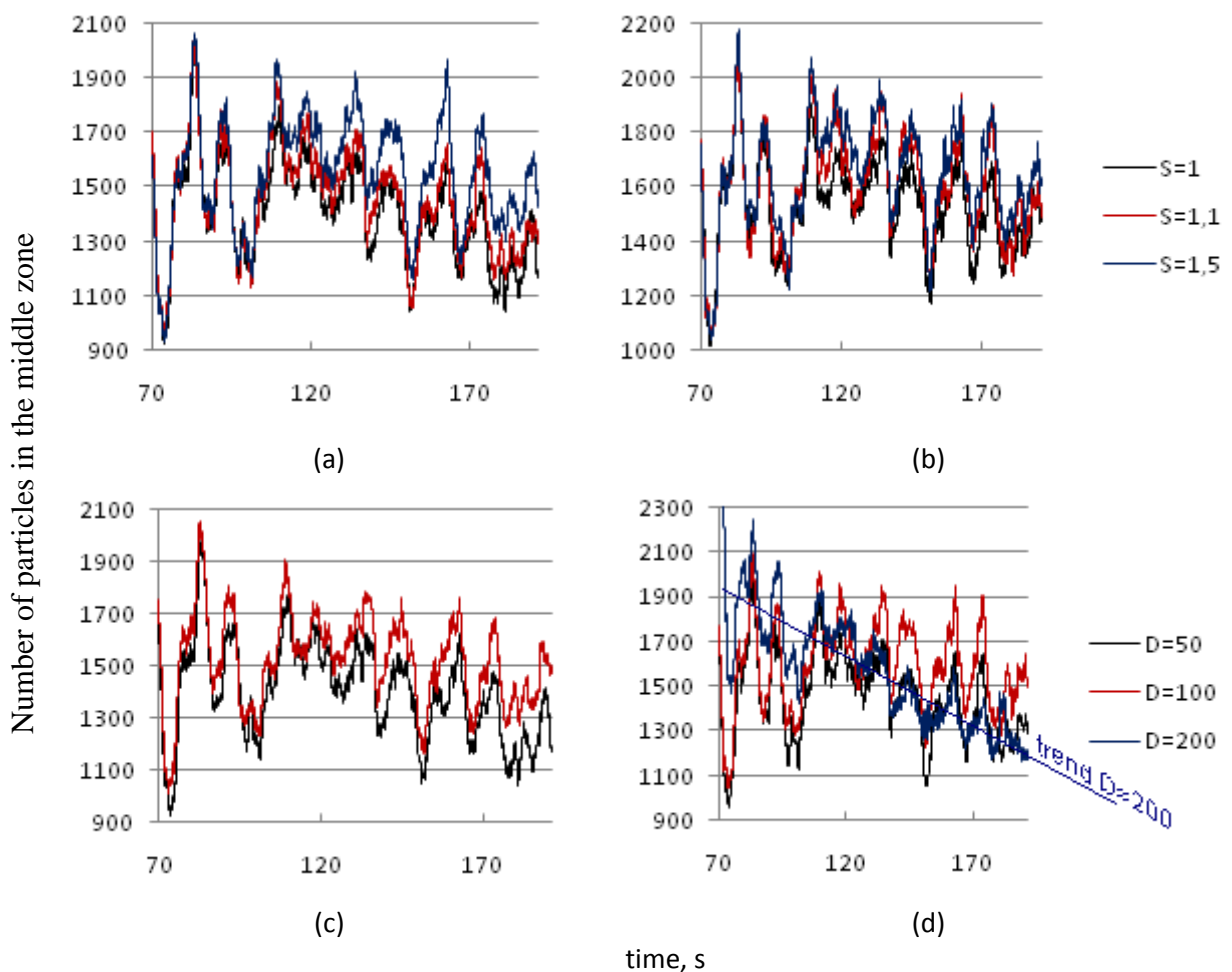


Figure 5.13: Oscillation of the number of particles in the middle zone of the ICF-1 (in the interval [260-310] mm from the bottom). The upper row: different $S=\rho_f/\rho_p$, but common diameter - (a) $D = 50 \mu\text{m}$, (b) $D=100 \mu\text{m}$; the lower row: different diameter D , but common liquid-to-particle density ratio - (c) $S=1.0$, (d) $S=1.1$. Numerical results.

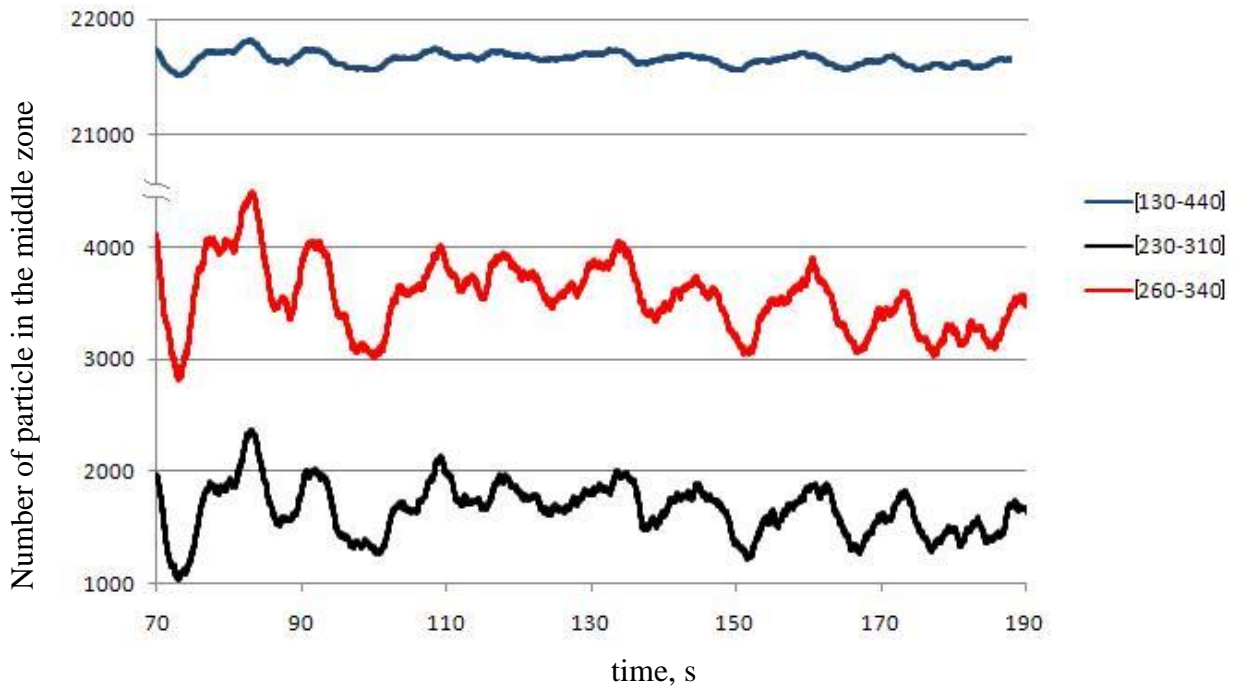


Figure 5.14: The oscillations of the number of 100- μm particles with liquid-to-particle density ratio $S = 1.0$ in the middle zone of ICF (numerical results). Different curves correspond to a different width of the middle zone. The height of the lower and the upper borders of these intervals is shown in the brackets in the legend (mm from the bottom).

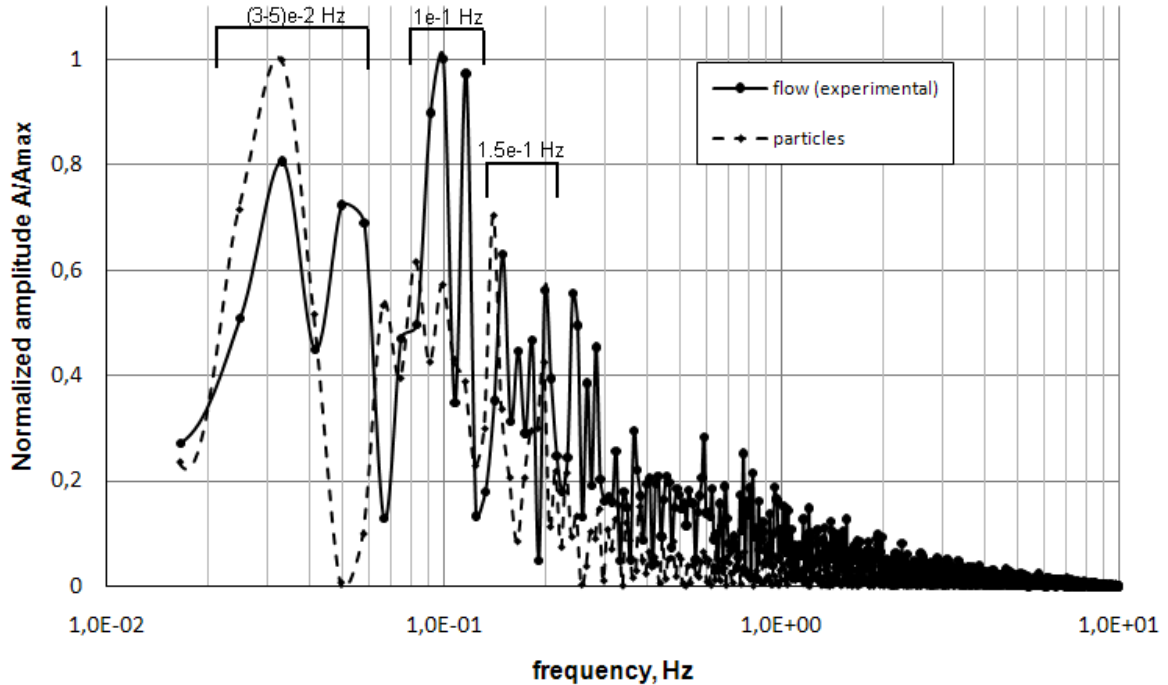


Figure 5.15: The spectra of the integral pulsations of the flow velocity (experimental data) and the number of particles in the middle zone of the ICF in the interval [260-310] mm from the bottom (numerical data). The spectrum of the particle oscillations is created for 100- μm inclusions with the liquid-to-particle density ratio $S=1.0$.

The particular ICF-1 was analyzed within this chapter, therefore, the mentioned dominating frequencies are relevant only for the particular case. However, the author believes that the researched tendency - the preferential particle exchange at the lower frequency than the dominating flow oscillations - is a general phenomenon. The realization of the general particle exchange mechanism in ICF and the dominating frequencies can give engineers the possibility to improve efficiency of stirring in such equipment.

5.3. Homogenization of the alloying particles in ICF¹

The oscillating mechanism of the exchange of inclusions between the zones of eddies was described in the last chapter. As it was discussed in the Chapter 2.2, such exchange is significant for some industrial applications like homogenization of alloying particles in ICF. And this particular problem will be analyzed in the present chapter.

As in was discussed in the introduction (the Chapter 1.1), the alloying particles are mixed in different metal melts (e.g. steel) to increase some properties, such as strength, hardness, wear resistance and others. Widespread alloying inclusion is carbon, which as well as many other admixtures remains in a solid state. The typical alloying elements and their densities are represented in Table 5.1. Usually the density of metals is not less than the density of inclusions, e.g. steel alloy ranges between 7.75 and 8.05 g/cm³ depending on the consistence of the alloy. Thereby, there are admixtures with approximately equal and smaller densities than the density of steel. Most alloying elements are pure conductive, and a great transition resistance appears on the surface between a particle and a metal, hence, we can consider non-conductive particles.

Table 5.1: Density of the typical alloying elements.

Alloying element (chemical index)	Density, g/cm ³
Nickel (Ni)	8.91
Manganese (Mn)	7.21
Chromium (Cr)	7.19
Vanadium (V)	6.0
Silicon (Si)	2.33
Boron (B)	2.08
Carbon (C)	1.8 - 2.3 ²

Generally, it is important to achieve homogeneous admixtures distribution to ensure a high quality of the alloy. At the same time, it is desirable to reduce the time of mixing in order to reduce energy consumptions and prevent melt overheating.

However, as it was discussed in the Chapter 4, the surface of the melt is not transparent and, consequently, it is not possible to control the rate of homogenization of admixtures visually. Moreover, the extremely high temperature of the melt makes the operative control of the alloy homogeneity very difficult. There are some technologies that provide the express analysis of the solidified samples of the metal (see e.g. *Böhlen et al., 2011; Ericsson et al., 2011*). However, these techniques are not very convenient for the determination of homogeneity. Taking

¹ This chapter develops the approach to the description of homogenization, which was published in paper *Ščepanskis et al. (2010)*.

² The density of amorphous carbon is 1.8 – 2.1 g/cm³ (*Lide ed., 2005*), the density of graphite is 2.267 g/cm³.

solidification analysis of a sample requires a significant time. Moreover, during the cooling of the melt in the sample, the concentration of the dissolved oxygen also changes and the inclusions growth. Therefore, additional analytical procedure should be applied to restore the initial distribution of inclusions in the melt.

Taking into account the mentioned problems, the numerical simulation remains a powerful tool for the investigation of the homogenization process. However, as it was discussed in the Chapter 2.2, only the LES simulation is relevant for the turbulent flow of ICF. Therefore, the proper calculations are very time-consuming, which make impossible the standard optimization procedure with many iteration steps of HD calculations for different parameters. Therefore, the present chapter presents the methodological approach for the optimization of the inclusion size (or determination of the mixing time if the size and density of inclusions are fixed), which can be performed in satisfactory time period. This approach is demonstrated on the example of ICF-1 in the present chapter, however, can be performed for ICF with any other parameters. The methodology contains the regression model based on several LES calculations of a particle laden flow according to the numerical model presented in the Chapter 3.

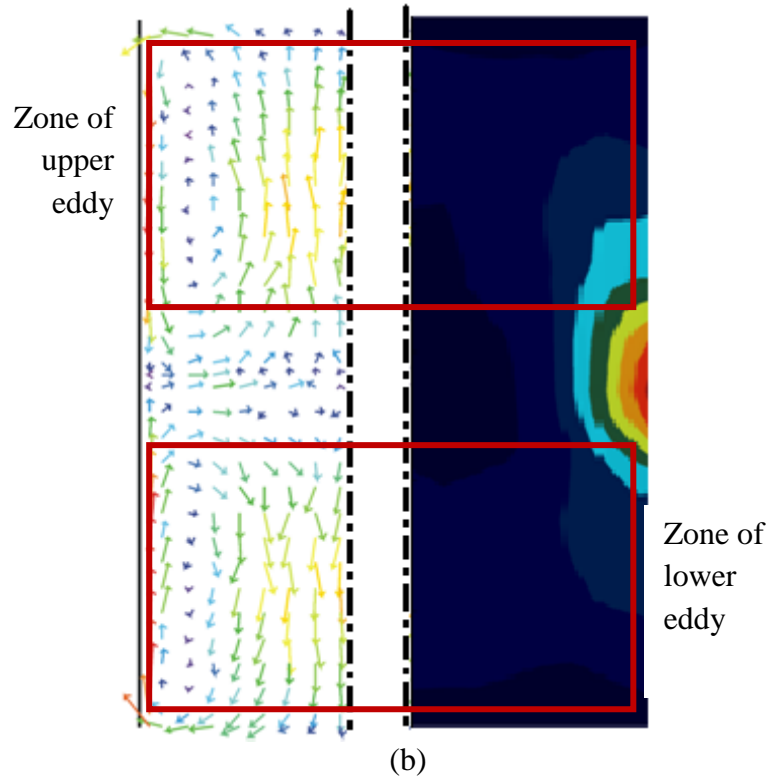
5.3.1 Regression model for an optimization problem

The process of homogenization of alloying particles is considered for about $3e+4$ particles with the diameter 50 μm , 100 μm and 200 μm and liquid-to-particle density ratio $S = \rho_f/\rho_p = 1.0; 1.1; 1.5$. The particles are input on a horizontal plane near the top surface of the crucible (like in the case described in the Chapter 4.3 (see also Figure 5.2), which roughly corresponds to the industrial process).

As it has already been discussed in the Chapter 5.2 the intensive pulsations of the flow and, consequently, of the particles in the middle zone between the main eddies favor the particle exchange and decrease the difference between the number of the particles in the zones of the upper and the lower eddies ΔN with the lapse of time (the scheme of the zones are shown on Figure 5.16). The thin layers near the top surface and the bottom of the crucible are excluded from the mentioned zones. So the process of homogenization takes place between the zones of two eddies, therefore, the difference between the particles in the zone of the upper eddy and those in the zone of the lower eddy are analyzed. The results of simulation show that the radial and the distribution of the particles inside the crucible rapidly becomes homogeneous (except a thin layer near the wall – see the discussion on the particle concentration there in the Chapter 5.1.2). Therefore, the thin layer near the wall, where EM force significantly attracts the particles to the wall, is also excluded from the zones within the homogenization analysis (Figure 5.16).

Figure 5.17 shows the evolution of ΔN (the subtraction of the number of the particles in the zone of the upper eddy and in the zone of the lower eddy) normalized with respect to the number of the particles N in both zones and for the particles with a different diameter. The process of homogenization is monotonous, but the rate increases with the decrease of the density ratio $S = \rho_f/\rho_p \geq 1$. The rate of the homogenization also depends on the size of particles. Despite of the general monotonous nature of the homogenization, some significant perturbations take place. Therefore, time of the homogenization (time to achieve $\Delta N/N = 0$ or any non-zero asymptotic value) cannot be simply defined from the curves on Figure 5.17 – the perturbations leads to significant errors. However, two quantitative parameters can describe the process.

$\Delta N/N$ decreases very rapidly in the first few seconds. This first stage of the homogenization is described with a quantitative parameter $\delta(S,D)$ (see Figure 5.19). After that the homogenization progresses slowly and can be described with a linear function. The quantitative parameter $a(S,D)$, which is the coefficient of a linear regression, describes this stage of the process (see also Figure 5.19). Finally, $\Delta N/N$ oscillates around one value (in the most cases this value is equal to zero).



(a) (b)
Figure 5.16: The scheme of the zones of the upper and the lower eddy. The location of zones is illustrated on the background of (a) an average flow and (b) turbulent kinetic energy (both are drawn on the half of the crucible).

The first stage of the homogenization corresponds to the time when the initial cloud of the particles comes to the middle zone of the crucible to the wall (see discussion in the Chapter 5.1.2). This stage apparently corresponds to the first maximum of the total number of particles in the zones of eddies (see Figure 5.18). After that the cloud comes to the unstable middle zone, which is excluded from the eddy zones, and, consequently, the minimum of N appears on Figure 5.18. The second homogenization stage is characterized by the exchange of particles between the zones of eddies through the middle zone.

The values of quantitative parameters $\delta(S,D)$ and $a(S,D)$ for different S and D are shown in Table 5.2. Figure 5.20 and Figure 5.21 graphically illustrate the dependence of the mentioned quantitative parameters of homogenization δ and a on S and D respectively. The linear approximation for these dependencies is also plotted. The most of lines are built on the basis of 3 points, which apparently is not enough for a linear regression, however, the line $S = 1.5$ (see Figure 5.20 b and Figure 5.21 b) consists of 5 points and proves the relevance of a linear regression.

The parameter of the initial stage of the homogenization δ decreases with the increase of S and increases with the increase of D (Figure 5.20). And the rate of the homogenization in the

second stage a increases with the increase of both S and D (Figure 5.21). Assuming the linear regression we can express these parameters as follows:

$$\delta(S,D) = 0.8 + 1.2e-3 \cdot D [\mu\text{m}] - 0.3 \cdot S, \quad \text{standard deviation: } 4.6e-2; \quad (5.2)$$

$$a(S,D) = -1.5e-2 + 2.0e-5 \cdot D [\mu\text{m}] + 3.4e-3 \cdot S, \quad \text{standard deviation: } 6.8e-4. \quad (5.3)$$

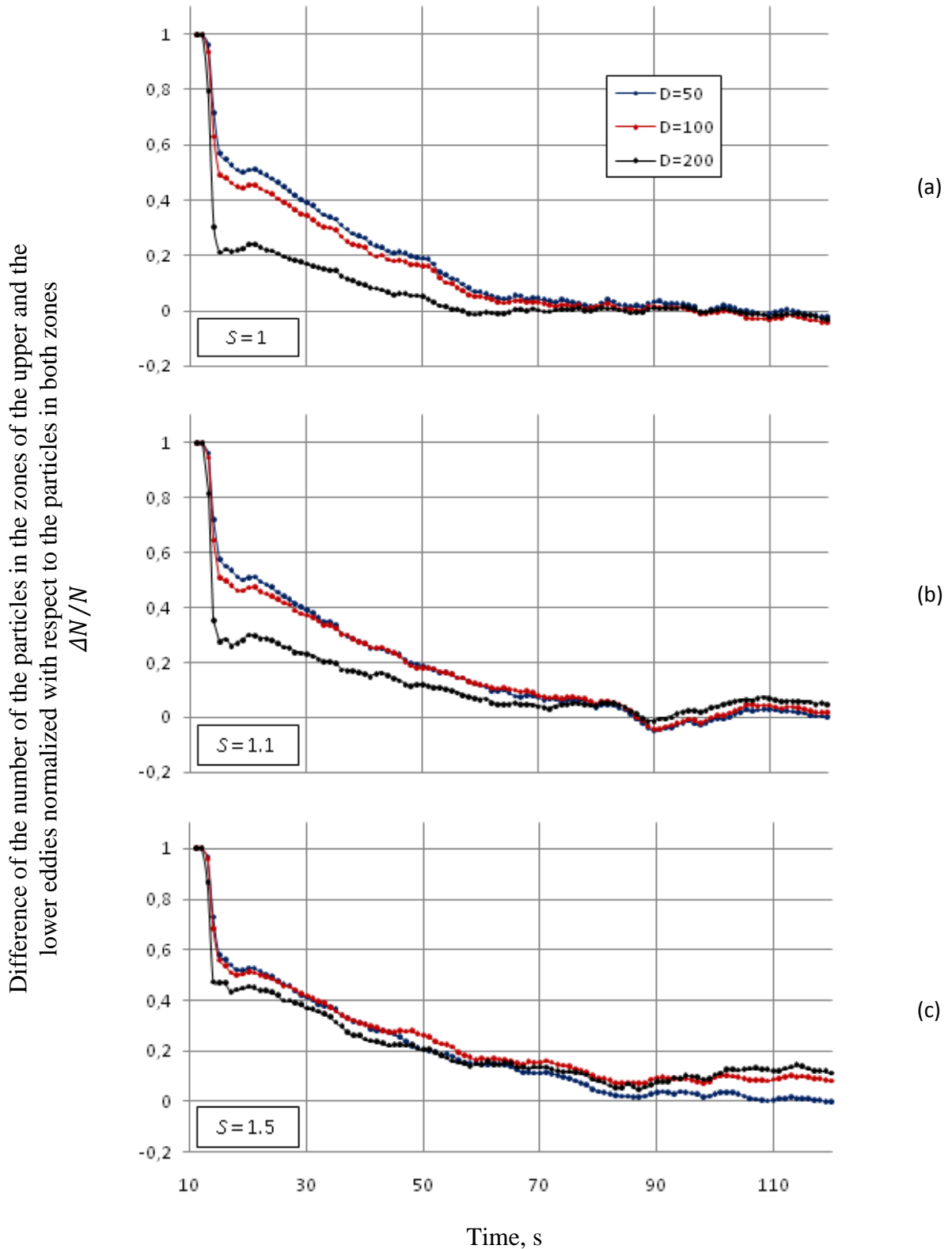


Figure 5.17: Difference between the number of the particles in the zone of the upper and the lower eddies normalized with respect to the number of particles in both zones. Liquid-to-particle density ratio: (a) $S = 1$; (b) $S = 1.1$; (c) $S = 1.5$.

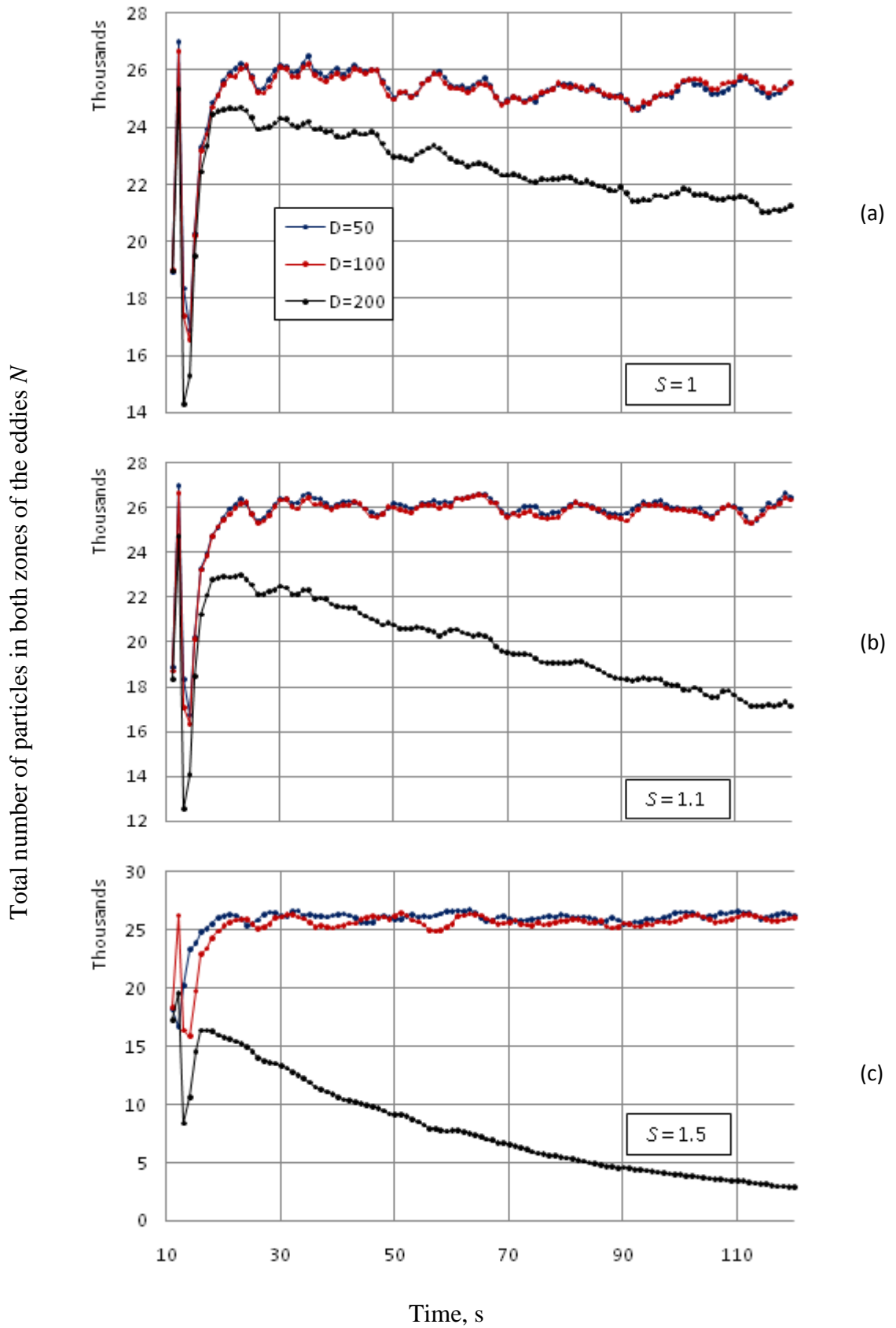


Figure 5.18: Total number of the particles in both zones of the eddies. Liquid-to-particle density ratio: (a) $S = 1$; (b) $S = 1.1$; (c) $S = 1.5$.

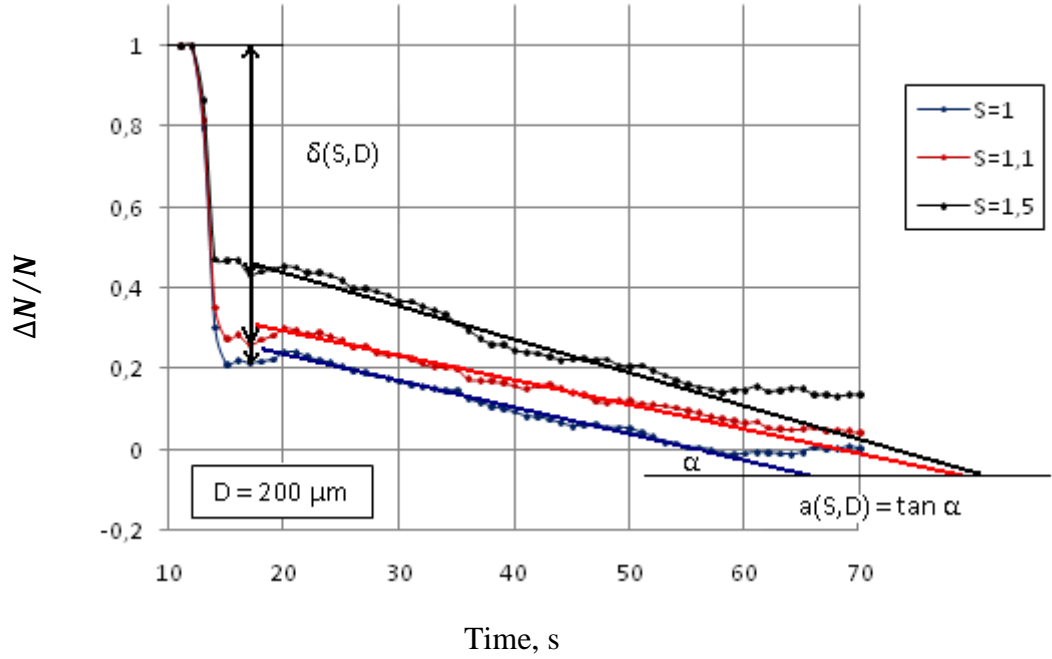


Figure 5.19: $\Delta N/N$ for particles with the diameter $200 \mu\text{m}$: the illustration of the homogenization quantitative parameters.

Table 5.2: The values of the quantitative parameters of the homogenization $\delta(S,D)$ and $a(S,D)$ (see Figure 5.19).

S	$D, \mu\text{m}$	δ	a, s^{-1}
1.0	50	0.49	$(-1.10 \pm 0.02)e-2$
	100	0.55	$(-1.00 \pm 0.02)e-2$
	200	0.79	$(-6.6 \pm 0.1)e-3$
1.1	50	0.50	$(-9.5 \pm 0.2)e-3$
	100	0.54	$(-8.8 \pm 0.2)e-3$
	200	0.74	$(-5.7 \pm 0.1)e-3$
1.5	50	0.46	$(-7.7 \pm 0.2)e-3$
	100	0.49	$(-6.7 \pm 0.2)e-3$
	180	0.53	$(-6.0 \pm 0.2)e-3$
	190	0.50	$(-6.8 \pm 0.2)e-3$
	200	0.52	$(-5.9 \pm 0.2)e-3$

Initial stage of a rapid homogenization takes $t_{1.st} = 7.3 \pm 1.2 \text{ s}$ from the beginning of admixing. On the second stage the homogenization can be described with following expression:

$$\frac{\Delta N}{N}(t_{1.st} + t) = [1 - \delta(S,D)] + a(S,D) \cdot t.$$

As it has already been discussed, $\Delta N/N$ becomes more or less constant after the second stage of the homogenization. In the most cases ($S = 1.0; 1.1$) this constant value is close to zero, that means the zero difference of the number of particles in the zones of the upper and the lower eddies. However, the significant density difference between the liquid and particles makes a complete homogenization impossible (see $S = 1.5$ case - Figure 5.17). The constant value

$(\Delta N/N)_\infty$ is positive (> 0) for the case $S = 1.5$ (except small particles $D = 50 \mu\text{m}$). Moreover, $(\Delta N/N)_\infty$ is different for the cases with different D , however, no trend can be observed. Therefore, the average value of $(\Delta N/N)_\infty = (8.4 \pm 1.2)e-2$ for the large particles with the density ratio $S = 1.5$.

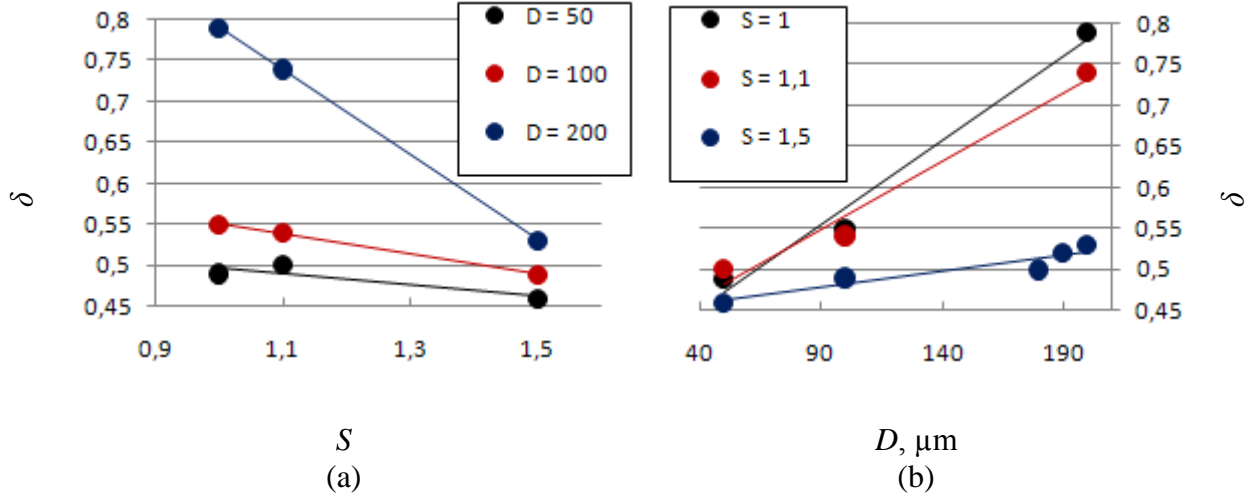


Figure 5.20: Quantitative parameter δ (see Figure 5.19) as a function of the liquid-to-particle density ratio S (a) and the diameter of particle D (b).

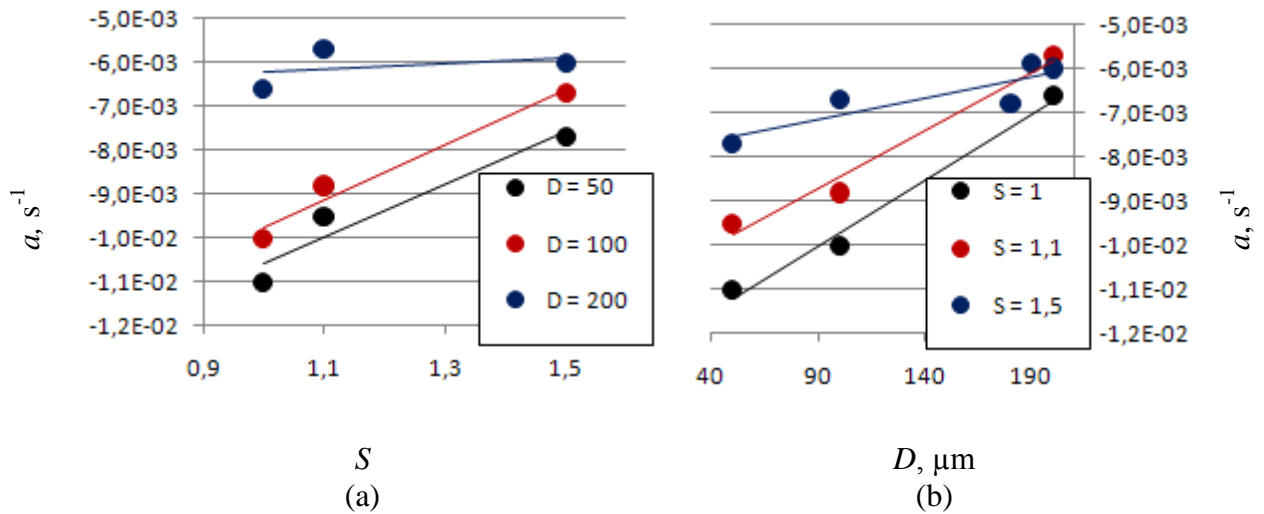


Figure 5.21: Quantitative parameter a (see Figure 5.19) as a function of the liquid-to-particle density ratio S (a) and the diameter of particle D (b).

Thus, the time of the second stage of homogenization $t_{2.st}$ can be defined from the following equation:

$$[1 - \delta(S, D)] + a(S, D) \cdot t_{2.st} = \left(\frac{\Delta N}{N}\right)_\infty.$$

And, consequently, the total time of homogenization

$$t_{hom}(S, D) = t_{1.st} + t_{2.st}(S, D) = t_{1.st} + \frac{(\Delta N/N)_\infty + \delta(S, D) - 1}{a(S, D)}. \quad (5.4)$$

Table 5.3 shows the values of t_{hom} , which are calculated using the equation (4). The values of δ and a as well as their errors are taken from the regressions (2 – 3).

Nevertheless, it should be pointed out that these results are relevant only for ICF-1. However, the method of the homogenization analysis and prediction, which is described in the present chapter, can be easily applied to an ICF of another size and with different EM parameters. The times of homogenization (the industrially important information) can be obtained in the same way also for another ICF. The fundamental origin of the dependencies mentioned above will be discussed in the next subchapter. These qualitative explanations testify universality of the approach.

Table 5.3: The time of the homogenization in ICF-1 for the particles with different D and S . The values are calculated taking into account equations (5.2–5.4).

S	$D, \mu\text{m}$	t_{hom}, s
1.0	50	53±9
	100	52±10
	200	47±11
1.1	50	58±9
	100	57±10
	200	53±13
1.5	50	80±13
	100	82±15
	180	85±19
	190	86±19
	200	86±20

5.3.2 Qualitative explanation of the dependences

Figure 5.18 illustrates the decrease of the particle number in the zones of the eddies for large inclusions ($D = 200 \mu\text{m}$) in ICF-1. That means the conglomeration of particles outside of the zones – near the wall. This process takes place due to the relative increase of EM force, which moves the non-conductive particle to the wall. The large particles preferentially concentrate there and create the agglomerations. Moreover, the simulation shows that the particles stuck to the wall move to the middle zone (where the maximum of EM force appears) governed by the flow motion and the non-homogeneous distribution of the force (see discussion in the Chapter 5.4).

Despite of the simple explanation of the particle deposition the analysis of the forces should be done to explain the dependence of the deposition rate on the liquid-to-particle density S . As it was described above, the initial particle cloud comes to the middle zone to the wall (see discussion in the Chapter 5.1.2). As it will be discussed below, the intensity of EM influence on a particle is different for different inclusions, therefore, the zone of the further analysis of the forces should be also different (from the center of mean the upper vortex to the middle of the crucible near the wall). However, let us consider the idealized case, where the analysis of the forces will be performed in the common zone for all type of inclusions – around the middle of the crucible, at the lower border of the upper mean eddy. The motion of the particle in this zone will also be considered. The flow changes the direction in this region (Figure 5.16 a). The drag coefficient C_D is decreasing as D^{-2} with the increase of the particle in size (expression 3.11). Thus, the drag force normalized with the mass in equation 3.16 is small for big particles and cannot change their trajectories. With the increase of the particle size, the direction of the particle velocity becomes more vertical in the considered zone (Figure 5.22).

Buoyancy and drag forces per mass unit linearly depend on $S = \rho_f/\rho_p$ (equations 3.16). The simulation shows that the velocity of the particles in the middle zone in both analyzed cases for different S is equal with the 10% tolerance, thus, the forces at $S > 1$ and $S = 1$ are the following (F/m corresponds to the corresponding terms in equation 3.16):

$$\frac{\left(\frac{F_{drag}}{m}\right)_{S>1}}{\left(\frac{F_{drag}}{m}\right)_{S=1}} \approx S > 1, \quad \left(\frac{F_{buoyancy}}{m}\right)_{S>1} = (1 - S) \cdot g,$$

$$\frac{\left(\frac{F_{em}}{m}\right)_{S>1}}{\left(\frac{F_{em}}{m}\right)_{S=1}} \approx S > 1.$$

The buoyancy and drag forces try to decrease the momentum and decelerate the particle (Figure 5.22 b, c). In the case $S = 1$, the buoyancy force is equal to zero and only the drag force tries to stop the particle (Figure 5.22 c). Therefore, in this case the deceleration of the particle is of less efficiency and the big particles with a greater probability come to the region of the lower eddy (Figure 5.22 c). The EM force per mass unit increases with the increasing S and pushes the particle to the wall. In the case $S > 1$, the particle can be efficiently decelerated and the relatively large EM force lets it stick to the wall in the middle zone (Figure 5.22 b). This is the reason of the decrease of N for the big light particles (Figure 5.18 c).

When a particle comes to the middle zone of the crucible near the wall, there are three possible ways to go: 1) the zone of the upper eddy, 2) the zone of the lower eddy and 3) stick to the wall. Figure 5.23 summarizes the conclusions on the above mentioned physical model and shows the increase and the decrease of the probability for the particle to come to one of these three areas with respect to the particle diameter D and S . This scheme can also explain the dependencies that are illustrated on Figure 5.20 and Figure 5.21. This model also can easily explain Figure 5.24, which illustrates the dependence of the deposition rate on the large particles on the density ratio S (see also Table 5.4).

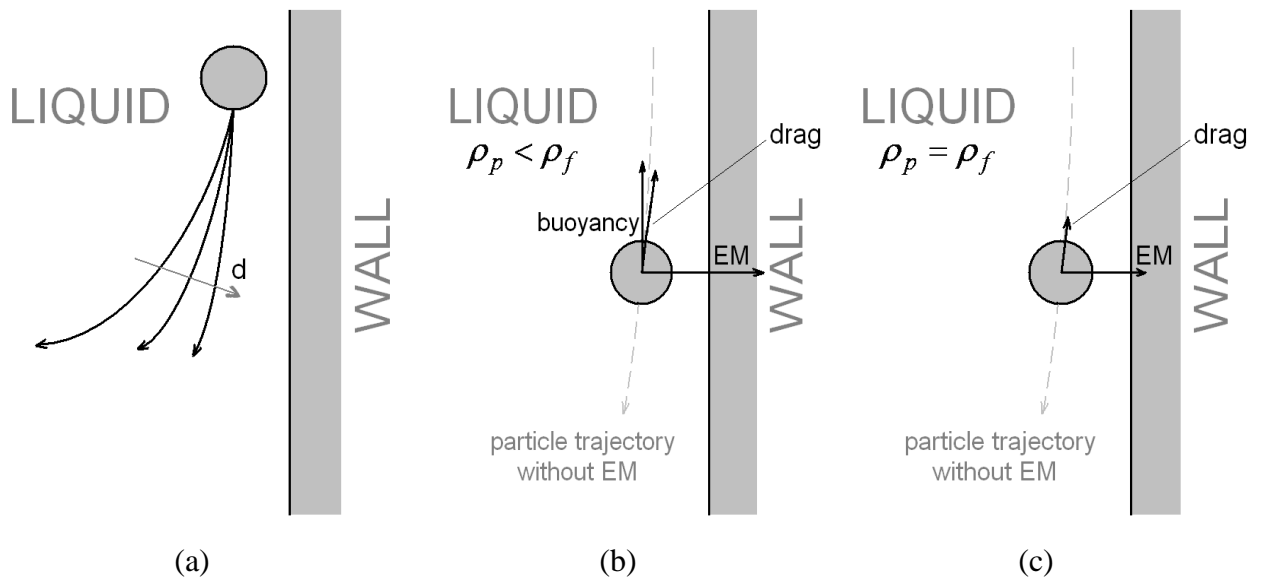


Figure 5.22: (a) simplified trajectories of the particle on the lower border of the upper mean eddy near the wall for cases with different diameters (the arrow shows the increasing of the diameter); (b), (c) directions of different forces applied to the big particles at $S > 1$ ($\rho_p < \rho_f$) and $S = 1$ ($\rho_p = \rho_f$) respectively.

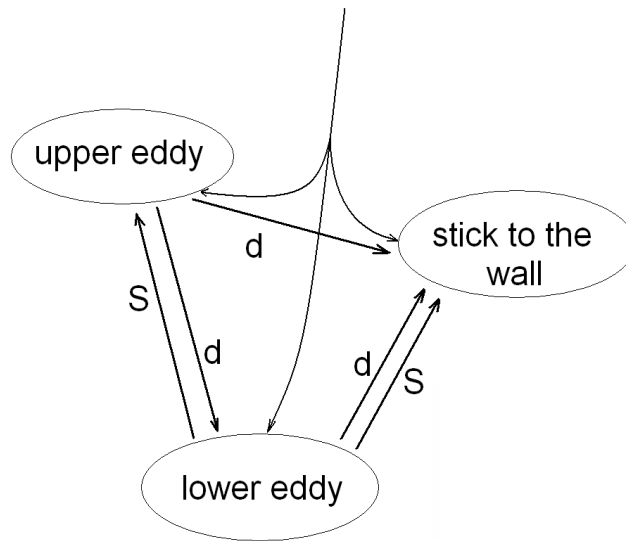


Figure 5.23: Possible ways for the particles after coming to the middle zone near the wall and the changes in the probability to choose one of the ways with respect to the particle diameter D and $S = \rho_p/\rho_f$. The arrows point to the zone, where the probability increases with the parameter increase over the arrow.

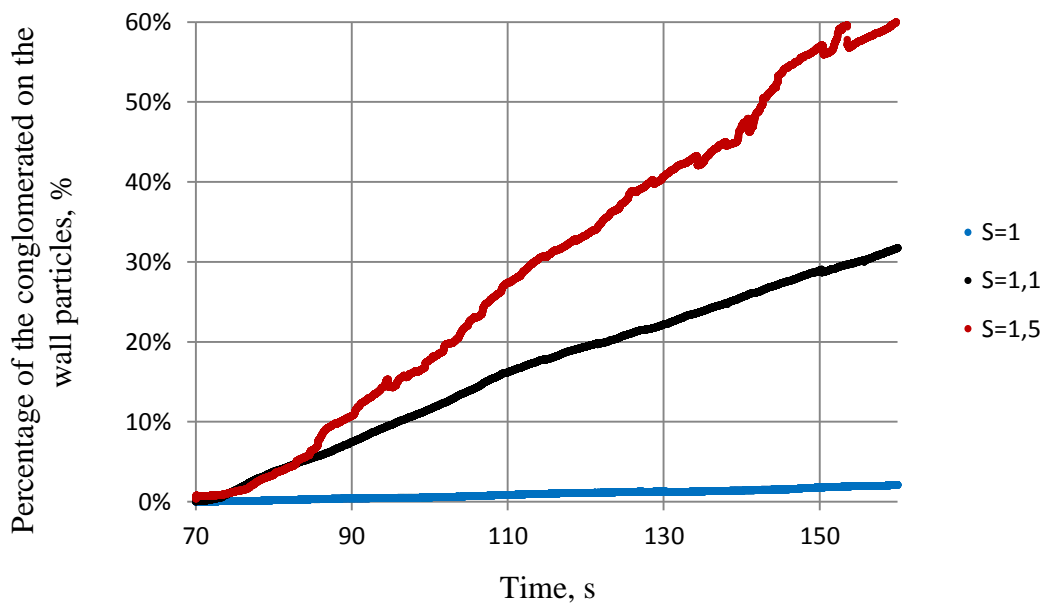


Figure 5.24: Percentage of the 200 μm particles conglomerated on the wall.

Table 5.4: Deposition rate (percentage from the total number of particles per second) of 200 μm particles in ICF-1.

S	1.0	1.1	1.5
Deposition rate (% per second)	2.2e-2	3.3e-1	6.7e-1

5.4. The dynamics of conglomeration of the inclusions on the wall of ICF

The previous Chapter 5.3.2 explained the phenomenon of the particle agglomeration on the wall of ICF. Moreover, Figure 5.24 demonstrates the monotonous increase of number of the particles, which are removed from the flow and form conglomerations at the wall. This process is mostly governed by EM force (see the Chapter 5.3.2). As far as the process is already generally described, this chapter will focus on the area distribution of the conglomerated particles and the migration of them on the wall.

Figure 5.25 demonstrates the time-dependent axial distribution of the particles conglomerated on the wall (the angularly averaged results) in ICF-1. The rows correspond to the cases of different particle density; the columns correspond to a different rate of semi-soft collision (see the Chapter 3.3.4). The figure shows that the particles start to form conglomeration on the wall at approximately 4th second from the beginning of the particle motion from the top surface. According to the flow pattern (Figure 2.4) the zone of the maximal concentration of conglomerated particles slips down in the direction to the middle zone of the crucible. However, it is shown on Figure 5.25 that the conglomerated particles mostly remain in the upper part of ICF. This fact corresponds to qualitative experimental observation, which is shown on Figure 4.7 and is expected due to the liquid-to-particle density ratio $S > 1$.

The theoretical modification of ICF-1, where magnitude of EM force in Navier-Stokes equation and the Lagrange equation is artificially decreased 2 times (such modification will be named further ICF-1A), was investigated in order to analyze the influence of the force on the particle conglomeration process. Obviously, the lower EM force is produced by the lower current in the inductor. The lower force in ICF-1A induces the motion of the conductive liquid with the lower velocity. However, at the same time the force pushes the non-conductive particles with the 2 time less effort that in the case of ICF-1A. As it was mentioned in the previous subchapter, drag force, which is proportional to velocity of the particle, competes with EM force in order to carry out stirring and prevent conglomeration process. Figure 5.26 shows the axial distribution of conglomerated particles in ICF-1A. It is clearly shown that the common process develops like in ICF-1 (Figure 5.25), however, the maximum of the concentration is slipping down more slowly than it is expected, due to lower velocity magnitude. The mentioned figures also show that the maximal value of the concentration decreases from ICF-1 to ICF-1A in the case of $S > 1$. Thus, the conglomeration process decelerated with the decrease of current (and, consequently, magnitude of EM force). That means that the direct influence of EM force on the non-conductive particles is stronger than indirect influence through the flow intensity.

Figure 5.25 and Figure 5.26 shows that the conglomeration process remains more or less the same for different particle-wall collision rate ($\varepsilon = \mu$). However, the number of the conglomerated particles insignificantly increase with the increase of $\varepsilon = \mu$ (harder collision) – see Figure 5.27.

Figure 5.28 helps to analyze the dynamics of axial distribution of conglomerated particles. In the case of liquid-to-particle density ration $S = 1.0$ (Figure 5.28 a) the curve of axial distribution change it single-pick shape to multi-pick after the 10th second from the beginning of stirring. The second pick also appears on Figure 5.28 b ($S = 1.1$), however, magnitude of this pick is much less than of the main one. The case $S = 1.5$ (Figure 5.28 c) also confirms the multi-pick shapes. Such multi-pick axial distribution can be also recognized on Figure 5.25 and Figure

5.26. It means that the particles are delivered to the wall in discrete portions. The time between these portions is approximately equal to the turnover of the mean vortex.

Finally, Figure 5.29 compares the axial distribution of the conglomerated particles of different density at the 18th second in ICF-1 and ICF-1A (the concentration is represented on the logarithmic scale). This figure shows that the maximum of concentration shifts to the top surface with increase of S (decrease of particle density).

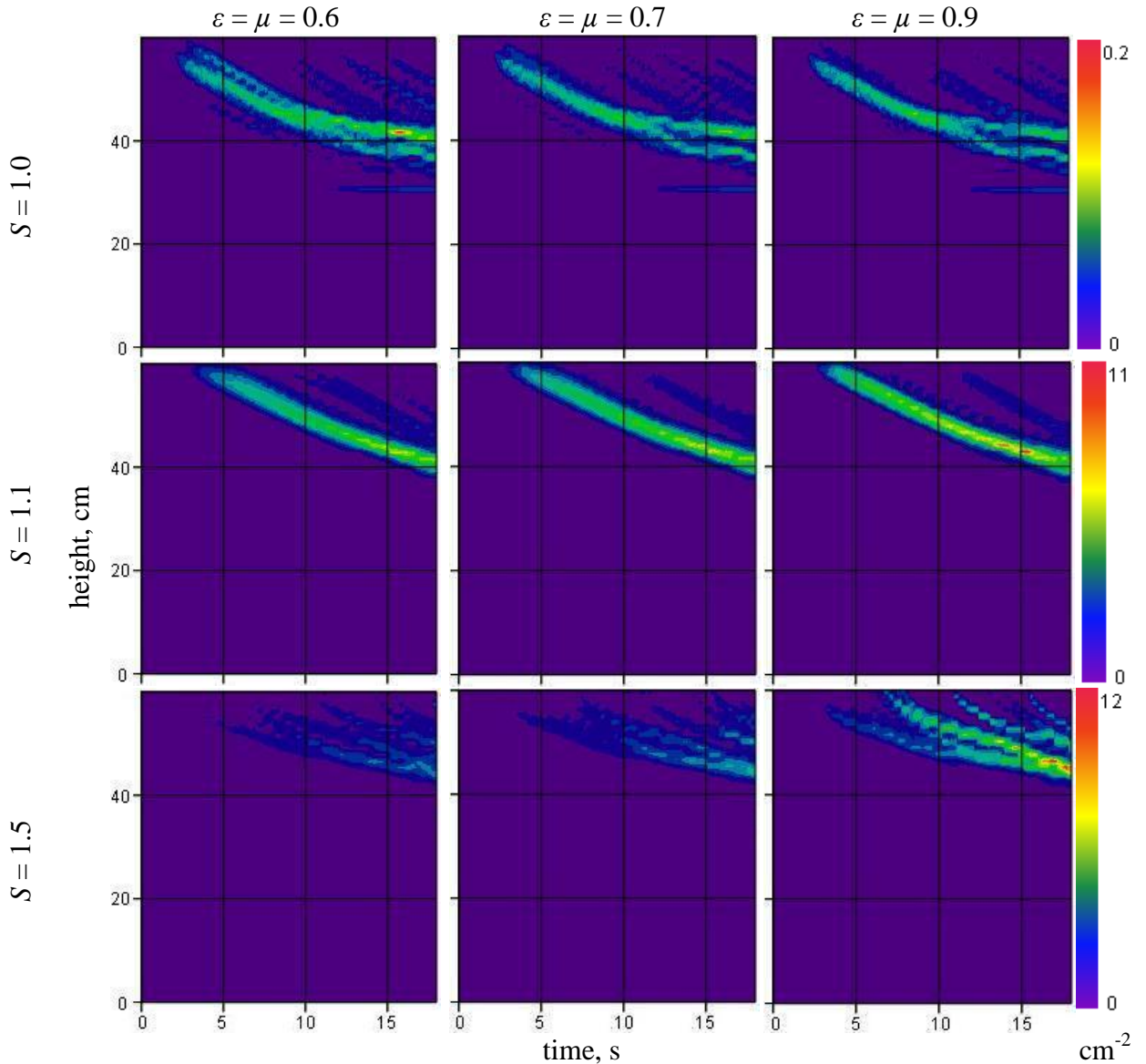


Figure 5.25: Axial distribution of surface concentration (cm^{-2}) of the conglomerated on the wall $300 \mu\text{m}$ particles in ICF-1. The columns correspond to a different softness of particle-wall collisions (the coefficients, which characterize the rate of semi-soft collision $\varepsilon = \mu$ are defined in Chapter 3.3.4). The rows correspond to different liquid-to-particle density ratio S . The results are angularly averaged.

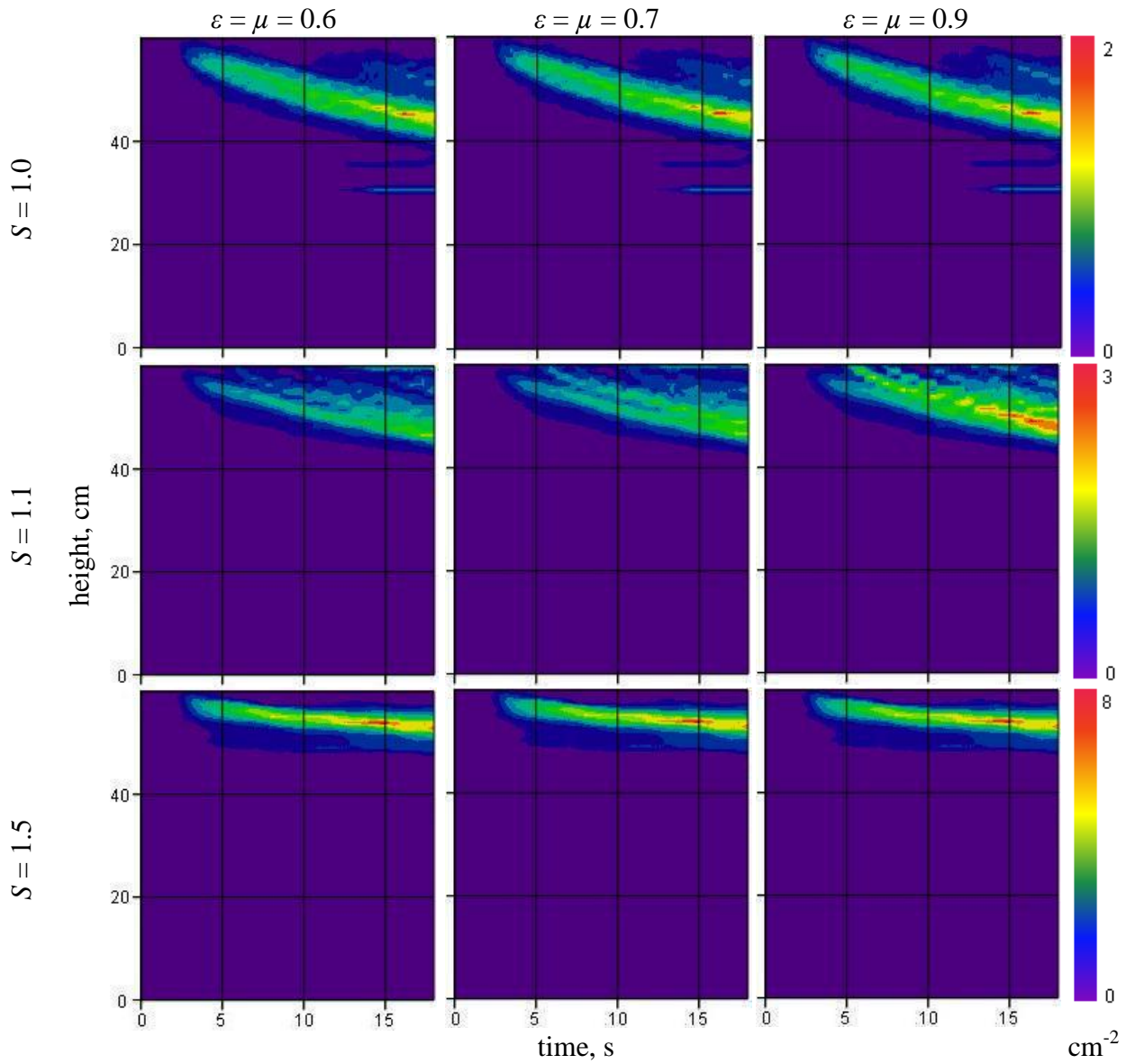


Figure 5.26: Axial distribution of surface concentration (cm^{-2}) of the $300\ \mu\text{m}$ particles conglomerated on the wall in ICF-1A. The columns correspond to a different softness of particle-wall collisions (the coefficients, which characterize the rate of semi-soft collision $\varepsilon = \mu$ are defined in the Chapter 3.3.4). The rows correspond to different liquid-to-particle density ratio S . The results are angularly averaged.

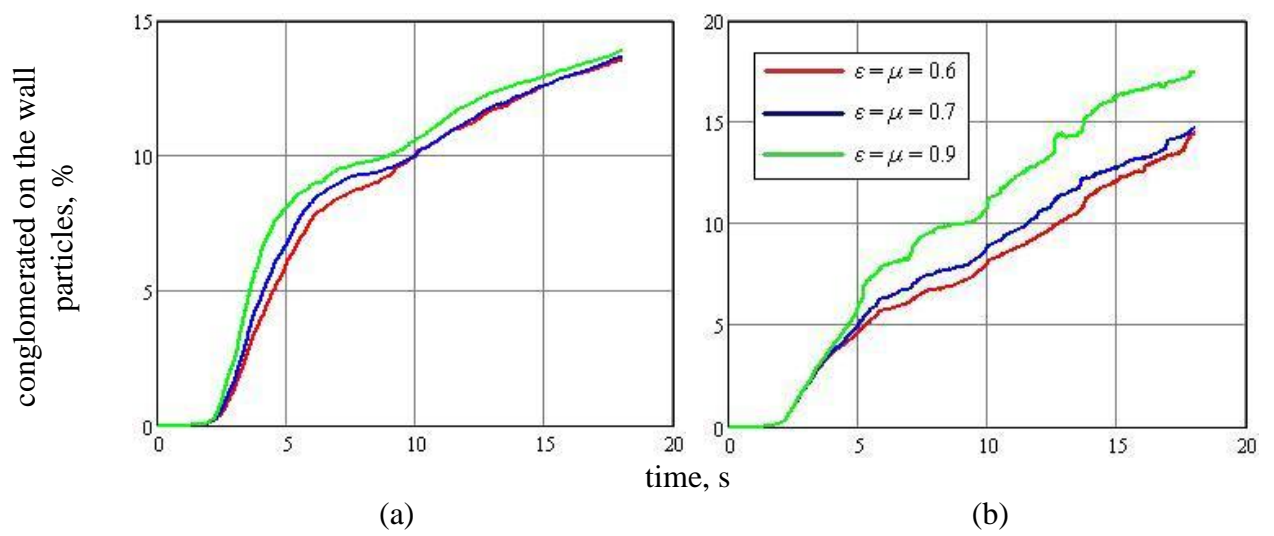


Figure 5.27: Percentage on the conglomerated 300 μm particles on the wall for different coefficients of semi-soft collision. $S = 1.1$. (a) ICF-1; (b) ICF-1A.

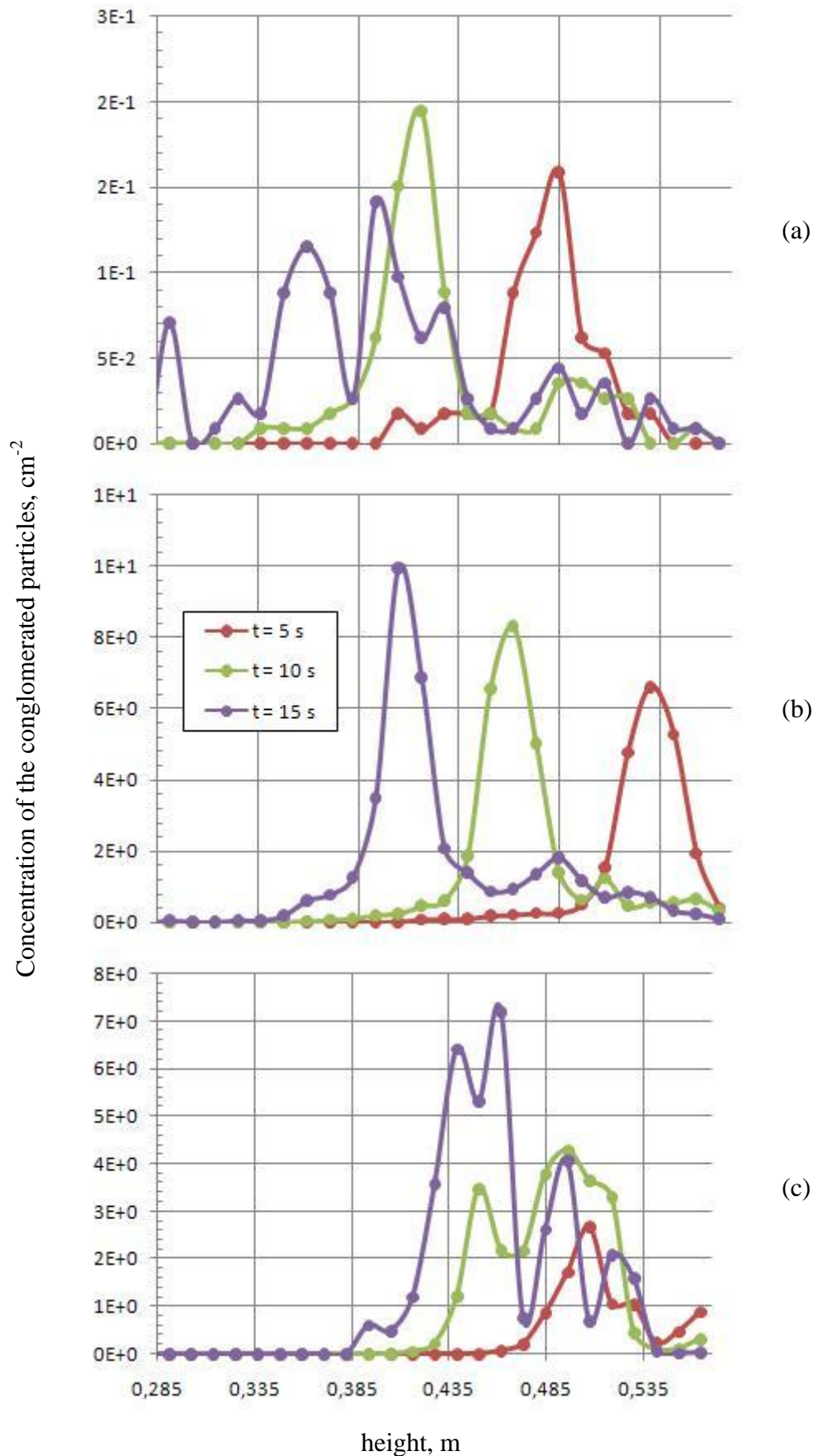


Figure 5.28: Dynamics of the axial distribution of concentration of the conglomerated $300 \mu\text{m}$ particles (the upper part of the crucible). (a) $S = 1.0$; (b) $S = 1.1$; (c) $S = 1.5$. The coefficients of semi-soft collision $\varepsilon = \mu = 0.9$. The results are angularly averaged.

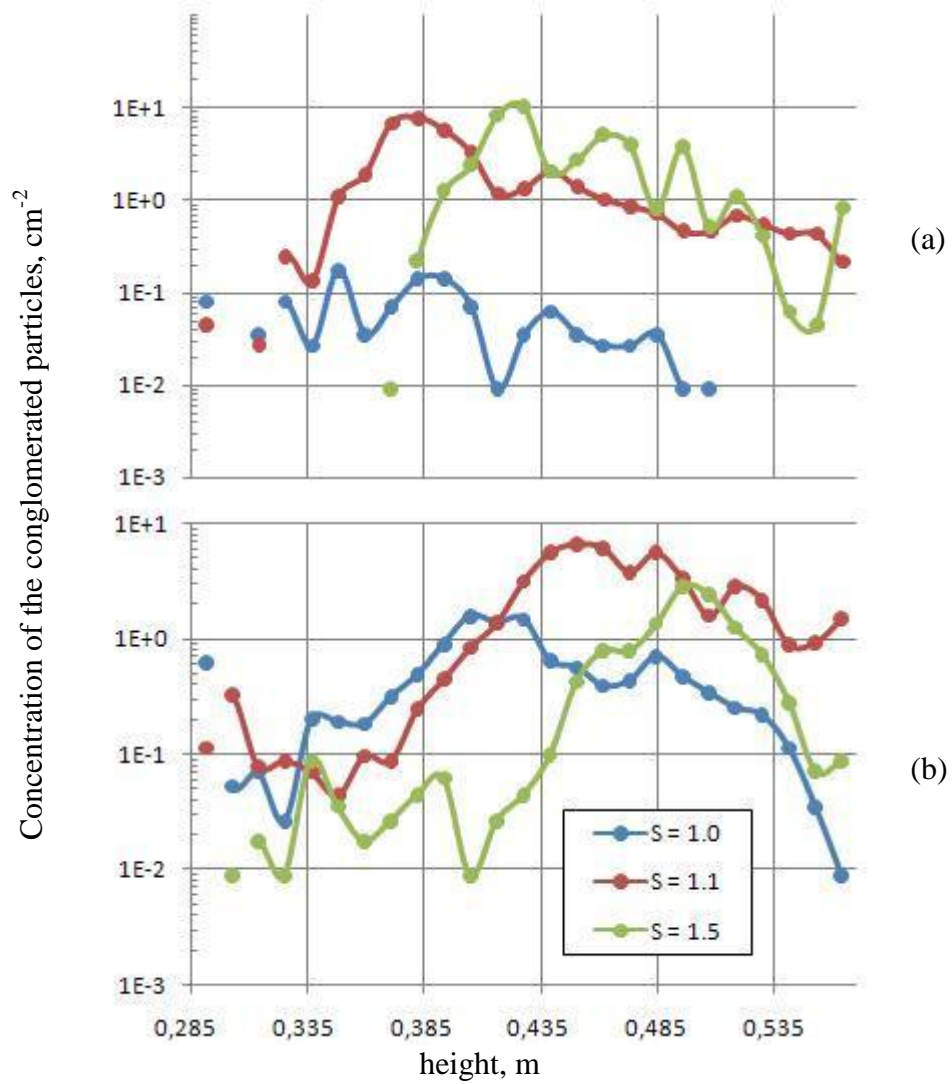


Figure 5.29: Axial distribution of the concentration of the conglomerated 300 μm particles (the upper part of the crucible) at the 18th second from the beginning of stirring. (a) ICF-1; (b) ICF-1A. The coefficients of semi-soft collision $\varepsilon = \mu = 0.9$. The results are angularly averaged.

6. Estimation of the growth of inclusions in the bulk of the flow and their deposition during the long-term operation of the furnaces

The chapters above dealt with transportation of solid inclusions of constant size in ICF. The relevant numerical model was proposed, verified and applied for investigation of different aspects of particle transportation processes in the turbulent recirculated flow in ICF. Moreover, it has already been discussed in the Chapter 2.2 that such flow in ICF is a typical example of the turbulent recirculated flow class that characterizes the melt motion in induction furnaces (ICF, CIF, cold crucible induction furnace and levitating droplet technology). That means that the model presented in the Chapter 3 is relevant for the simulation of all of the mentioned melting and stirring equipment. However, the solution of the specific problems of the particular types of furnaces often needs additional models of a particle behaviour. As it was discussed in the Chapter 1.1 the urgent problem during a long-term operation of CIF is connected with the deposition formation process. This phenomenon and the proper extension of a particle transportation model will be discussed within this chapter.

It was pointed out in the Chapter 5.3.2 that the rate of deposition process due to EM force increases with the increase of the size of particles. Relatively large particles, apparently, cannot form dense structure; the agglomeration of such inclusions creates the matter with pores or sponge like build up formation. Therefore, the hypothesis can be put toward that the sponge like deposition (see Figure 1.1) if fulfilled by agglomeration of the large particles, which are previously grown in the bulk of a melt, on the wall and with another particles, which are kept at the wall by EM force.

The present chapter will analyze two mentioned processes: the size evolution of inclusions in the bulk of the melt and their agglomeration by the wall or with other particles. However, many phenomena can influence the mentioned processes, but it is not the goal of the present thesis to describe them all. E.g., the growth of inclusions can be fulfilled by diffusion, collisions, oxidation etc. The present chapter will not describe the chemical oxidation phenomenon, but it will limit the discussion with diffusion and collision models.

Moreover, the mentioned deposition processes, as it can be observed on Figure 2.7, is slow, the characteristic time of them is much longer than the time of the particle transportation processes that are described above (see, e.g. time of the homogenization in ICF-1 in Table 5.3). As far as the proposed LES-based particle tracking model is time consuming, it is not possible to couple it directly with size evolution and deposition and obtain significant results. Some summarization and generalization of tracking results should be done before the next step. However, such aim can be defined only as the further extension of the present investigation and goes significantly beyond of the declared objectives of the thesis. Therefore, the estimation of the mentioned processes will be done within this chapter. Nevertheless, this estimation will give the chance to evaluate and analyze the processes that can lead to the sponge-like deposition in the channel of CIF, and it will forecast the deposition rate.

6.1. Size evolution of oxide inclusions in the bulk of the melt

6.1.1 Theoretical description

Two different processes, which can lead to a size evolution of particles, will be analyzed below:

- the diffusion-limited Ostwald ripening (*Ostwald, 1897*),
- the collisions of the particles and clustering.

Ostwald ripening is the process of the dissolution of small particles and the redeposition of the dissolved material on the surfaces of larger particles. This thermodynamically-driven spontaneous process occurs because larger particles are more energetically favored than smaller particles. The system tries to lower its overall energy so molecules on the surface of a small particle will diffuse into the solution. When all small particles do this the free atoms in the solution are supersaturated and condense on the surface of larger particles. Therefore, all smaller particles are shrinking, while larger particles are growing, and overall the average size will increase. After an infinite amount of time, the entire population of particles will become one, huge, spherical particle to minimize the total surface area. But due to EM force this asymptotical state will be not achieved and the particles with an arbitrary size will be removed from the melt by deposition on the wall.

Lifshitz & Slyozov (1961) performed a mathematical investigation of the Ostwald ripening. Steady-state volume concentration C_R close to the surface of a particle depends on the radius R as follows:

$$C_R = C_\infty + \frac{\alpha}{R}, \quad \alpha = \frac{\sigma}{kT} V_a C_\infty,$$

where C_∞ is the concentration of saturated solution, σ is the surface tension, $k=1.38e-23$ J/K is the Boltzmann constant, T is temperature, V_a is the volume of the atom of the dissolved substance.

Assuming supersaturation rate $\Delta = C - C_\infty \ll 1$ (C is the particular volume concentration of the impurities), we can express the diffusion flow of the dissolved substance per area unit as follows:

$$j = D \left. \frac{\partial C}{\partial r} \right|_{r=R} = \frac{D}{R} (C - C_R) = \frac{D}{R} \left(\Delta - \frac{\alpha}{R} \right), \quad (6.1)$$

where D is diffusion coefficient. Consequently,

$$\frac{dR}{dt} = \frac{D}{R} \left(\Delta - \frac{\alpha}{R} \right). \quad (6.2)$$

When the radius of the particle is equal to its critical value $R_{cr} = \alpha/\Delta$ (the solution of the stationary equation), the particle is in the tranquility with the solution. If $R > R_{cr}$, a particle grows, otherwise dissolves. We should underline that Δ and consequently R_{cr} is changing in time as the function of temperature and concentration. However, the changes of a particle size should be calculated within each step of time, which is used for the calculation of hydrodynamics, temperature and concentration fields. Thereby, by assuming $R(t=0) = R_0$, the author of this thesis obtained the solution of differential equation (6.1) for instant Δ and R_{cr} :

$$t \cdot D \Delta = \frac{R^2 - R_0^2}{2} + R_{cr} \cdot (R - R_0) + R_{cr}^2 \cdot \ln \frac{R - R_{cr}}{R_0 - R_{cr}}$$

or the same in non-dimensional form:

$$t \cdot \theta = (r - 1) \left(\frac{r+1}{2} + r_{cr} \right) + r_{cr}^2 \cdot \ln \frac{r - r_{cr}}{1 - r_{cr}}, \quad (6.3)$$

where $r = R/R_0$, $r_{cr} = R_{cr}/R_0$ and $\theta = D \Delta/R_0^2$. Figure 6.1 shows the solution of equation (6.3). Only $r < 1$ solution is meaningful, if $r_{cr} > 1$, and only $r > 1$ otherwise. This means that the particle, which is larger than critical one, will grow, and dissolve otherwise. As far as $f(r)$, which stands for the right part of equation (6.3), is monotonous, the Newton method can be used to solve the equation $f(r) - \theta t = 0$.

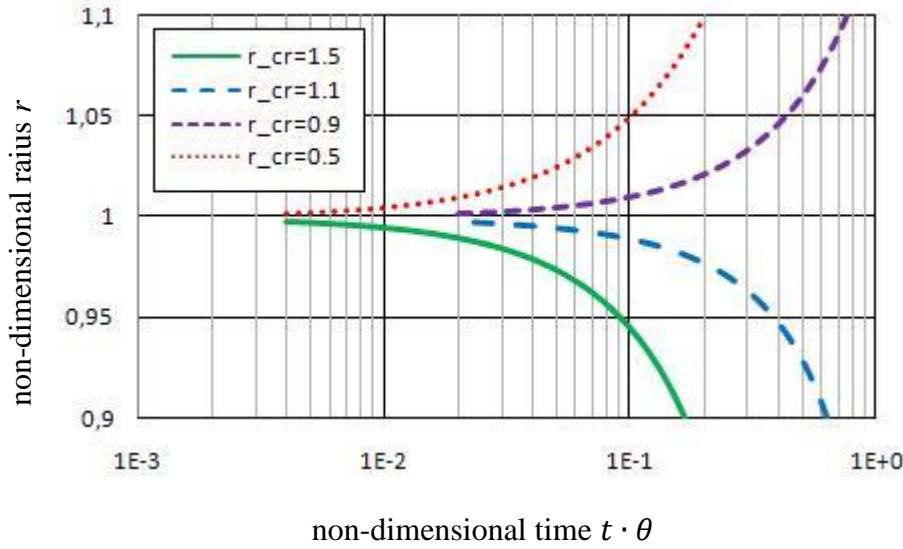


Figure 6.1: The diffusion limited growth / dissolution of a particle, assuming instant supersaturation rate Δ and the critical radius R_{cr} . Non-dimensional radius r depending on non-dimensional time ($t \cdot \theta$) for different non-dimensional critical radius r_{cr} .

For the particular inclusions $R_{cr} = \alpha/\Delta = (\sigma V_a C_\infty)/(kT\Delta)$ and $\theta = D \Delta/R_0^2$ can be estimated through the expression for saturation concentration (Bethers et al., 1994)

$$C_\infty(T) = \frac{\rho_{melt}}{\rho_{incl}} \left(1 + e^{\frac{\varepsilon}{RT}}\right)^{-1}, \quad (6.4)$$

where ρ_{melt} and ρ_{incl} are density of the melt and solid inclusions respectively, $R = 8.31 \text{ J}/(\text{mol} \cdot \text{K})^{-1}$ and bounding energy ε can be calculated using the thermodynamic expression (Bethers et al., 1994)

$$\varepsilon = \varepsilon_{incl}^f + \varepsilon_{incl}^v - \sqrt{\varepsilon_{incl}^v \cdot \varepsilon_{melt}^v}, \quad (6.5)$$

where ε_{incl}^v and ε_{incl}^f are inclusion's enthalpy of vaporization and enthalpy of fusion respectively, ε_{melt}^v is the metal's enthalpy of vaporization. Diffusion coefficient D can be found out following the Stokes-Einstein estimation (Einstein, 1906).

For the estimation of the significance of the particle collision we will follow the model, presented by Toh et al. (2007). As the equation of agglomeration phenomena, following relations are chosen by neglecting the term of velocity fluctuation which has a scarce contribution:

$$N_{ij}^T = 1.3\alpha_T \left(\frac{d_i+d_j}{2}\right)^3 \sqrt{\frac{\rho_f E}{\mu}} \cdot n_i n_j, \quad \alpha_T = 0.727 \cdot \left[\frac{\mu}{A} \left(\frac{d_1}{2}\right)^3 \sqrt{\frac{\rho_f E}{\mu}}\right]^{-0.242}, \quad (6.6)$$

$$N_{ij}^S = \frac{2\pi\Delta\rho g}{9\mu} \cdot (d_i + d_j)^3 \cdot \left|\frac{d_i-d_j}{2}\right| \cdot n_i n_j, \quad (6.7)$$

$$N_{ij}^B = \frac{2kT}{3\mu} \left(\frac{1}{d_i} + \frac{1}{d_j}\right) (d_i + d_j) \cdot n_i n_j, \quad (6.8)$$

$$N_{ij} = N_{ij}^T + N_{ij}^S + N_{ij}^B, \quad (6.9)$$

where N_{ij} represents the collision frequency per unit of time and volume (the suffices T, S and B represent turbulent, Stokes and Brownian terms), $\Delta\rho$ is the density difference between liquid metal and inclusions, d_i and d_j are the diameters of inclusions, μ is the dynamic viscosity of

liquid metal, E is turbulent energy dissipation rate, n_i and n_j are number of inclusions per unit volume, $A = 0.45e-20$ J is the Hamaker constant (*Taniguchi & Kikichi, 2000*).

6.1.2 Estimation of the size evolution rate

Let us estimate now the typical time of the growth / dissolution of the inclusions in the steel melt. We can assume aluminium oxide (Al_2O_3) as a typical inclusion. This material is usually about 65% of all inclusions in the steel melt in CIF. Moreover, other less distributed inclusions, such as magnesium oxide (MgO) and silicon oxide (Si_2O), have close physical properties. Table 6.1 displays the time to double a particle volume (in the case of dissolution – decrease the volume 2 times). The table shows that small particles (less than $0.1 \mu m$) change their size mostly due to the Ostwald ripening process. Contrary, the turbulent collisions influence the growth of bigger particles. However, the typical time of the collision growth of bigger particles can be underestimated, because of probably overestimation of the concentration, which can result from the assumption of the equal concentration of each size group.

Table 6.1 estimated the growth and the dissolution of the particles for different values of the relative supersaturation. Let us estimate now this value at two scenario, which are favorable for the growth of the inclusions in CIF and, consequently, for the sponge-like build-up formation.

The first scenario simulates the change of the temperature regime of the CIF operation. The power of the furnaces is decreased for weekends or night time, when the production process is temporarily interrupted. The supersaturation of the dissolved inclusions can appear as the difference between the saturated concentration at the temperatures of the working and weekend regimes due to the quick change of the temperature of the melt. If we assume that the temperature is changed from 1883 K (100 K above the melting point of the steel) to 1823 K (40 K above the temperature of solidification), than we can calculate the relative supersaturation: $\Delta/C_\infty = 0.472$. Table 6.2 shows the estimation of the time, which is necessary to double the volume of a particle according to this scenario. If we assume the weekend period about $2.2e+5$ s, it becomes evident that described processes can significantly increase the size of the inclusions and, consequently, favor the porous clogging. Turbulent collisions will drive this process, if the concentration of bigger particles is enough, but at the opposite case the particles will grow also within the Ostwald model. Moreover, due to the Ostwald ripening the smallest inclusions will rapidly achieve the size, when collision model gives significant results. Therefore, the tracing of the inertia particles in CIF should be done, coupling it with the size evolution model. The authors plan to carry out this simulation soon.

The second scenario describes the growth of a particle, travelling along the channel of CIF (Figure 6.2). *Baake et. al (2010)* simulated the temperature distribution in CIF and found the melt in the channel overheated for at least 34 K in respect to the melt temperature in the bath. Taking into account the low velocity of the transit flow in the channel, the time, when a particle migrates along the channel, can be estimated as 1 min (*Pavlovs et al., 2011*). Assuming the linear distribution of the temperature along the channel (from the maximum in the lowest point and the minimum at the throat - Figure 6.2), we can estimate the growth of the particle – the results are shown on Table 6.3. The growth of particles according to this scenario is not so significant as it is at the first scenario, however, the coupling of them can give more precise results of the neck clogging.

Table 6.1: Time necessary to change twice the volume of a Al_2O_3 particle in a steel melt. Comparison of the collision and the Ostwald ripening models. Presented results are calculated for 215 kW CIF, assuming the homogeny distributed inclusions with the common volume concentration 1%, the concentration of particles in the each size group is assumed equal. The degree of turbulent energy dissipation rate E is calculated equal to $1\text{e-}2 \text{ m}^2/\text{s}^3$.

The temperature of the melt is **100 K over the melting temperature** of steel

Diameter of particles, m	Collision model time, s	The Ostwald ripening					
		Relative supersaturation Δ/C_∞					
		1e+0		1e-1		1e-2	
		process	time, s	process	time, s	process	time, s
1e-8	-	growth	2.82e-3	dissolution	6.45e-3	dissolution	4.50e-3
1e-7	1.42e+0	growth	2.18e-1	growth	2.82e+0	dissolution	6.45e+0
1e-6	2.00e+1	growth	2.13e+1	growth	2.18e+2	growth	2.82e+3
1e-5	2.03e+1	growth	2.13e+3	growth	2.13e+4	growth	2.18e+5
1e-4	2.03e+1	growth	2.13e+5	growth	2.13e+6	growth	2.13e+7

The temperature of the melt is **40 K over the melting temperature** of steel

Diameter of particles, m	Collision model time, s	The Ostwald ripening					
		Relative supersaturation Δ/C_∞					
		1e+0		1e-1		1e-2	
		process	time, s	process	time, s	process	time, s
1e-8	-	growth	4.16e-3	dissolution	9.50e-3	dissolution	6.61e-3
1e-7	1.42e+0	growth	3.21e-1	growth	4.16e+0	dissolution	9.50e+0
1e-6	2.00e+1	growth	3.14e+1	growth	3.21e+2	growth	4.16e+3
1e-5	2.03e+1	growth	3.13e+3	growth	3.14e+4	growth	3.21e+5
1e-4	2.03e+1	growth	3.13e+5	growth	3.13e+6	growth	3.14e+7

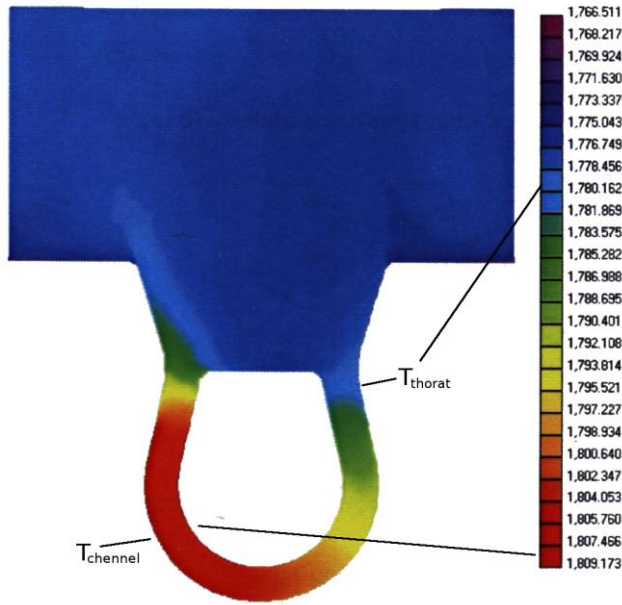


Figure 6.2: Temperature distribution in the central vertical cross-section of 215kW CIF ($^{\circ}\text{K}$). From Kirpo (2008-PhD).

Table 6.2: Time necessary to change twice the volume of a Al_2O_3 particle in a steel melt, assuming the relative supersaturation 0.472, which corresponds approximately to the transitions from working to weekend regime of the CIF operation. The other parameters are the same as in the Table 6.1.

Diameter of particles, m	Collision model time, s	The Ostwald ripening	
		process	time, s
1e-7	1.42e+0	growth	6.99e-1
1e-6	2.00e+1	growth	6.66e+1
1e-5	2.03e+1	growth	6.31e+3
1e-4	2.03e+1	growth	6.28e+5

Table 6.3: The estimation of the increase of a particle after the travel through the channel of CIF. The channel overheat is assumed linearly distributed from the neck to the maximum of 34 K over the neck temperature at the lower point of the channel. The time of the particle travel is assumed equal to 1 min.

Initial radius of the particle R_0 , m	Relative increase of the particle $R/R_0 - 1$
1e-7	3.7e+0
1e-6	1.1e-1
1e-5	1.2e-3
1e-4	1.2e-5
1e-3	1.2e-7

6.2. Agglomeration of the particles with the wall¹

It was already discussed in Chapter 5.4 that the non-conductive inclusions can be pressed to the wall by EM force. If the particle is pressed to the wall or to another particle for the long time, the surface diffusion process can agglomerate them. The present chapter will consider this process theoretically and estimate it in the conditions of induction furnaces.

1. Surface diffusion

Surface diffusion is a general process, which describes the motion of atoms at solid material in order to minimize the overall energy. The surface atom mass flux ζ depends on the chemical potential as follows (*Gomer, 1983*):

$$\zeta = -D_s \frac{\rho_A}{k_B T} \nabla \mu, \quad (6.10)$$

where ρ_A is the surface density of the atoms and D_s is the surface diffusion coefficient. In the isotropic surface energy cases the local chemical potential to become a function of curvature k . This dependence can be described using Gibbs-Thomson equation (*Bakker et al., 1990*):

$$\mu(k) = \mu(0) + \gamma \Omega k, \quad (6.11)$$

where Ω is the atomic volume and γ is the surface tension. The equation for the surface change within the surface diffusion process can be derived from the continuity equation and expressions (6.10, 6.11):

$$v_n = B \Delta_s k; \quad B = \frac{D_s \gamma \rho_A \Omega^2}{k_B T}, \quad (6.12)$$

where v_n is the normal component of velocity of a surface element, and Δ_s is the surface Laplace operator.

The surface diffusion coefficient typically meets the Arrhenius behavior in the case the tunneling effect is negligible (*Seebauer & Allen, 1995*):

$$D_s = D_0 e^{-\frac{E_{diff}}{k_B T}}, \quad (6.13)$$

where D_0 represents pre-experimental factor and E_{diff} is activation energy. The literature studies leads to a significantly wide dispersion of the coefficient's value for Al_2O_3 . The values and references are shown in Table 6.4. Significant difference appears due to different experimental processes, from which the proper values of diffusion coefficients were calculated. The result by *Sajgalik et al. (1987)* (the second row in Table 6.4) was obtained from the direct measurement of the neck growth between Al_2O_3 grains in sintering experiment, therefore, this result will be used for the purposes of the present investigation. Moreover, the values of all experiments in Table 6.4 show that the surface diffusion coefficient at the temperature T_a is 2 - 4 times larger than at T_b . This fact points out that the sintering process is much faster at the operational regime of the furnace.

2. Simulation of the neck growth during the sintering process

This chapter will describe the simulation of the sintering process between the particle and the wall, or a small particle and a big particle. The surface diffusion process, which is governed by equation (6.12), was simulated for two spheres: 20 μm and 2 μm in diameter. One sphere is much bigger than another, therefore, this case can be assumed also equal to the particle-wall

¹ The investigation, presented in this chapter, was carried out together with Mārtiņš Brics, who is a PhD student at the University of Rostock, during his ERASMUS internship at the University of Latvia from November, 2011 till January, 2012.

sintering case. In the beginning of the simulation the particles are connected with the small cylindrical neck with the radius $R_n = 0.2 \mu\text{m}$ and distance between the spheres is $0.04 \mu\text{m}$. The neck like this usually appears due to the collision of the particles and is observed as brittle initial necks of the sintering process (see Figure 6.3). The result of the simulation of the neck growth process is shown on Figure 6.4 a and time dependence of the neck diameter is shown on Figure 6.4 b. First 8 second is the transitional period of the initial neck growth. After that the growth can be approximated with the function

$$D_n(t) = a \cdot (t + t_0)^b, \quad (6.14)$$

where D_n is the diameter of the neck; the coefficients a and b are found by the least square method: $a = (1.4 \pm 0.5) \times 10^{-1} \mu\text{m} \cdot \text{s}^{-b}$, $t_0 = 13 \pm 1 \text{ s}$, $b = (28.4 \pm 0.7) \times 10^{-2}$. The time correction t_0 appears due to the used initial neck in the simulation. As it is shown by *German (1996)*, such approximation of the neck growth can be used till the neck is less than 60% of the particle radius.

Table 6.4: Values of surface diffusion coefficient for Al_2O_3 at the temperatures $T_a = 1748 \text{ K}$ (D_s^a) and $T_b = 1688 \text{ K}$ (D_s^b). The values are calculated according to expression (6.13) using the values of D_0 and E_{diff} from the references mentioned in the last column. The temperatures T_a and T_b correspond to the ordinary and the weekend regimes of CIF operation (see the Chapter 2.5).

$D_0, \text{m}^2/\text{s}$	$E_{diff}, \text{kcal/mol}$	$D_s^a, \text{m}^2/\text{s}$	$D_s^b, \text{m}^2/\text{s}$	reference
4.05e+1	108	1.11e-12	3.67e-13	<i>Gaddipati & Scott (1986)</i>
1.50e+5	124	4.04e-11	1.13e-11	<i>Sajgalik et al. (1987)</i>
1.50e+6	130	7.13e-11	1.87e-11	<i>Maruyama & Komatsu (1975)</i>
2.00e+2	110	3.08e-12	9.96e-13	<i>Huang et al. (1975)</i>
2.38e+1	95	2.80e-11	1.05e-11	<i>Aksaf & Pask (1972)</i>
4.20e+2	118	6.41e-13	1.90e-13	<i>Gupta (1978)</i>

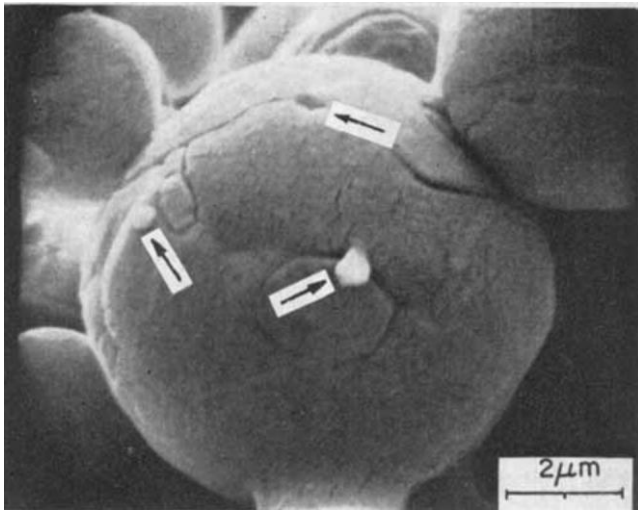


Figure 6.3: The initial stage of sintering of Al_2O_3 balls. The arrows point the tracks of broken initial necks. From *Rao & Culter (1972)*.

Moreover, it is possible to generalize the expression (6.14) for the particular $20 \mu\text{m}$ particle at temperature T_a (see Table 6.4). Expression (6.12) shows that $v_n \sim R \cdot \Delta_s k$ and, as far as the Laplacian of curvature is inversely proportional to the squared radius, $v_n \sim R^{-1}$. At the same time v_n is normal component of the surface element velocity that is a volume change: $v_n \sim R^2 dR/dt$.

Thus, $R(t) \sim t^{-4}$. The same can be derived for the process of the dependence on temperature. Therefore, taking into account (6.13), the expression (6.14) can be generalized as follows:

$$D_n(R, T, t) = 0.139 \cdot R \cdot \left[t \cdot \left(\frac{R_{ref}}{R} \right)^4 \frac{T_a}{T} e^{-\frac{E_{diff}}{k_B} \left(\frac{1}{T} - \frac{1}{T_a} \right)} \right], \quad (6.15)$$

where R_{ref} is the radius of the particle in the reference simulation that is 10 μm , the other quantities are defined in the Chapter 1. Considering the expression (6.15), it can be noted that at the temperature of the channel furnace operation T_a the neck growth 3.7 time faster than at the “weekend” temperature T_b (see the explanation of the temperature regimes of the channel furnace in the Chapter 2.5). The sintering process of the particle with the diameter 20 μm at the temperature T_a will occur 625 times faster than of the 10 μm sphere.

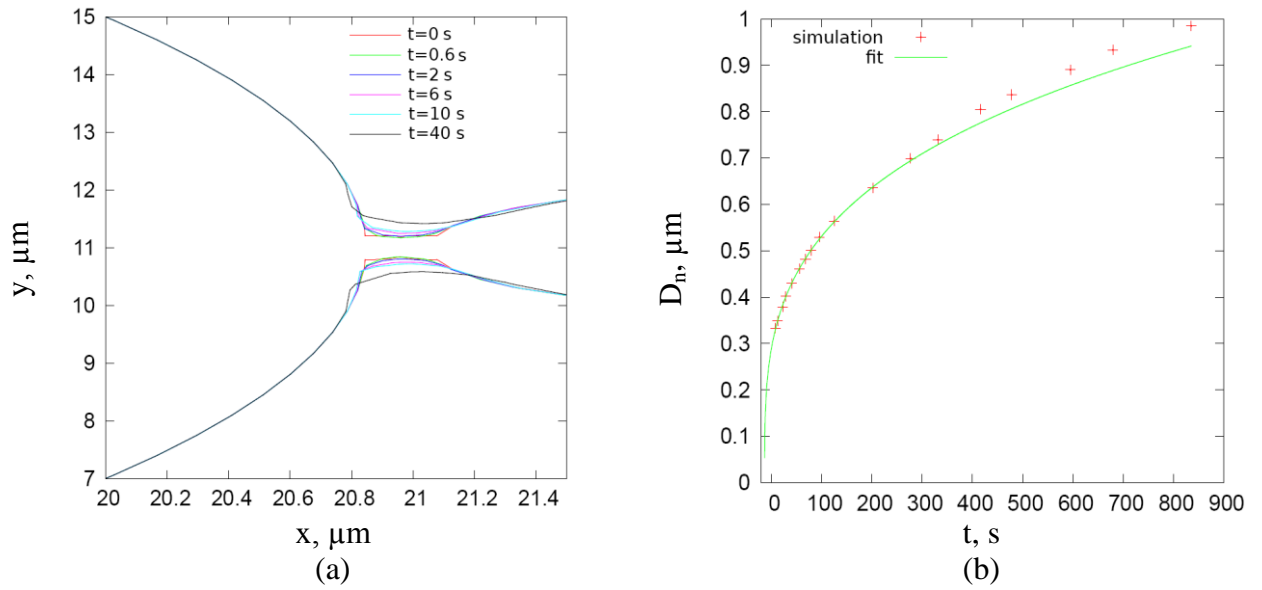


Figure 6.4: Dynamics of the neck growth during the sintering of two spheres: 20 μm and 2 μm in diameter. (a) The cross section in different time moments from the beginning of sintering; (b) The minimal neck diameter as the function of time. The curve is fitted with the function $D_n = a \cdot (t + t_0)^b$. The least square method gave $a = (1.4 \pm 0.5) \text{e-}1 \mu\text{m} \cdot \text{s}^{-b}$; $t_0 = 13 \pm 1$ s; $b = (28.4 \pm 0.7) \text{e-}2$.

3. Sintering of particles to the wall

The previous subchapter described the mechanism and the time dependence of the sintering of the particle to the wall of the same material. However, it is also important to understand how long the particle will be under such conditions, which are favorable for the sintering process. When the solid inclusion touches the wall, the neck between the particle and the wall start to grow due to the surface diffusion effect. However, the flow still influences such inclusion. If all forces acting on the particle are compensated by elasticity force between the particle and the neck and the stress does not achieve the critical value than the neck is continuing to grow until the sintering process will completely integrate the inclusion into the wall, otherwise, the flow will break the neck.

The following forces influence the attached particle: buoyancy force $F_{buoyancy}$, EM force F_{EM} , flow drag force F_{drag} and lift force F_{lift} . The elasticity between the neck and the particle F_{elast} compensates all mentioned forces, therefore, let us sum them:

$$\mathbf{F}^{ext} = \mathbf{F}_{buoyancy} + \mathbf{F}_{EM} + \mathbf{F}_{drag} + \mathbf{F}_{lift}. \quad (6.16)$$

The neck breaks when the stress exceeds the critical value σ_{break} . The total stress can be assumed as the superposition of bend and stretch stresses (σ_{bend} and σ_{stretch} respectively), which act in tangential and normal directions to the wall surface respectively. Taking into account this superposition let us define unity vectors in tangential (\mathbf{e}_{\parallel}) and normal (\mathbf{e}_{\perp}) directions and separate \mathbf{F}^{ext} :

$$F_{\parallel}^{\text{ext}} = \mathbf{F}^{\text{ext}} \cdot \mathbf{e}_{\parallel}; \quad \mathbf{e}_{\perp} = \frac{\mathbf{F}^{\text{ext}} - F_{\parallel}^{\text{ext}} \mathbf{e}_{\parallel}}{|\mathbf{F}^{\text{ext}} - F_{\parallel}^{\text{ext}} \mathbf{e}_{\parallel}|}; \quad F_{\perp}^{\text{ext}} = \mathbf{F}^{\text{ext}} \cdot \mathbf{e}_{\perp},$$

$$\sigma_{\text{stretch}} = \frac{F_{\parallel}^{\text{ext}}}{\pi R_n^2}; \quad \sigma_{\text{bend}} = \frac{4|F_{\perp}^{\text{ext}}|R}{\pi R_n^3}.$$

The expression for bend stress is proposed following the Euler-Bernoulli beam theory (*Gere & Timoshenko, 1996*).

The critical values for compressive and tensile strength for Al_2O_3 are found in *Shackelford & Alexander (2001)* handbook – see Figure 6.5.

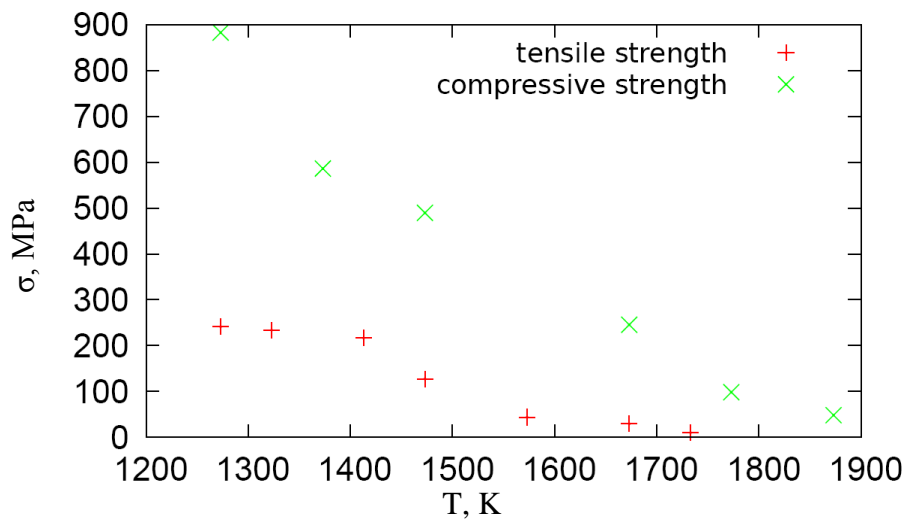


Figure 6.5: Compressive and tensile strength for Al_2O_3 at different temperatures. From *Shackelford & Alexander (2001)*.

The buoyancy and EM force in expression (6.16) can be calculated as they are defined in the Chapter 3.2.2, however, the drag and lift forces at the wall will have another expressions. Lift force for an attached particle is defined by *Leighton & Acrivos (1985)*:

$$\mathbf{F}_{\text{lift}} = 0.576 \cdot Re_G \mu \dot{\gamma} d^2 \mathbf{e}_{\parallel}, \quad (6.17)$$

where $Re_G = \dot{\gamma} d^2 / \nu$ is shear Reynolds number, $\dot{\gamma}$ stands for the shear rate. *Cherukat & McLaughlin (1994)* proposed another expression for such case, however, in the case of negligible neck length it becomes the same as the expression (6.17). Drag force can be defined as in *O'Neill (1968)*:

$$\mathbf{F}_{\text{drag}} = 8.025 \cdot \mu \dot{\gamma} d^2 \frac{\mathbf{u}_f}{|\mathbf{u}_f|}. \quad (6.18)$$

Expressions (6.17) and (6.18) are valid only for $Re_G \ll 1$, therefore $F_{\text{lift}} \ll F_{\text{drag}}$ at the wall. Thus, the neck breaks mostly due to drag force.

Taking into account the flow properties in 215 kW CIF (*Kirpo, 2009-PhD*), the forces in (6.16) can be estimated in the lower point of channel and near the neck of the mentioned CIF, as these points corresponds to the maximal and minimal values of the forces. The results are shown on Table 6.5. Then taking into account values of the critical tress (Figure 6.5), the critical

thickness of the sintering neck is calculated (see Table 6.6). The sintering time, which is necessary to achieve the critical thickness of the neck, is calculated using the sintering model (6.15). Analyzing the dynamics of the sintering process in CIF and the critical value of the neck thickness, it can be concluded that the particles with the diameter of approximately 10 μm can be easily sintered to the wall in CIF. The affectivity of sintering of larger particles depends on the flow conditions, therefore, should be analyzed in the transient simulation.

Table 6.5: Estimation of the forces acting on the attached to the wall Al_2O_3 particle in 215 kW CIF (N/m^3). Drag and lift forces depend on the particle size, therefore, they are given in respect to the particle radius in the reference case (10 μm) for better comparison with other forces.

	minimal value	maximal value
Buoyancy force		$3.0\text{e}+4$
EM force	$3.6\text{e}+4$	$1.6\text{e}+5$
Drag force	$1.1\text{e}+6 R_{\text{ref}}/R$	$1.1\text{e}+7 R_{\text{ref}}/R$
Lift force	$6.2 R/R_{\text{ref}}$	$6.2\text{e}+2 R/R_{\text{ref}}$

Table 6.6: The minimal thickness of the sintering neck normalized to the particle size R_n^{break}/R and time to growth to critical thickness t_{sint} (according to the model (6.15)) in the channel of CIF.

	minimal value	maximal value
R_n^{break}/R	0.8%	1.7%
$t_{\text{sint}}, \text{S}$	$6.2\text{e}-3 (R/R_{\text{ref}})^4$	$3.1\text{e}-2 (R/R_{\text{ref}})^4$

7. Summery

The thesis contains several innovations, which determine the scientific importance of the present work.

- 1) The LES based Euler-Lagrange model in the limit of dilute conditions is created and the work proved that it is able to describe the dynamics of the solid inclusions in the recirculated turbulent flow of liquid metal. The statistical analysis of the forces, which influence the particle motion, showed the necessity to include drag, EM, buoyancy, lift, acceleration and added mass forces in the equation of the particle motion (the Lagrange equation).
- 2) The numerical model, algorithm and specific tools are created on the basis of the open source software *OpenFOAM*. The *solidParticle* library and some others libraries were considerably modified and developed for the goals of the thesis.
- 3) The new experimental technique, which gives a possibility to verify the numerical model experimentally, was proposed in this thesis. It deals with ferromagnetic (iron) particles in the flow of the Wood's metal inside the cylindrical vessel in the solenoid with alternative current.
- 4) The behavior of solid inclusions in the recirculated turbulent flow of liquid metal inside ICF was analyzed using developed mathematical model and experimental technique.
- 5) The analytical model for the prediction of the homogenization time of inclusions in ICF was created, interpolated the results of several simulations for the ICF of laboratory scale. Despite the fact that this model is relevant only for particular ICF, the developed methodology can be applied for industrial furnaces as well.
- 6) Finally, we observed another process of particle behavior – size evolution and deposition. The theoretical investigation stressed two possible physical phenomena, which can lead to the growth of the inclusions: the diffusion limited Ostwald ripening and turbulent collisions and clustering. At the basis of the Lifshitz & Slyozov mathematical model for the Ostwald ripening of the single grain the non-dimensional solution for the case of quasi-instant conditions was obtained within this work, which gives the possibility to estimate the growth process of the inclusions in metallurgical furnaces.

8. Conclusions

- 1) Drag, EM, buoyancy, lift, acceleration and added mass forces should be included in the equation of the particle motion (the Lagrange equation) for the correct description of the dynamics of inertial particles in the considered flows of liquid metal.
- 2) In some conditions the motion of electrically non-conductive particles in liquid metal can be fulfilled by magnetic particles.
- 3) The new experimental technique first time allowed to investigate the behavior of particles in the flow of liquid metal and, thus, verified the mathematical model.
- 4) Turbulent pulsations in the middle zone of the crucible fulfill the homogenization of inclusions in the melt:
 - the particle exchange between the zones of eddies has maxima at the same frequencies as the oscillation of the flow velocity;
 - oscillation of the flow with the higher frequencies does not influence the particles;
 - low frequency pulsations are greater for particles due to their inertia.
- 5) The particles with the liquid-to-particle density rate S close to unity homogenize more rapidly than in the case of $S > 1$ (light particles). The main reason of such trend was found in the force relative proportion in the middle zone of the crucible near the wall.
- 6) Big particles have tendency to stick to the wall due to the relatively large EM force. The rate of such deposition and their axial dynamics depends on liquid-to-particle density ratio.
- 7) Size evolution of particles is significant for the estimation of the deposition rate.
- 8) The average size of the inclusions can significantly increase when the system is switched to another EM regime, e.g., during the weekend reduction of the power. This process can ensure the sponge-like clogging.

9. Outlook

Despite of the models and analysis presented in this thesis, the author realizes that many open questions concerning the behavior of the solid inclusions in the described flow class still remains. The mentioned questions can be separated in two parts: general fundamental questions and engineering investigations.

Thinking about fundamental description of the proper phenomena, we can point two directions, where the new investigations hopefully will appear in the nearest future. It is the experimental investigation of the full dynamics of the particle motion in the flows of liquid metal using the neutron imaging technology. The first steps on this way have already been done by the team of scientists, including the author of this thesis. The second direction is the direct numerical simulation of such flows in the single-phase and two-phase cases. Many research centers have already super computers and clusters that have enough powerful to solve such task. We can imagine that such results can possibly bring a lot of new knowledge about this specific class of turbulence like the LES was brought decade ago.

The investigations for the engineering and industrial proposes were not directly the goal of the present thesis, however, the developed models can be used for the objectives of the optimization of the design of induction furnaces. Nevertheless, the author realizes that it is yet the long way to go to obtain the engineering applicable results in the area of the present investigation. Therefore, the author expresses the hope, that engineers will continue investigations, pay attention and put their knowledge to achieve the industrial results.

References

1. Aksaf, I. A. and Pask, J. A. (1972), Stable and metastable equilibria in the system $\text{SiO}_2\text{-Al}_2\text{O}_3$, *Journal of the American Ceramic Society* 55, pp. 507-512.
2. Aldama, A. A. (1990), Filtering Techniques for Turbulent Flow Simulation, *Lecture Notes in Engineering* 56, Springer-Verlag, New York/Berlin.
3. Alipchenkov, V. M. and Zaichik, L. I. (2004), Statistical model of particle motion and dispersion in an anisotropic turbulent flow, *Fluid Dynamics* 39, pp. 735-747.
4. Antonia, R. A. and Kim, J. (1994), Low-Reynolds-number effects on near-wall turbulence, *Journal of Fluid Mechanics* 276, pp. 61-80.
5. Arneodo, A., Benzi, R., Berg, J., Biferale, L., Bodenschatz, E. et al. (2008), Universal intermittent properties of particle trajectories in highly turbulent flows, *Physical Review Letters* 100, art. no. 254504.
6. Arnol'd, V. I. (1964), Instability of dynamical systems with several degrees of freedom, *Soviet Mathematics, Doklady* 5, pp. 581-585.
7. Baake, E., Jakovičs, A., Pavlovs, S. and Kirpo, M. (2010), Long-term computations of turbulent flow and temperature field in the induction channel furnace with various channel design, *Magnetohydrodynamics* 46, pp. 461-474.
8. Baake, E., Muhlbauer, A., Jakowitsch, A. and Andree, W. (1995), Extension of the k- ϵ model for the numerical simulation of the melt flow in induction crucible furnaces, *Metallurgical and Materials Transactions B* 26B, pp. 529-536.
9. Bakker, H., Bonzel, H. P., Bruff, C. M., Dayananda, M. A., Gust, W., Horvth, J., Kaur, I., Kidson, G., LeClaire, A. D., Mehrer, H. et al. (1990), Diffusion in solid metals and alloys, *Landolt-Börnstein, New Series, Group III* 26.
10. Basset, A. B. (1888), *A treatise on hydrodynamics with numerous examples*, vol. 2, Deighton, Bell and Co.
11. Batchelor, G. K. (1967), *An introduction to fluid dynamics*. Cambridge University Press, Cambridge.
12. Bethers, U., Jakovics, A., Jekabsons, N., Madzulis, I. and Nacke, B. (1994), Theoretical investigation of the conditions of the build-up formation in induction channel furnaces, *Magnetohydrodynamics* 30, pp. 201-210.
13. Bethers, U., Jakovičs, A., Jekabsons, N., Madžulis, I. and Nacke, B. (1995), Modelling of the deposit formation in channel-type induction furnaces, *Magnitnaya Gidrodinamika [Magnetohydrodynamics]* 31 (3-4), pp. 307-315.
14. Biferale, L., Boffetta, G., Celani, A., Lanotte, A. and Toschi, F. (2005), Particle trapping in three-dimensional fully developed turbulence, *Physics of Fluids* 17, art. no. 021701.
15. Böhlen, J.M., Li, K., Dorier, J.L. and Halasz, E. (2011), Advances in the ultra-fast inclusion analysis in steel by spark OES-phenomenology, improvements and calculation of inclusions' composition and size, *CETAS*, pp. 101-108.
16. Bojarevics, A., Bojarevics, V., Gelfgat, Yu. and Pericleous, K. (1999), Liquid metal turbulent flow dynamics in a cylindrical container with free surface: experiment and numerical analysis, *Magnetohydrodynamics* 35, pp. 258-277.

17. Boussinesq, J. (1877), Essai sur la théorie des eaux courantes [The essay for theory of fluids], *MémMémoires présentés par divers savants à l'Académie des Sciences*[Memoirs presented by the various scientists of the Academy of Science] 23 (1), pp. 1–680.
18. Bou-Zeid, E., Meneveau, C. and Parlange, M. (2005), A scale-dependent Lagrangian dynamic model for large eddy simulation of complex turbulent flows, *Physics of Fluids* 17, art. no. 025105.
19. Branover, G. G. and Tsinover, A. B. (1970), *Magnitnaya gidrodinamika neszhimayemyh sred*[Magnetohydrodynamics of incompressible medium]. Nauka, Moscow.
20. Brennen, C. E. (2005), *Fundamentals of multiphase flow*, Cambridge University Press.
21. Brooke, J. W., Kontomaris, K., Hanratty, T. J. and McLaughlin, J. B. (1992), Turbulent deposition and trapping of aerosol at the wall, *Physics of Fluids A* 4, pp. 825-834.
22. Carneiro, J. N. E., Kaufmann, V. and Polifke, W. (2008), Implementation of a moments model in OpenFOAM for polydispersed multiphase flows, *Proceeding of Open Source CFD International Conference*, Berlin, Germany.
23. Carneiro, J. N. E., Kaufmann, V. and Polifke, W. (2009), Numerical simulation of droplet dispersion and evaporation with a moments-based CFD model, *Proceeding of 20th International Congress of Mechanical Engineering*, Gramado, RS, Brazil, November, 15-20.
24. Carneiro, J. N. E., Kaufmann, V. and Polifke, W. (2010), Eulerian simulation of polydisperse flows using a moments model with a relaxation approach for the moment transport velocities, *Proceeding of 7th International Conference on Multiphase Flow*, Tampa, FL.
25. Celani, A. and Vergassola, M. (2001), Statistical geometry in scalar turbulence, *Physical Review Letters* 86, pp. 424-427.
26. Chertkov, M., Pumir, A. and Shraiman, B. I. (1999), Lagrangian tetrad dynamics and the phenomenology of turbulence, *Physics of Fluids* 11, pp. 2394-2410.
27. Cherukat, P. and McLaughlin, J. B. (1994), The initial lift on a rigid sphere in a linear shear flow field near a flat wall, *Journal of Fluid Mechanics* 263, pp. 1-18.
28. Chevillard, L. and Meneveau, C. (2006), Lagrangian dynamics and statistical geometric structure of turbulence, *Physical Review Letters* 97, art. no. 174501.
29. Choi, H., Moin, P. and Kim, J. (1993), Direct numerical simulation of turbulent flow over riblets, *Journal of Fluid Mechanics* 255, pp. 503-539.
30. Choi, H., Moin, P., Kim, J. (1994), Active turbulence control for drag reduction in wall-bounded flows, *Journal of Fluid Mechanics* 262, pp. 75-110.
31. Constantin, P. (2001), An Eulerian-Lagrangian approach for incompressible fluids: local theory, *Journal of the American Mathematical Society* 14, pp. 263-278.
32. Crowe, C. T., Sommerfeld, M. and Tsuji, Y. (1998), *Multiphase flows with droplets and particles*, Boca Raton, Florida, CRC Press.
33. Deardorff, J. W. (1970), A numerical study of three-dimensional turbulent channel flow at large Reynolds numbers, *Journal of Fluid Mechanics* 41, pp. 453 - 480.
34. Dems, P., Carneiro, J. N. E. and Polifke, W. (2011), Large Eddy Simulation on particle-laden swirling flow with a presumed function method of moments, *Proceeding of 8th International Conference on CFD in Oil & Gas, Metallurgical and Process Industries SINTEF/NTNU*, Trondheim, Norway.
35. Drewek, R. (1996), *Verschleißmechanismen in Induktions-Rinnenöfen für Gußeisen und Aluminium*, *Forschr.-Ber. VDI 21 (193)*, Düsseldorf, VDI-Verlag.

36. Eaton, J. K. and Fessler, R. J. (1994), Preferential concentration of particles by turbulence, *International Journal of Multiphase Flow* 20, Suppl., pp. 169-209.
37. Eggels, J. G. M., Unger, F., Weiss, M. H., Westerweel, J., Adrian, R. J., Friedrich, R. and Nieuwstadt, F. T. M. (1994), Fully developed turbulent pipe flow: a comparison between direct numerical simulation and experiment. *Journal of Fluid Mechanics* 268, pp. 175-209.
38. Einstein, A. (1906), Eine neue Bestimmung der Moleküldimensionen[One new purpose of the dimensions of molecules], *Analen der Physik[Annals of Physics]* 19, pp. 289-305.
39. El-Kaddah, N. and Szekely, J. (1983), The turbulent recirculating flow field in a coreless induction furnace, a comparison of theoretical predictions with measurements, *Journal of Fluid Mechanics* 133, pp. 37-46.
40. El-Kaddah, N., Szekely, J., Taberlet, E. and Fautrelle, Y. (1986), Turbulent recirculating flow in induction furnaces: a comparison of measurements with predictions over a range of operating conditions, *Metallurgical and Materials Transactions B* 17B, pp. 687-693.
41. Emmons, H. W. (1951), The laminar-turbulent transition in a boundary layer. Part I, *Journal of Aerospace Science* 18, pp. 490-498.
42. Ericsson, O. T., Karasev, A. V. and Jönsson, P. G. (2011), Effect of Slag Protection System and Sample Geometry on Homogeneity on Total Oxygen Content in Samples from Liquid Steel, *Steel Research International* 82 (3), pp. 222-229.
43. Falkovich, G., Gawedzki, K. and Vergassola, M. (2001), Particles and fields in fluid turbulence, *Reviews of Modern Physics* 73, pp. 913-975.
44. Friedrich, R., Hüttl, T. J., Manhart, M. and Wagner, C. (2001), Direct numerical simulation of incompressible turbulent flows, *Computers & Fluids* 30, pp. 555-579.
45. Frisch, U. (1995), *Turbulence: the legacy of A. N. Kolmogorov*. Cambridge, Cambridge University Press.
46. Frishfelds, V., Jakovičs, A., Nacke, B. and Baake, E. (2009), Diffusion limited growth-up of channels of ICF and its influence on integral flow through the channel, *Magnetohydrodynamics*, 45 (4), pp. 613-621.
47. Gaddipati, A. R. and Scott, W. D. (1986), Surface mass transport of alumina, *Journal of Materials Science* 21 (2), pp. 419-423.
48. Gere, J. M. and Timoshenko, S. P. (1996), *Mechanics of materials*. PWS Publishing Company, Boston.
49. German, R. M. (1996), *Sintering theory and practice*. Willey, New York.
50. Gmelin, L. and Durrer, R. (1964), *Metallurgie des Eisens [Metallurgy of cast iron]* 5, 4th ed. Verlag Chemie GmbH, Weinheim.
51. Gomer, R. (1983), Surface diffusion, *Vacuum* 33 (9), pp. 537-542.
52. Guala, M., Lühti, B., Liberzon, A., Tsinober, A. and Kinzelbach, W. (2005), On the evolution of material lines and vorticity in homogeneous turbulence, *Journal of Fluid Mechanics* 533, pp. 339-359.
53. Gupta, T. K. (1978), Instability of cylindrical voids in alumina, *Journal of American Ceramic Society* 61 (5-6), pp. 191-195.
54. *Handbook on lead-bismuth eutectic alloy and lead properties, materials compatibility, thermal-hydraulics and technologies* (2007). Nuclear energy agency.
55. Härtel, C. and Kleiser, L. (1998), Analysis and modelling of subgrid-scale motion in near-wall turbulence, *Journal of Fluid Mechanics* 356, pp. 327-352.
56. Hinze, J. O. (1959), *Turbulence*. McGraw-Hill, New York.

57. Hopf, E. (1948), A mathematical example displaying the features of turbulence, *Communications on Pure and Applied Mathematics* 1, pp. 303 - 322.
58. Huang, F. H., Henrichsen, R. A. and Cue-Yu-Li (1975), A study of capillarity and mass transport on the Al₂O₃ surface, *Materials Science Research* 10, pp. 173-186.
59. Hyers, R. W. (2005), Fluid flow effects in levitated droplets, *Measurement Science and Technology* 16, pp. 394-401.
60. Issa, R. I. (1985), Solution of the Implicitly Discretized Fluid Flow Equations by Operator-Splitting, *Journal of Computational Physics* 62, pp 40-65.
61. Jasak, H. (1996), *Error Analysis and Estimation for the Finite Volume Method with Applications to Fluid Flow*, PhD Thesis, Department of Mechanical Engineering, Imperial College of Science, Technology, and Medicine, London.
62. Kaftori, D., Hetsroni, G. and Banerjee, S. (1995), Particle behaviour in the turbulent boundary layer. I. Motion, deposition, and entrainment, *Physics of Fluids* 7, pp. 1095-1106.
63. Kaftori, D., Hetsroni, G. and Banerjee, S. (1995), Particle behaviour in the turbulent boundary layer. II. Velocity and distribution profiles, *Physics of Fluids* 7, pp. 1107-1121.
64. Kageyama, R. and Evans, J. W. (1998), A mathematical model for the dynamic behaviour of melts subjected to electromagnetic forces. Part 1, *Metallurgical and Materials Transactions B* 29B, pp. 919-928.
65. Kallio, G. A. and Reeks, M. W. (1989), A numerical simulation of particle deposition in turbulent boundary layer, *International Journal of Multiphase Flow* 15, pp. 433-446.
66. Kaupuzs, J., Jakovics, A. and Nacke, B. (2003), Stability conditions of the build-up formation on the surface of the refractory, *Magnitnaya Gidrodinamika [Magnetohydrodynamics]* 39 (4), 2003, pp. 419-427.
67. Ke, H., Moin, P. and Kim, J. (1997), Direct numerical simulation of turbulent flow over a backward-facing step, *Journal of Fluid Mechanics* 330, pp. 349-374.
68. Kim, J., Moin, P. and Moser, R. (1987), Turbulence statistics in fully developed channel flow at low Reynolds number, *Journal of Fluid Mechanics* 177, pp. 133-166.
69. Kirpo, M. (2008), *Modeling of turbulence properties and particle transport in recirculated flows* (PhD-thesis), University of Latvia, Riga.
70. Kirpo, M., Jakovičs, A. and Baake, E. (2005), Characteristics of velocity pulsations in turbulent recirculated melt flow, *Magnetohydrodynamics* 41, pp. 199-211.
71. Kirpo, M., Jakovičs, A., Baake, E. and Nacke, B. (2007), Analysis of experimental and simulation data for the liquid metal flow in a cylindrical vessel, *Magnetohydrodynamics* 43, pp. 161-172.
72. Kirpo, M., Jakovičs, A., Baake, E. and Nacke, B. (2009), LES study of particle transport in turbulent recirculated liquid metal flows, *Magnetohydrodynamics* 45, pp. 439-450.
73. Kolmogorov, A. N. (1941a), Lokalnaya struktura turbulentsnosti v neszhimayemoy vyazkoy zhidkosti pri ochen bolshih chislah reinoldsa, *Doklad Akademii Nauk SSSR* 30 (4), pp. 299; translated into English by Kolmogorov, A. N. (1991), The local structure of turbulence in incompressible viscous fluid for very large Reynolds number, *Proceedings of the Royal Society of London A* 434, pp. 9-13.
74. Kolmogorov, A. N. (1941b), Dissipatsiya energii v lokalnoy izotropnoy turbulentsnosti [Dissipation of energy in locally isotropic turbulence], *Doklad Akademii Nauk SSSR* 32, pp. 16-18; translated into English by Kolmogorov, A. N. (1991), The local structure

- of turbulence in incompressible viscous fluid for very large Reynolds number, *Proceedings of the Royal Society of London A* 434, pp. 15–17.
75. Kraichnan, R. H. (1966), Isotropic turbulence and inertial-range structure, *Physics of Fluids* 9, pp. 1728-1752.
 76. Krumin', Yu. K. (1969), *Vzaimodeystviye begushchego magnitnogo polya s provodyashchey sredoy [Interaction of running magnetic field and conductive medium]*. Zinatne, Riga.
 77. Kuhn, H. A., Hughes, W. F. and Gaylord, E. W. (1962), Measurements of viscosity of liquid Wood's metal, *British Journal of Applied Physics* 13, p. 527.
 78. Kulick, J. D., Fessler, J. R. and Eaton, J. K. (1994), Particle response and turbulence modification in fully developed channel flow, *Journal of Fluid Mechanics* 277, pp. 109-134.
 79. Kumar, L., Manjunath, B. S., Patel, R. J., Markandeya, S. G., Agrawal, R. G. et al. (2012), Experimental investigations on melting of lead in a cuboid with constant heat flux boundary condition using thermal neutron radiography, *International Journal of Thermal Sciences* 61, pp. 15-27.
 80. Ladyzhenskaya, O. (1963), *The Mathematical Theory of Viscous Incompressible Flow*, revised English edition. Gordon & Breach, New York; translated from the Russian by Silverman, R. A.
 81. Landau, L. D. and Lifshitz, E. M. (1959), *Fluid Mechanics*. Pergamon Press, Oxford; translated by Sykes, J. B. and Reid, W. H. from original Russian published in 1944.
 82. Landau, L. E. and Lifshitz, E. M. (1959), *Fluid mechanics*, Pergamon.
 83. Launder, B. E. and Spalding, D. B. (1972), *Mathematical Models of Turbulence*, Academic Press, London and New York.
 84. Launder, B. E., Reece, G. J. and Rodi, W. (1975), Progress in the development of a Reynolds stress turbulence closure, *Journal of Fluid Mechanics* 68, pp. 537–566.
 85. Lavrent'ev, M. A. and Shabat, B. V. (1973), *Metody teorii funkciy kompleksnogo peremennogo [The methods of the theory of the functions of a complex variable]*, Nauka (Science).
 86. Lee, M. J., Kim, J. and Moin, P. (1987), Turbulent structure at high shear rate. Proceedings of the 6th Symposium on Turbulent Shear Flows, Toulouse, France, September 7 - 9.
 87. Leenov, D. and Kolin, A. (1954), Theory of electromagnetophoresis I. Magnetohydrodynamic forces experienced by spherical and symmetrically oriented cylindrical particles, *Journal of Chemical Physics* 22, pp. 683-689.
 88. Legendre, D. and Magnaudet, J. (1997), A note on the lift force on a bubble or a drop in a low-Reynolds-number shear flow, *Journal of Fluid Mechanics* 9, pp. 3572-3574.
 89. Legendre, D. and Magnaudet, J. (1998), The lift force on a spherical bubble in a viscous linear shear flow, *Journal of Fluid Mechanics* 368, pp. 81-126.
 90. Lehmann, E. H., Vontobel, P., Frei, G., Kuehne, G., Kaestner, A. (2011), How to organize a neutron imaging user lab? 13 years of experience at PSI, CH, *Instruments and Methods in Physics Research A* 651, pp. 1–5.
 91. Leighton, D. and Acrivos, A. (1985), The lift on a small sphere touching a plane in the presence of a simple shear flow, *Zeitschrift für Angewandte Mathematik und Physik [Magazine of applied mathematics and physics]* 36 (1), pp. 174-178.
 92. Leenov, D. and Kolin, A. (1954), Theory of electromagnetophoresis. I. Magnetohydrodynamic forces experienced by spherical and symmetrically oriented cylindrical particles, *Journal of Chemical Physics* 22, pp. 683-689.

93. Leray, J. (1933), Etude de diverses équations intégrales non linéaires et de quelques problèmes que pose l'hydrodynamique [The study on the various non-linear integral equations and on the some problems of hydrodynamics], *Journal de Mathématiques Pures et Appliquées [Journal of the pure and applied mathematics]* 12, pp. 1–82.
94. Leray, J. (1934), Essai sur les mouvements d'un liquide visqueux que limitent des parois [Essai on the movement of the viscous fluid limited by the walls], *Journal de Mathématiques Pures et Appliquées [Journal of the pure and applied mathematics]* 13, pp. 331–418.
95. Li, A. and Ahmadi, G. (1992), Dispersion and deposition of spherical particles from point sources in a turbulent channel flow, *Aerosol Science and Technology* 16 (4), pp. 209-226.
96. Lide, D. R., ed. (2005). *CRC Handbook of Chemistry and Physics* (86th ed.). Boca Raton (FL), CRC Press.
97. Lifshitz, I. M. and Slyozov, V. V. (1961), The kinetics of precipitation from supersaturated solid solution, *Journal of Physics and Chemistry of Solids* 19, pp. 35-50.
98. Lim, J., Choi, H. and Kim, J. (1998), Control of streamwise vortices with uniform magnetic fluxes, *Physics of Fluids* 10, pp. 1997-2005.
99. Lorenz, E. N. (1963), Deterministic nonperiodic flow, *Journal of the Atmospheric Sciences* 20, pp. 130–141.
100. Loth, E. (2000), Numerical approaches for motion of dispersed particles, droplets and bubbles, *Progress in Energy and Combustion Science* 26, pp. 161-223.
101. Lühti, B., Tsinober, A. and Kinzelbach, W. (2005), Lagrangian measurement of vorticity dynamics in turbulent flow, *Journal of Fluid Mechanics* 528, pp. 87-118.
102. Marchioli, C., Picciotto, M. and Soldati, A. (2004), Interactions between turbulence structure and inertial particles in boundary layers: mechanisms for particle transfer and preferential distribution, in *Modelling and experimentation in two-phase flow*, (ed. Bertola, V.), CISM Courses and Lectures, Springer 450, pp. 383-434.
103. Maruyama, T. and Komatsu, W. (1975), Surface diffusion of single-crystal Al₂O₃ by scratch-smoothing method, *Journal of American Ceramic Society* 58, pp. 338-339.
104. McKee, S., Watson, R., Cuminato, J. A. and Moore, P. (1999), Particle tracking within turbulent cylindrical electromagnetically-driven flow, *International Journal for Numerical Methods in Fluids* 29, pp. 59-74.
105. McLaughlin, J. B. (1989), Aerosol particle deposition in numerically simulated channel flow, *Physics of Fluids* 1, pp. 1211-1224.
106. McLaughlin, J. B. (1991), Inertial migration of small sphere in linear shear flows, *Journal of Fluid Mechanics* 224, pp. 261-274.
107. Mei, R., Adrian, R. J. and Hanratty, T. J. (1991), Particle dispersion in isotropic turbulence under Stokes drag and Basset force with gravitational settling, *Journal of Fluid Mechanics* 225, pp. 481-495.
108. Moffatt, H. K. (1991), Electromagnetic stirring, *Physics of Fluids A* 3 (5), pp. 1336-1343.
109. Moiser, R. and Moin, P. (1987), The effect of curvature in wall-bounded turbulent flows, *Journal of Fluid Mechanics* 175, pp. 479-510.
110. Moore, D. J. and Hunt, J. C. R. (1983), Electromagnetic stirring in the coreless induction furnace, *Progress in Astronautics and Aeronautics* 84, pp. 359-373; this is the revised version of the original paper in the Proceedings of the 3rd Beer-Sheva

- International Seminar on MHD flows and Turbulence, Ed. by Branover, H., Lykoudis, P. S. and Yakhot, A., Beersheva, Israel, March 23-27, 1981.
111. Mordant, N., Metz, P., Michel, O. and Pinton, J.-F. (2001), Measurement of Lagrangian velocity in fully developed turbulence, *Physical Review Letters* 87, art. no. 214501.
 112. Na, Y. and Moin, P. (1998), Direct numerical simulation of a separated turbulent boundary layer, *Journal of Fluid Mechanics* 370, pp. 175-201.
 113. Nelkin, M. (2000), Resource letter TF-1: turbulence in fluids, *American Journal of Physics* 68, pp. 310-318.
 114. Neves, J. C., Moin, P. and Moser, R. D. (1994), Effect of convex transverse curvature on wall-bounded turbulence. Part 1: The velocity and vorticity, *Journal of Fluid Mechanics* 272, pp. 349-381.
 115. Neves, J. C., Moin, P. and Moser, R. D. (1994), Effect of convex transverse curvature on wall-bounded turbulence. Part 2: The pressure fluctuations, *Journal of Fluid Mechanics* 272, pp. 383-406.
 116. O'Neill, M. E. (1968), A sphere in contact with a plane wall in a slow linear shear flow, *Chemical Engineering Science* 23 (11), pp. 1293-1298.
 117. Odar, F. and Hamilton, W. S. (1964), Forces on a sphere accelerating in a viscous fluid *Journal of Fluid Mechanics* 18, pp. 302-14.
 118. Oliveira, P. J. and Issa, R. I. (2001), An Improved PISO Algorithm for the Computation of Buoyancy-Driven Flows, *Numerical Heat Transfer Part B* 40, pp 473-493.
 119. Orszag, S. A. and Patterson, G. S. (1972), Numerical simulation of turbulence: statistical models and turbulence, *Lecture Notes in Physics* 12, pp. 127–147, Springer-Verlag, Berlin.
 120. Ostwald, W. (1897), Studien über die Bildung und Umwandlung fester Körper [Studies about formation and transformation of solid bodies], *Zeitschrift für physikalische Chemie [Physical Chemistry Magazine]* 22, pp. 289-330.
 121. Ott, S. and Mann, J. (2000), An experimental investigation of the relative diffusion of particle pairs in three-dimensional turbulent flow, *Journal of Fluid Mechanics* 422, pp. 207-223.
 122. Pandya, R. V. R. and Mashayek, F. (2002), Two-fluid Large-Eddy simulation approach for particle-laden turbulent flows, *International Journal of Heat and Mass Transfer* 45, pp. 4753-4759.
 123. Perot, B. and Moin, P. (1995), Shear-free turbulent boundary layers. Part1: Physical insights into near-wall turbulence. *Journal of Fluid Mechanics* 295, pp. 199-227.
 124. Perot, B. and Moin, P. (1995), Shear-free turbulent boundary layers. Part1: New concepts for Reynolds stress transport equation modelling of inhomogeneous flows. *Journal of Fluid Mechanics* 295, pp. 229-245.
 125. Perrier, D., Fautrelle, Y. and Etay, J. (2003), Free surface controlled by magnetic field, *ISIJ International* 43, pp. 801-806.
 126. Poincaré, H. (1899), *Les Methodes Nouvelles de la Mécanique Celeste [The New Methods of the Celestial Mechanics]* 1–3. Gauthier Villars, Paris.
 127. Pope, S. B. (2000), *Turbulent flows*. Cambridge, Cambridge University Press.
 128. Pope, S. B. (2004), Ten questions concerning the large-eddy simulation of turbulent flows, *New Journal of Physics* 6, art. no.35.
 129. Prandtl, L. (1925), Bericht über Untersuchungen zur ausgebildeten Turbulenz [Report about the investigation of developed turbulence], *Zeitschrift für Angewandte*

- Mathematik und Mechanik [Magazine of Applied Mathematics and Mechanics]* 5, pp. 136–139.
130. Pumir, A., Shraiman, B. I. and Chertkov, M. (2000), Geometry of Lagrangian dispersion in turbulence, *Physical Review Letters* 85, pp. 5324-5327.
 131. Pumir, A., Shraiman, B. I. and Chertkov, M. (2001), The Lagrangian view of energy transfer in turbulent flow, *Europhysics Letters* 56, pp. 379-385.
 132. Rao, W. R. and Culter, I. B. (1972), Initial sintering and surface diffusion in Al_2O_3 , *Journal of The American Ceramic Society* 55 (2), pp. 170-171.
 133. Reynolds, O. (1894), On the dynamical theory of turbulent incompressible viscous fluids and the determination of the criterion, *Philosophical Transactions of the Royal Society of London. A* 186, pp. 123–161.
 134. Richards, W. J., Gibbons, M. R. and Shields, K. C. (2004), Neutron tomography developments and applications, *Applied Radiation and Isotopes* 61 (4), pp. 551-559.
 135. Richardson, L. F. (1922), *Weather Prediction by Numerical Process*. Cambridge University Press.
 136. Ruelle, D. and Takens, F. (1971), On the nature of turbulence. *Communications in Mathematical Physics* 20, pp. 167–192.
 137. Sadoway, D. R. and Szekely, J. (1980), A new experimental technique for the study of turbulent electromagnetically driven flows, *Metallurgical and Materials Transactions B* 11B, pp. 334-336.
 138. Saffman, P. G. (1965), The lift on a small sphere in a slow shear flow, *Journal of Fluid Mechanics* 22, pp. 385-400.
 139. Sajgalik, P., Panek, Z. and Uhrik, M. (1987), The surface diffusion coefficient of MgO and Al_2O_3 , *Journal of Materials Science* 22 (12), pp. 4460-4464.
 140. Sato, Y. and Yamamoto, K. (1987), Lagrangian measurement of fluid-particle motion in an isotropic turbulent field, *Journal of Fluid Mechanics* 175, pp. 183-199.
 141. Ščepanskis, M., Jakovičs, A. and Baake, E. (2011), Statistical analysis of the influence of forces on particles in EM driven recirculated turbulent flows, *Journal of Physics: Conference Series* 333, art. no. 012015.
 142. Ščepanskis, M., Jakovičs, A., Baake, E. and Nacke, B. (2012), Analysis of the oscillating behavior of solid inclusions in induction crucible furnaces, *Magnetohydrodynamics* 48 (4), pp. 677 – 686.
 143. Ščepanskis, M., Jakovičs, A., Nacke, B. and Baake, E. (2012), Numerical analysis and experimental verification of the behaviour of solid inclusions in induction crucible furnaces, *J. Iron Steel Res. Int.* 19, suppl. 1, pp. 713-716.
 144. Schiller, L. and Naumann, Z. (1933), Uber die grundlegenden Berechnungen bei der Schwerkraftaufbereitung [On the fundamental calculation of gravity preparation], *Verein Deutscher Ingenieure [Union of German Engineers]* 77, pp. 318-20.
 145. Seebauer, E. G. and Allen, C. E. (1995), Estimating surface diffusion coefficients, *Progress in surface science* 49 (3), pp. 265-330.
 146. Shackelford, J. F. and Alexander, W. (2001), *CRC materials science and engineering handbook*. CRC Press LLC, Boca Raton.
 147. Shilov, E. I., Bojarevičs, V., Freibergs, J. A. and Shcherbinin, E. V. (1989), *Electrically induced vortical flows*, Kluwer Academic Publishers, Dordrecht.
 148. Smale, S. (1965), Diffeomorphisms with many periodic points, in *Differential and Combinatorial Topology*, Princeton University Press, Princeton, pp. 63–80.

149. Snyder, W. H. and Lumley, J. L. (1971), Some measurements of particle velocity autocorrelation functions in a turbulent flow, *Journal of Fluid Mechanics* 48, pp. 41-71.
150. Spalart, P. R. (1988), Direct simulation of a turbulent boundary layer up to $Re_\theta = 1410$, *Journal of Fluid Mechanics* 187, pp. 61-98.
151. Spitans, S., Jakovics, A., Baake, E. and Nacke, B. (2013), Numerical Modeling of Free Surface Dynamics of Melt in an Alternate Electromagnetic Field: Part I. Implementation and Verification of Model, *Metallurgical and Materials Transactions B* 44 (3), pp. 593-605.
152. Spītāns, S., Jakovičs, A., Baake, E. and Nacke, B. Numerical Modeling of Free Surface Dynamics of Melt in an Alternate Electromagnetic Field, *Magneto hydrodynamics* 47, pp. 461-473.
153. Takahashi, K. and Taniguchi, S. (2003), Electromagnetic separation of non-metallic inclusions from liquid metal by imposition of high frequency magnetic field, *ISIJ International* 43, pp. 820-827.
154. Taniguchi, S. and Brimacombe, J. K. (1994), Application of pinch force to the separation of inclusion particles from liquid steel, *ISIJ International* 34, pp. 722-731.
155. Taniguchi, S. and Kikuchi, A. (2000), Removal of non-metallic inclusion from liquid metal by AC-electromagnetic force, *Proceeding of 3rd Symposium on Electromagnetic Processing of Materials*, Tokyo (Japan), p. 315-320.
156. Tarapore, E. D. and Evans, J. W. (1977) Fluid velocities in induction melting furnaces: Part II. large scale measurements and predictions, *Metallurgical and Materials Transactions B* 7B, pp. 345-351.
157. Taylor, G. I. (1921), Diffusion by continuous movements, *Proceedings of the Royal Society of London A* 20, pp. 196-211.
158. Taylor, G. I. (1935), Statistical theory of turbulence, *Proceedings of the Royal Society of London A* 151, pp. 421-478.
159. Todnem, O. R. (1967), *Induction melting furnace*, US patent no. 3303260, 07.02.1967.
160. Toh, T., Yamamura, H., Kondo, H., Wakoh, M., Shimasaki, S. and Taniguchi, S. (2007), Kinetic evaluation of inclusions removal during levitation melting of steel in cold crucible, *ISIJ International* 47, pp. 1625-1632.
161. Toschi, F. and Bodenschatz, E. (2009), Lagrangian properties of particles in turbulence, *Annual Review of Fluid Mechanics* 41, pp. 375-404.
162. Toschi, F., Biferale, L., Boffetta, G., Celani, A., Devenish, B. J. and Lanotte, A. (2005), Acceleration and vortex filaments in turbulence, *Journal of Turbulence* 6, art. no. N15.
163. Trakas, C., Tabeling, P. and Chabrierie, J. P. (1984), Etude experimentale du brassage turbulent dans le four a induction [The experimental reserach on the turbulent stirring in induction furnances], *Journal de Mécanique Théorique et Appliquée [Journal of Theoretical and Applied Mechanics]* 3, pp. 345-370.
164. Tsinober, A. (2001), *An Informal Introduction to Turbulence*. Kluwer Academic Publishers, Dordrecht.
165. Umbrashko, A., Baake, E., Nacke, B. and Jakovics, A. (2006), Modeling of the turbulent flow in induction furnaces, *Metallurgical and Materials Transactions B* 37B, pp. 831-838.
166. Umbrashko, A., Baake, E., Nacke, B. and Jakovics, A. (2008), Thermal and hydrodynamic analysis of the melting process in the cold crucible using 3d modeling, *Heat Transfer Research* 39, pp. 413-421.

167. Umbraško, A. (2011), *Heat and mass transfer in electromagnetically driven recirculated turbulent flows* (PhD-thesis), University of Latvia, Riga.
168. Van Artsdalen, E. R. and Yaffe, I. S. (1955), Electrical conductance and density of molten salt systems: KCl-LiCl, KCl-NaCl and KCl-KI, *The Journal of Physical Chemistry* 59, pp.118-127.
169. Vincent, A. and Meneguzzi, M. (1991), The spatial structure and statistical properties of homogeneous turbulence, *Journal of Fluid Mechanics* 225, pp. 1-20.
170. Virant, M. and Dracon, T. (1997), 3D PTV and its application on Lagrangian motion, *Measurement Science and Technology* 8, pp. 1539-1552.
171. Volk, R., Calzavarini, E., Verhille, G., Lohse, D., Mordant, N., Pinton, J.-F. and Toschi, F. (2008), Acceleration of heavy and light particles in turbulence: Comparison between experiments and direct numerical simulations, *Physica D* 237, pp. 2084-2089.
172. Wagner, C. (1996), *Direkte numerische Simulation turbulenter Strömungen in einer Rohrerweiterung [Direct numerical simulation of turbulent flow in the tube obstacle]*, VDI-Fortschrittsberichte 7 (283), Düsseldorf.
173. Wagner, C. and Friedrich, R. (2004), Direct numerical simulation of momentum and heat transport in idealized Czochralski crystal growth configurations, *International Journal of Heat and Fluid Flow* 25, pp. 431-443.
174. Wang, Q. and Squires, K. D. (1996), Large eddy simulation of particle deposition in a vertical turbulent channel flow, *International Journal of Multiphase Flow* 22, pp. 667-683.
175. Williams, D. F. (2006), Report ORNL/TM-2006/69 on *Assessment of candidate molten salt coolants for the NGNP/NHI heat-transfer loop*. Oak Ridge National Laboratory, Oak Ridge, TN, USA.
176. Yakhot, V. and Orszag, S. A. (1986), Renormalization group analysis of turbulence. I. Basic theory, *Journal of Scientific Computing* 1, pp. 3-51.
177. Yuan, H. and Prosperetti, A. (1994), On the in-line motion of two spherical bubbles in a viscous fluid, *Journal of Fluid Mechanics* 278, pp. 325-349.

Appendix1. Implementation of EM force to *pisoFoam* solver in OpenFOAM¹

Implementation of EM field to Navier-Stokes equation OpenFOAM's *pisoFoam* solver is done as follows:

```
volVectorField FF = - F/rho0 + beta*(T0 - T)*g;
```

```
fvVectorMatrix UEqn
(
    fvm::ddt(U)
    + fvm::div(phi, U)
    + turbulence->divDevReff(U)
);
```

```
UEqn.relax();
```

```
if (momentumPredictor)
{
    solve(UEqn == -fvc::grad(p)-FF);
}
```

Definition of the volume force.
F – Lorentz force field, which is calculated in ANSYS and imported in OpenFOAM;
rho0 – density of the liquid;
beta – the coefficient of thermal expansion;
T – temperature field;
T0 – reference temperature;
g – free fall acceleration.

Left part of the Navier-Stokes equation:
 1st row - first time derivation of velocity *U*;
 2nd row - convection of velocity *U*; *phi* is the velocity flux;
 3rd row – the special routine for LES calculation of the viscous term².
 This function discretizes the differential operators and creates the matrix.

Relaxation of previously created matrix.

The predictor step:
 The implicit left side matrix, described above, and stored in the array *UEqn* multiplied by the solution vector, which is supplemented with created volume force field *FF*.

The temperature field is calculated within PISO loop (explicit corrector steps):

```
volScalarField alphaEff = turbulence->nuEff()/Prt;
```

Definition of the scalar field of effective thermal diffusivity³ *alphaEff*, which is calculated as ratio of effective viscosity (taking into account turbulence effect) *nuEff* and turbulent Prandtl number *Prt*⁴.

¹ This implementation was done by Dr. phys. Miksims Kirpo in OpenFOAM-1.5, however, was never published. The author of this thesis is transferred it to OpenFOAM-1.6.

² $divDevReff(\mathbf{U}) = -\nabla^2(\nu_{eff}\mathbf{U}) - \nabla \cdot \{\nu_{eff}dev[(\nabla\mathbf{U})^T]\}$, where operator $dev(\mathbf{A}) = \mathbf{A} - \frac{1}{3}trace(\mathbf{A})\mathbf{I}$, \mathbf{I} is identity matrix. ν_{eff} is effective kinematic viscosity, which includes the turbulence viscosity effect.

³ Thermal diffusivity $\alpha = \frac{k}{\rho C_p}$, where k is thermal conductivity, ρ is density, C_p is heat capacity.

⁴ The turbulent Prandtl number is defined as follows: $Prt = \frac{C_p \mu}{k} = \frac{\nu}{\alpha}$, where μ and ν are dynamic and kinematic viscosity, other physical quantities are explained in the footnote 2.

```
fvScalarMatrix TEqn
(
    fvm::ddt(T)
    + fvm::div(phi, T)
    - fvm::laplacian(alphaEff, T)
    - Q/(rho0*Cp0)
);
TEqn.solve();
```

<p>The matrix for thermal equation is created: 1st row – first time derivation of temperature T; 2nd row – convection of T; 3rd row – thermal diffusion term; 4th row – the external Joule heat source Q, divided with density ρ_0 and heat capacity Cp_0.</p>

<p>Solution of the linear set of the equations.</p>

Finally, velocity field is corrected by the volume force after the non-orthogonal pressure loop¹:

```
U -= rUA*(fvc::grad(p)+FF);
```

<p>Velocity field U is corrected by the subtraction of the multiplication of scalar field rUA^2 and the subtraction of pressure gradient and volume force FF.</p>

¹see e.g. *Jasak (1996)*.

²Scalar field rUA is defined as \mathbf{A}^{-1} , where \mathbf{A} is diagonal matrix of $UEqn$ coefficients.

Appendix2. Modification of OpenFOAM libraries for particle tracking

First of all, the initial clouds of particles are created directly in the solver:

```
solidParticleCloud particlesCloud1(mesh,
"Cloud1");
solidParticleCloud particlesCloud2(mesh,
"Cloud2");
solidParticleCloud particlesCloud3(mesh,
"Cloud3");
...
```

The numbered objects of the `solidParticleCloud` class are defined for different virtually independent particle clouds. `mesh` is the variable, which points to the numerical grid; "`Cloud#`" is the name of the particle cloud.

As it is shown above, few clouds (without any limitation in number) can be created simultaneously. These clouds will virtually independently move in the flow, that is one cloud does not affect another one way or another. Such realization is possible under dilute conditions and is very useful for the case studies of particle motion at the same EM and HD parameters. The computational time for the calculation of turbulent flow is usually much longer than the time for particle tracking even for large clouds. Therefore, such approach allows to make simultaneous calculation and to separate analysis of the clouds with different properties (e.g. density, size of particles etc.) calculating the flow only once. The properties of each cloud (`Cloud1` in the example) are read as follows:

```
Info<<"\nFrom
constant/particlePropertiesCloud1:" << endl;
Info<<"rhop = " << particlesCloud1.rhop()
<< endl;
Info<<"e = " << particlesCloud1.e() << endl;
Info<<"mu = " << particlesCloud1.mu() <<
endl;
```

`rhop` is the density of particles; `e` and `mu` are the coefficients of elasticity of collisions (normal and tangential components respectively) – see the next subchapter.

Mentioned parameters (which are common for the whole cloud) are defined in `constant/particleProperties` file in the case folder.

Some additional fields should be calculated from the HD data to solve the Lagrange equation (see expressions (3.12, 3.17) and the Lagrange equation (3.16)):

```
curlU = fvc::curl(U);
UcurlU = U ^ curlU;
dUdt = fvc::ddt(U);
gradU = fvc::grad(U);
```

Vector field $\text{rot } \mathbf{u}_f$;
vector field $\mathbf{u}_f \times \text{rot } \mathbf{u}_f$;
vector field of the flow acceleration $d\mathbf{u}_f/dt$;
tensor field $\partial u_{f,i}/\partial x_j$, where i and j are indexes for components of vector in the Cartesian coordinates.

Now all particle clouds are created, parameters are defined and the necessary flow fields calculated. The particle tracking algorithm is applied for each cloud:

```
Info<< "Moving particles from Cloud1." <<
endl;
particlesCloud1.move(g, NumofIter);
Info<< "Moving particles from Cloud2." <<
endl;
particlesCloud2.move(g, NumofIter);
...
```

Function *move*, which contains the Lagrange tracking algorithm, is applied for each particle cloud.

The arguments of function *move* are:
g is the vector of free fall acceleration;
NumberofIter is the number of the Lagrange time steps (see Figure 3.1 and the discussion in the beginning of the present subchapter).

The tracking of the particles in the cloud is fulfilled by *move* function of *solidParticleCloud* class, which is defined as follows:

```
void Foam::solidParticleCloud::move(const
dimensionedVector& g, const double&
NumofIter)
{
    const volScalarField& rho =
mesh_.lookupObject<const
volScalarField>("rho");
    const volVectorField& U =
mesh_.lookupObject<const
volVectorField>("U");
    const volScalarField& nu =
mesh_.lookupObject<const
volScalarField>("nu");
    const volVectorField& F =
mesh_.lookupObject<const
volVectorField>("F");
    const volVectorField& curlU =
mesh_.lookupObject<const
volVectorField>("curlU");
    const volVectorField& UcurlU =
mesh_.lookupObject<const
volVectorField>("UcurlU");
    const volVectorField& dUdt =
mesh_.lookupObject<const
volVectorField>("dUdt");
    const volTensorField& gradU =
mesh_.lookupObject<const
volTensorField>("gradU");

    interpolationCellPoint<scalar>
rhoInterp(rho);
    interpolationCellPoint<vector> UInterp(U);
    interpolationCellPoint<scalar>
nuInterp(nu);
    interpolationCellPoint<vector> FInterp(F);
```

Definition of function *move* of the class *solidParticleCloud*:

Firstly, all flow field are read here.

Secondly, all fields are interpolated at the position of each particle.

```

    interpolationCellPoint<vector>
    curlUInterp(curlU);
    interpolationCellPoint<vector>
    UcurlUInterp(UcurlU);
    interpolationCellPoint<vector>
    dUdtInterp(dUdt);
    interpolationCellPoint<tensor>
    gradUInterp(gradU);

    solidParticle::trackData td(*this, rhoInterp,
    UInterp, nuInterp, FInterp, curlUInterp,
    UcurlUInterp, dUdtInterp, gradUInterp,
    g.value());
    td.NumofIter = NumofIter;

    Cloud<solidParticle>::move(td);
}

void Foam::solidParticleCloud::writeFields()
const
{
    solidParticle::writeFields(*this);
}

```

The interpolated values of the fields at the position of the particle are collected to the structure *td*

and function *move* of the class *solidParticle* is called with the structure *td* as an argument.

The new positions of the particles of the current cloud are written to the proper file using *writeField* function.

Finally, each individual particle is tracked by the move function of *solidParticle* class according to the Lagrange algorithm:

```

bool
Foam::solidParticle::move(solidParticle::track
Data& td)
{
    td.switchProcessor = false;
    td.keepParticle = true;
    const polyMesh& mesh = cloud().pMesh();
    const polyBoundaryMesh& pbMesh =
    mesh.boundaryMesh();

    scalar deltaT = mesh.time().deltaT().value();
    scalar tEnd = (1.0 - stepFraction())*deltaT;
    scalar dtMax = tEnd;

    while (td.keepParticle &&
    !td.switchProcessor && tEnd > SMALL)
    {

        scalar LagrangianTimeStep =
    tEnd/td.NumofIter;

        for (int i=0; i<td.NumofIter; i++)
        {

```

Definition of function *move* of the class *solidParticle*.

Switchers that indicate beginning and end of the particle tracking.

Definition of the mesh and faces of its cells for goals of the present function.

Definition of the time, which is left for the next HD time step (see Figure 3.1). *stepFraction()* function indicated the crossing of the cell face.

Thus, the HD time step is split to several intervals, each of them corresponds to the particle stay within one cell.

while cycle goes through all mentioned intervals until achieves the end of HD time step.

Definition of the Lagrange time step as the interval of the particle motion within one cell divided with *NumofIter*.

for cycle through all the Lagrange time steps within the interval of staying in one cell.

```

        scalar tEndLagrangian =
LagrangianTimeStep;
        scalar dtMaxLagrangian =
tEndLagrangian;
        while (td.keepParticle &&
!td.switchProcessor && tEndLagrangian >
SMALL)
        {
                scalar dt =
min(dtMaxLagrangian, tEndLagrangian);

                label celli = cell();

                dt *= trackToFace(position() +
dt*U_, td);
                tEnd -= dt;
                tEndLagrangian -= dt;
                stepFraction() = 1.0 -
tEnd/deltaT;

                cellPointWeight cpw(mesh,
position(), celli, face());
                scalar rhoc =
td.rhoInterp().interpolate(cpw);
                vector Uc =
td.UInterp().interpolate(cpw);
                scalar nuc =
td.nuInterp().interpolate(cpw);
                vector Fc =
td.FInterp().interpolate(cpw);
                vector curlUc =
td.curlUInterp().interpolate(cpw);
                vector UcurlUc =
td.UcurlUInterp().interpolate(cpw);
                vector dUdtc =
td.dUdtInterp().interpolate(cpw);
                tensor gradUc =
td.gradUInterp().interpolate(cpw);

                vector UfmpcurlU = UcurlUc -
(U_ ^ curlUc);
                cellPointWeight cpwMdh(mesh,
position() -
UfmpcurlU/mag(UfmpcurlU)*d_/2.0, celli,
face());
                cellPointWeight cpwPdh(mesh,
position() +
UfmpcurlU/mag(UfmpcurlU)*d_/2.0, celli,
face());

                scalar rhop = td.spc().rhop();
#include "lagrangianEqn.H"

```

Further routine defines the variables, which indicate the end of the Lagrange time step and manage the tracking until it.

Definition of the time step dt that will be used for the numerical solution of the Lagrange equation (3.16).

Remember which cell the particle is in. Since this will change if a face is hit.

trackToFace function of *lagrangian* library moves the particle to the end position or to the nearest cell face, if it appears on the trajectory.

The remained time to the end of time step is corrected after that.

Definition of the values of flow density (*rhoc*), viscosity (*nuc*), EM force (*Fc*), rot \mathbf{u}_f (*curlUc*), $\mathbf{u}_f \times \text{rot } \mathbf{u}_f$ (*UcurlUc*), acceleration $d\mathbf{u}_f/dt$ (*dUdtc*) and the tensor $\partial u_{f,i}/\partial x_j$ (*gradUc*) at the particle position after its motion.

The vector *UfmpcurlU* points the perpendicular to the particle motion direction, which is the direction of the lift force (see expression (3.17)): $\mathbf{u}_f \times \text{rot } \mathbf{u}_f - \mathbf{u}_p \times \text{rot } \mathbf{u}_f$.

cpwMdh and *cpwPdh* define the points at the opposite surfaces of the particle, which are situated on the line, which is perpendicular to the particle motion direction and crosses the center of a particle. These points will be used for definition of non-dimensional share stress *Sr*.

Read density of the particle material.

The solution of the Lagrange equation (3.16)

```

        if (onBoundary() &&
td.keepParticle)
        {
            if
(isType<processorPolyPatch>(pbMesh[patch(face())]))
            {
                td.switchProcessor =
true;
            }
        }
    }
    return td.keepParticle;
}

```

– will be discussed in details later.

The management of the particle tracking in the case than it is on the boundary of the calculation region (wall) is described here.

The solution of the linearized Lagrange equation (3.16) is coded within *lagrangianEq.H* routine:

```

vector Uprev_ = U_;

scalar magUr = mag(Uc - U_);
scalar ReFunc = 1.0;
Re_ = magUr*d_/nuc;
if (Re_ > 0.01)
{
    ReFunc += 0.15*pow(Re_, 0.687);
}
//Drag coefficient
scalar Dc =
(24.0*nuc/d_)*ReFunc*(3.0/4.0)*(rhoc/(d_*rho));

//Non-dimension shear stress
vector forceDir = UcurlUc - (U_ ^ curlUc);
forceDir /= mag(forceDir);
Sr_ = mag(gradUc & forceDir)*d_/magUr;

//Lift coefficient
scalar LhighRe =
0.5*(1.0+16.0/Re_)/(1.0+29.0/Re_);
scalar eps = sqrt(Sr_/Re_);
scalar J = 2.255 / pow(1.0+0.2/pow(eps,2.0),1.5);
scalar PI = 3.14159265;
scalar LlowRe =
6.0/(pow(PI,2.0)*sqrt(Sr_*Re_))*J;
scalar Lc;
if (Re_ > 10)
Lc = LhighRe;
else

```

Before calculation of the new value of \mathbf{u}_p ($U_$) it is saved as the value at the previous time step U_{prev} .

Calculation of the drag coefficient D_c according to the Schiller-Naumann approximation (3.11).

Calculation of the non-dimensional shear stress $Sr_$:

$$Sr = |\partial \mathbf{u}_f / \partial \mathbf{s}| \cdot d / U$$

Calculation of the lift coefficient L_c according to the McLaughlin-Legendre-Magnaudet approximation (expressions (3.13-3.15)).

$Lc = \text{sqrt}(\text{pow}(Lc\text{lowRe},2.0)+\text{pow}(Lc\text{highRe},2.0));$

//Added mass coefficient

$Ac_ = \text{pow}(Uc-U_,2)/(d_*\text{mag}(dUdtc-dUdt_));$
 $\text{scalar } AMc = 2.1 - 0.132/(0.12+\text{pow}(Ac_,2));$

//Equation of motion

$\text{scalar } U_x = U_.\text{component}(0);$
 $\text{scalar } U_y = U_.\text{component}(1);$
 $\text{scalar } U_z = U_.\text{component}(2);$
 $\text{scalar } Ucx = Uc.\text{component}(0);$
 $\text{scalar } Ucy = Uc.\text{component}(1);$
 $\text{scalar } Ucz = Uc.\text{component}(2);$
 $\text{scalar } \text{curl}Ucx = \text{curl}Uc.\text{component}(0);$
 $\text{scalar } \text{curl}Ucy = \text{curl}Uc.\text{component}(1);$
 $\text{scalar } \text{curl}Ucz = \text{curl}Uc.\text{component}(2);$
 $\text{scalar } U\text{curl}Ucx = U\text{curl}Uc.\text{component}(0);$
 $\text{scalar } U\text{curl}Ucy = U\text{curl}Uc.\text{component}(1);$
 $\text{scalar } U\text{curl}Ucz = U\text{curl}Uc.\text{component}(2);$
 $\text{scalar } Fcx = Fc.\text{component}(0);$
 $\text{scalar } Fcy = Fc.\text{component}(1);$
 $\text{scalar } Fcz = Fc.\text{component}(2);$

tensor LeftPart;

$\text{LeftPart}.xx() = 1.0 + AMc*0.5*\text{rho}c/\text{rho}p + Dc*dt$
 $- (1.0+AMc*0.5)*\text{rho}c/\text{rho}p*\text{grad}Uc.xx()*dt;$
 $\text{LeftPart}.xy() = \text{rho}c/\text{rho}p*Lc*\text{curl}Ucz*dt -$
 $(1.0+AMc*0.5)*\text{rho}c/\text{rho}p*\text{grad}Uc.yx()*dt;$
 $\text{LeftPart}.xz() = -\text{rho}c/\text{rho}p*Lc*\text{curl}Ucy*dt -$
 $(1.0+AMc*0.5)*\text{rho}c/\text{rho}p*\text{grad}Uc.zx()*dt;$
 $\text{LeftPart}.yx() = -\text{rho}c/\text{rho}p*Lc*\text{curl}Ucz*dt -$
 $(1.0+AMc*0.5)*\text{rho}c/\text{rho}p*\text{grad}Uc.xy()*dt;$
 $\text{LeftPart}.yy() = 1.0 + AMc*0.5*\text{rho}c/\text{rho}p + Dc*dt$
 $- (1.0+AMc*0.5)*\text{rho}c/\text{rho}p*\text{grad}Uc.yy()*dt;$
 $\text{LeftPart}.yz() = \text{rho}c/\text{rho}p*Lc*\text{curl}Ucx*dt -$
 $(1.0+AMc*0.5)*\text{rho}c/\text{rho}p*\text{grad}Uc.zy()*dt;$
 $\text{LeftPart}.zx() = \text{rho}c/\text{rho}p*Lc*\text{curl}Ucy*dt -$
 $(1.0+AMc*0.5)*\text{rho}c/\text{rho}p*\text{grad}Uc.xz()*dt;$
 $\text{LeftPart}.zy() = -\text{rho}c/\text{rho}p*Lc*\text{curl}Ucx*dt -$
 $(1.0+AMc*0.5)*\text{rho}c/\text{rho}p*\text{grad}Uc.yz()*dt;$
 $\text{LeftPart}.zz() = 1.0 + AMc*0.5*\text{rho}c/\text{rho}p + Dc*dt$
 $- (1.0+AMc*0.5)*\text{rho}c/\text{rho}p*\text{grad}Uc.zz()*dt;$

vector RightPart;

$\text{RightPart}.x() = (1.0+AMc*0.5*\text{rho}c/\text{rho}p)*U_x +$
 $dt*(Dc*Ucx - 3.0/(4.0*\text{rho}p)*Fcx +$
 $\text{rho}c/\text{rho}p*Lc*U\text{curl}Ucx +$
 $(1.0+AMc*0.5)*\text{rho}c/\text{rho}p*dUdtc.x());$
 $\text{RightPart}.y() = (1.0+AMc*0.5*\text{rho}c/\text{rho}p)*U_y +$
 $dt*(Dc*Ucy - 3.0/(4.0*\text{rho}p)*Fcy +$
 $\text{rho}c/\text{rho}p*Lc*U\text{curl}Ucy +$
 $(1.0+AMc*0.5)*\text{rho}c/\text{rho}p*dUdtc.y());$
 $\text{RightPart}.z() = (1.0+AMc*0.5*\text{rho}c/\text{rho}p)*U_z +$

Calculation of the added mass coefficient Ac (expression (3.11)).

Definition of the matrices of the equation $\text{LeftPart} \cdot U_ = \text{RightPart}$, which corresponds to the linearized Lagrange equation (3.16).

```

dt*(Dc*Ucz - (1.0 - rhoc/rhop)*mag(td.g()) -
3.0/(4.0*rhop)*Fcz + rhoc/rhop*Lc*UcurlUcz +
(1.0+AMc*0.5)*rhoc/rhop*dUdtc.z());

```

```

U_ = SolveLinearEqn(LeftPart, RightPart);

```

```

if (dt!=0)

```

```

dUdt_ = (U_-Uprev_)/dt;

```

The mentioned matrix equation is solved using the Gauss method.

Definition of the particle acceleration $dUdt_$.

Appendix3. Particle-wall collision treatment

solidParticle library contains the following treatment of the particle velocity when it collides with the wall:

```
void Foam::solidParticle::hitWallPatch
(const wallPolyPatch& wpp,
solidParticle::trackData& td)
{
    vector nw =
wpp.faceAreas()[wpp.whichFace(face())];
    nw /= mag(nw);

    scalar Un = U_ & nw;
    vector Ut = U_ - Un*nw;

    if (Un > 0)
    {
        U_ -= (1.0 + td.spc().e())*Un*nw;
    }
    U_ -= td.spc().mu()*Ut;
}
```

hitWallPatch function of the *solidParticle* class manage the collision of the particles with the wall and treat the proper *move* function routine.

Definition of the unity vector *nw* of normal direction to the wall at the place of collision.

Un is normal to the wall component of a particle velocity;

Ut is tangential component of velocity.

Definition of particle velocity after the collision.